Cavity Expansion Analysis with Applications to Cone Penetration Test and Root-Soil Interaction

by

Peizhi Zhuang BEng, MEng

Thesis submitted to the University of Nottingham for the degree of Doctor of Philosophy

May 2017

Abstract

As one of the most versatile and reliable in-situ devices, cone penetrometers have been extensively used in soil exploration (e.g. soil classification, soil profiling, back-calculation of soil properties etc.) both experimentally and theoretically over the past 80 years. To improve its site accessibility, reduce the required sample size with minimal boundary effects, or model soil penetration by plant roots or earthworms, cone penetrometers with various sizes are often employed both in the field and laboratory. Consequently, size-dependent performance may appear, and this is one of the subjects of this research.

A series of cone penetration tests with three sized cone penetrometer (12mm, 6mm, 3mm) on the Leighton Buzzard sand with two fractions (E and C) was performed at the 1g condition. Evident size effects were observed both in the cone tip resistance and shaft friction. To account for the observed size-dependent behaviour, theoretical methods based on the cavity expansion theory were developed in addition to the available experimental findings. Firstly, a size-dependent (a/d_{50}) quasi-static cavity expansion solution was developed by improving the conventional cavity expansion theory incorporating with a strain gradient theory of plasticity. A stiffer response is modelled for a smaller cylindrical/spherical cavity with this solution. Based on the analogy of cone penetration and quasi-static cavity expansion, the developed size-dependent expansion solution for spherical cavities was employed to quantify the size effect in the cone tip resistance, and fair good agreements were achieved between the theoretical prediction and experimental results. Subsequently, the scale effect observed in shaft friction resistance was explained in terms of the interface frictional strength and mobilised lateral soil stress. The size-dependent (R_i/d_{50}) interface frictional strength was discussed based on the available experimental data of other researchers, and an improved solution based on the elastic cylindrical cavity expansion solution was derived to quantify the size dependency (D/d_{50}) of the mobilised lateral stress on the shaft. In the light of above discussions, dominating factors influencing the size-dependent behaviours in the cone penetration test are summarised.

The other objective of the present research was to model the mechanical interaction between a growing root tip and the surrounding soil. Two elastic solutions for computing the stress and displacement fields around a displacement-controlled ellipse were developed based on the complex variable theory of elasticity and Fourier series method. By assuming the axial cross section of a root tip as a half-ellipse, the two-dimensional soil response to a short-term growing root tip was discussed with the derived elastic solutions. Benefits of radial swelling of the root tip to its axial penetration were summarised, and an approximate analytical method to estimate the soil resistance mobilised by a short-term root growth was suggested and employed in the present root tip-soil interaction analyses.

In addition, influences of the additional shear stress in the process of static and quasi-static cavity expansion were analysed with an elastic-perfectly-plastic model. For Tresca materials, a non-equal initial stress field was considered in the static stress solution, and a quasi-static expansion solution was then derived for a cavity deforming in a hydrostatic stress field considering the material compressibility. The static stress solution is capable of calculating the stress redistribution around a circular rotating probe, and the large-strain quasi-static solution may be useful in theoretical predictions of the tip resistance of a rotating penetrometer (or pile) which has been often utilised in needle cone penetration tests for modelling the root tip elongation. Then the introduced methods in above solutions were applied to the static stress analysis of a circular cavity surrounded by the Mohr-Coulomb material under a non-equal stress field. Based on the conformal mapping function proposed by Detournay and Fairhurst (1987), both a loading and unloading analysis were carried out with the derived analytical solution. It can provide a simple method to predict the plastic failure zone and calculate the stress redistribution around a circular excavation (e.g. tunnel, pipeline) either under loading or unloading.

Keywords: CPT, quasi-static cavity expansion, size effect, mechanical interaction of root-soil, two-dimensional cavity analysis

Acknowledgements

The research presented in this thesis was carried out at the University of Nottingham during the period of Oct. 2013 to Nov.2016 under the supervision of Prof. Hai-Sui Yu and Prof. Sacha Mooney. They brought me this interesting and challenging topic and gave me constant guidance, supervision, and encouragement in this period, which are pivotal and greatly helpful for my study. I want to acknowledge, and sincerely say thanks to them. Many thanks for the invaluable advice on the cavity expansion theory and cone penetration tests from Prof. Hai-Sui Yu, my main supervisor, and his financial support for my research. I am also indebted to Prof. Sacha Mooney for his instructive suggestions about the study of root tip growth and great help and encouragement in the thesis writing.

I would like to thank Dr. Alec Marshall, Dr. Pin-Qiang Mo for their assistance, suggestions, and time for helping in the design, implementation and data analysis of the cone penetration tests. I am also grateful to Jim Meakin and Luke Bedford for their technical support in developing my experimental apparatus. The great help from Dr. Nian Hu in the calculation of the solution presented in Chapter 3 is also greatly appreciated. Sincere thanks also go to Dr. Otto Jan Bakker and Dr. John de Bono for their help in proofreading Chapter 6 and Chapter 7 of the thesis respectively.

Many thanks also go to my friends at Nottingham and colleagues in the Nottingham Centre for Geomechanics. You all make my work and life at Nottingham more enjoyable, productive, and memorable. It must be one of the greatest experience in my life.

I would like to thank my internal examiner, Prof. Matthew Hall, for their encouragement, advice, and annual assessment of my Ph.D. study. The invaluable advice and great encouragements for the present research from my external examiner, Prof. Wei Wu, are also greatly appreciated.

In addition, I would like to thank the financial support provided by the University of Nottingham and the China Scholarship Council for my study.

Last but not the least, I would like to thank my grandparents, parents, and family for their love, support, encouragement, and belief. Thanks to Rui for her enduring understanding, love and support throughout.

This thesis is dedicated to my grandfather in heaven

for bringing me up with so much love,

and giving me the time and courage to succeed.

Table of Contents

List of Figures

List of Tables

Chapter 1

Introduction

1.1 Background

Supply of water and nutrients and mechanical supports from the soil are vital for nature plants, so the growth performance of plants is considerably affected by the soil physical environment. Intensive cropping/grazing system and overuse of heavy machinery in modern agriculture have degraded the physical conditions of arable soil (Hamza and Anderson, 2005; Nawaz et al., 2013). Soil compaction is one major type of degradation which has a profound influence on soil sustainability and root function and therefore has far-reaching consequences on the agricultural production (Hettiaratchi et al., 1990; Lipiec et al., 2012; Tracy et al., 2011). This problem exists worldwide and has been recognised for a long time, but it is still not easy to locate and rationalise due mainly to its location in the subsoil often without evident marks on the soil surface (Hamza and Anderson, 2005). Therefore, effective and quick detection and evaluation of the soil compaction would be of great interests in practice, and deeper understandings of the root growth behaviour under mechanical impedance may provide more solutions for improving and using the over-compacted soils during soil management and plant cultivation.

Among a vast number of in-situ devices, the static cone penetrometer is considered as one of the most versatile and reliable tools available for soil exploration (Bengough et al., 2000; Lunne et al., 1997). It has been widely employed both in the geotechnical engineering (Lunne et al., 1997; Robertson and Cabal, 2015; Sanglerat, 1972; Schmertmann, 1978) and the agricultural engineering (Sudduth et al., 2004; To and Kay, 2005; Whalley et al., 2007). In geotechnical practices, as summarised by Lunne et al. (1997), CPT is generally employed: (1) to determine sub-surface stratigraphy and identify materials; (2) to estimate geotechnical parameters; (3) to provide results for direct geotechnical design. The standard soil cone penetrometers used in the agriculture engineering field are mainly employed to investigate and evaluate the in-situ topsoil conditions (compaction, trafficability, spatial variation etc.) for soil management (ASAE, 2004; Bengough et al., 2000). Apart from the standard sized cone penetrometers (>10mm as described in Chapter 2), smaller sized penetrometers have also been frequently employed in soil explorations (Aydan et al., 2014; Bolton et al., 1999; Kim et al., 2015; Monfared, 2014; Tumay et al., 2001). In particular, needle cone penetrometers are regarded as the best tool to estimate the soil resistance experienced by root growth (Bengough and Mullins, 1990) even with evident overestimations as summarised in Tab. 1-1. Overall, the cone penetration test provides a versatile and quick tool in various soil investigations, but penetrometers in a wide range of sizes are often used for different purposes and their performances may vary with the size (Balachowski, 2007; Eid, 1987; Lima and Tumay, 1991; Wu and Ladjal, 2014).

In view of the above concerns, some experimental and theoretical work are carried out in this thesis in order to explain the potential size-dependent behaviour and model the root tip-soil interaction. A series of 1g cone penetration tests with different sizes were performed to physically reveal the potential size effect, and the theoretical analyses are conducted mainly based on the newly developed cavity expansion solutions.

1.2 Brief review of cavity expansion theory in geomaterials

Cavity expansion theory for geomaterials is concerned with the theoretical study of changes in stresses, porewater pressures and displacements caused by the expansion and contraction of cylindrical or spherical cavities (Yu, 2000). With different emphases for applications in a wide range, cavity solutions can be broadly categorised into three classes: static solutions, quasi-static solutions, and dynamic expansion solutions. Developments of analytical/semi-analytical solutions and potential applications of solutions in each class are briefly introduced as follows. In this study, attentions are mainly concentrated on some low-speed penetration problems (e.g. root tip growth, static cone penetration test (CPT)), in which potential dynamic effect caused by the cavity expansion is usually negligible. Therefore, more attention was deliberately paid to review the developments of solutions belonging to the former two classes.

In general, the stress and deformation fields around a cavity can be obtained by means of solving a governing equation system constituted of stress equilibrium equations, displacement compatibility conditions, and stress-strain relationships with response to given boundary conditions. The complexity of these equations greatly depends on the geometry and stress boundary conditions, the concerned deformation level and the adopted constitutive model. Different assumptions are often made in solutions of different classes, and below discussions briefly highlight these differences.

(1) Solutions for static analysis of cavities

Just as its name implies, neither the dynamic effect nor the kinematic process will be considered in the static cavity analysis. In other words, the stress and deformation responses of a static problem are solely determined by the involved static boundary conditions. In this case, deformation analyses are usually carried out with small-strain theories. Due to above simplifying assumptions, analyses of problems in this branch are relatively simple comparing with solutions in the other two classes, and analytical solutions, therefore, are available for more types of materials and boundary conditions. For example, elastic solutions for two-dimensional analysis of cavities with various shapes and stress boundary conditions (Muskhelishvili, 1963; Savin, 1970), elastic solutions for cavities in a semi-infinity plane (Sagaseta, 1987; Strack, 2002; Verruijt, 1997), elastic-perfectly-plastic solutions for circular cavities under non-uniform stress boundary conditions (Detournay, 1986; Galin, 1946; Tokar, 1990). In the geotechnical engineering field, solutions in this class were often employed in the static stability analysis of cavities and calculations of the static stress and deformation fields around a cavity, such as in the analysis of wellbore stability (Aifantis, 1996; Yu, 2000), prediction of deformation around tunnels (Brady, 2004; Detournay and John, 1988), calculation of the radial stress distribution around piles (Foray et al., 1998; Turner and Kulhawy, 1994; Wernick, 1978). In this study, new static solutions either with the linear elastic or with elastic-perfectly-plastic models were developed, and they will be separately presented in Chapter 4 - 7. More detailed introductions about developments related to these solutions will be given respectively in these chapters.

(2) Quasi-static cavity solutions

In a quasi-static cavity expansion analysis, the stress equilibrium conditions at a given moment are dealt with as a static problem, but the displacement analysis around the cavity is considered to account for the continuous deformation process which was initiated by Bishop et al. (1945). Generally, the cavity is assumed to steadily expand or contract in a monotonic manner, and the deforming speed is assumed to be sufficiently low which allows the dynamic effect to be negligible. To describe the cumulative deformation, a large strain analysis is usually necessary, especially when it is applied to predict the limit expansion pressure. So far, available rigorous analytical solutions for quasi-static cavity analyses mainly rely on the basic assumptions that the geometry and stress boundary conditions are centrally symmetric. In these analytical attempts, two basic methods have been widely employed to calculate the large deformation: total strain approach and incremental velocity method (Durban and Fleck, 1997; Yu and Carter, 2002).

In the former approach, the total finite strains are often described with the definition of natural strains which shows good performances in applications to the radial symmetric problem. The strains and stresses are assumed to depend on the current position of soil particles and their initial positions, therefore it may be termed as Lagrangian methods. By relating the finite strains to the static stresses based on the compressibility equation, a quasi-static solution could be obtained with direct integrations along the deformation history. This method was proposed by Chadwick (1959) in an elastic-perfectly-plastic analysis with the associated Mohr-Coulomb criterion, and then it was extended to non-associated Mohr-Coulomb materials by Bigoni and Laudiero (1989); Yu and Houlsby (1991) in expansion solutions and by Yu and Houlsby (1995) in a contraction analysis. In addition, this method also facilitated developments of some other analytical/semi-analytical solutions which based on hardening/softening soil models (Cao et al., 2001; Chen and Abousleiman, 2012; Collins and Yu, 1996; Mo and Yu, 2016; Papanastasiou and Durban, 1997).

In the second approach (the incremental velocity method), a scale of ‘time’ is usually introduced based on the characteristic of self-similarity (Hill, 1950; Yu and Carter, 2002). Strains in this method are calculated in a function of the current position (radius) and time, so it may be termed as the Eulerian approach. In Hill’s approach, the elastic-plastic boundary is regarded as the scale of “time” or progress of the expansion. It provides a rigorous method to calculate the steady expansion pressure for cavities expanding from zero radius. An approximate solution of the limit expansion pressure was obtained with this approach by Carter et al. (1986) for cohesive-frictional soils, and subsequently, a rigorous analytical similarity solution was developed by Yu and Carter (2002). In addition, the material time derivative can also be transformed to other types based on the similarity characteristic, for example, the method of Durban and Fleck (1997), which has been both applied in quasi-static (Masri and Durban, 2006b) and dynamic cavity expansion analyses (Durban and Masri, 2004; Masri and Durban, 2006a).

Apart from above two approaches, large strain deformations also can be described with some other methods. For cavities deforming in materials without volume loss, the large deformation process can be easily expressed with the condition of equal volume (e.g. undrained clay) (Gibson and Anderson, 1961). Furthermore, the soil compressibility can also be considered by means of introducing a rigidity index as demonstrated by Vesic (1972). Both cylindrical and spherical solutions have been developed with this method for cohesive-frictional soils. Subsequently, Baligh (1976) extended Vesic's solution by adopting a curved Mohr-Coulomb criterion. Additionally, Vrakas (2016) stated that the large strain expansion process can be approximated with the corresponding small strain displacement solution by multiplying a hyperbolic function in a hydrostatic stress environment, which made a small strain deformation solution possibly practicable in a quasi-static cavity expansion analysis. Moreover, by assuming the medium around the cavity composed by an assemblage of thin cylindrical (spherical) shells, some semi-analytical solutions considering the non-linear property of soils were also frequently used, for example, those from Ladanyi (1972); Salgado et al. (1997).

Quasi-static cavity expansion/contraction theory for geomaterials has wide applications in estimating the bearing capacity of shallow and deep foundations (Randolph et al., 1994; Vesic, 1972), interpreting *in-situ* soil testing (e.g. pressuremeter test, cone penetration test) (Gibson and Anderson, 1961; Salgado et al., 1997; Yu, 2006), predicting deformation around tunnels (Marshall, 2012; Yu and Rowe, 1999). More comprehensive review and discussion about the development of quasi-static cavity expansion theory and its applications in geotechnical engineering refers to Yu (2000).

(3) Dynamic cavity expansion solutions

In dynamic cavity expansion analyses, the target inertia effect has to be taken into account due to the high deforming speed of cavitation. Comparing with quasi-static cavity expansion solutions, an additional term with regard to the expansion velocity of the cavity wall is usually included in dynamic expansion solutions (Katzir and Rubin, 2011; Rosenberg and Dekel, 2008). The dynamic cavity expansion was often regarded as self-similar in analytical/semi-analytical analyses (Crozier and Hunter, 1970; Durban and Fleck, 1997; Durban and Masri, 2004; Hunter and Crozier, 1968; Masri and Durban, 2006a). Consequently, the inertia effect caused by a high-speed expansion can be expressed in terms of a conceptual 'time' scales (e.g. the instantaneous cavity radius), and then solutions can be obtained by solving the equation system consisted of the stress equilibrium equations, constitutive models, and conditions of conservation of matter. The dynamic cavity expansion analysis can provide a useful theoretical tool for modelling various high-speed expansion problems, such as projectile penetration, underground explosion, impact cratering etc.(Ning et al., 2013; Rosenberg and Dekel, 2008; Satapathy, 2001; Warren and Forrestal, 1998).

1.3 Differences between cone penetration and root-tip growth

Apart from the above engineering applications, the cone penetrometer also provides the best estimate of the soil resistance to the root growth in soils (Bengough and Mullins, 1990; Mckenzie et al., 2013). Different to standard penetrometers (>10mm), needle sized probes with various shapes and testing methods have been developed in studies of this specific topic (Barley et al., 1965; Bengough and Mullins, 1991; Iijima et al., 2003; Misra et al., 1986b). However, it was found that the soil resistance measured by a pushing-in metal probe is about 2-8 times higher than that experienced by the root tip growth (Bengough et al., 2000; Bengough and Mullins, 1990), for example, the direct comparisons listed in Tab. 1-1. To account for this discrepancy, potential contributing factors are discussed first, and more targeted theoretical and experimental explorations will be presented in following chapters of this thesis.

The flexible root tip can physically adapt to stress and structure variations in the surrounding soil by altering the preferential growing direction (tortuous growth path) to take advantage of pre-existing pores/cracks or weakening areas in the soil, changing the growth sequence (size and shape) to reduce the axial soil resistance, excreting mucilage and sloughing off border cells to lubricate the interface as detailed in Section 5.1. However, the rigid cone penetrometer measures the average soil resistance in a zone around the cone tip with a straight penetration pathway. The metal-soil interface frictional resistance is much higher than that between the root tip and surrounding soils (Mckenzie et al., 2013). In addition, although the macroscopic spatial variation of soil strength and structure can also be detected by the metal cone, it cannot equivalently reflect the changes in a scale smaller than its size. If a penetrometer with a comparable size of the root tip is used, the microstructure of soil (non-local behaviours) may significantly influence the cone tip resistance, which has not been clearly identified as discussed in Chapter 3 and Chapter 4. The size-strengthening effect in this dimension level may lead to higher soil resistances to the rigid penetrometer, which may partly lead to the concerned discrepancy.

Tab. 1-1 Comparison of measured resistances on roots and needle penetrometers

Reference	Stolzy and Barley (1968)	Whiteley and Dexter (1981)	Misra et al. (1986b)	Bengough and Mullins (1991)	Bengough and McKenzie (1997)	Iijima et al. (2003)
Soil	remoulded sandy loam	remoulded cores and Undisturbed field clods (fine sandy loam)	artificial aggregates with different size (loam)	undisturbed cores of sandy loam	remoulded cores of sandy loam	compacted sandy loam soil
Seed species	Pea	Pea	Pea, Cotton, Sunflower	Maize	Maize	Maize
Probe diameter (mm)	3	1, 1.25, 1.5, 1.75, 2	1	0.5 and 1	1	0.98
Probe semi-angle (°)	30	30	30	30 (5)***	7.5	15
Penetration rate (mm/min)	0.17 (1cm/hr)	3	3	4	2	1
Probe penetration depth	maxium q_c at 5mm	4mm	4mm	when it reaches constant value	Plateaued at 2-6mm	10mm-20mm
Cross-section of the root: Diameter (mm)	1.2-1.3	1.06-1.23	0.44-1.40	Initial:1.12-1.14 Final:1.35-1.36	Around 1.1	Intact: 1.10-1.16 Decapped:1.11-1.53
Cross-section of the root: Distance behind apex	3 to 5mm	Around 4mm	1mm and at the air gap	2 to 5	1-6mm	2 to 5 mm
Resistance ratio = (probe / root)*	Around 2	2.6-5.3	1.8-3.8	4.5-7.5	2.5-4.8	Intact: 3.1 Decapped:1.8
Number of replicates	2	120	324	14	19	10

* The point resistance (penetration force/ cross-section area) are compared directly.

Detailed reviews and further discussions about above aspects will be given in following chapters later. Apart from them, investigations about another two commonly mentioned factors, tip shape and penetration speed, probably contributing to the concerned discrepancy (Bengough et al., 2000; Bengough and Mullins, 1990) are reviewed as follows.

(1) Shape effect of the tip

The tip shape determines the mode of soil deformation during penetrations, therefore the mobilised soil response, stress distribution and pore pressure dissipation around the tip may vary with changes of its shape (Greacen et al., 1968; Levadoux and Baligh, 1986). The soil deformed by a blunt penetrometer is more like a spherical compression. However, a cutting penetration may occur around a sharp cone instead, and the caused soil deformation is more closely approximated by the expansion of a cylindrical cavity.

Experimental and theoretical analyses showed that changes of the cone tip resistance with the tip shape greatly depends on the interface friction/adhesion property (Durgunoglu and Mitchell, 1973; Meyerhof, 1961). In general, the tip resistance of a steel penetrometer (smooth or semi-rough interface) may decrease with decreases of the apex angle (be sharper). For example, a slight decrease was reported by Koolen and Vaandrager (1984) with cones of tip angles varying from 180^o to 30^o on 67 different agricultural fields. Sharp decreases were observed by Silvestri and Fahmy (1995) with cones of tip angles from 180^o to 34.7^o in penetration tests on artificial clays and no obvious change of tip angles from 34.7^o to 7.5^o was found. In contrast, the end resistance of cones with perfect rough surfaces (or experiencing great adhesion forces) may sharply increase with decreases of the tip angle when it is smaller than 30^o and becomes insensitive to the changes of tip angles from 30^o-180^o since the formation of a front soil cone (Kim et al., 2006; Muromachi, 1974).

A root tip deforms the ahead soil more laterally (Greacen et al., 1968). The induced soil deformation is different to that caused by a blunt probe, so penetrometers with sharp tips were suggested to model the root tip growth in soil (Bengough and Mullins, 1991; Bengough et al., 1997; Whalley et al., 2000). For a more sharp cone, a larger contact area it possesses with the same base size and the interface friction applies more close to the penetration direction, so the mobilised frictional resistance will take a relatively larger proportion of the total resistant. Contrarily, due to the lubricating effect caused by mucilage excretions and the sloughing off of border cells around the root cap, a much lower soil frictional resistances is experienced by the root cap than a metal interface (Mckenzie et al., 2013). Therefore, to quantify the axial contribution of the interface friction is very important when a shape cone penetrometer is utilised to estimate the soil resistance encountered by the root elongation. Influencing factors to the soil-structure interface friction are summarised in Section 4.2, and frictional properties of the root-soil interface are discussed in Section 5.1.1. It needs to point out that much effort has been made to reduce the interface frictional resistance between the metal penetrometer and the surrounding soil by means of rotating the penetrometer (Bengough et al., 1997; Mckenzie et al., 2013; Sadeghi et al., 2014; Waldron and Constantin, 1970), lubricating the interface (Tollner and Verma, 1987), or add a sliding soft continuum skin (Sadeghi et al., 2013) etc.. The rotating technique was more frequently used. Its penetration mechanism was studied by Bengough et al. (1997), and additional influences of the induced shear stress on the soil deformation are further analysed in Chapter 6. Penetration mechanisms of the other two methods have received less attention. Overall, more effort is required to better model the interface frictional behaviour between the root tip and soil, and better performance may be acquired with a combination use of these techniques.

(2) Penetration rate effect

The specified rate of penetration for performing standard cone penetration tests (CPT) is 20±5 mm/s (1200±300 mm/min) in geotechnical practices and around 30 mm/s (1800 mm/min) in agricultural engineering (ASAE, 2003). However, roots elongate typically at a rate of 1mm/h (0.0167mm/min) or less (Bengough et al., 2000; Waldron and Constantin, 1970), therefore slower penetration rates are generally utilised in needle cone penetration tests aiming to model the root tip-soil interaction as realistic as possible. Contradictory rate effects were reported in tests with variable penetration rates around the speed of root tip elongation (Gerard et al., 1972). Almost doubled soil resistance was measured at the rate of 0.0029 mm/min (0.175mm/hr) than that with the rate of 1mm/min (60mm/hr) in tests conducted by Cockroft et al. (1969). Increases of 25%-36% with a tenfold increase in penetration rate, varying with soil matric suctions, were observed by Waldron and Constantin (1970) in tests with insertion rates ranging from 0.0035 mm/min to around 1 mm/min. Little attention has been diverted to explaining this opposite influence in needle penetration tests, and it was usually believed that the tip resistance monotonically increases with an increasing penetration rate (Bengough et al., 1997; Gerard et al., 1972;

Voorhees et al., 1975). However, non-monotonic dependencies of the tip resistance on the penetration rate have been recognised in penetration tests over a wider speed range (Bemben and Myers, 1974; Kim et al., 2006; Roy et al., 1982). It was extensively studied from the geotechnical perspective with emphasis on the inverse strengthening effect with a decreasing rate (Chung et al., 2006; Finnie and Randolph, 1994; Jaeger et al., 2010; Kim et al., 2008; Lehane et al., 2009; Schneider et al., 2007a; Silva et al., 2006; Suzuki and Lehane, 2015). It was generally explained (Chung et al., 2006; Lehane et al., 2009) as: (1) while the condition around an advancing penetrometer is undrained ($v > v_{up}$), the measured tip resistance decreases as the rate of penetration is decreased, which is dominated by the viscous effect (strain rate effect); (2) once the penetration rate reduced sufficiently for partial consolidation to occur ($v_{pf} < v < v_{up}$), the tip resistance increases with decreases of the penetration rate due to the local strengthening of soil ahead of the penetrometer. Therefore, there are two transition points are usually concerned to distinguish the different rate effects, which are the point (v_{up}) from undrained to partially drained response where the viscous and partial consolidation effects balance out and the point (v_{pf}) where fully drained conditions are reached with sufficiently slow penetration rates. Real values of these two transition points vary with soil type and properties (e.g. clay contents, hydraulic properties), penetrometer size, soil stress history, etc. (Chung et al., 2006; Jaeger et al., 2010; Kim et al., 2008; Suzuki and Lehane, 2015). Detailed summaries of related investigations on the penetration rate effect in CPTs refers to Lunne et al. (1997); Suzuki (2015).

The commonly used penetration rates of needle CPTs for modelling root tip-soil interaction are much faster than the usual root growth speed, ranging from 50 to 600 times (Mckenzie et al., 2013). These penetration rates may lie in the range of $v_{pf} < v < v_{up}$ in some cases (Bemben and Myers, 1974; Kim et al., 2006), in which the rate effect may relatively large, depending on the drainage condition around the advancing cone. In addition, the water flow in the close vicinity of roots (rhizosphere) is very different to that around a metal probe due to the dynamic water uptake of roots. The hydraulic conductively and water retention in this zone are greatly determined by root exudates, especially the function of mucilage (Carminati et al., 2010; Carminati and Vetterlein, 2013; Carminati et al., 2016). Therefore, to better evaluate the rate effect in affecting the soil resistance encountered by a growing root tip and an advancing rigid cone, not only the potentially significant rate effect in the needle cone penetration test needs to be determined (e.g. small sized piezocone with additional measurement of the pore water pressure (Schneider et al., 2007a)), influences of the complex physical and chemical interaction of root exudates and soil particles also need to be considered.

In addition, apart from above aspects, interactions between neighbouring roots, in reality, may also affect the soil penetration of an individual root (Bengough and Mullins, 1990).

1.4 Objectives and outline of the thesis

Eight chapters are included in this thesis. At first, a brief introduction about the background of this research is given in Chapter 1. Afterwards, the main contents are presented in chapter 2 to chapter 7. Specifically, to physically shed lights on the potential size effect in cone penetration tests, a series of 1g cone penetration tests has been conducted. The test design, preparation, implementation and results are presented in Chapter 2. To account for the size-dependent cone tip resistance, a strain gradient-dependent cavity expansion solution is developed in Chapter 3. Explanations for size effects observed in the present cone penetration tests (with regards to shaft friction and tip resistance respectively) are presented in Chapter 4 based on some available experimental findings and the developed theoretical methods. Subsequently, the mechanical response of the surrounding soil to a short-term root tip growth is studied in Chapter 5. Two elastic solutions for a displacement-controlled elliptical cavity were developed based on the complex variable theory of elasticity, and they were employed to evaluate the influence of root radial swelling to the axial elongation in theory. Considering the common use of rotating penetrometers in estimating the soil resistance experienced by a growing root tip, cavity expansion analyses in Tresca materials with an additional consideration of the inner shear stress are carried out in Chapter 6. As a continuation of the methods described in Chapter 5 and Chapter 6, an analytical solution for the two-dimensional elastic-plastic cavity analysis in Mohr-Coulomb materials is developed in Chapter 7. A non-equal initial soil stress field can be considered while calculating the static stress and strain distributions around a circular cavity both under loading and unloading conditions. Finally, a summary of the main findings in the present research and some suggestions for related further research are given in Chapter 8.

Chapter 2

1g laboratory cone penetration tests

2.1 Introduction

Since its first application in soil site investigation from the 1930s, cone penetration test (CPT) experienced lots of developments in aspects of physical functionality and methods of interpretation. To promote its application and standardisation, some specific standards were recommended in different areas, for example, standards listed by Lunne et al. (1997) for geotechnical engineers and from American Society of Agricultural Engineers (ASAE, 2004) for practices in the agriculture engineering. Not surprisingly, the specified devices and testing procedures in these two areas are more or less different for different purposes. To be specific:

To evaluate the strength and stability of soil or the safety of structures on the soil, deep penetrations with various data readings are required in geotechnical practices. The standard cone penetrometer in this area is usually composed of a series of cylindrical rods (35.7mm in diameter), one side friction sleeve (area 150cm^2) close to the cone and a conical tip (apex angle of 60^o) (Lunne et al., 1997). In addition, in order to provide more spaces for sensors or increase ruggedness of the penetrometer, a larger sized standard penetrometer of the same shape was also recommended in ASTM-D5778-12 (2012), which has a base diameter of 43.7 mm. To acquire more information simultaneously, the penetrometer is increasingly equipped with various sensors (such as stress sensors, geo-environmental sensors, geophone etc.), benefiting from developments in sensor technology and data acquisition system.

For applications in the agricultural engineering, ASAE specified two different sized soil cone penetrometers as shown in Fig. 2.1 (ASAE, 2004). They are mainly employed to measure the soil resistance to penetration at relatively shallow depths (Bengough et al., 2000). The designed soil penetrometers also consist of cylindrical shafts with a conical tip at the end. These recommended penetrometers are smaller in size, cones are sharper (12.83mm in diameter for small cone, 20.27mm large cone, cone tip angle of 30^o) than the standard cone penetrometers in geotechnical practices, and the shaft diameter is reduced to eliminate the side soil friction.

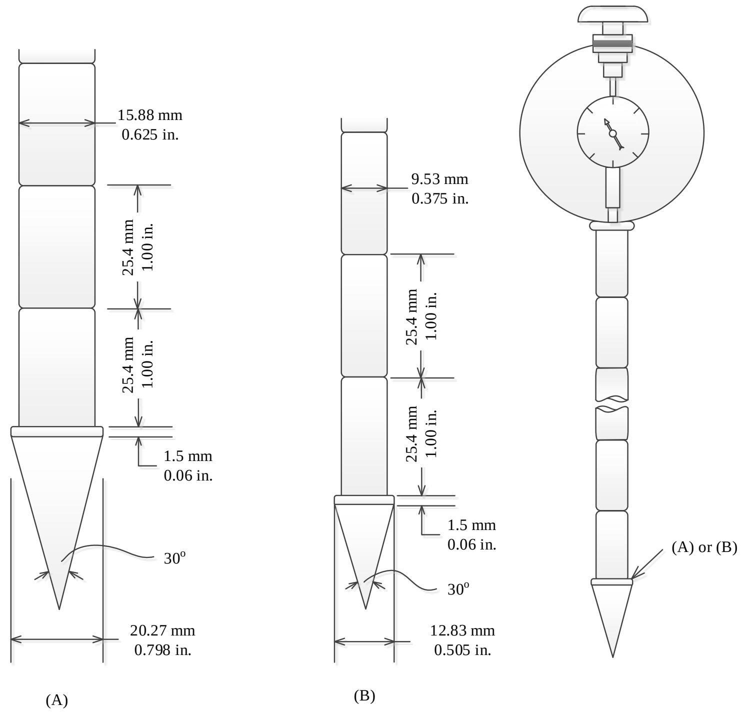

Fig. 2.1 Standard soil cone penetrometers from ASAE (2004)

In addition, various nonstandard penetrometers (circular shaft with a conical tip) have also often been developed for some specific applications (Abouzar and Sepideh, 2015; Aydan et al., 2014; Bengough et al., 2000; Bolton et al., 1993; Eid, 1987; Kurup et al., 1994; Ngan-Tillard et al., 2011; Tumay et al., 1998). Among them, small sized cone penetrometers have attracted growing interests due to some inherent advantages, such as

(1) Smaller downward thrust needed, which is energy-saving and can improve its mobility and site accessibility in the field (Kurup and Tumay, 1998). It may be beneficial in applications in sites with insufficient space for large devices, ground exploration on the moon and the Mars etc.;

(2) Higher sensitivity to variation of the soil stratigraphy (for example, to identify the thin hard or weak layer) (Mo, 2014; Schmertmann, 1978);

(3) Smaller sized sample required in the laboratory tests to get rid of the potential boundary effect, and it can effectively reduce the labour, time and cost in sample preparation (Eid, 1987) (e.g. in chamber calibration tests), especially for CPT on the centrifuge platform.

Additionally, needle cone penetrometers with a diameter ranging from 1 to 3mm have been frequently employed to estimate the soil resistance encountered by the root tip during growth since their geometrical similarity (Bengough et al., 2000). Overall, cone penetrometers with different sizes have their own advantages in different applications, but their performance may significantly vary in some conditions, especially among small sized probes. Considering the wide application and promising prospect of small sized cone penetrometers both in the geotechnical and agricultural field, the potential influence of size variation in cone penetration tests will be discussed in this study.

2.2 Review of size-dependent behaviours in end soil resistance

Soil resistances experienced by a vertically moving object generally consist of end resistance and side friction. The end resistance usually is the major concern in cone penetration tests, especially for applications in the agricultural engineering. In addition, the side friction acting on very small sized probes is not easy to be precisely measured. Hence, present tests will be designed with priority to study the size effect in the tip resistance, and some existing researches on this topic are reviewed before the test design.

In general, the bearing mechanism of foundations varies with their physical characteristics, mechanical properties of soil, loading types, embedment depth, stress environment, water condition etc. (Meyerhof, 1951). Accordingly, possible size-dependent behaviour in the end bearing resistance may perform differently with variations of these factors. For clarity, they are broadly subdivided into three groups based on differences in the bearing mechanism (or foundation types), and possible explanations of the size effect in each group will be briefly summarised as follows.

2.2.1 Size effect of the bearing capacity factor in surface footing tests

For a vertically loaded footing resting on a free surface of uncemented sand deposit, the ultimate bearing capacity can be expressed as $q_{ult} = N_\gamma \gamma B_s / 2$. Size effects of this kind of shallow foundation are usually discussed in terms of the non-dimensional bearing factor N_γ. It is found that, in general, N_γ increases with decreases of the transversal width/diameter of the foundation. To account for this size effect, a large amount of investigations by means of physical model tests (Cerato and Lutenegger, 2007; Kimura et al., 1985; Tatsuoka et al., 1991; Toyosawa et al., 2013; Yamaguchi et al., 1976) and numerical simulations (Loukidis and Salgado, 2010; Siddiquee et al., 1999; Tejchman and Herle, 1999; Yamamoto et al., 2009) has been carried out in the past several decades, and two main reasons were generally concluded: the stress-level dependency of sand strength and progressive failure phenomenon along the slip lines. Specifically:

(1) The ultimate bearing capacity of footing foundations usually gets higher with increasing sizes of the footing (Cerato and Lutenegger, 2007). In general, the peak friction angle of sands decreases with an increasing mean normal effective stress, especially under relatively low confining stress levels (Bolton, 1986; Krabbenhoft et al., 2012). Therefore, the nonlinear shaped failure envelope has been incorporated into a series of methods to account for the size-dependent behaviour of N_γ (Bolton and Lau, 1989; Hettler and Gudehus, 1988; Kutter et al., 1988; Ueno et al., 1998; Zhu et al., 2001).

(2) The shear strength of soil along the slip line is not simultaneously mobilised with an increasing loading, and it is closely related to the strain level. Along the localised strain zone (shear band), the induced strain level usually decreases with the increasing distances away from the foundation. It means that the mobilised friction angle of soil close to the foundation may reduce to a post-peak value (even to the critical state value φ_{cv}) when the global failure occurs, and only a portion of the soil along the slip line is deforming at its peak strength. Physical tests found that a higher strain level would be induced by a wider structure (Kimura et al., 1985; Yamaguchi et al., 1976). Therefore, the progressive failure phenomenon is often considered as one important reason in explaining the mentioned size effect (Conte et al., 2013; De Beer, 1965), and it sometimes is also regarded as the particle size effect due to the high dependency of the shear band width with the mean particle size (Siddiquee et al., 1999; Tatsuoka et al., 1991).

Overall, the mobilised soil shear strength greatly depends on the induced stress and strain level, and different levels of them are usually produced by different sized footings at failure. These dependencies were commonly employed to account for the observed size difference of N_γ individually or in combination. Basically, the mentioned size effect may be a consequence of combined effects of these two aspects (Perkins and Madson, 2000; Siddiquee et al., 1999; Tatsuoka et al., 1991). A strong evidence supporting this view is that the stress level effect caused by variations of the foundation size not only influences the friction strength of sands but also impacts the potential or degree of progressive failure (Perkins and Madson, 2000).

2.2.2 Size effect of the end bearing resistance in pile foundations

As summarised by Meyerhof (1983) and Chow (1996), the end bearing resistance of piles (q_b) statistically reduces with increases of the pile diameter based on relative large databases of full-scale pile loading tests, and the finding of Chow (1996) has been directly applied in the CPT-based pile design method of ICP-05 (Jardine et al., 2005). Possible explanations of this size effect have been discussed by White and Bolton (2005), Borghi et al. (2001) etc., and they were summarised as follows:

(1) Partial mobilisation effect. There are many different criterions to determine the end bearing capacity of piles, for example, with reference to a given settlement (s_p) or to a given changing rate of the load-settlement curve. The applied displacement in pile loading tests is usually smaller than the required displacement to reach the 'plunging' load for continued penetration. Before reaching that fully mobilised or steady bearing capacity, q_b would be highly correlated to s_p / D_p and proportionally increase with it. Therefore, if q_b is determined by the load that required to a specific settlement, the level of mobilisation of the ultimate soil resistance will be clearly different for different sized piles. In other words, a higher level of the soil resistance will be mobilised by a smaller pile with the same displacement due to the larger value of s_p / D_p.

(2) Partial embedment effect. This effect may become significant in two typical conditions: shallowly embedded piles and piles with end bases resting close to an interface of two layers with contrasting strengths (local inhomogeneity). Firstly, for shallow pile foundations, this effect is mainly due to the difference in the embedment ratio of different sized piles within the same embedment depth (Mo, 2014). Secondly, for a deep pile foundation, this size effect may be caused by the difference in the sensitivity of different sized piles to hard/weak layers around the concerned horizon (Mo et al., 2016). Some simple methods for estimating the end resistance around a weak/hard layer have been proposed and used, for example, methods given by Meyerhof (1983); White and Bolton (2005).

(3) Shaft-based interaction model (Borghi et al., 2001). This model states that the downward shaft shear stress leads to an increase of the mean stress on the level of the pile base, and the increased mean stress is able to increase the end bearing resistance. Based on an assumed friction distribution curve along the shaft, it is found that the contribution

of this effect varies with the pile size, which shows that a higher ratio of increase would be experienced by a smaller pile.

(4) Local strength and deformation characteristics around the interface. The interface friction strength and localised deformation behaviours (shear band forming, sand particle crushing, shear dilation etc.) are, more or less, influenced by the particle size and pile size (Jardine et al., 2005). Therefore, these effects may also lead to some size-dependent differences in some small sized model tests, but their influences on practical pile foundations might not be that evident.Terzaghi, 1943

Among above factors, White and Bolton (2005) attributed the size-dependent behaviour mainly to the partial mobilisation effect and the partial embedment effect through reassessing the compiled database of Chow (1996). It was found no trend of q_b varying with the pile diameter when these two effects were eliminated, but it is believed that the other two reasons may also play important roles in some cases, for example, in small sized pile model tests.

2.2.3 Size effect of tip resistance in continuous penetration tests

As summarised by Durgunoglu and Mitchell (1973), the penetration resistance (q_c) varies with the relative penetration depth, size of probe, soil friction angle, soil compressibility, in-situ stress level, cone angle, cone surface roughness etc.. Among these factors, the possible probe size effect is studied with priority in this research.

Attempting to identify the possible size effect in the cone tip resistance, a large number of penetration tests has been carried out both in laboratory conditions (Balachowski, 2007; Bengough and Mullins, 1990; Bolton et al., 1993; De Beer, 1963; Eid, 1987; Lee, 1990; Phillips and Valsangkar, 1987; Tollner and Verma, 1987; Wu and Ladjal, 2014) and in-situ measurements (Dexter and Tanner, 1973; Kurup and Tumay, 1998; Lima and Tumay, 1991; Sudduth et al., 2004; Thomas, 1965). These physical approaches can be generally categorised into three groups as:

(1) Penetration tests with different sized probes at 1g condition (or the same gravity condition).

(2) “Modelling of models” procedure. Model a given prototype diameter (D_i) by using cones of different diameters (d_i) at different acceleration levels ($n_{i\times}$g) on the centrifuge platform.

(3) Prototype probes of different sizes are modelled by using a same sized probe running at different acceleration levels (n g) on the centrifuge platform.

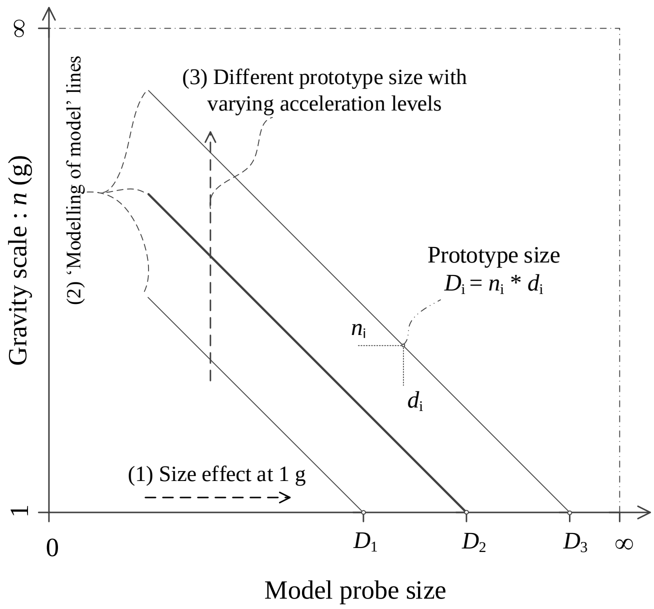

Fig. 2.2 Illustration of methods exploring size-dependent behaviours in CPT

Size parameters appearing in cone penetration tests mainly include the probe diameter (D_{CPT}), grain size (mean particle size d_{50}), penetration depth (H), the surface roughness (R_i). In general, their influences on the tip resistance are closely related to the probe diameter, such as the H/D_{CPT} effect and D/d_{50} effect. Differences caused by variations of D_{CPT} are all referred as the size effect depending on the probe diameter here. Conserved conditions in above physical approaches are different. As a consequence, dominant size factors (size effect) may vary among these three physical approaches (e.g. (Klinkvort et al., 2013)), and they are discussed in order as follows.

(1) Size effect observed in 1g penetration tests

With the same g-level, a same initial stress level at the same depth can be achieved in sands of similar states. Therefore, q_c at the same embedment depth (or values at the steady state) is usually compared to maintain the initial stress level. At a same initial stress level, the size-dependent tip resistance may mainly due to the geometry size effect (H/D effect) in shallow depths and the strain-level dependent behaviour (D/d_{50} effect) in deep depths (Eid, 1987; Lee, 1990), but these effects cannot be easily separated in this kind of tests.

1) In calibration chamber tests

In geotechnical engineering, calibration chambers are commonly employed to simulate the field soil condition in the laboratory (e.g. detailed in the section 2.3.3.1). Different sized penetrometers were usually used to evaluate the lateral boundary effect (Parkin and Lunne, 1982), but potential influences caused by variations of the penetrometer size were seldom excluded. The required diameter ratio of the chamber over the penetrometer (B/D_{CPT}) to get rid of the lateral boundary effect may vary with sand density, sand compressibility, boundary conditions and so forth. For calibration chamber tests with typical dense silica sands, B/D_{CPT} of value as high as 50-70 may be required (Jamiolkowski et al., 2003; Mayne and Kulhawy, 1991; Pournaghiazar et al., 2012; Salgado et al., 1998), but no boundary effect would be found in loose sands when B/D_{CPT} becomes as low as 20 (Eid, 1987). Based on some calibration chamber test results and field data, Schmertmann (1978) reported that no size effect was found in tests with D_{CPT} in the range of 25.2mm (base area 5cm^2) to 50.5mm (20cm^2), even perhaps to 71.4mm (40cm^2), as long as the soil particles are very small relative to the cone diameter. The experimental findings presented in Tab. 2-1 and Fig. 2.3 indicate that the variation of penetrometer size leads to evident size-dependent differences of the tip resistance as well as the lateral boundary effect, at least the results from tests on loose sands.

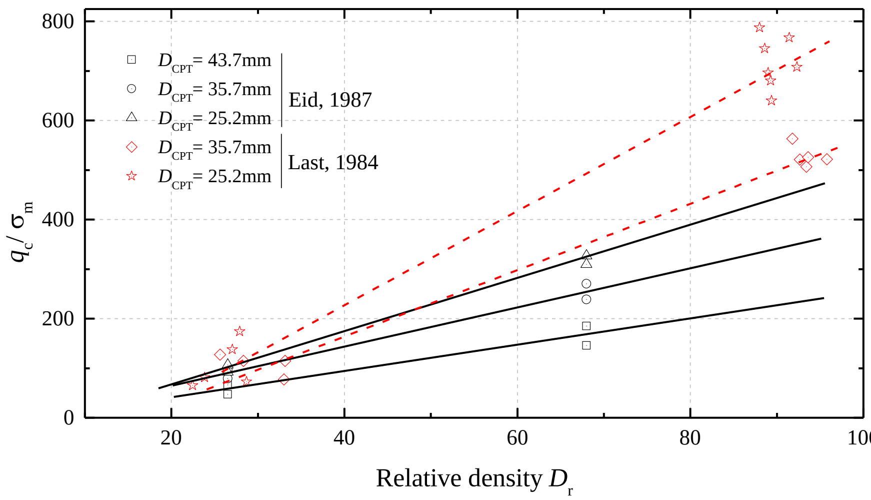

Fig. 2.3 Normalised cone tip resistance vs. relative density (after Eid (1987))

Tab. 2-1 Size variation of the cone tip resistance in calibration chamber tests

Reference	Sand	D_{CPT}	Chamber Boundary	B/D_{CPT}	Sand relative density	q_c

Last (1984)*	Hokksund sand	25.2mm	BC1**	48	Loose (30%)	
		35.7mm		34	Dense (90%)	Greater with the smaller penetrometer
Eid (1987)	Monterey No. 0/30 sand (d_{50}=0.45mm)	23.2mm	BC1	65	Loose (24%) Dense (63%)	
		35.7mm		42		
		43.7mm		34		

* after Eid (1987). ** defined in Fig. 2.13.

To exclude the size effect in CPTs is useful to improve the accuracy in quantifying the lateral boundary effect in tests within calibration chambers. In general, smaller sized samples are required by tests with smaller sized probes, which can effectively reduce the labour, time and costs in sample preparation in turn. Additionally, tests with smaller sized samples can also facilitate to achieve visualisation of internal soil deformations during penetrations, which may give more insight into the soil-structure interaction. For example, cone penetration tests by using transparent soil and particle image velocimetry (Ni et al., 2010) or the X-ray computed tomography technique (Ngan-Tillard et al., 2005; Paniagua et al., 2013).

2) In-situ cone penetration tests

Different trends of q_c with varying cone diameters have also been observed in in-situ cone penetration tests as summarised by Eid (1987); Lima and Tumay (1991). Field experimental evidence indicating significant size effect refer to (Kurup and Tumay, 1998; Lima and Tumay, 1991; Sudduth et al., 2004; Sweeney, 1987; Tumay et al., 2001). In specific, Sweeney (1987) reported that size effect of q_c exits between a small (22.8mm, 4.1cm^2) sized cone penetrometer and the standard one (35.7mm, 10cm^2) on dense sands in field tests. Lima and Tumay (1991) also found that a smaller sized penetrometer gives a higher value of q_c based on a series of deep-sounding CPTs in fields of sandy, silty and clayed soils. Statistical analysis showed that q_c measured with the standard penetrometer can be effectively estimated by multiplying a factor of 0.85 with that obtained with a 12.7mm (1.27cm^2) sized cone penetrometer, and no significant variation was found between q_c from the standard and 43.7mm (15cm^2) sized cone penetrometer. Subsequently, Kurup and Tumay (1998) and Tumay et al. (2001) reported that the average q_c obtained with a 16.0mm (2cm^2) sized penetrometer is about 10% higher than that with the standard cone penetrometer in applications to various in-situ sites. In addition, Sudduth et al. (2004) reported that the average cone resistance measured with the ASAE standard small cone penetrometer (base diameter 12.8mm) was 30% higher than that with the ASAE standard large cone (base diameter 20.3mm) based on a large number of shallow cone penetration tests on eight field sites of silty clay loam or silt loam. In sum, above findings indicated that stiffer soil responses would be experienced by smaller penetrometers. However, a non-significant variation of q_c with different sized cone penetrometers has also been reported in some field tests (De Ruiter, 1982; Sanglerat, 1972; Schmertmann, 1978). Sanglerat (1972) concluded that size effect is negligible for penetrometers (piles) of diameters varying from 36 to 110mm in all soils. De Ruiter (1982) also suggested that no significant variation in q_c with cone sizes varying from 25.2 ($5cm^2$) to 43.7mm ($15cm^2$).

3) Other 1g penetration tests

Apart from above tests with penetrometers of sizes around the standard ones, some other cone penetration tests with a larger range of penetrometer sizes or needle sized cone penetrometers have also been performed both by geotechnical and agricultural researchers. Different observations about the size effect were also reported (Bengough and Mullins, 1990) (e.g. listed in Tab. 2-2). Although no consensus has been generally achieved about influences of the concerned size effect, it is believed the size effect (size-strengthening phenomenon) may be much more significant or likely to perform in needle cone penetration tests than tests with the standard sized penetrometers. It may partly contribute to the concerned discrepancy (higher soil resistance on needle cone penetrometers than that on the root tip) as discussed in the first chapter.

Tab. 2-2 Experimental results of size effect in miniature cone penetration tests

Reference	Soil	D_{CPT} /mm	Penetration rate	Sample size and Boundary condition	Depth of compared q_c	Size effect
Barley et al. (1965)	remoulded sandy loam	1, 2, 3	1 cm/hr	diameter 7.2cm height 2cm confined radially with closely fitting metal rings or unconfined	--	Not significant
Gooderham (1973)*	--	1,2	--	--	--	Greater q_c with smaller D_{CPT}
Muromachi (1974) **	Yodo clay (remoulded)	5.7-50	1.7mm/sec	--	--	Increase with decrease of D_{CPT}
Bradford (1980)	undisturbed	3.8,5.1	--	--	--	Not significant
Whiteley et al. (1981)	remoulded loam at 20% water content	1,1.25, 1.5,1.75,2	3mm/min	confined cores of 20mm height and 50mm diameter	4 times of D_{CPT}	Not significant
Whiteley and Dexter (1981)	remoulded (various soil textures)	1, 1.25, 1.5, 1.75, 2	3mm/min	20mm in height, 50mm in diameter (and containers of 25mm and 73mm in diameter) Laterally confined	8mm	Increase with decrease of D_{CPT}
Tollner and Verma (1987)	remoulded sandy and silty soils	9.5, 12.8, 15.9, 19.1, 25.4	8mm/sec	polyethylene container	12-15cm	Increase with decrease of D_{CPT}

Bengough and Mullins (1991)	undisturbed cores of sandy loam	0.5,1	4mm/min	56mm diameter 40mm height	When it reach constant value	Greater q_c with smaller D_{CPT}
Ladjal (2013)	coarse uniform quartz sand (d_{50}=0.9mm) Both loose and dense	2, 5, 10	3mm/min	rigid cylindrical mould of 83mm in diameter and 14mm in height	Average 5-8 times of D_{CPT}	Increase with decrease of D_{CPT}
Wu and Ladjal (2014)	coarse uniform quartz sand (d_{50}=0.9mm) Both loose and dense	0.5, 0.8, 1, 1.5 ,2	3mm/min	rigid cylindrical mould of 83mm in diameter and 14mm in height	Depth greater than 5 times of D_{CPT}	Increase with decrease of D_{CPT}

* It refers to Bengough and Mullins (1990). It showed that the penetration resistance encountered by 1mm sized probe was 35% to 74% greater than that of 2mm sized probe.

** The apex angle of used end cones in this research is 30^{o}, and it is 60^{o} for others.

*** Notice that various sample boundary conditions have been applied in these tests, and some of the measured cone tip resistances may also be influenced by the boundary (lateral and base) effects.

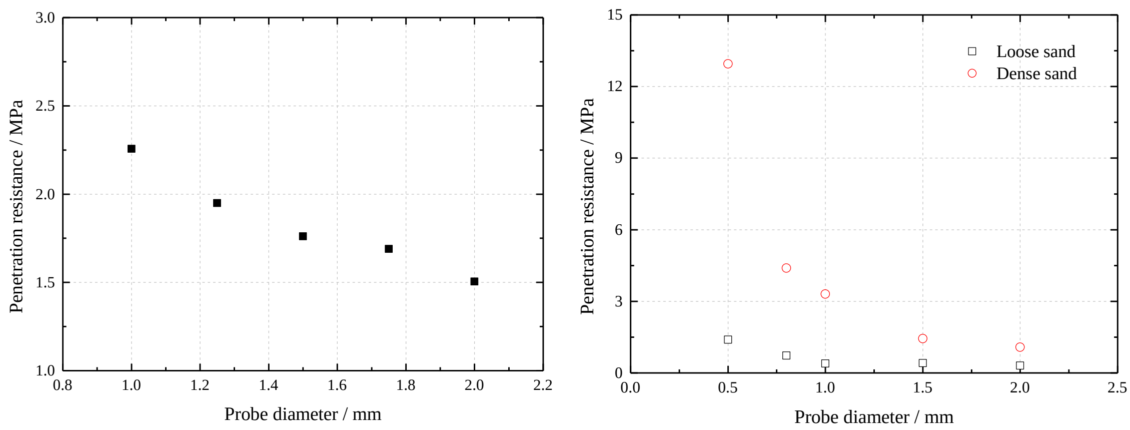

(a) Whiteley and Dexter (1981) (b) Wu and Ladjal (2014)

Fig. 2.4 Experimental data with size effect in needle cone penetration tests

A number of theoretical and empirical methods for interpretations of the standard cone penetration test has been established as reviewed in Chapter 4, but it might be inappropriate to directly apply them to analyse the miniature cone penetration tests due to uncertainties of the penetrometer size effect. Based on this consideration, the possible size-dependent behaviours in cone penetration tests with small sized penetrometers were studied theoretically and physically in this research.

(2) Size effect in "Modelling of models" cone penetration tests

Probe with the same prototype dimension can be modelled by satisfying the required similitude conditions in tests of "modelling of models". However, the grain size cannot be easily scaled with the same geometry scaling law in this kind of tests. By plotting the normalised tip resistance against the normalised penetration depth (the same stress levels), the grain size effect could be evaluated with this method (Balachowski, 2007; Bolton et al., 1999; Kim et al., 2015). Mainly based on a series of 'modelling of model' cone penetration tests conducted on the Cambridge geotechnical centrifuge platform (Lee, 1990), Bolton et al. (1993) proposed that this size effect will gradually vanish when D/d_{50} gets larger than 20. In other words, when D/d_{50} is larger than 20, negligible size effect would be performing to the cone tip resistance, which has also been demonstrated by Kim et al. (2015); Phillips and Valsangkar (1987). This provides a useful reference value to avoid or eliminate the influence of grain size effect, which is not easy to be isolated in other routine tests and has been widely adopted in model test designs.

(3) Size effect with same sized penetrometer at different g-levels

By inserting a same sized probe at different g-levels, penetrations of probes in different prototype sizes can be modelled. In this method, the ratio of the model probe size to the mean particle size (D/d_{50}) is conserved, but the value of H/D usually is different at depths with a same initial stress level (Lee, 1990). Significant size effects were observed in cone penetration tests with coarse sand by Balachowski (2007) when D/d_{50} falls to 17.1, especially in shallow penetration depths, but no evident size effect was found in tests of D/d_{50}=37.5 in the medium dense sand. In addition, the observed size effect attenuates with an increase of the stress level due to the increasingly confined dilatancy in the sheared zones.

In the light of above discussions, no consensus about the size effect in q_c has been achieved, and the degree of its influences in cone penetration tests may vary with soil types, soil state, stress environment, boundary conditions and so forth. As summarised by Eid (1987), existing thoughts about this topic can be categorised into three schools. The first group suggests that there is no size effect, at least for practical purposes (Sanglerat, 1972; Schmertmann, 1978). This conclusion was drawn mainly based on tests with penetrometers of sizes around the standard one for practical engineering applications. The second school states that the size effect exists, but only for shallow penetrations. It usually suggests that a depth of penetration of 20 diameters in dense sands, and 10 diameters in loose sands is enough to eliminate any size influences (De Beer, 1963; Kerisel, 1964). In the third school, the size effect in the tip resistance exists both in shallow depths and deep penetrations in some cases, but it varies with the penetration depth, and different dominant factors contribute to the size-dependent behaviour (Balachowski, 2007). It is believed that the opinion of the third school may more comprehensive, but more effort is needed to figure out the working mechanism of the size effects and then to identify/quantify the governing factors of these effects at different conditions.

2.3 Experimental material and apparatuses

The penetration mechanisms of CPT in sand and in clay are quite different (Yu, 2006), so reasons leading to the size-dependent tip resistance may accordingly different between them. Previous studies indicate that the size effect is more significant and frequently observed in cone penetration tests with sands when the probe size gets comparable with the mean grain size (for example D/d_{50}<20). To more clearly capture the size effect, present cone penetration tests were conducted on sand first. Then in view of above discussions, it is known that two typical geometry sizes (D_{CPT} and d_{50}) may play great roles in determining these size-dependent behaviours. Hence, both of them were discussed in present CPTs. Overall, a series of miniature cone penetration test with different sized penetrometers and sands with different particle fractions was designed and conducted as introduced below. In addition, considering the wide applications of small sized penetrometers in model tests, shallow foundations, and agricultural engineering practices (tests on topsoil or needle CPT), present cone penetration tests mainly focused on behaviours within shallow penetration depths at the 1g condition.

2.3.1 Testing material

Two grades of the widely used Leighton Buzzard sand (Fraction C (Brown et al., 2000; Law, 2008; Lee, 1990; Yang et al., 2011), Fraction E (Lee et al., 2001; Marshall, 2009; Mo, 2014; Tan, 1990)), supplied by David Ball Ltd U.K., were selected in present tests. It is a natural, uncrushed silica sand with rounded/sub-rounded shape of particles, and is free from silt, clay or organic matter (Kingston et al., 2008). Fraction C is the 300mm-600mm sieve fraction and is usually referred to as 25/52. Fraction E is the 90mm-150mm sieve fraction and is usually referred to as 100/170. Their basic physical properties are listed in Tab. 2-3.

Tab. 2-3 Basic parameters of used sands

Sand type	Median grain size	Special gravity	Maximum void ratio	Minimum void ratio	Friction angle
	d_{50} / mm	G_s	e_{max}	e_{min}	φ_{cs} / °
Fraction C (FC)	0.51	2.65*	0.805	0.55	32*
Fraction E (FE)	0.12	2.65†	1.014†	0.613†	32†

Note: * estimated by Lee (1990). † estimated from Tan (1990). φ_{cs} is the critical state friction angle.

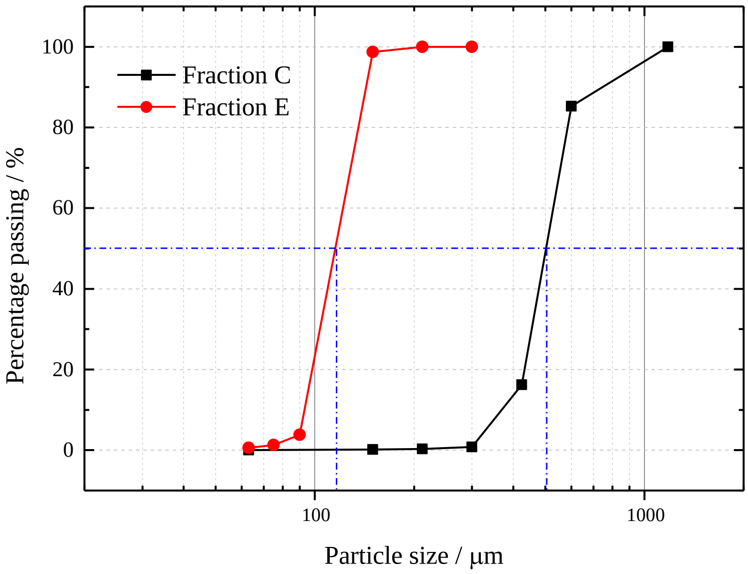

Fig. 2.5 Particle size distribution curves

Particle size distribution curves of the used sands are shown in Fig. 2.5. The maximum and minimum densities of Fraction C sand were measured with the methods specified in BS 1377-4:1990. The Leighton Buzzard sand has a relatively high ability to resist crushing, therefore it is anticipated that no significant particle breakage would take place in present 1g shallow cone penetration tests (<3MPa with penetration depths less than 300mm) (De Beer, 1963).

2.3.2 Miniature cone penetrometers

Three sized probes with conical tips were designed and machined as shown in Fig. 2.6. All penetrometers have the same apex angle of 60° and are made from stainless steel with smooth (polished) surfaces.

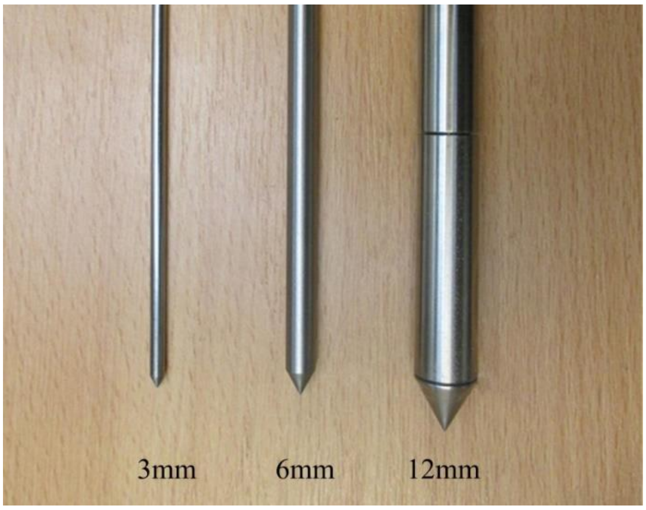

Fig. 2.6 Cone penetrometers with different diameters

2.3.2.1 Penetrometer with 12mm diameter

This penetrometer is designed to be able to measure the tip resistance and sleeve friction separately. As shown in Fig. 2.7, it is made up of three parts: ① tip cone, and ② friction sleeve, and ③ a long tube shaft. Its geometric shape is consistent with the conventional standard cone penetrometer (Lunne et al., 1997), but the key dimensions are reduced with the same scale (2.975:1), which include the length of friction sleeve (45mm) and the tube diameter (12mm). To ensure the soil resistance will be fully transferred to the given sections with strain gauges, two gaps with a width of 0.5mm between each part were set. After ensuring the attached strain gauges perform well, all parts were assembled and the gaps were sealed with silicone rubber to avoid sands getting in.

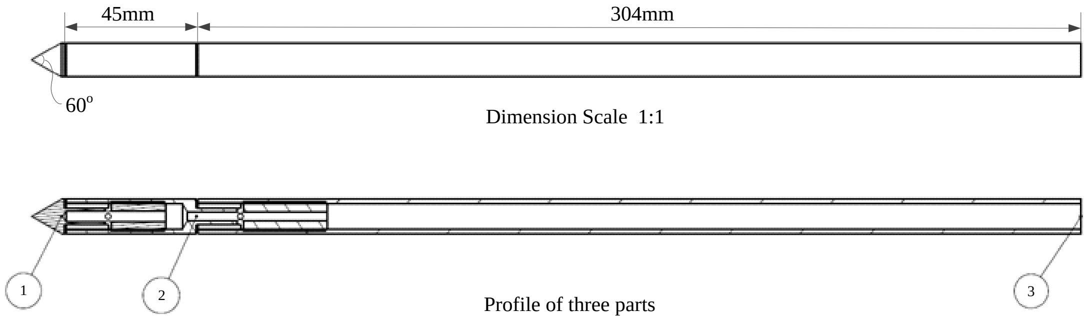

Fig. 2.7 Sketch of the 12mm penetrometer

Four strain gauges were attached to two specific sections as shown in Fig. 2.8, which measure the tip resistance and side friction separately. The foil strain gauges 'FCA-3-350-23' supplied by Tokyo Sokki Kenkyujo Co., Ltd (with a gauge length of 3mm; gauge resistance of 350±1.0 Ω; temperature compensation for 23×10^{-6}/°C; the transverse sensitivity of 0.2%, and a gauge factor of 2.16±1%) were used. As designed, the pressure applying on the cone tip surface would be transferred to the cross-section 1, and this part of pressure together with the soil friction acting on the side sleeve would be measured by strain gauges attached on the cross-section 2.

Fig. 2.8 Position of strain gauges

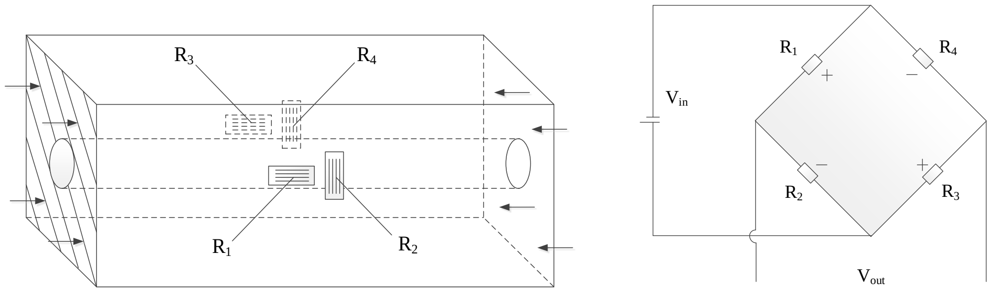

Fig. 2.9 Full-bridge circuit to measure the axial strain

Soil resistances experienced by a vertically moving penetrometer ideally distribute along the axial direction. However, sometimes bending may occur due to nonuniformity of the sand sample or eccentric load effect from the actuator. Additionally, the strain gauge is susceptible to the temperature change. To eliminate potential influences of bending strains and compensate the temperature effect, a full-bridge circuit with four active strain-gauge elements was applied to measure the axial strain as shown in Fig. 2.9.

2.3.2.2 Penetrometers of 6mm and 3mm in diameter

Technically, the tip resistance of small sized penetrometers can also be measured separately, for example, to fabricate a cylindrical shaft comprising two detached parts: an inner rod with a reduced diameter and a hollow ‘coat’ to bear the side friction (Barley et al., 1965; Cockroft et al., 1969; Monfared, 2014). However, it has high and soaring demands on the mechanical processing and material strength with increases of the shaft length or decreases of the probe diameter. In present tests, penetrations with depths around 200-300mm are required, which determines that above ideas are not easy to put into practice for penetrometers of 6mm and 3mm in diameter. Therefore, only the total load both during the pushing in and pulling out process were measured with a load cell mounted on the top of these two probes. The length of 3mm sized penetrometer was set as 200mm to reduce the potential influence of deflection as detailed in Fig. 2.10.

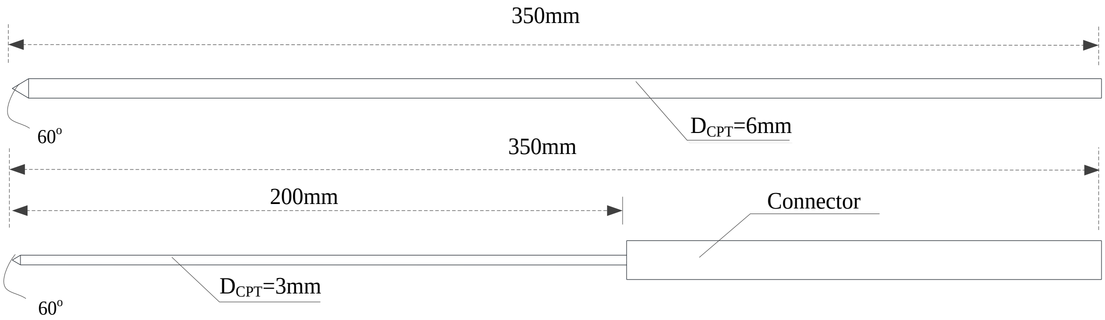

Fig. 2.10 Dimensions of penetrometers with 6mm and 3mm in diameter

To get rid of the shaft friction, penetrometers with reduced shaft in diameter, normally 70%-80% of the cone, were often employed to measure the cone index in the agricultural engineering (ASAE, 2004; Bengough and Mullins, 1990; Sudduth et al., 2004; Whiteley and Dexter, 1981), but this method was not adopted here because the side friction cannot be ideally avoided with this method in present tests (with relatively deep penetrations on the cohesionless dry sand).

2.3.2.3 Calibration of load cell and strain gauges

A load cell with a capacity of 2kN provided by Load Cell Shop was installed at the top of these penetrometers to measure the total resistance. Before the testing, the load cell is calibrated with known weights, and then the strain gauges were calibrated with the load cell. The loading range of calibration tests covered the expected maximum resistance based on some preliminary penetration tests as given in Fig. 2.11. Fig. 2.11 (b) shows that good linear correlations existed between the observed changes of strain gauges and results measured by the load cell.

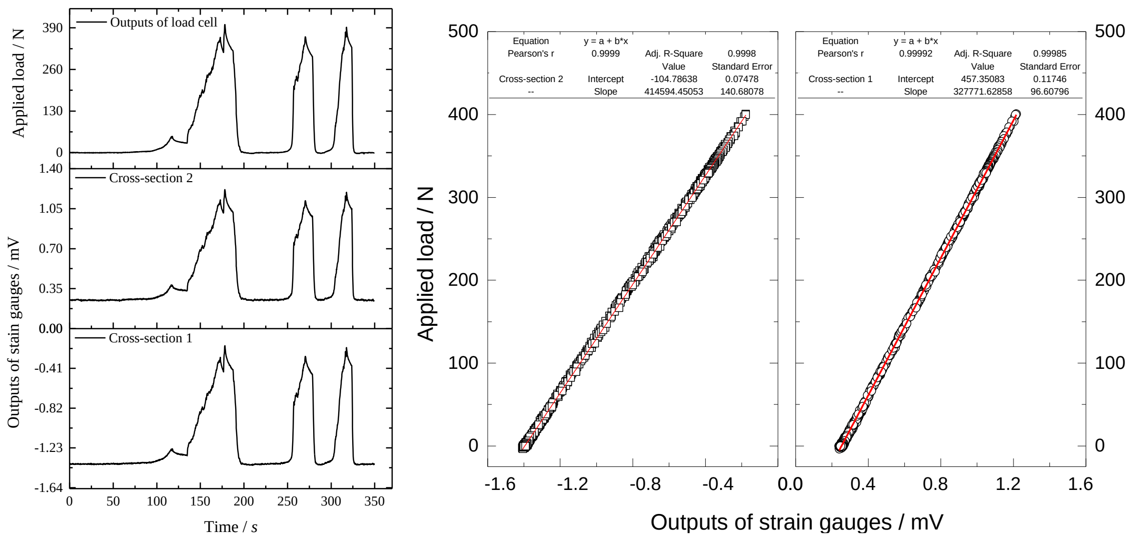

(a) Loading/unloading circles (b) Correlations of strain gauge outputs and applied loads

Fig. 2.11 Calibration test for the 12mm sized penetrometer

2.3.2.4 Surface roughness of the cone penetrometer

The surface roughness of the 12mm sized penetrometer was measured with a 3D optical microscope (Contour GT-I from Bruker Nano Surfaces Division). The arithmetical mean roughness (R_a) is taken as the surface roughness index in this research since its wide applications in describing the friction characteristics of the soil-structure interface (Dietz, 2000; Schneider, 2007).

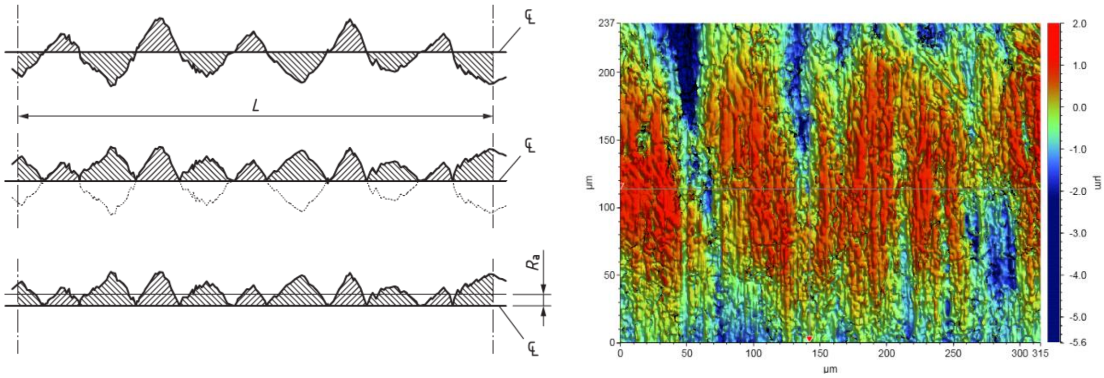

Fig. 2.12 Definition of 'R_a' (after BS-1134-2010) and measured surface texture

The surface roughness of other two sized penetrometers of similar surface conditions (made from similar stainless steels and polished in the same manner) are estimated with the measured data which lies in the range of 0.490-0.688 *um* based on measurements of several surface areas. An average R_a with a value of 0.607 *um* will be used to describe the surface roughness of present penetrometers in later interpretations.

2.3.3 Sample container and loading frame

2.3.3.1 Calibration chamber

To calibrate the performance of CPT under simulated field conditions in the laboratory, Ron Lilley and Holden first designed, built and commissioned a large flexible-boundary calibration chamber in 1969 (Holden, 1971). In following decades, the chamber calibration test experienced a rapid development worldwide (Ghionna and Jamiolkowski, 1991; Mayne and Kulhawy, 1991), and it has been widely accepted and employed by geotechnical communities to calibrate and evaluate in-situ testing devices in laboratory conditions (Holden, 1991; Houlsby and Hitchman, 1988; Jamiolkowski et al., 2003; Parkin and Lunne, 1982). Four typical types of boundary conditions can be achieved with common calibration chambers as shown in Fig. 2.13. Other types of boundaries have also been attempted, aiming to reduce influences from the boundary effect or more realistically simulate the semi-infinite field condition. Noticeably, the one developed and calibrated by Foray (1991); Huang and Hsu (2005); Zohrabi et al. (1995) provides a more plausible tool to simulate the condition exerted by the infinite soil mass, which intermediates between BC1 and BC3 by applying a constant stiffness in the radial direction, and it was referred to as BC5 by Huang and Hsu (2005).

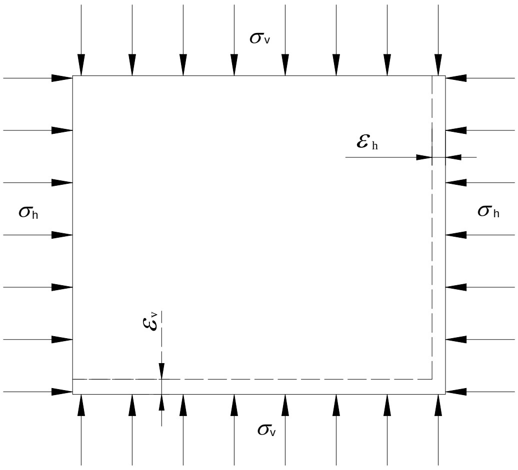

BC1: $\sigma_v =$ const $\sigma_h =$ const.

BC2: $\Delta\varepsilon_v = \Delta\varepsilon_h = 0$

BC3: $\sigma_v =$ const. $\Delta\varepsilon_h = 0$

BC4: $\Delta\varepsilon_v = 0$ $\sigma_h =$ const.

Fig. 2.13 Boundary conditions of chambers (Ghionna and Jamiolkowski, 1991)

Most of the previous chamber calibration tests aiming at clarifying the chamber size and boundary effect were conducted under the boundary condition of BC1 (Salgado et al., 1998). However, devices required to attain these boundary requirements are complicated, space-consuming and not widely available. Alternatively, containers with rigid walls have also been widely used in laboratory penetration tests at 1g condition (Arshad et al., 2014; Ni et al., 2010) and particularly on centrifuge platforms (Balachowski, 2007; Bolton and Gui, 1993; Kim et al., 2015; Mo, 2014; Phillips and Valsangkar, 1987). To further investigate the performance of miniature cone penetrometers within a rigid-walled container, the steel container used by Mo (2014) was employed in the present tests.

For a rigid walled container, Last (1979) reported that no significant side boundary effect was found when the diameter ratio of the container to the penetrometer ($R_d = B / D_{\text{CPT}}$) is 28. Bolton and Gui (1993) suggested a diameter ratio larger than 40 for dense sand to avoid the potential side boundary effect. In addition, the ratio $R_s = S_p / D_{\text{CPT}}$ (S_p is the distance of penetration location to the closest side wall) has also been frequently used to indicate this side boundary effect. Phillips and Valsangkar (1987) found the side boundary effect was negligible even when S_p / D_{CPT} became 5 in tests with the Fraction B Leighton Buzzard sand with a relative density of 97%. Similar results were also reported by Lee (1990) (S_p / D_{CPT} =5.2) and Kim et al. (2015) (S_p / D_{CPT} =7) in tests with dense sands. Additionally, the side boundary effect attenuates with decreases of sand relative density. The employed rigid steel cylindrical chamber is 490mm in diameter and 500mm in height (Mo, 2014). The smallest diameter ratio is 40.8 for testing with the 12mm penetrometer (490/12=40.8, 490/6=81.7, 490/3=163.3), so above container size requirements for eliminating the side boundary effect can be sufficiently satisfied in present tests.

It is worth noting that the side boundary effect applied by a rigid container may be quite different to that by calibration chambers with a flexible side boundary, and different limits of B/D_{CPT} to avoid this effect are required as previously discussed. This difference was attributed to the friction mobilised on the rigid side wall which leads to a lower coefficient of earth pressure (Parkin and Lunne, 1982) and the reduction of effective stresses near the side wall (Kim et al., 2015). Theory of soil arching probably can be used to analyse the former phenomenon (Cho et al., 2014; Paik and Salgado, 2003). The second reason may be explained that the side rigid wall would inevitably disturb the sand deposition in its close region, which may reduce the energy produced during the free falling and, consequently, lead the sand in the vicinity of the side wall to be more or less looser than those deposited in undisturbed zones.

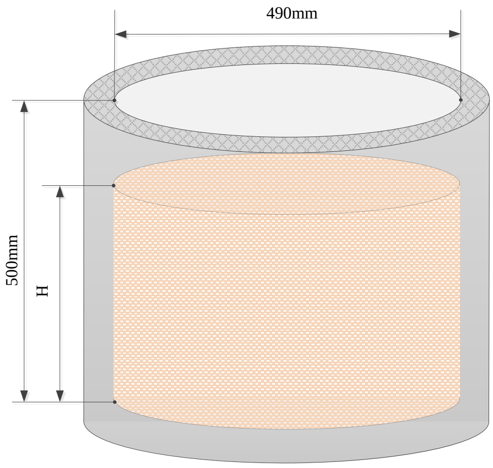

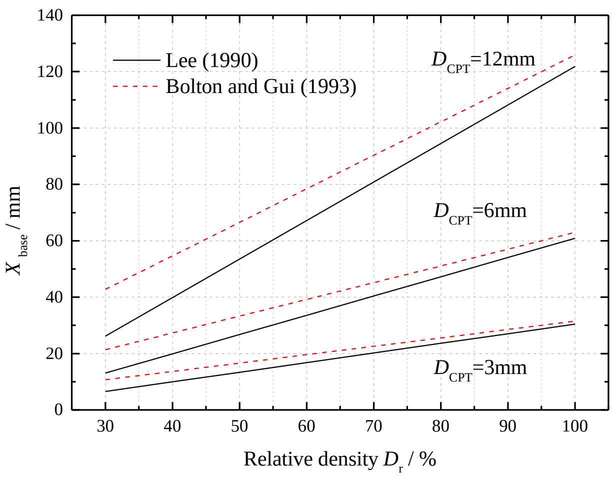

Fig. 2.14 The schematic of sand container   Fig. 2.15 Potential base boundary effect

In addition, the boundary effect from the rigid base may be avoided by ensuring that the effective penetration depth does not enter the limit space range specified by Eq.(2.1) and Eq. (2.2).

$$\frac{X_{base}}{D_{CPT}} = 0.1139 \times (100 D_r) - 1.238 \qquad \text{(Lee, 1990)} \qquad (2.1)$$

$$\frac{X_{base}}{D_{CPT}} = 0.099 \times (100 D_r) + 0.596 \qquad \text{(Bolton and Gui, 1993)} \qquad (2.2)$$

where X_{base}, *mm*, is the minimum required distance from the bottom base to the cone tip to get rid of the base boundary effect as presented in Fig. 2.15.

2.3.3.2 Actuator for driving probes

Two actuators were utilised in present cone penetration tests. The first one actuator was developed and used by Liu (2010) and Mo (2014), which mainly consists of a motor, lead screw, and reaction frame as illustrated by Mo (2014). A maximum displacement of 220*mm* at any moving speed up to 5mm/s can be achieved by controlling the power supply of the motor. A series of cone penetration tests with dense samples of the Fraction C sand at a moving speed of approximately 1mm/s was carried out with this actuator. After that, to achieve a deeper penetration, a new linear actuator from SKF (CAHB-10, rated load: 500N, stroke: 300mm) was employed to drive the probe by attaching it to a new loading frame as shown in Fig. 2.16. Another series of tests both on the Fraction C sand and the Fraction E sand (with different densities) was conducted with the new actuator. A moving speed of approximately 1.5 mm/s, which is easy to control with an integer value of voltage input, was kept in this series of tests. A bit change of the penetration rate exist between these two series of tests, but it, in fact, would not cause any differences in results of the present cone penetration tests on dry sands as demonstrated later.

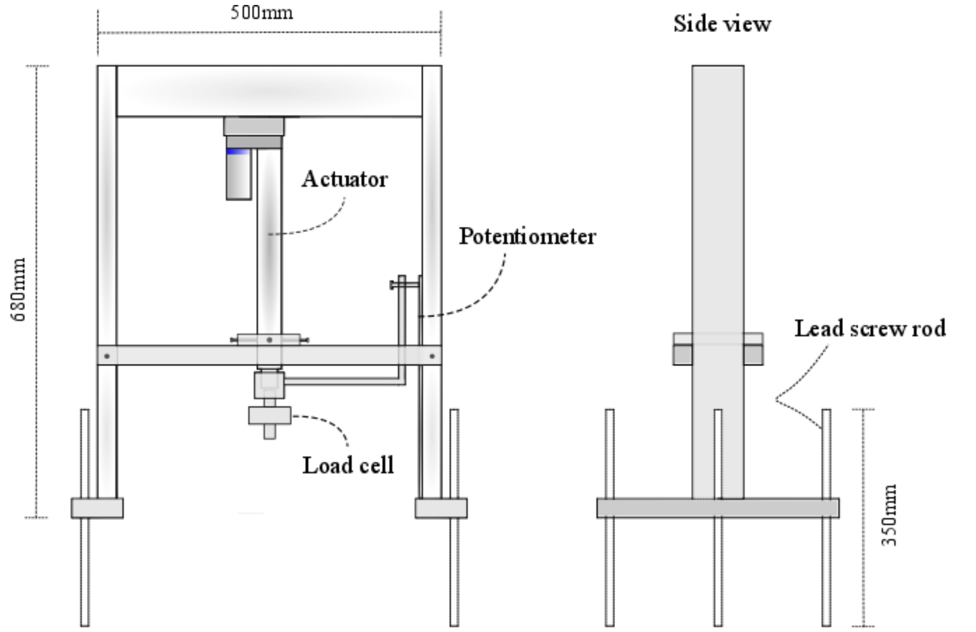

Fig. 2.16 Schematic of the loading frame

This loading frame is easy to be fixed to the side wall of the container with six lead screws, and the initial height of the penetrometers to the sand surface is adjustable by changing the position of nuts on the screw rods. A linear sliding-type potentiometer with a length range of 300mm is fixed on the loading frame to record displacements of the penetrometer.

2.3.3.3 Equipment assembly

In the process of assembling, the key step is to fix the frame horizontally and firmly to the container with a designed space between the cone tip and the sand surface, and it is of great importance to guarantee the probe moves vertically. Then measuring cables should be carefully connected to the data acquisition system (SCXI-1000 from national instruments). An acquisition frequency of 0.2s was set to collect the reading of load cell and strain gauges. Assembled models are displayed in Fig. 2.17.

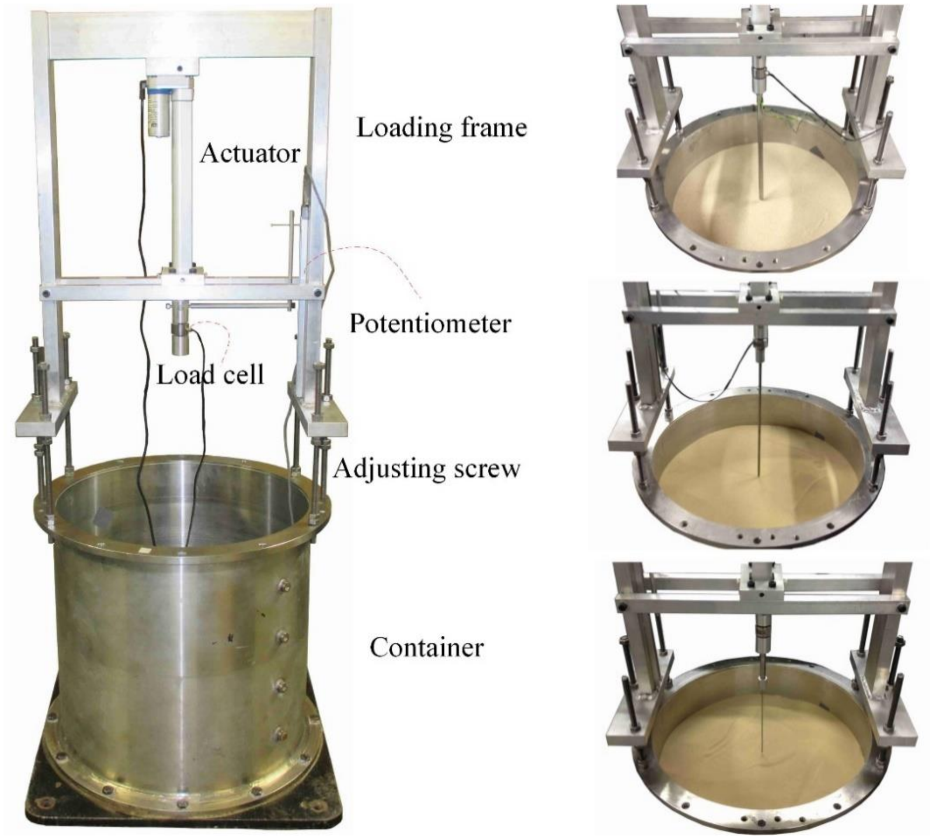

Fig. 2.17 Assembled loading frame, container, and penetrometers

2.4 Sample preparation and testing programme

2.4.1 Sample preparation

Air pluviation method is a mainstream approach for dry sand sample preparation in the laboratory, especially for large-size samples (Miura and Toki, 1982; Rad and Tumay, 1987; Schnaid, 1990; Zhao, 2008). It has advantages not only to reconstitute uniform and repeatable sand samples with desired densities in a wide range (Rad and Tumay, 1987; Schnaid, 1990) but also to simulate the soil fabric similar to that found in natural deposits formed by sedimentation (Oda et al., 1978). Therefore, the sand raining deposition technique was adopted in this research for sample preparation, and the pouring equipment introduced by Mo (2014) was followed as shown in Fig. 2.18. Dave and Dasaka (2012) presented a comprehensive study on a similar travelling sand pluviator and concluded that the size of the orifice, the height of fall, and the combination of sieves greatly determine the deposited sample density and uniformity. Therefore, different combinations of these three factors were repeatedly attempted to achieve a desired initial sand state. Zhao (2008) and Mo (2014) found that the flowing rate is the strongest controlling factor in determining the sample density, so changing the flow rate was taken as the first option to control the sample density. Specifically, the flow rate was mainly controlled by changing the number and size of orifices on the plate as shown in Fig. 2.19.

In tests with the fraction C sand, samples of two relative densities were prepared, which are labelled as dense samples ($D_r = 90\%$) and medium dense samples ($D_r = 65\%$) respectively. Specific plates (in Fig. 2.19) with different sized orifices were placed on the position 'A' of Fig. 2.18, and a constant height (H_C=50cm) of the hopper to the sand surface was kept during each preparation. A maximum variation of 6% of the sample relative density was produced with present sand pouring methods. In addition, three sample states were prepared with the fraction E sand, including dense samples ($D_r = 90\%$, H_C=120mm), medium dense samples ($D_r = 65\%$, H_C=40mm), and loose samples ($D_r = 40\%$, H_C=50mm) with variations within 5%. The employed plate was placed on the position 'B' of Fig. 2.18, and a 2mm grid-sieve was added on the position 'C' while preparing samples with the Fraction E sand. It is worth noting that the classification of sand states are different with those specified by BS EN ISO 14688-2: 2004, which are 'very dense' in the range of $D_r = 85\% \sim 100\%$, 'dense' in the range of $D_r = 65\% \sim 85\%$, and medium dense in the range of $D_r = 35\% \sim 65\%$.

The perforated plate and height of hopper were repeatedly confirmed by pouring the sand into a cuboid calibration box (approximately in size of 200mm×200mm×100mm). Some replicate penetration tests were also carried out to double check the sand density poured in the rigid container as discussed later. In addition, it needs to explain that the height and horizontal position were controlled manually and the pourer needs to be refilled several times during the whole process of each preparation. These factors might reduce the uniformity of samples without precise control, especially while preparing sand samples with high flow rates, for example, in sample preparations with the Fraction C sand, and relatively looser samples with the Fraction E sand. To reduce the potential influences stemming from these factors, the height was carefully checked during the preparation, and the pourer was moved smoothly with a constant speed and frequency, spatially. As shown in Fig. 2.18, samples with desired sand relative densities were prepared with given preparation methods. The repeatability and uniformity of deposited samples will be further discussed later based on duplicate cone penetration tests. The concerned size effect in CPT will be evaluated by directly comparing results from different samples with the same preparation method, which means small variations of the relative density among samples will be omitted.

Fig. 2.18 Schematic of the used sand pourer

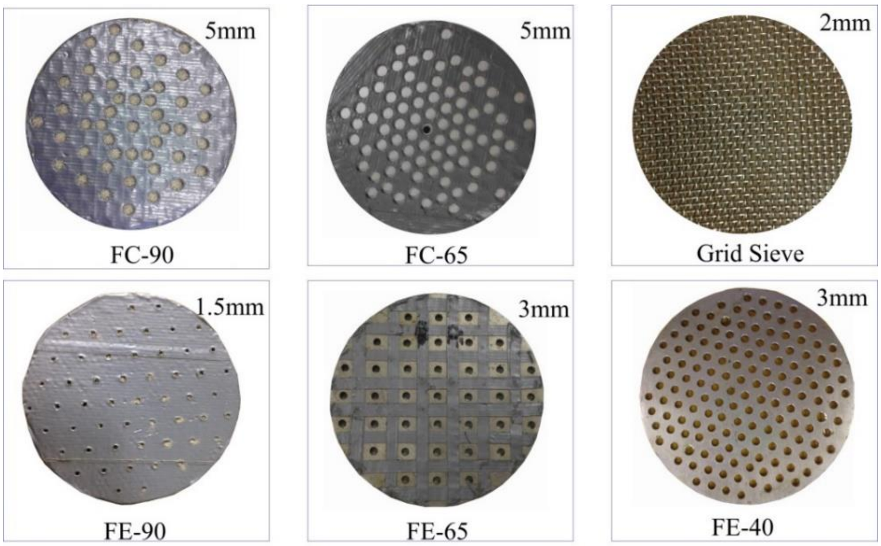

Fig. 2.19 Orifice diameters of perforated plates and the used grid sieve size

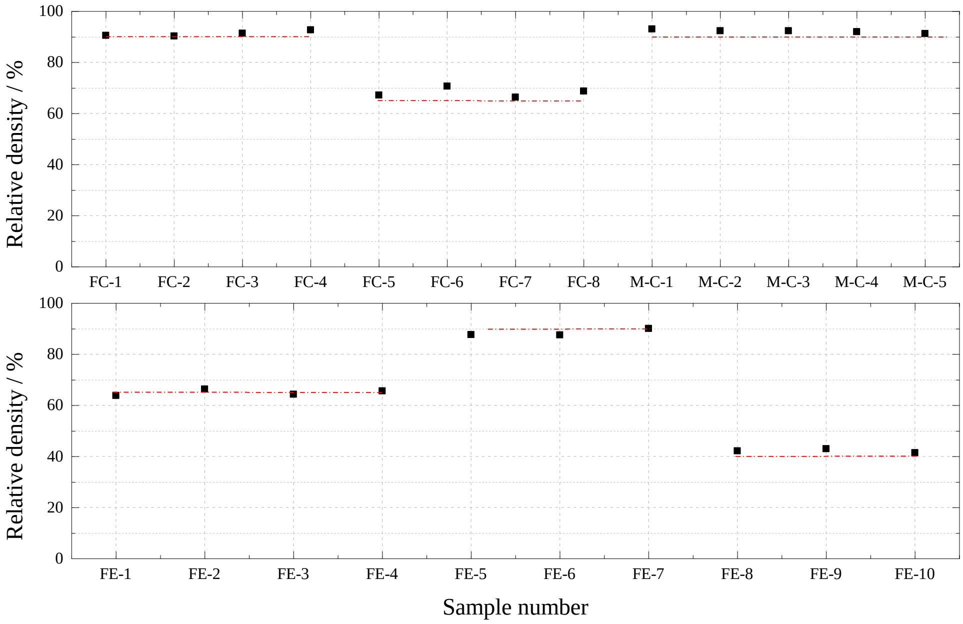

Fig. 2.20 Relative densities of prepared sand samples

2.4.2 Testing programme

Aiming to explore the size effect in the cone penetration test, two sets of CPTs were conducted on dry sand samples of different relative densities as listed in Tab. 2-5. The Leighton Buzzard sand with two ranges of particle distribution and cone penetrometers of three sizes were applied in these tests in order to enlarge the range of the size ratio of D_{CPT}/d_{50} as tabulated in Tab. 2-4. For tests with the new actuator, all penetrations were only executed in the center point of each sample to avoid any potential influences from the side boundary. Additionally, multiple penetration tests were also conducted in dense samples of the Fraction C sand with Mo's (2014) actuator as listed in the three part of

Tab. 2-5. This series of tests is mainly used to check the potential side boundary effect and penetration rate effect. Multiple penetrations with different sized probes were executed after the first penetration at the centre. The penetration position and sequence are expressed in Fig. 2.21, and the green and blue circles represent 40 times of diameters of 6mm CPT and 3mm CPT respectively.

Tab. 2-4 Size ratios of CPT diameters over the median particle

Sand \ CPT	D_{CPT}/d_{50}		
	12mm CPT	6mm CPT	3mm CPT
FC: 0.51mm	23.5	11.8	5.9
FE: 0.12mm	100	50	25

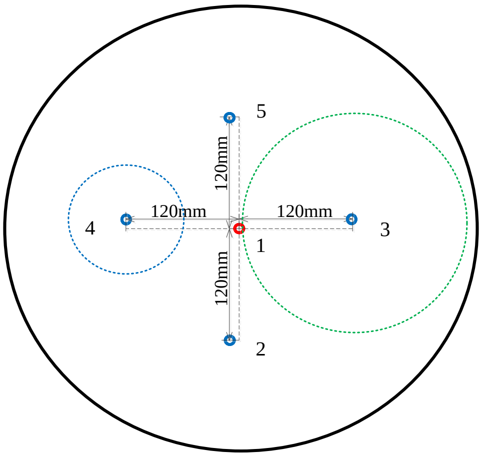

Fig. 2.21 Insertion position layout and testing sequence of multiple penetrations

Tab. 2-5 Details of sand sample for each test

Test No.	Relative density (%)	Depth of sample (mm)	Penetrometer size	Testing date	Test ID
FE-01	63.8	398	6 mm	2015.12.10	FE-6-M
FE-02	66.4	392	3 mm	2015.12.10	FE-3-M
FE-03	64.3	398	12 mm	2015.12.10	FE-12-M
FE-04	65.6	399	6 mm	2015.12.16	FE-6-M*
FE-05	87.7	378	12 mm	2015.12.14	FE-12-D
FE-06	87.6	376	6 mm	2015.12.15	FE-6-D
FE-07	90.1	315	3 mm	2015.12.16	FE-3-D
FE-08	42.1	414	12 mm	2016.1.25	FE-12-L
FE-09	43	412	12 mm	2016.1.26	FE-12-L*
FE-10	41.4	413	6 mm	2016.1.26	FE-6-L

Test No.	Relative Density (%)	Depth of Sample (mm)	CPT size	Date	ID
FC-01	90.5	386	12 mm	2016.1.19	FC-12-D
FC-02	90.3	385	12 mm	2016.1.20	FC-12-D*
FC-03	91.4	385	6 mm	2016.1.20	FC-6-D
FC-04	92.7	344	3 mm	2016.1.20	FC-3-D
FC-05	67.2	397	12 mm	2016.1.21	FC-12-M
FC-06	70.6	395	12 mm	2016.1.21	FC-12-M*
FC-07	66.3	397	6 mm	2016.1.22	FC-6-M
FC-08	68.8	395	3 mm	2016.1.22	FC-3-M
Test No.	Relative Density (%)	Depth of Sample (mm)	Penetration sequence	Date	
M-C-01	93	325	6/6/6	2014.11.25	Identified with test number
M-C-02	92.3	342	12/12/6/6/3	2014.11.30	
M-C-03	92.3	343	3/6/6/3/12	2014.12.01	
M-C-04	92	346	12/12/6/3/3	2014.12.03	
M-C-05	91.3	342	6mm CPT with different speeds	2014.12.05	

Note: The tests are identified with codes comprising the sand fraction, penetrometer size and sand density classification. ‘*’ represents the test for checking sample repeatability.

2.4.3 Repeatability and uniformity of sample

As aforementioned, the sand pouring method was repeatedly calibrated with a small sized calibration box, and the sand density of each sample was re-examined by weighting the deposited sample and measuring its average volume. Considering that the operation in controlling the spatial movement of the hopper (height and horizontal position) may exert influences on the repeatability and uniformity of samples with the present manually controlled sand pouring method, some duplicated samples were prepared and tested with the same sized probes as shown in Fig. 2.22 to check these concerns. It is seen that good repeatability can be achieved with these employed preparation methods, but a relatively big discrepancy of the load reading appeared in duplicate tests with the medium dense sample of the Fraction C sand, a maximum value around 10%. This is mainly because of the required particle flow rate is very high in this case, which makes it not easy to keep the pourer move very evenly as previously mentioned. In the contrary, the preparation of dense Fraction E sand sample is easy to be controlled since the sand flow rate is very slow with the present method which has been well calibrated and used in our laboratory, so it was not repeated again here.

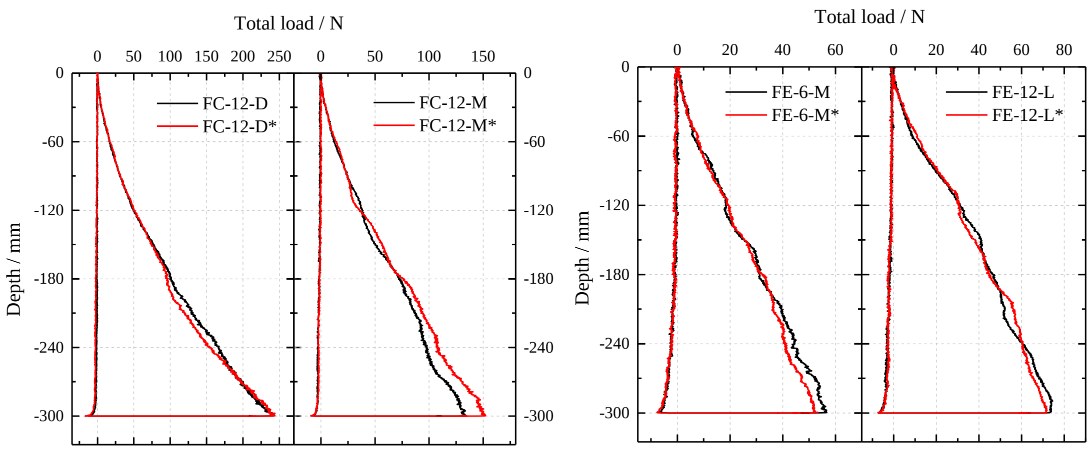

Fig. 2.22 Tests with duplicated sand samples

It is believed that the potential spatial variation of sand uniformity may highly depend on the operation. Samples with different relative densities were prepared by the same procedure, so, technically, it should have similar influences on all deposited samples. Hence, the sample uniformity was checked with the dense Fraction C sand as a reference. Moreover, to reduce the potential interaction effect of multiple insertions and the boundary effect, the 6mm sized probe was chosen. As shown in Fig. 2.23, almost the same response was acquired with penetrations in different positions, which demonstrates that good uniformity was prepared. In addition, the right graph of Fig. 2.23 indicates that the penetration speed in the range of 1mm/s-4mm/s applied a nonsignificant effect on the present cone penetration tests with dry sand, which fully covers the applied penetration speeds in our tests. Therefore, the penetration rate effect is negligible in analyses of present tests. Similar rate effect has also been observed in other cone penetration tests with dry or fully drained sand samples in a wider rate range about 1mm/s-20mm/s (Gui et al., 1998; Kim et al., 2015).

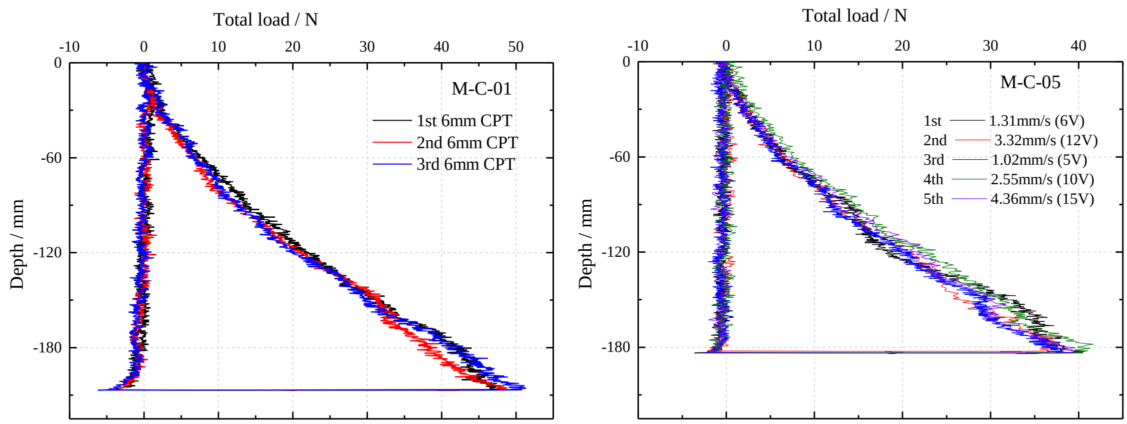

Fig. 2.23 Multiple penetration results for checking sample uniformity and rate effect

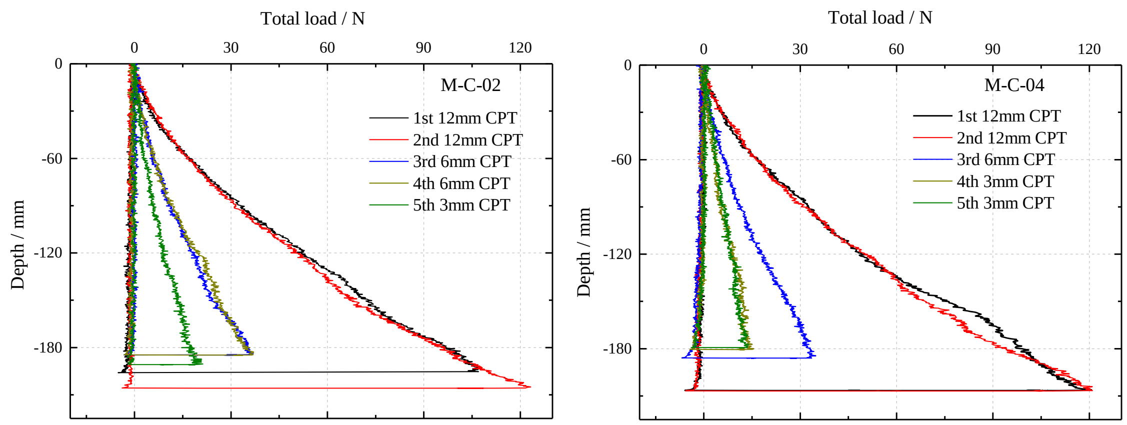

Fig. 2.24 Tests on the same sample with different insertion points

Good repeatability and uniformity of sand samples with present preparation methods can also be confirmed with results shown in Fig. 2.24. More importantly, Fig. 2.24 displays that the results of penetration at the centre point ($S_p / D_{\mathrm{CPT}} = 20.5$) closely agree with those measured at the subsequent positions of $S_p / D_{\mathrm{CPT}} = 10$ with the 12mm sized penetrometer. It indicates that the side boundary applied negligible influences on the readings even while S_p / D_{CPT} became as small as 10 in dense samples of our tests. This finding is compatible with the aforementioned experimental results from Kim et al. (2015); Lee (1990); Phillips and Valsangkar (1987). Therefore, the side boundary effect will not be considered in the following results analyses of the present tests.

2.5 Results of cone penetration tests

2.5.1 Test readings

Total soil resistance (Q_{total}) imposed on an advancing probe consist of two main parts: the pressure on the cone tip (Q_{tip}) and the side friction along the shaft (Q_{shaft}). In interpretations of the cone penetration test, as illustrated in Fig. 2.25, the named cone tip resistance (q_c) is commonly used, which equals to divide Q_{tip} by the base area (A_b). The side friction is usually discussed with two kinds of defined friction resistance. One is the measured average sleeve friction ($\overline{f}_s$), and the other one is defined as the average shaft friction ($\overline{\tau}_{as}$), which equals to divide Q_{shaft} by the surface area of embedded shaft (A_{shaft}).

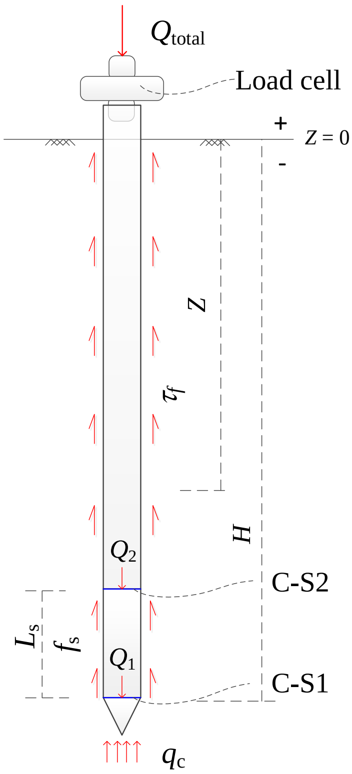

Fig. 2.25 Schematic of load and stress notations

$$Q_{\text{total}} = Q_1 + Q_{\text{shaft}} = q_c A_b + \int_0^H \pi D_{\text{CPT}} \tau_f d_z = q_c A_b + \overline{\tau}_{as} A_{\text{shaft}} \tag{2.3}$$

$$Q_{\text{sleeve}} = Q_2 - Q_1 = \int_0^{L_s} \pi D_{\text{CPT}} f_s d_{L_s} = A_s \overline{f}_s \tag{2.4}$$

$$Q_{tip} = \pi D_{CPT}^2 q_c / 4 \tag{2.5}$$

All direct test readings are present in Fig. 2.27 and Fig. 2.28. It shows the head load almost linearly increases with the advancing penetration depth, and similar trends have also been observed by Arshad et al. (2014); Deeks and White (2006); Durgunoglu and Mitchell (1973); Ferguson and Ko (1981); Klinkvort et al. (2013); Mo (2014) (as compared in Fig. 2.26). Some small unsteady deviations from the approximately linear trend were detected in tests on loose samples. This may be mainly caused by the error of unstable operation in the preparations of samples with high particle flow rates as previously mentioned.

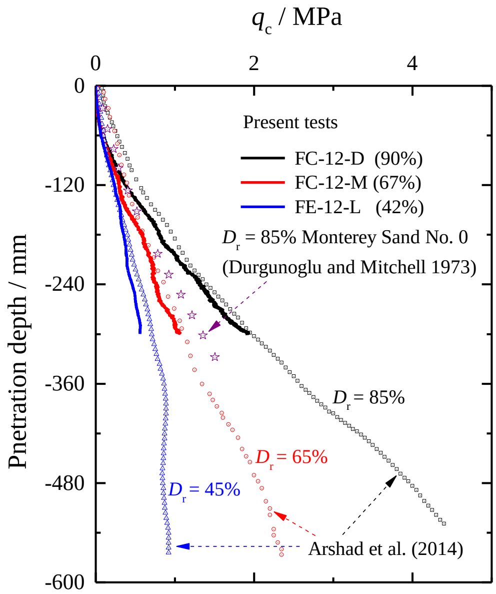

Fig. 2.26 Comparison with similar cone penetration tests with silica sands

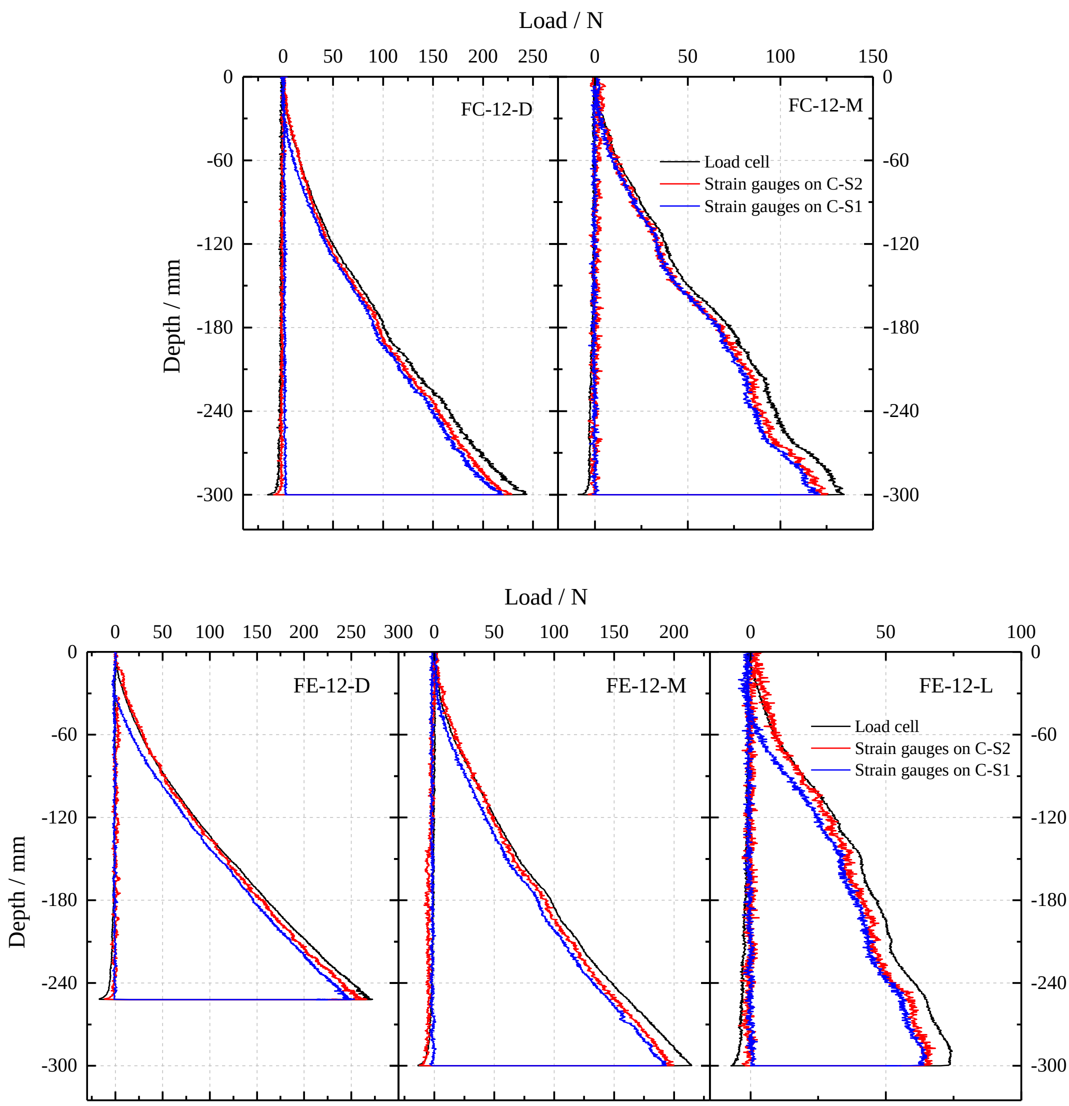

Fig. 2.27 All readings of tests with the 12mm penetrometer

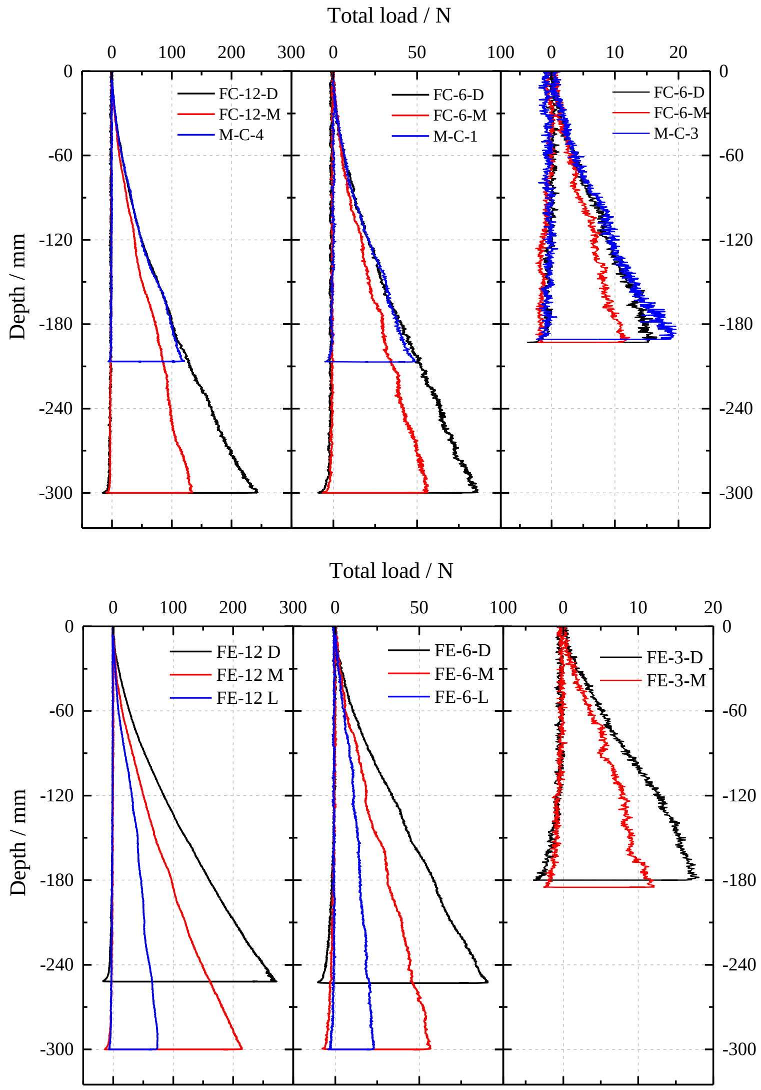

Fig. 2.28 Variation of head loads with relative density (both on FC sand and FE sand)

2.5.2 Estimation of the shaft friction during penetrations

As aforementioned, the employed 3mm and 6mm sized probes are not capable to directly measure the encountered tip resistance. Therefore, it is necessary to separate the shaft friction from the recorded total resistance. For this purpose, two independent empirical methods are proposed and compared based on the data obtained with the12mm sized penetrometer in similar conditions as follows.

2.5.2.1 Method 1: based on the ratio of Q_{tip}/Q_{total}

Based on the test readings given in Fig. 2.27, it is found that the shaft friction always takes a small proportion of the total resistance in all these tests with the 12mm sized penetrometer (around 10%). Interestingly, further investigation demonstrates that the ratio of Q_{tip}/Q_{total} in all these tests regularly stabilises to some values when the penetration depth gets deeper than 10-15D_{CPT} as shown in Fig. 2.29. This trend can be analysed with Eq.(2.6) which contains two non-dimensional parameters: $\bar{\tau}_{as} / q_c$ and H / D_{CPT} as

$$\frac{Q_{\text{shaft}}}{Q_{tip}} = 4\frac{\bar{\tau}_{as}}{q_c}\frac{H}{D_{CPT}} \rightarrow \text{const.} \tag{2.6}$$

Analogous trends were also reported by Deeks and White (2006); Klotz (2000); Mo (2014) in centrifuge tests with 12mm sized circular piles, but relatively lower ratios of $Q_{\text{tip}}/Q_{\text{total}}$ were measured therein, which distributes in a range of 0.6-0.8. Higher values were observed by Borghi et al. (2001) in the centrifuge tests (50g) with 12.5mm sized flat-ended circular piles in a very compressible sand, which is around 0.99 and 0.9 for smooth and rough piles respectively. These discrepancies might be due to their differences in the sand type, pile roughness, stress level, and tip shape.

Equation (2.6) indicates that the ratio of $Q_{\text{shaft}}/Q_{\text{tip}}$ is inversely proportional to the probe size at the same penetration depth, but no direct dependency of the non-dimensional value of $\bar{\tau}_{as} / q_c$ on D_{CPT} was observed. Based on this, an approximate method is proposed to estimate the tip resistance of tests with the 6mm and 3mm sized penetrometers with available readings of the head load. It is assumed that such a steady state also exists in penetration tests with the 3mm and 6mm sized probes, and $\bar{\tau}_{as} / q_c$ at the same depth does not vary with the probe size for tests with similar sand samples. In fact, it implicitly assumed that possible differences caused by the probe size have the same contribution level to the tip resistance and the average shaft friction at a same initial stress level.

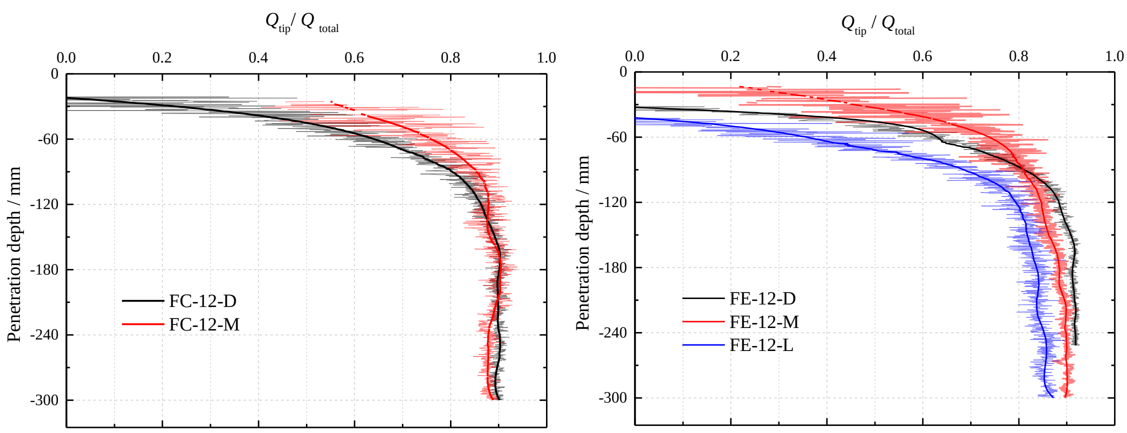

Fig. 2.29 Ratios of the shaft friction to the total resistance

The exact embedment depth when the steady state is reached is not precisely quantified here, and a constant value of $\bar{\tau}_{as} / q_c$ is applied in the whole penetration process in following estimations. Therefore, the tip resistance at penetration depths less than 10-15D_{CPT} will be slightly overestimated. Based on above assumptions, the ratio of $Q_{\mathrm{shaft}} / Q_{tip}$ with different sized probe has a relationship as: 12mm: 6mm: 3mm = 1:2:4 at the same penetration depth. Then the constant ratio of $Q_{\mathrm{tip}}/Q_{\mathrm{total}}$ in tests with the probes of 6mm and 3mm in diameter are estimated as calculated in Tab. 2-6.

Tab. 2-6 Measured and estimated $Q_{\mathrm{tip}}/Q_{\mathrm{total}}$

$Q_{\mathrm{tip}}/Q_{\mathrm{total}}$	FC sand		FE sand			CPT size
	Dense	Medium dense	Dense	Medium dense	Loose	
Measured*	0.898	0.887	0.916	0.896	0.849	12mm
Estimated	0.815	0.797	0.845	0.812	0.738	6mm
Estimated	0.688	0.662	0.731	0.683		3mm

* averaged values with data from the embedment depth of 180mm to the deepest position.

Similar ratios were reported by Barley et al. (1965) in needle cone penetration tests in a loam topsoil, which was $Q_{\mathrm{tip}}/Q_{\mathrm{total}}$ =13% with a 3mm sized probe and 45% with a probe of 1mm diameter. In addition, Aydan et al. (2014) obtained $Q_{\mathrm{tip}}/Q_{\mathrm{total}} \approx 50\%$ which calculated with an estimated $Q_{f,t} / Q_{f,c}$ of 2/3 while pressing a 1mm sized probe into soft rocks.

2.5.2.2 Method 2: based on the measured friction during the extraction

The soil resistance during extraction totally comes from the mobilised shaft friction in present tests (no base suction). This reading was often used to estimate the shaft friction during penetrations in cases lack of direct measurements. Therefore, resistances during both the insertion and extraction process were recorded in implementations of the present tests, and a typical loading procedure is presented in Fig. 2.30. Firstly, the probe is pressed in continuously with a constant speed. When the actuator reaches its maximum stroke, the penetration will be stopped. A noticeable drop in the resistance, approximately 10%, immediately appeared while it ceased. A similar phenomenon was also reported by Tollner and Verma (1987) and Mo (2014). They interpreted it with a stress relaxation concept, and then the creep effect makes a further slow reduction. Subsequently, the probe is pulled out with the same speed.

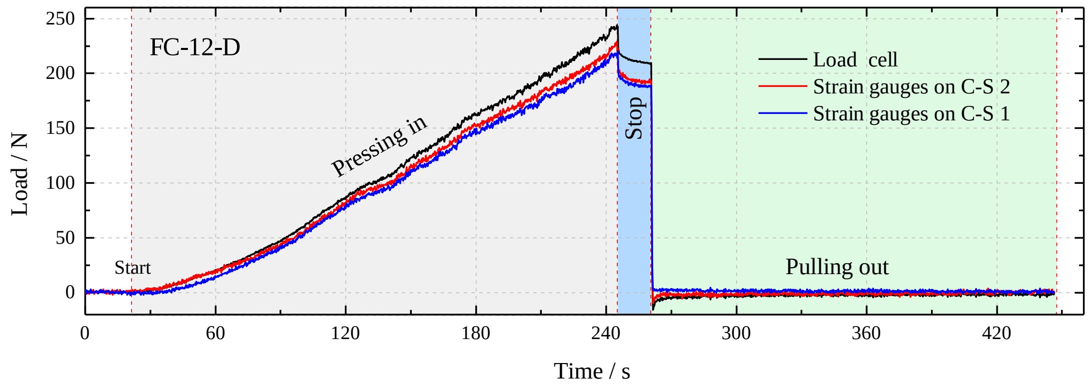

Fig. 2.30 Typical load-time curve (FC-12-D)

Sometimes the shaft friction capacity while pushing in is roughly approximated by equalling to the friction measured during the extraction (Ferguson and Ko, 1981; Ladjal, 2013; White and Lehane, 2004) when the shaft friction just takes a very small portion of the whole resistance. However this approximation will lead to more errors when the shaft friction takes a relatively large portion because the ratio of maximum tensile to compressive shaft capacity, $Q_{f,t}/Q_{f,c}$, usually is below unity (De Nicola and Randolph, 1993, 1999; Deeks and White, 2006; Fioravante et al., 2010a; Fleming et al., 2009; Lehane et al., 1993). As reviewed by Lehane et al. (2005b), all of the four representative CPT-based design methods (Fugro-05, ICP-05, NGI-05,UWA-05) for driven piles in sands specified the shaft friction in tension is lower than that in compression under the same conditions. To accurately estimate the friction resistance during penetrations, the friction characteristics in present penetration tests are studied first based on the CPT results obtained with the 12mm sized penetrometer as shown in Fig. 2.31.

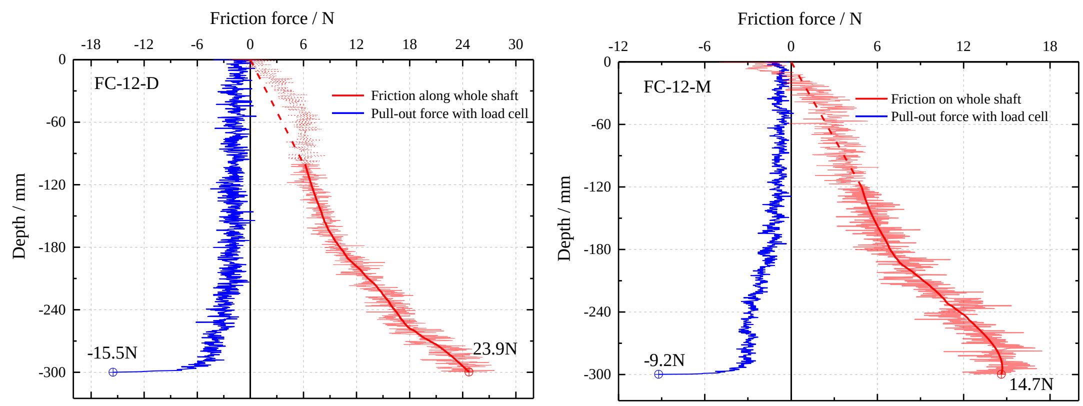

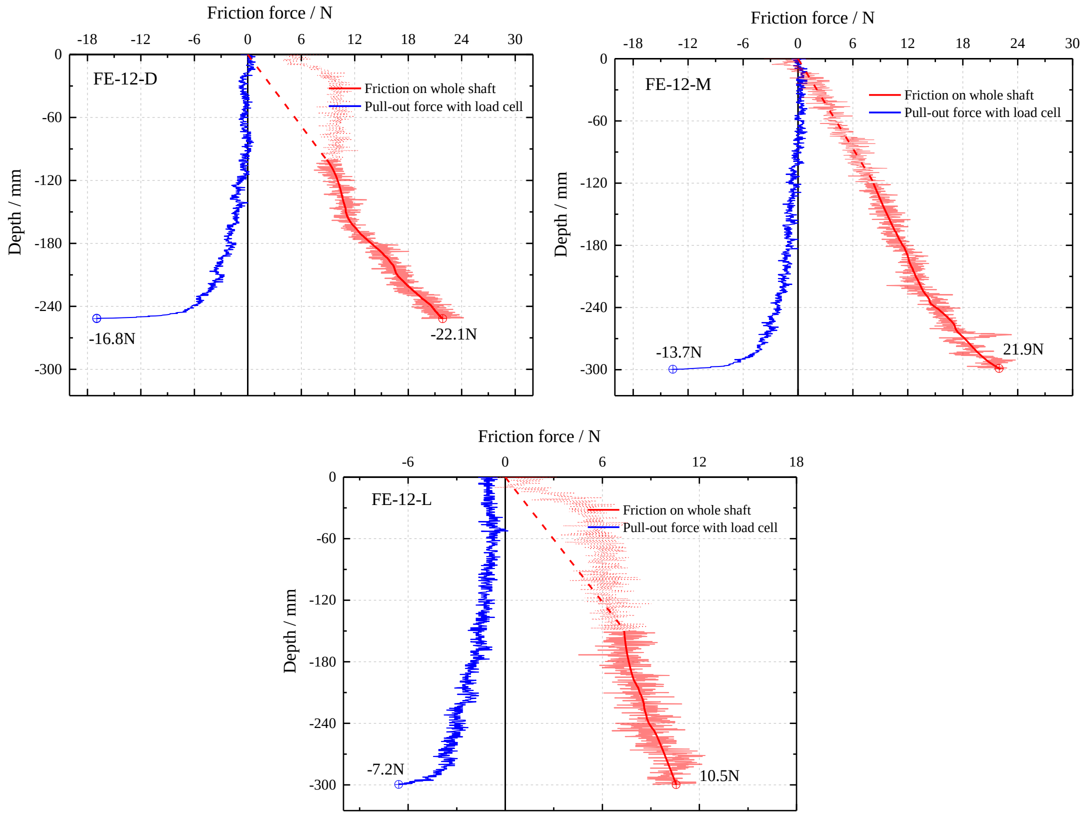

Fig. 2.31 Friction forces during processes of insertion and extraction

In Fig. 2.31, it shows that the encountered shaft friction resistance is relatively small. It approximately linearly increases with an advancing depth during penetration, but results at relatively shallow penetration depths deviated from this trend in some cases, which probably resulted from that the loads acquired by the strain gauges on the Cross-section 1 unreasonably decrease to some small negative values at initial stages. These shifting might be caused by a minor load release which took place around the cone tip when the sleeve starts bearing resistance. This phenomenon vanished or became negligible when the penetration depth gets deeper than $10D_{\mathrm{CPT}}$. Comparing with the total resistance, this fluctuation is very small even at the initial penetration stages. Subsequently, friction resistances during the extraction reached a maximum value almost immediately when the probe is pulled out. Then it drops rapidly in initial displacements of 5-10mm, especially in tests within dense sand samples.

The maximum tensile shaft capacity, $Q_{f,t}$, and the corresponding maximum compressive friction resistance, $Q_{f,c}$, are tabulated in Tab. 2-7. It is found that the ratio of $Q_{f,t}/Q_{f,c}$ distributes in a range of 0.62-0.76 in these tests which fairly consists with the range of 0.52-0.86 that reported by De Nicola and Randolph (1999) in a series of centrifuge tests with closed/open-ended model piles. It is also comparable with values acquired by Deeks and White (2006) from centrifuge tests with the same sized model pile. Similarly, Schmertmann (1978) recommended the ultimate tension friction can be computed as 2/3 of the compression friction, and UWA-05 method gave a scale of 0.75 between the tension friction and the compression friction (Lehane et al., 2005c).

Strength and deformation properties in the soil-structure interface are complex. Potential reasons explaining the difference of skin friction on piles under compression and tension in cohesionless soils were discussed by De Nicola and Randolph (1993), Lehane et al. (1993), Randolph (2003), Deeks and White (2006) and others, which mainly include: (1) pile expansion under compression or contraction under tension due to Poisson's ratio effect; (2) principal stress rotation resulted from changes of the loading direction; (3) difference in total stress field of soil around the loaded pile in either direction. The level of influences from these effects may vary with pile compressibility, embedment depth, interface dilation characteristics, initial stress environment, soil stiffness and installation method etc.. According to the Coulomb failure criterion (Eq.(2.7)), the above difference can be mainly ascribed to their direct or indirect influences to the radial effective stress field because the frictional coefficient at failure might not significantly vary with the change of the loading direction as will be discussed in Chapter 4.

$$\tau_f = \sigma_{rf} \tan \delta_f \tag{2.7}$$

Although extensive evidence confirmed that significant size effect may behave in the interface friction strength when the ratio of D_{CPT} / d_{50} are relatively small as detailed in Chapter 4, no observation indicates that the ratio of $Q_{f,t} / Q_{f,c}$ varies with the probe size. And similar ratios of $Q_{f,t} / Q_{f,c}$ were obtained in tests with different probes as previously stated. Therefore, it is hypothesised the same value of $Q_{f,t} / Q_{f,c}$ exists within tests conducted in duplicated sand samples as presented in Tab. 2-7.

Tab. 2-7 Measured and predicted maximum friction forces

Sand state	CPT size	Max. friction force $Q_{f,t}$/N	$Q_{f,c}$/N	$Q_{f,t} / Q_{f,c}$	CPT size	Max. $Q_{f,t}$/ N	Predicted Max. $Q_{f,c}$/N
FC-dense	12mm	15.5	23.9	0.648	6mm	9.58	14.75
					3mm	3.78	5.82
FC-	12mm	9.2	14.7	0.626	6mm	6.25	10.08

medium dense					3mm	2.46	3.98
FE-dense	12mm	16.8	22.1	0.76	6mm	10.36	13.63
					3mm	3.96	5.21
FE-medium dense	12mm	13.7	21.9	0.625	6mm	7.66	12.25
					3mm	2.63	4.21
FE-loose	12mm	7.2	10.5	0.685	6mm	4.31	6.63

2.5.2.3 Comparison of methods determining the shaft friction

Based on the data of tests with the 12mm sized penetrometer, above two methods for predicting the shaft friction during penetration are compared in Fig. 2.32. It is shown, excepting the aforementioned fluctuation at initial penetration depths, the calculated friction capacities with both of these two methods agree fairly well with the measured values, and the method 1 gives a slightly closer prediction. In addition, the required pull-out forces are relatively very small in present tests, so the accuracy of data measurement might be limited by the resolution of the used load cell at some degrees. Therefore, the proposed method 1 will be adopted to estimate the encountered shaft friction with the 6mm and 3mm sized probes during penetration in following analyses.

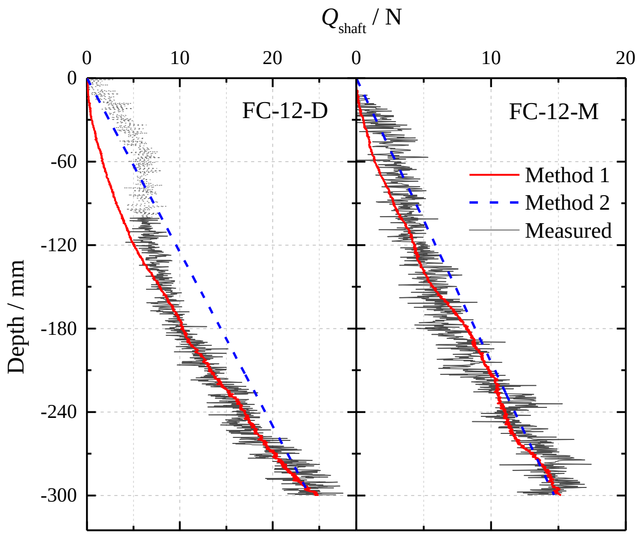

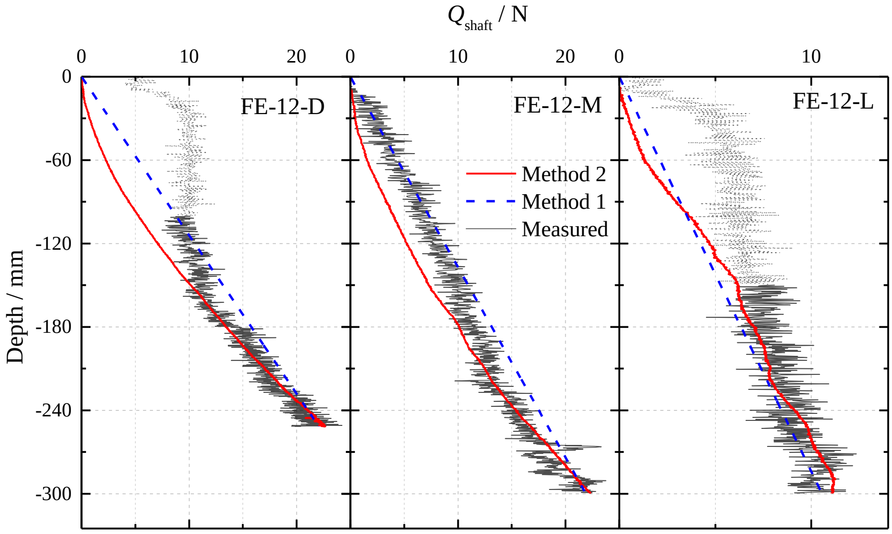

Fig. 2.32 Measured and predicted shaft friction during penetrations

2.5.3 Results of tip resistances

Tip resistances calculated based on above two methods are compared with the measured values with the 12mm sized penetrometer as shown in Fig. 2.33. Satisfactory predictions can be made by these two methods when the penetration depth gets deeper than 10 D_{CPT}. Relatively big gaps appeared at initial penetration depths (as previously explained), but the maximum gap value is less than 0.06 MPa.

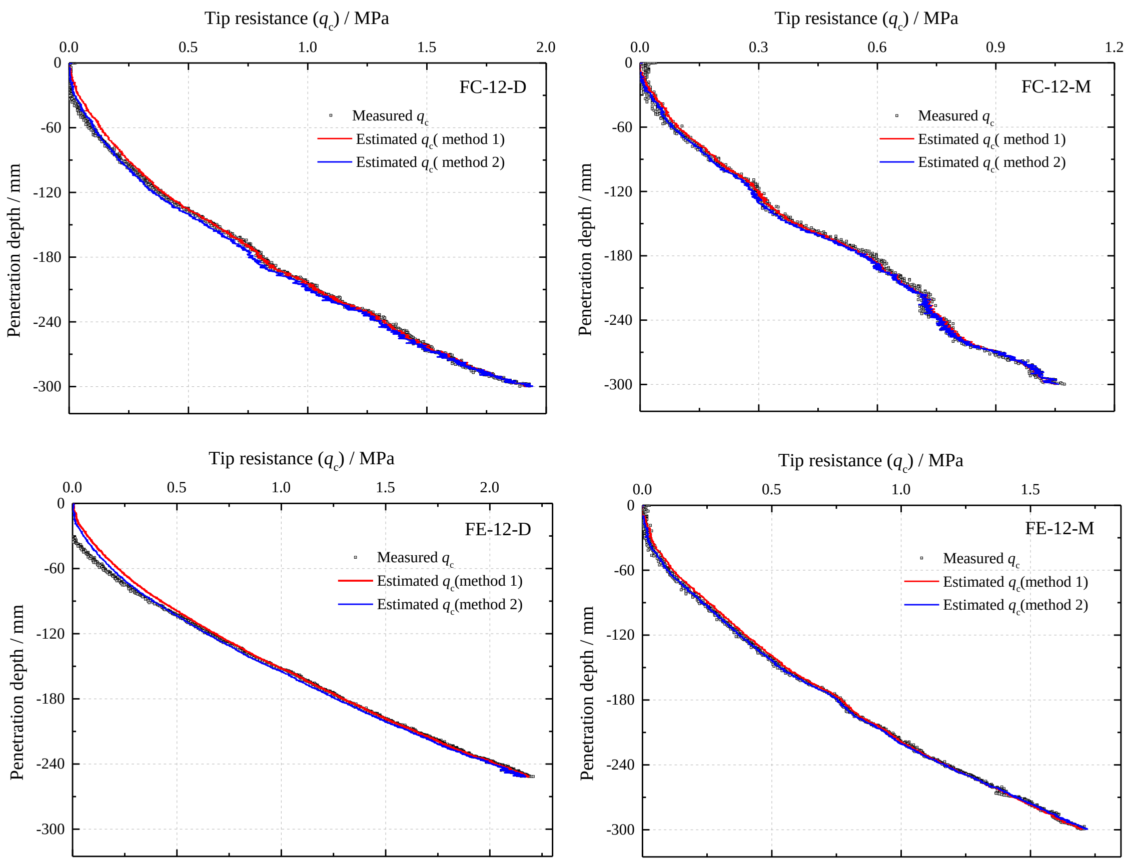

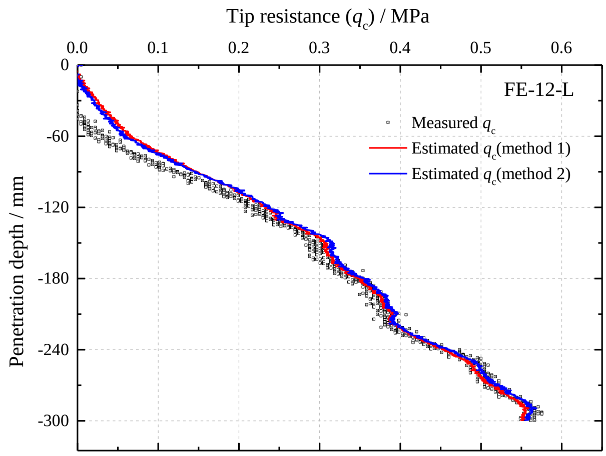

Fig. 2.33 Measured and predicted tip resistance (12mm CPT)

Then based on the Method 1, the measured (12mm CPT) and calculated tip resistances in all tests are summarised in Fig. 2.34, and some preliminary conclusions can be drawn as

(1) Similar to readings of the total load, the tip resistance grows approximately linearly with the advancing penetration depth and is very sensitive to the variation of sand relative density. Higher soil resistances were generally experienced in denser samples.

(2) Tip resistances measured in samples with the Fraction E sand are generally higher than those obtained within the Fraction C sand at similar conditions (sand state and penetration depth).

(3) Higher tip resistances were measured by smaller probes in the same sand with similar conditions (sand state and penetration depth).

Further analyses of the experimental results and explanations to above findings will be detailed in Chapter 4.

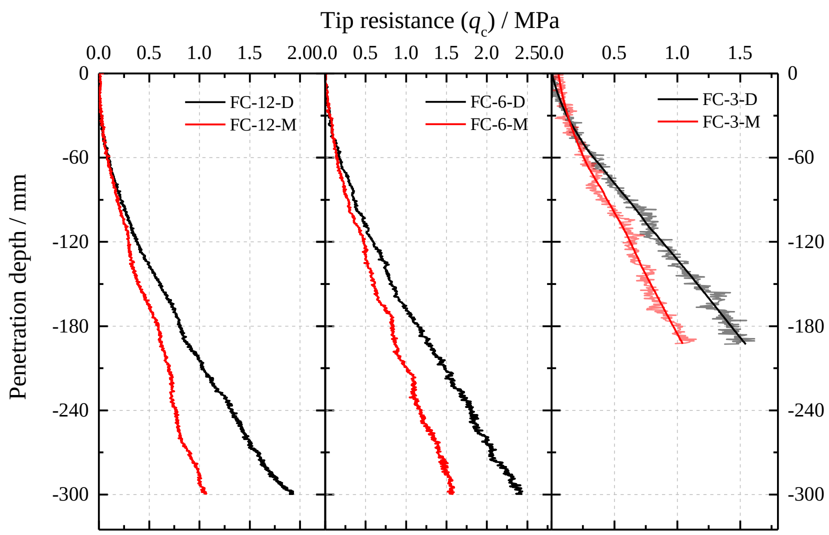

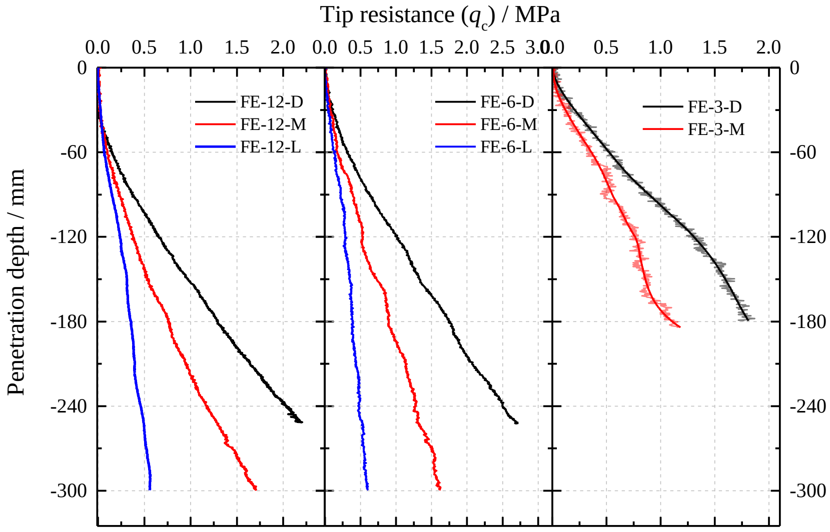

Fig. 2.34 Variation of tip resistances with sand relative density

Different normalisation methods have often been used to analyse the CPT data obtained with different experimental techniques, for example, the method given by Bolton and Gui (1993) for CPTs executed on the centrifuge, the method given by Jamiolkowski et al. (2003) for interpretation of CPT in calibration chambers. Here for simplicity, all tip resistances are normalised by the initial vertical stress (q_c / σ_{v0}) at corresponding depths (Durgunoglu and Mitchell, 1975) as shown in Fig. 2.35. It shows that q_c / σ_{v0} gradually get stable with increasing depths, especially in tests on relatively loose samples or with smaller penetrometers. This phenomenon will be discussed in Chapter 4 with the concept of relative critical depth. In addition, the normalised tip resistance obtained with the smaller probes show more fluctuations with the depth, which may indicate that the smaller probe has a higher sensitivity to detect the variation of soil state along the penetration profile (Lunne et al., 1997). These slight periodic deviations captured by the smaller probes actually represent the influence caused by the error in controlling the pouring height during sample preparations, which are not obvious in curves obtained with the 12mm sized penetrometer in similar sand samples.

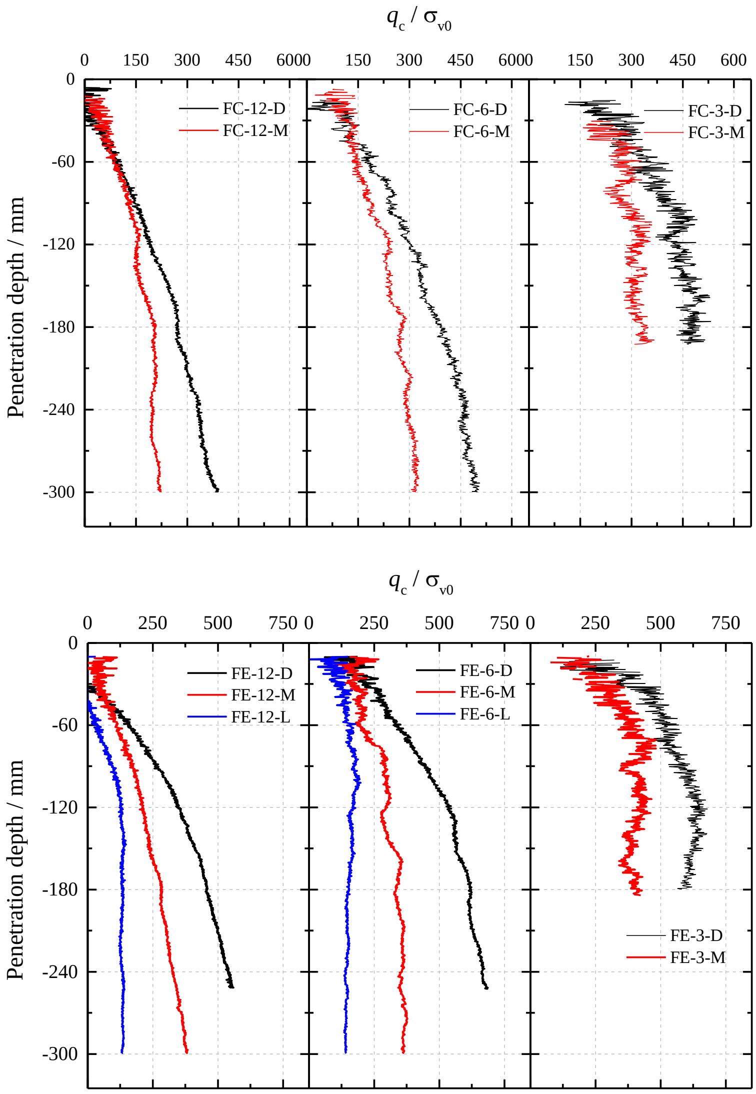

Fig. 2.35 Variation of the normalised tip resistance with relative density

2.6 Chapter summary

To account for the size effect in cone penetration tests, a series of miniature CPTs in deposited dry sand samples were carried out. The design, preparation and implementation procedures were presented in this chapter. Three different sized cone penetrometers were designed, and silica Leighton Buzzard sand with two fractions (C and E) were used to prepare the test samples with the air pluviation method. Overall, 23 sand samples with different relative densities were prepared, and 41 penetrations were executed. All test results and some preliminary analyses were presented in the final section of this chapter. These results will be employed to reveal and explain the size dependent behaviours in relatively shallow penetrations, which will be further interpreted in next two chapters by theoretical approaches and compared with other available experimental findings.

Chapter 3

Size-dependent large strain cavity expansion solutions for sands

3.1 Introduction

Cavity expansion theory is a specific theoretical approach to study the evolution of stress and deformation fields associated with an expanding cavity. Benefiting from some simplifying assumptions on the boundary conditions, constitutive law, and/or compatibility equations, a large number of closed-form cavity expansion solutions has been obtained by researchers for different applications (Hill, 1950; Savin, 1970; Yu, 2000). In particular, due to its successful applications in the calculation of pile bearing capacity, interpretation of *in situ* tests (e.g. pressuremeter tests, cone penetration tests), prediction of tunnel deformation and wellbore stability analysis etc. (Yu, 2000), analytical quasi-static cavity expansion analysis experienced a great deal of developments over the last half-century in the geotechnical field (Baligh, 1976; Cao et al., 2002; Carter et al., 1986; Chadwick, 1959; Collins and Yu, 1996; Gibson and Anderson, 1961; Ladanyi, 1972; Mo et al., 2014; Salgado et al., 1997; Vesic, 1972; Yu and Carter, 2002; Yu and Houlsby, 1991; Yu and Rowe, 1999). Most of them were built in the framework of classical continuum theories, and, as a consequence, the real cavity size generally applies no effect on the limit expansion pressure which is of great interests in practical applications. However, cavity size-dependent behaviour is often reported in tests with hollow cylindrical specimens (Elkadi and Van Mier, 2006; Enever and Wubailin, 2001; Papamichos and Van Den Hoek, 1995), pile side frictional resistance (Balachowski, 2006; Foray et al., 1998; Garnier and König, 1998; Lehane et al., 2005a; Turner and Kulhawy, 1994; Wernick, 1978), end bearing capacity of shallow and deep foundations (Cerato and Lutenegger, 2007; Chow, 1996; De Beer, 1963; Toyosawa et al., 2013) and tip resistance of cone penetration tests (Balachowski, 2007; Bolton et al., 1999; Eid, 1987; Lee, 1990; Lima and Tumay, 1991; Wu and Ladjal, 2014) (as reviewed in Chapter 2). It is generally found that the smaller the structure size is, the stiffer soil response may be experienced. Therefore, improvements of the conventional cavity expansion solution to take the size effect into account may be of great significance in promoting its practical applications.

In fact, increasing interests have been attracted to account for the widespread size effects (Aifantis, 1999). By considering higher-order deformation gradients in the constitutive models or additional degrees of freedom (Mühlhaus and Aifantis, 1991), different types of material internal length scales have been introduced into several branches of high-order theories of elasticity and plasticity (Aifantis, 1996, 1999, 2003; Fleck et al., 1994; Mindlin, 1964; Nix and Gao, 1998; Zhu et al., 1997). Based on strain gradient elasticity theories, the size effect or localisation phenomenon around a cavity (e.g. a thick-walled cylinder) was studied by some elastic solutions (Aifantis, 1996; Collin et al., 2009; Eshel and Rosenfeld, 1970). Furthermore, the size effect has also been considered in some elastic-plastic cavity analyses. For example, by introducing a Laplacian term of the effective plastic strain into the yield criterion, Gao (2002, 2003a, 2006) presented several analytical solutions both for cylindrical and spherical cavities based on Hencky's type deformation theory. Tsagrakis et al. (2004) developed an analytical solution with a similar deformation-type strain gradient theory of plasticity and a numerical solution with a strain gradient plasticity of flow version for expanding thick-wall cylinders. They demonstrated that a continuous displacement field can be obtained without inclusion of extra boundary conditions in the deformation theory based solution (Tsagrakis et al., 2006). Unfortunately, these constitutive relations are not very appropriate for describing the behaviour of sands, and restrictions on the infinitesimal deformation and/or incompressibility of materials further limit their applications in the geotechnical field. Accordingly, some attempts were made to extend these solutions for applications to granular materials. Ladjal (2013) introduced a second-order strain gradient into the Drucker-Prager yield criterion, and two approximate spherical cavity expansion solutions with different inclusion methods of the strain gradient term were developed by neglecting the elastic strains in the plastic region. Based on a 'couple-stress' type strain gradient theory, Zhao et al. (2007) presented an elastic-plastic analysis of a pressurised cylinder based on a modified Tresca-type criterion, and then Zhao (2011) extended this solution to cohesive-frictional materials both for cylindrical and spherical cavities. However, these solutions were also established with the small strain assumption which is not appropriate for describing the accumulative large deformation in a continuous expansion process. In addition, by adopting a different 'couple-stress' type of strain gradient elastoplasticity theory, Zervos et al. (2008) presented a numerical analysis on the pressurised thick-walled cylinder based on the finite element technique. Overall, present size-dependent cavity expansion solutions mainly focused on the static analysis or infinitesimal deformation problems. Finite deformation quasi-static cavity expansion solutions with consideration of the size effect were seldom studied in the analytical or semi-analytical manner.

By incorporating a second-order strain gradient term into the conventional Mohr-Coulomb yielding criterion, size dependent behaviour with respect to the cavity size and mean particle diameter are captured for a cylindrical or spherical cavity continuously expanding in sands. Rigorous solutions can be obtained by numerically solving the established second-order differential governing equation system with a simple iteration technique. Additionally, semi-analytical/analytical approximate solutions are also developed by neglecting the elastic increments of total strains in the plastic zone. The adopted basic assumptions are briefly introduced in the following two sections. Subsequently, combined solutions both for cylindrical and spherical cavities are presented in Section 3.4 and Section 3.5, and their performances are analysed and discussed in Section 3.6. The chapter conclusion is drawn in the final section.

3.2 Problem definition and basic assumptions

A cavity with an initial radius of a_0 is embedded in an infinite medium with an initial hydrostatic pressure, p_0. When extra uniform pressures, Δp, are gradually applied on the inner wall, the cavity will expand outwards monotonically from a_0 (initial radius) to a (current radius). It is assumed that the loading speed is slow enough (e.g. quasi-static) to allow the potential dynamic effect to be negligible. Governing equations of this problem are established based on requirements of geometry compatibility, stress equilibrium and the constitutive model as follows.

According to the fact of axial symmetry of a cylindrical cavity, the plane around a cylinder is specified in the cylindrical polar coordinates (r, θ, z), and the plane strain assumption with respect to the z-direction is adopted. In addition, the spherical polar coordinates (r, θ, φ) are employed to describe the spatial locations of points in the process of a spherical cavity expansion.

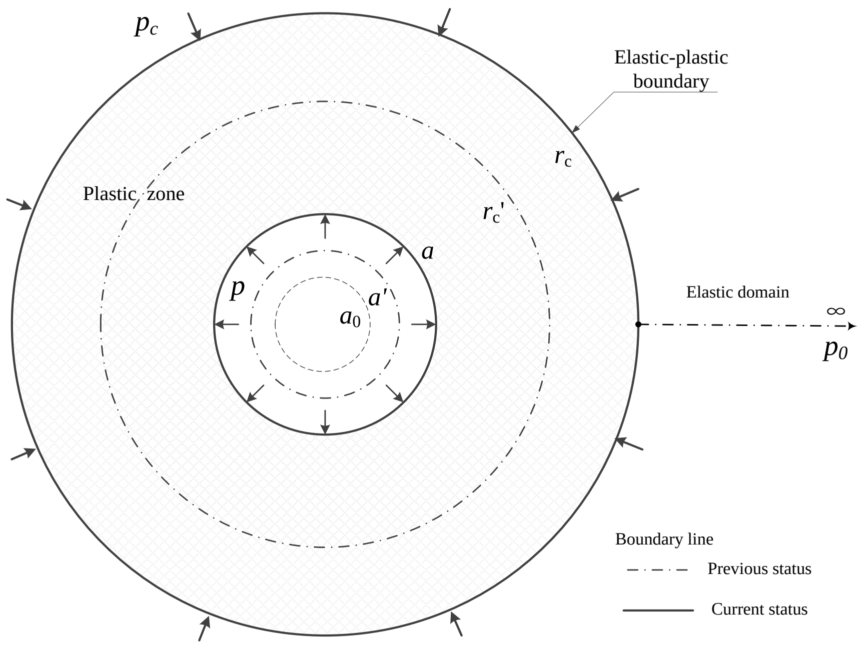

Fig. 3-1 Boundary conditions during cavity expansion under pressures

(1) Equilibrium condition

With changes of the stress configuration during a symmetrical expansion, stress equilibrium condition in the radial direction as Eq.(3-1) should be always satisfied.

$$\sigma_\theta - \sigma_r = \frac{r}{k}\frac{\partial \sigma_r}{\partial r} \tag{3-1}$$

where σ_θ and σ_r represent the circumferential and radial principal stress components respectively. $k=1$ for a cylindrical cavity, and $k=2$ for a spherical cavity.

(2) Compatibility equation

A combination of small deformation assumption in the elastic region and large strain analysis for the plastic deformation is adopted in this solution (Bigoni and Laudiero, 1989; Chadwick, 1959; Yu and Houlsby, 1991). In large deformation analyses of cavity expansion problems, two basic categories as the total strain approach and the incremental velocity method were commonly adopted as discussed by Yu and Carter (2002) (also see in Section 1.2). Here the former approach is followed. During strictly symmetrical expansions, it was found the definition of natural strains (logarithmic strain as given in Eq.(3-2 a,b)) suffices to describe the accumulative geometric changes without any limitation of deformation degree.

$$\varepsilon_r = \ln\frac{dr}{dr_0} \quad , \quad \varepsilon_\theta = \ln\frac{r}{r_0} \tag{3-2 a,b}$$

Then, by eliminating r_0, the geometric compatibility condition for large deformation can be derived as

$$[1 - e^{(\varepsilon_\theta - \varepsilon_r)}]dr = rd\varepsilon_\theta \tag{3-3}$$

For small deformation analysis (Hughes et al., 1977), the relationships between radial strain, tangential strain, and radial displacement can be expressed as

$$\varepsilon_r = \frac{du}{dr} \quad , \quad \varepsilon_\theta = \frac{u}{r} \tag{3-4 a,b}$$

and the compatibility condition for small strain analysis goes to

$$\varepsilon_r - \varepsilon_\theta = \frac{rd\varepsilon_\theta}{dr} \tag{3-5}$$

(3) Constitutive model of material

At initial expansion stages, medium around the cavity behaves elastically, obeying the generalised Hooke's law. Once the yield criterion is satisfied, a plastic zone will start forming from the inner cavity wall and continuously enlarge outwards with an increasing expansion pressure. As previously discussed, size-dependent behaviours were often observed in many common applications of the cavity expansion theory when the cavity size is in a comparable level of the characteristic material length, so it is necessary to incorporate material length scales into the governing equations. Motivated by Aifantis (1984, 1987), several types of strain gradient-dependent theory of plasticity have been developed with different inclusion methods of high-order strain gradients for different materials (Zbib and Aifantis, 1989), for example, they were included in the expression of the flow stress (Al Hattamleh et al., 2004; Mühlhaus and Aifantis, 1991), in the plastic flow rule (dilatancy condition) (Vardoulakis and Aifantis, 1989) or in the friction and dilation properties simultaneously (Vardoulakis and Aifantis, 1991).

For sands, the friction angle, in general, is significantly strain-dependent. On the contrary, the dilation property less depends on the strain level, and a unique dilation angle is usually predicted with the same stress level and sand relative density (Bolton, 1986; Chakraborty and Salgado, 2010; Schanz and Vermeer, 1996). Therefore, the non-local effect of sands will be taken into account by means of including high-order strain gradients into the friction strength of the classical Mohr-Coulomb yield criterion. Additionally, Al

Hattamleh et al. (2004) stated that the contribution of strain gradients terms higher than the second order is minimal. Hence, only a second-order strain gradient is incorporated to modify the friction property as given in Eq.(3-6). The yield criterion is expressed in terms of principal stresses as

$$f = \bar{\alpha}\sigma_1 - \sigma_3 \tag{3-6}$$

where σ_1 and σ_3 are the major and minor principal stress respectively. $\bar{\alpha}$ represents the modified stress flow number associated with the friction angle φ of sands.

$$\bar{\alpha}(\gamma_p, \nabla^2\gamma_p) = \alpha(\gamma_p) + c_g\nabla^2\gamma_p \tag{3-7}$$

where c_g is a phenomenological strain gradient coefficient, and γ_p is the equivalent shear plastic strain. ∇^2 is the Laplacian operator. $\alpha(\gamma_p)$ represents the homogenous part of the strain-dependent friction strength in the conventional theory of plasticity (Salgado et al., 1997). In the perfectly-plastic Mohr-Coulomb model, it equals to $\alpha = \tan^2(45^o + \varphi/2)$ as a constant, and it is adopted to describe the homogeneous deformation in this solution. The inhomogeneous evolution of underlying microstructures is represented by the included second order strain gradient term.

3.3 Physical definition of the gradient coefficient

In the classical continuum mechanics, the stress at one point depends on the local deformation history of that point only. To account for the heterogeneity of material or long-range interactions of points, the nonlocal mechanics concept is adopted, in which stresses at one point will be determined by deformation histories of all points in a Representative Volume Element (RVE), V . V reflects a phenomenal scope of nonlocal contributing points, which is defined as a mesoscale index ($= 4\pi R_g{}^3/3$ in three dimensions, and $= \pi R_g{}^2$ for the plane problem). As stated by Mühlhaus and Aifantis (1991); Vardoulakis and Aifantis (1991), the average strain $\bar{\gamma}_p$ within a symmetric neighbourhood of x can be expressed by Taylor series expansion when the nonlocal behaviour becomes dominant.

$$\bar{\gamma}_p = \frac{1}{V}\int_V \dot{\gamma}_p(x_i + \xi_i)d_V \tag{3-8}$$

$$\dot{\gamma}_p(x_i+\xi_i)=\dot{\gamma}_p(x_i)+\nabla\dot{\gamma}_p(x_i)\xi_j+\frac{1}{2!}\nabla^2\dot{\gamma}_p(x_i)\xi_j\xi_k+\cdots \tag{3-9}$$

where ξ_i is a vector along the radial direction and $|\xi_i|<<R_g$. ∇ is the gradient operator, and $\nabla^2\cdot=\nabla(\nabla\cdot)$. Substituting Eq.(3-9) into Eq.(3-8) gives

$$\bar{\gamma}_p=\gamma_p(x_i)+\frac{1}{\pi R_g^{\,2}}[\frac{R_g^{\,3}}{3}\nabla\gamma_p(x_i)\int_0^{2\pi}n_j d_\theta+\frac{1}{2!}\frac{R_g^{\,3}}{4}\nabla^2\gamma_p(x_i)\int_0^{2\pi}n_j n_k d_\theta+\cdots] \qquad \text{(2D) (3-10)}$$

where $\int_0^{2\pi}n_j d_\theta=0$, $\int_0^{2\pi}n_j n_k d_\theta=\pi\delta_{ij}$ (i from 1 to 2).

$$\bar{\gamma}_p=\gamma_p(x_i)+\frac{3}{4\pi R_g^{\,3}}[\frac{R_g^{\,4}}{3}\nabla\gamma_p(x_i)\int_0^{2\pi}n_j d_\theta+\frac{1}{2!}\frac{4R_g^{\,5}}{15}\nabla^2\gamma_p(x_i)\int_0^{2\pi}n_j n_k d_\theta+\cdots] \qquad \text{(3D) (3-11)}$$

where $\int_0^{2\pi}n_j d_\theta=0$, $\int_0^{2\pi}n_j n_k d_\theta=\frac{2\pi}{3}\delta_{ij}$ (i from 1 to 3).

A combined expression considering the contribution of the second order strain gradient can be summarised as

$$\bar{\gamma}_p=\gamma_p+C_{nD}\nabla^2\gamma_p \tag{3-12}$$

where the coefficients are $C_{2D}=R_g^{\,2}/8$ and $C_{3D}=R_g^{\,2}/10$ respectively.

Back to the modified friction strength, by assuming it varies slowly and monotonically with $\bar{\gamma}_p$ (or $(\bar{\gamma}_p-\gamma_p)<<1$), non-local contributions of neighbouring points to the overall macroscopical friction property of sands can be physically related to the internal material characteristic length by introducing a new material parameter H_g which is defined to indicate the rate of variation of the friction property with the nonhomogeneous deformation.

$$\bar{\alpha}=\alpha(\gamma_p)+H_g\cdot(\bar{\gamma}_p-\gamma_p)\quad,\quad H_g=\left.\frac{d\bar{\alpha}}{d\bar{\gamma}_p}\right|_{\bar{\gamma}_p=\gamma_p} \tag{3-13}$$

Consequently,

$$c_g=H_g C_{nD}=H_g l_g^{\,2} \tag{3-14}$$

Dimension analysis shows 'c_g' has a dimension of $[L^2]$. Physically, H_g performs like a non-dimensional index ruling the size-strengthening (positive) phenomenon, and 'l_g' is an intrinsic material length indicating the statistical contributing area to the local deformation. These two microscopic material parameters have not been clearly identified or defined yet, especially with experimental methods. Alternatively, in the application to sands, the inherent material length (l_g) is approximately represented by the mean particle size ($l_g \approx d_{50}$) as suggested by Vardoulakis and Aifantis (1991) based on the analysis of shear band spacing in granular materials. For H_g, it was assumed to mainly vary with γ_p (Aifantis, 1996; Al Hattamleh et al., 2004) or as well as $\nabla^2\gamma_p$ (Vardoulakis and Aifantis, 1991) in different models. For simplicity, it was often approximately set as a constant value with close relations to the elastic shear modulus (Gao, 2002; Ladjal, 2013; Tsagrakis et al., 2004; Zbib, 1994). In practice, the elastic soil stiffness is often normalised by σ_{atm} (atmospheric pressure, 100kPa) (Mitchell and Soga, 2005), which depends on the confining pressure level and packing conditions of sand particles. This expression is followed to represent H_g as in Eq.(3-15), but an additional adjustment coefficient ρ is included to represent the difference between them.

$$c_g = \rho(G/\sigma_{atm})d_{50}^{\ 2} \tag{3-15}$$

A similar form of H_g was suggested by Vardoulakis and Aifantis (1991) in a model with modification of the friction property in the yield criterion. G/σ_{atm} can be estimated with a number of empirical equations (Bui, 2009; Hardin and Black, 1966; Mitchell and Soga, 2005), which includes relationships based on the cone tip resistance (Baldi et al., 1991; Rix and Mayne, 1993; Rix and Stokoe, 1991; Schnaid et al., 2004) as applied in Chapter 4. For simplicity, c_g is assumed as constant for a given expansion problem in this solution, and further discussions will be given in the following section of 4.3.2.2.

3.4 Cavity expansion analysis

3.4.1 Elastic solutions

Initially, the surrounding soil deforms purely elastically. According to the generalised Hooke's law, stress-strain relationships in rate version can be expressed as

$$\dot{\varepsilon}_r = \frac{\partial \dot{u}}{\partial r} = \frac{1}{M}[\dot{\sigma}_r - \frac{k\nu}{1-\nu(2-k)}\dot{\sigma}_\theta] \tag{3-16}$$

$$\dot{\varepsilon}_\theta = \frac{\dot{u}}{r} = \frac{1}{M}\left\{-\frac{\nu}{1-\nu(2-k)}\dot{\sigma}_r + [1-\nu(k-1)]\dot{\sigma}_\theta\right\} \tag{3-17}$$

‘Standard’ stress boundary conditions for the defined problem are

$$\sigma_r\big|_{r=a} = -p \quad , \quad \sigma_r\big|_{r\to\infty} = -p_0 \quad , \quad \sigma_\theta\big|_{r\to\infty} = -p_0 \tag{3-18 a,b,c}$$

Then the elastic stress-strain relations can be integrated directly as

$$\varepsilon_r^e = \frac{1}{M}[\sigma_r - \frac{k\nu}{1-\nu(2-k)}\sigma_\theta + \frac{(1-2\nu)p_0}{1-\nu(2-k)}] \tag{3-19}$$

$$\varepsilon_\theta^e = \frac{1}{M}\left\{-\frac{\nu}{1-\nu(2-k)}\sigma_r + [1-\nu(k-1)]\sigma_\theta + \frac{(1-2\nu)p_0}{1-\nu(2-k)}\right\} \tag{3-20}$$

where $M = \dfrac{E}{1-\nu^2(2-k)}$. E is Young’s modulus. $G = E/2(1+\nu)$ represents the shear modulus. ν is the Poisson’s ratio.

Elastic stress components and the radial displacement can be readily derived based on the equilibrium equation (Eq.(3-1)), compatibility equation (Eq.(3-5)) and stress boundary conditions (Eq.(3-18 a,b,c)). Here the solution from Yu and Houlsby (1991) are followed.

$$\sigma_r^e = -p_0 - (p-p_0)(\frac{a}{r})^{1+k} \tag{3-21}$$

$$\sigma_\theta^e = -p_0 + \frac{1}{k}(p-p_0)(\frac{a}{r})^{1+k} \tag{3-22}$$

$$u_e = r - r_0 = \frac{p-p_0}{2kG}(\frac{a}{r})^{1+k} r \tag{3-23}$$

3.4.2 Elastic-plastic analysis

A second-order strain gradient term was introduced into the yield criterion, but this additional term would not alter the direction of principal stress in this symmetric expansion problem. Therefore, the inequalities given in Eq.(3-24 a,b) are still valid (Gao, 2003b; Tsagrakis et al., 2006) as they were in conventional elastic-perfectly-plastic models. The major and minor principal stress directions remain in the circumferential and radial directions respectively (taking tension as positive), which generally provides fundamental basis for analytical cavity expansion analyses in soils (Mo et al., 2014; Yu and Houlsby, 1991),

$$\sigma_\theta \geq \sigma_z \geq \sigma_r \quad \text{(Cylindrical)} \quad , \quad \sigma_\theta = \sigma_\varphi \geq \sigma_r \quad \text{(Spherical)} \tag{3-24 a,b}$$

Hence the modified yield criterion in Eq.(3-6) can be rewritten as

$$[\alpha + c_g(\frac{k}{r}\frac{\partial \gamma_p}{\partial r} + \frac{\partial^2 \gamma_p}{\partial r^2})]\sigma_\theta = \sigma_r \tag{3-25}$$

No effects will be produced by the strain gradient term when the material just enters the plastic flow state ($\nabla^2 \gamma_p \big|_{r=r_c} = 0$), so the modified yield criterion will recover to the conventional one as $\alpha\sigma_\theta = \sigma_r$ at the elastic-plastic boundary ($r = r_c$). Based on the radial stress continuity condition at $r = r_c$, the experienced pressure at the elastic-plastic surface (p_c) can be directly obtained with previous elastic stress solutions.

$$p_c = p_{1y} = \frac{k(\alpha - 1)p_0}{\alpha + k} + p_0 = 2kG\delta + p_0 \quad , \quad \delta = \frac{(\alpha - 1)p_0}{2G(\alpha + k)} \tag{3-26}$$

It is evident that p_c is position-independent, and it can be regarded as an initial threshold value (p_{1y}) to differentiate the elastic region and plastic region in calculations. The stress, strain and displacement components in the elastic region can be readily obtained by directly replacing a with the radius of the elastic-plastic boundary r_c from the preceding elastic solutions.

In the present strain gradient-dependent theory of plasticity, only the yield criterion is modified, and the plastic flow is still determined by the conventional flow rules. The plastic strain rates are assumed to be proportional to '$\dot{\gamma}_p$', and the plastic flow directions are determined with the normality condition with respect to the plastic potential function g (Al Hattamleh et al., 2004).

$$\dot{\varepsilon}_{ij}^p = \frac{\partial g}{\partial \sigma_{ij}} \dot{\gamma}_p \tag{3-27}$$

A non-associated flow rule corresponding to the Mohr-Coulomb model is adopted for characterising the plastic deformation of sands. As a result,

$$\dot{\varepsilon}_r^p = -\dot{\gamma}_p \quad , \quad \dot{\varepsilon}_\theta^p = \frac{\beta}{k}\dot{\gamma}_p \tag{3-28 a,b}$$

where $\beta = (1+\sin\psi)/(1-\sin\psi)$. ψ is the dilation angle of sand.

When the plastic potential and yield surface become coincident (that is $\beta = \alpha$), the associated flow rule will be recovered, and the relations are identical to those derived with the principle of plastic power equivalence by Papanastasiou and Durban (1997). The total strain rates can be expressed with combinations of their elastic (Eq.(3-16), Eq.(3-17)) and plastic components (Eq.(3-28 a,b)), that is $\dot{\varepsilon}_{ij} = \dot{\varepsilon}_{ij}^{e} + \dot{\varepsilon}_{ij}^{p}$. Then principal strains are available by integrating them from the initial phase to the current state as

$$\varepsilon_r = \frac{1}{M}[\sigma_r - \frac{k\nu}{1-\nu(2-k)}\sigma_\theta + \frac{(1-2\nu)p_0}{1-\nu(2-k)}] - \gamma_p \qquad (3\text{-}29)$$

$$\varepsilon_\theta = \frac{1}{M}\left\{-\frac{\nu}{1-\nu(2-k)}\sigma_r + [1-\nu(k-1)]\sigma_\theta + \frac{(1-2\nu)p_0}{1-\nu(2-k)}\right\} + \frac{\beta}{k}\gamma_p \qquad (3\text{-}30)$$

All governing equations were presented by now. By substituting Eq.(3-29)and Eq.(3-30) into the compatibility equations, two typical second-order ordinary differential equation systems can be established in terms of variables of σ_r , σ_θ and γ_p . The equation system consists of Eq.(3-1), Eq.(3-3) and Eq.(3-25) is for large deformation analysis, and that formed by Eq.(3-1), Eq.(3-5) and Eq.(3-25) suits for small deformation analysis. In the elastic-plastic analysis, conventional boundary conditions can be obtained from the stress and strain continuity conditions at the elastic-plastic surface as usual.

$$\sigma_r\big|_{r=r_c} = -p_c \ , \ \sigma_\theta\big|_{r=r_c} = -p_0 + \frac{1}{k}(p_c - p_0) \ , \ \gamma_p\big|_{r=r_c} = 0 \qquad (3\text{-}31 \text{ a,b,c})$$

An extra boundary condition is obtained by assuming the first-order derivative of the equivalent shear plastic strain vanishes at the elastic-plastic surface as given in Eq.(3-32) (Mühlhaus and Aifantis, 1991; Tsagrakis et al., 2004).

$$\left.\frac{\partial\gamma_p}{\partial r}\right|_{r=r_c} = 0 \qquad (3\text{-}32)$$

3.5 Approximate size-dependent solutions

Due to the inclusion of the second-order term of the equivalent plastic shear strain in the modified yielding criterion, an explicit expression of γ_p in term of the spatial position becomes an important prerequisite for deriving an analytical solution of the established governing equation system (Gao, 2003a; Tsagrakis et al., 2004). However, it cannot be achieved prior to knowing the plastic stress field in the present flow-type plasticity model as shown in Eqs.(3-39) and (3-41). Alternatively, aiming to more straightforwardly express responses of the whole governing equation system to the additional Laplacian term, it is assumed that the elastic strain increments are negligible compared with plastic strain increments. Therefore, Eq.(3-33 a,b) is obtained as

$$\dot{\varepsilon}_r = \dot{\varepsilon}_r^p = -\dot{\gamma}_p \quad , \quad \dot{\varepsilon}_\theta = \dot{\varepsilon}_\theta^p = \frac{\beta}{k}\dot{\gamma}_p \tag{3-33 a,b}$$

Integrating them from r_c to r gives

$$\varepsilon_r = -\gamma_p + \varepsilon_r^e\Big|_{r=r_c} \quad , \quad \varepsilon_\theta = \frac{\beta}{k}\gamma_p + \varepsilon_\theta^e\Big|_{r=r_c} \tag{3-34 a,b}$$

With this further simplification, explicit expressions of γ_p are derived based on previous compatibility conditions as below.

3.5.1 Approximate finite strain cavity expansion analysis

Recalling the compatibility condition with finite strain definitions in Eq.(3-3), a simple differential equation about γ_p is built as

$$\frac{k}{\beta}\frac{dr}{r} = \frac{d\gamma_p}{1-e^{[(\beta/k+1)\gamma_p+(k+1)\delta]}} \tag{3-35}$$

An explicit expression of γ_p in terms of the spatial position is obtained based on the strain boundary condition of $\gamma_p\Big|_{r=r_c} = 0$.

$$\gamma_p = \frac{k}{\beta+k}\left\{\ln[\frac{r^{(k/\beta+1)}}{C_1+r^{(k/\beta+1)}}]-(k+1)\delta\right\} \qquad (C_1 = \eta r_c^{(\frac{k}{\beta}+1)},\ \eta = e^{-(k+1)\delta}-1) \tag{3-36}$$

Then the Laplacian term of γ_p becomes

$$\nabla^2\gamma_{p-c} = -(\frac{\beta+1}{\beta^2})\frac{C_1 r^{(1/\beta-1)}}{[C_1+r^{(1/\beta+1)}]^2} \qquad \text{(Cylindrical polar coordinates)} \tag{3-37}$$

$$\nabla^2\gamma_{p-s} = \frac{2C_1}{\beta^2}\frac{[\beta C_1 - 2r^{(2/\beta+1)}]}{r^2[C_1+r^{(2/\beta+1)}]^2} \qquad \text{(Spherical polar coordinates)} \tag{3-38}$$

In this case, the problem can be simply studied with Eq.(3-39) which consists of the yield criterion and the equilibrium equation.

$$\frac{d\sigma_r}{\sigma_r} = \frac{k}{r}(\frac{1}{\bar{\alpha}} - 1)dr \tag{3-39}$$

Based on previous 'standard' boundary conditions, the required internal expansion pressure is obtained as

$$p = p_c(\frac{r_c}{r})^{k(1-\frac{1}{\alpha})}\exp[-\int_a^{r_c}(\frac{1}{\bar{\alpha}} - \frac{1}{\alpha})dr] \tag{3-40}$$

It is evident that this solution is exactly the same as the conventional elastic-perfectly-plastic static stress solution (Bigoni and Laudiero, 1989; Chadwick, 1959; Vesic, 1972; Yu and Houlsby, 1991) while the strain gradient effect is neglected, that is $\bar{\alpha} = \alpha$.

Furthermore, movements of the elastic-plastic boundary during a continuous expansion can be derived by substituting the logarithm strains into the below compressibility equation.

$$\beta\varepsilon_r + k\varepsilon_\theta = \beta\,\varepsilon_r^e\Big|_{r=r_c} + k\varepsilon_\theta^e\Big|_{r=r_c} = (1-\beta)k\delta \tag{3-41}$$

with a solution of

$$\frac{r_c}{a} = [\frac{1-e^{(1-\beta)k\delta/\beta}(a_0/a)^{(k/\beta+1)}}{1-e^{(1-\beta)k\delta/\beta}(1-\delta)^{(k/\beta+1)}}]^{\frac{\beta}{\beta+k}} \tag{3-42}$$

Theoretically, the solution neglecting the elastic increment of the total strain in the plastic zone would produce relatively less over-prediction to the required expansion pressure than that ignoring all the elastic strain in plastic region, and Eq.(3-42) can reduce to the later one (Bigoni and Laudiero, 1989; Yu and Houlsby, 1991) by putting the left part of Eq.(3-41) to be zero. The approximate limit expansion pressure can be calculated with Eq.(3-39) and Eq.(3-42). It is worth emphasising that no non-conventional boundary condition is required in this approximate analysis when the Laplacian term is explicitly available in term of the spatial position not like the previous rigorous solution, and a similar conclusion was also suggested by Tsagrakis et al. (2004).

3.5.2 Approximate small strain cavity expansion analysis

In symmetric expansion problems with infinitesimal deformations, the compatibility condition of Eq. (3-5) derived based on the small strain definitions is often employed to describe the geometric variation. Consequently, the equivalent plastic shear strain and corresponding Laplacian term can be obtained respectively as

$$\gamma_p^s = \frac{k(k+1)\delta}{k+\beta}[(\frac{r_c}{r})^{(\frac{k}{\beta}+1)} - 1] \qquad \text{and} \qquad \nabla^2\gamma_p^s = (k+1)\delta(\frac{\beta^{2-k}+2k-1}{\beta^2})\frac{r_c^{(k/\beta+1)}}{r^{(k/\beta+3)}} \tag{3-43}$$

The superscript of γ_p^s indicates the small strain case. Subsequently, by substituting the Laplacian term of γ_p^s into Eq.(3-39), an analytical stress solution can be derived with the previous standard stress boundary conditions.

$$\sigma_r = -p_c(\frac{r_c}{r})^{k(1-\frac{1}{\alpha})}\left[\frac{c_g(k+1)\delta}{\alpha}(\frac{\beta^{2-k}+2k-1}{\beta^2})(\frac{r_c}{r})^{(\frac{k}{\beta}+1)}\frac{1}{r^2}+1\right]^{\frac{k}{\alpha}\frac{\beta}{(k+3\beta)}} \tag{3-44}$$

Similarly, the displacement solution of plastic deformation is available as

$$u_p\Big|^P = r - r_0 = r\delta\left\{\frac{(k+1)\beta}{\beta+k}[(\frac{r_c}{r})^{(1+\frac{k}{\beta})} - 1] + 1\right\} \tag{3-45}$$

The role of the additional strain gradient in the present size-dependent model can be more explicitly expressed in the above analytical solutions. It is shown that the defined material length l_g was successfully introduced into the stress expressions through c_g. The stress components depend on not only the non-dimensional geometrical quantities of the expansion but also on the real cavity size independently. The size effect attenuates with increases of the cavity radius, and the present stress solutions can exactly recover to those derived from corresponding local theories when the gradient effect vanished (ρ =0, or $(d_{50}/a)^2 \propto 0$).

3.6 Results analysis and discussion

The present solutions can be used to calculate the stresses and strains during a quasi-static expansion process or in any given static state, both of which are of wide use in practical applications. To improve the calculation efficiency, all stress components and material stiffness are normalised with respect to the initial confining pressure (p_0), and the spatial position is normalised with the current cavity radius (a) which can be regarded as a 'time scale' during the cavity expansion. In a non-dimensional form, the modified friction property becomes

$$\bar{\alpha} = \alpha + \rho\frac{G}{\sigma_{atm}}(\frac{d_{50}}{a})^2(\frac{k}{\bar{r}}\frac{\partial\gamma_p}{\partial\bar{r}} + \frac{\partial^2\gamma_p}{\partial\bar{r}^2}) \tag{3-46}$$

where $\bar{r}=r/a$, is the normalised radial position of material points.

Initially, the cavity expands in a purely elastic stage. The entire elastic stress and displacement fields can be analytically calculated with given elastic solutions. Once plastic deformations take place, iterations are required to compute the propagation of the elastic-plastic boundary under monotonically increasing internal loadings. In short, with a trial value of r_c/a, the stress and deformation information within the plastic region can be obtained by integrating the governing equation system in a given range of [1, r_c/a]. Then the one-to-one correspondence between r_c/a and a/a_0 during continuous expansions is confirmed with a simple bisection iteration technique. According to the significantly different response of the plastic deformation to the increase of r_c/a (as illustrated in Fig. 3-2), the calculation is subdivided into two phases. Specifically, in the initial expansion phase, r_c/a rises rapidly and monotonically with an increasing cavity expansion, but it reaches a plateau soon afterwards, in which the equation system is highly sensitive to a small variation of r_c/a. Results in the first expansion phase can be efficiently computed by assigning increasing values of r_c/a, and a high iteration accuracy can be guaranteed by controlling the absolute difference between the given value of a/a_0 and the back calculated value with a tolerance less than 10^{-5}. Contrarily, calculations in the second expansion stage are more tractable by means of assigning increasing values of a/a_0 due to the difficulty in estimating an appropriate initial iteration interval of r_c/a. Above integrations are accomplished with the ode113 solver in Matlab (2013a) here. An intensified boundary layer would be arisen by the present governing equations due to the inclusion of the strain gradient term (also indicated by Eq.(3-46)), so methods based on the boundary layer theory may provide more efficient tools for solving this type of problem (Holmes, 2012). It is out of the scope of this research and will be attempted in future work.

By following this calculation procedure, with the initial stress of $p_0 = 50\text{kPa}$ and soil properties ($G/p_0 = 350$, $\varphi = 40^{\text{o}}$, $\psi = 15^{\text{o}}$, $\nu = 0.3$, $d_{50} = 1\text{mm}$ unless redefinition), performances of the present size-dependent (abbreviated as SD in following graphs) solutions are discussed as below.

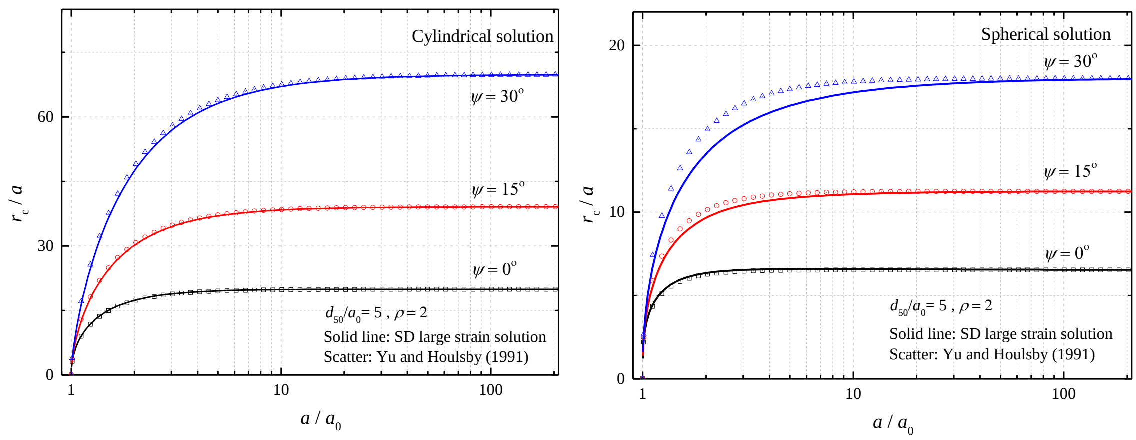

Fig. 3-2 Propagation of elastic-plastic boundaries with expansions

3.6.1 Analysis of stress and strain distributions

When the strain gradient effect vanishes, present solutions should reduce to the corresponding elastic perfectly-plastic cavity expansion solution, e.g. the solution of Yu and Houlsby (1991). Therefore, this solution is employed as a reference to discuss the concerned size-dependent behaviours included in the present solution as follows.

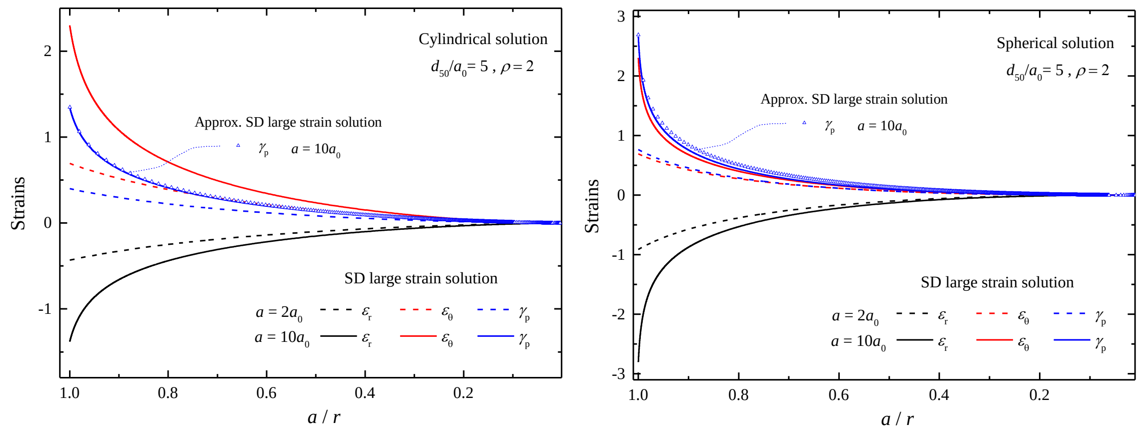

Fig. 3-3 Strain distributions within different expansion degrees

In a given instant, γ_p dramatically reduces in the close vicinity of the inner cavity and becomes slowly-varying in values close to zero while away from this zone. This trend intensifies with an increasing expansion level as illustrated in Fig. 3-3. It indicates contributions of the additional Laplacian term (first and second order space derivatives of γ_p) attenuate with an increasing distance away from the inner cavity wall and vanishes at the elastic-plastic boundary as specified by the non-standard boundary condition. This characteristic guarantees that the stress continuity conditions at the elastic-plastic boundary would always be satisfied as demonstrated in Fig. 3-4. It is shown that greater radial compression pressures are predicted by the size-dependent solutions at the cavity wall, and it gradually recovers to the solution of Yu and Houlsby (1991) at positions away from the inner boundary as expected. On the contrary, lower values of the stress in the circumferential direction are predicted by the size-dependent solutions, which returns to the conventional solutions with an increasing distance to the cavity wall as well. In addition, solutions based on the large strain and small strain compatibility conditions naturally gave similar results at small degrees of expansion as proven in Fig. 3-4.

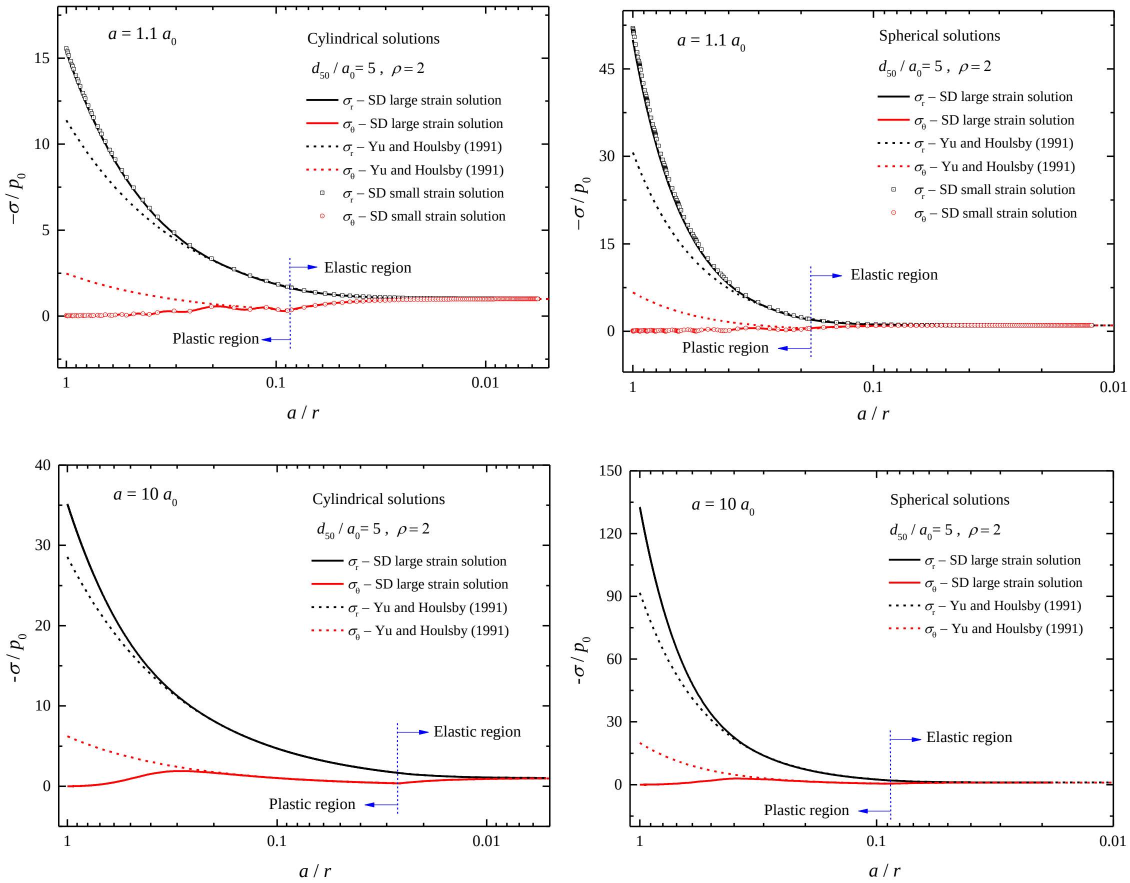

Fig. 3-4 Stress distributions within different expansion degrees

In a quasi-static expansion process, the elastic and plastic responses are determined both by the static stress equilibrium conditions and the accumulative deformation of expansions. Comparing with conventional solutions, the plastic stress field in present size-dependent solution is altered due to the additional inclusion of strain gradient terms in the yield criterion. As a consequence, the deformation characteristics would be disturbed more or less, which explains the induced changes of the range of plastic region (e.g. Fig. 3-2). The additional Laplacian term in Eq.(3-36) will gradually lose effect with a continuously increasing cavity radius, and the conventional yield criterion will be recovered with a sufficiently large cavity radius. This feature can be more straightforwardly observed with the approximate explicit expressions of the Laplacian term as presented in Fig. 3-5.

It is shown that the additional term in the yield criterion gradually grows to a peak value at small deformation levels (relatively small values of a/a_0), and then drops to around zero with increasingly large cavity radii. These additional influences mainly concentrate in a vicinity close to the cavity wall. Furthermore, the criterion deciding the elastic zone and plastic zone remains due to the unchanged elastic model and stress continuity conditions as given in Eq.(3-26). Therefore, just a small variation of the range of the plastic zone is caused, and a steady propagation of the elastic-plastic boundary with cavity expansions (r_c/a) will be reached with similar speeds as the corresponding conventional solutions (e.g. Fig. 3-2). This feature essentially determines that a constant radial expansion pressure will be predicted in the steady expansion state by conventional elastic-perfectly-plastic models (Bishop et al., 1945; Hill, 1950; Yu, 2000).

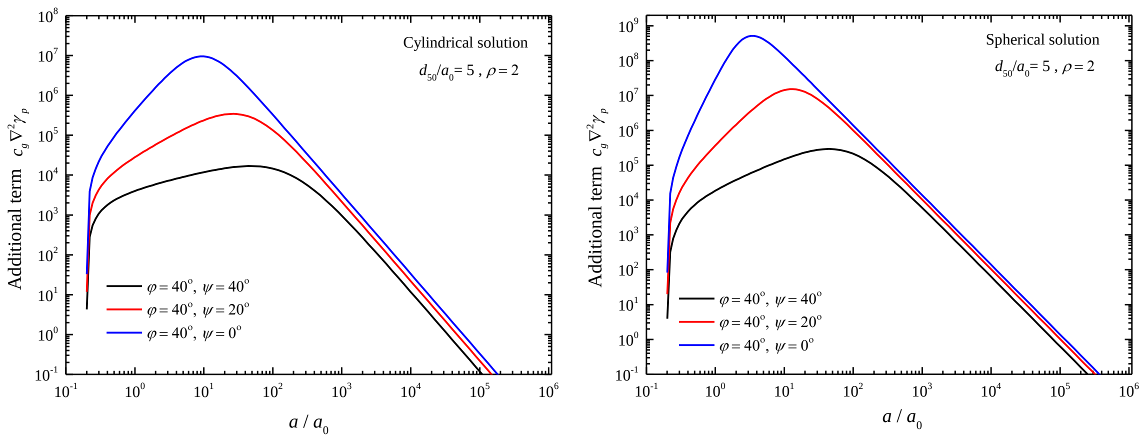

Fig. 3-5 Approximate values of the strain gradient term (Eq.(3-37) and Eq.(3-38))

In addition, notice that the additional Laplacian term applies different degrees of influences on the stress components in different directions (e.g. the speed recover to the conventional solutions). In other words, the variable of σ_r and σ_θ has different responses to the governing equation system, especially in the intensified zone close to the inner boundary. However, the radial pressure-expansion response is more concerned in the quasi-static analysis since its wide applications in practices, for example, estimating indentation/penetration resistance of cones, predicting the axial bearing capacity of piles, back-calculating soil properties etc., so the dependence of radial expansion pressure on the additional strain gradient term during quasi-static expansions will be emphasized in the following analyses.

3.6.2 Strain gradient effects on the radial expansion pressure

In conventional quasi-static cavity expansion solutions, the instantaneous cavity size makes homogenous contributions to the pressure-expansion response. Specifically, the deformation history is determined by a/a_0. At initial expansion stages, the required expansion pressure monotonically rises with increases of a/a_0. Then the required expansion pressure rapidly reaches a limit value when the steady expansion state is reached (r_c / a became constant), and the real cavity size will no longer apply influence during afterwards expansions. However, due to the inclusion of strain gradients in the yield criterion, the geometric sizes (a_0, a, and d_{50}) will all exert individual influences on the magnitude of the required internal pressure. Specifically, a / a_0 represents the expansion degree (cumulative strain level), r_c / a indicates the cavity deformation state, and d_{50} / a determines the contribution of the strain gradient term to the overall response together with the defined parameter of H_g. Influences of these factors in a quasi-static expansion process will be discussed by comparing with results calculated with the solution of Yu and Houlsby (1991), and parameter analyses of present size-dependent solutions and evaluation of the proposed approximate solutions will also be given in this section.

The initial cavity size a_0 is also concerned in quasi-static cavity expansion analyses in layered granular soils and was sometimes estimated with the mean particle size (Mo et al., 2016). However, providing that the soil particles of the same size d_{50} are tightly arranged and their centroid positions lie on the vertexes of a series of regular triangles (or regular tetrahedrons) in the plane (or three-dimensional) condition, the initial cavity radius equals $d_{50}/6.46$ $[=(2\sqrt{3}/3-1)d_{50}]$ (or $d_{50}/4.45$ $[=(\sqrt{6}/2-1)d_{50}]$) for the cylindrically (or spherically) expanding cavity. Based on this rough estimation, a_0 changes approximately around this range in following calculations.

(1) Radial expansion pressure during a continuous expansion

As presented in Fig. 3-6, by comparing with the conventional elastic perfectly-plastic solution, a stiffer initial elastic-plastic response is predicted by the present solution, and higher peak values of the required expansion pressure are rapidly reached before entering the steady deformation state. The predicted peak value is higher for the cavity expands from a smaller radius since the greater corresponding value of d_{50}/a at peaks. Then the internal radial pressure gradually decreases with further expansions and reduces to the limit value calculated by the conventional cavity expansion solution in a relatively large expansion radius as expected. Overall, a material characteristic length is incorporated in the present solution, which determines the magnitude of size effect as well as the defined material microscopic parameter H_g. Before the strain gradient effect vanishes, the present size-dependent solution predicts stiffer responses with smaller cavities in the continuous expansion process ($a_0 \rightarrow a$).

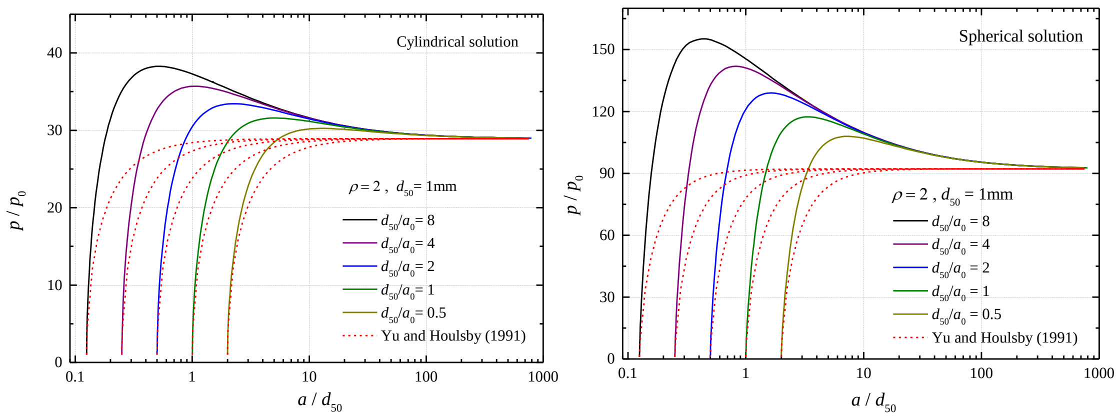

Fig. 3-6 Pressure-expansion curves during continuous expansions with different a_0

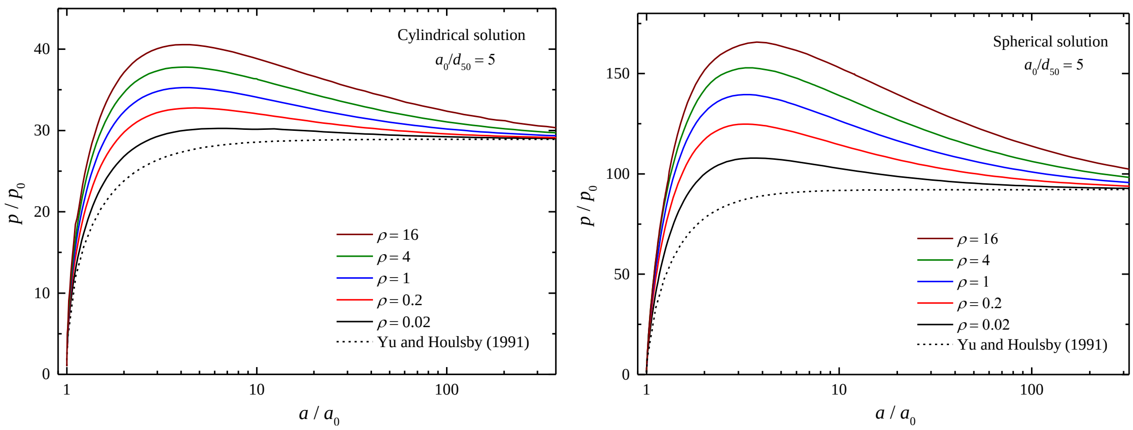

Fig. 3-7 Variation of the radial expansion pressure with different ρ

The incorporated size-dependent hardening effect significantly varies with the normalised gradient coefficient $\bar{c}_g$ $(= \rho(G/p_0)(d_{50}/a)^2)$ as demonstrated in Fig. 3-6 and Fig. 3-7. For a given cavity expanding in a known material, appropriate determination of the value of H_g $(= \rho(G/p_0))$ may play an important role in quantifying the concerned size effect in practical applications. In addition, with given c_g, performances of present solutions with varying friction and dilation properties of sands are illustrated in Fig. 3-8 respectively. Parameter analysis shows greater size effects appeared in cases of larger dilation angle and smaller friction angle in results of the calculated internal radial pressures. However, c_g may vary with the dilation and friction properties of sands, so dependencies of the size effect on these two parameters should be further confirmed based on experimental results.

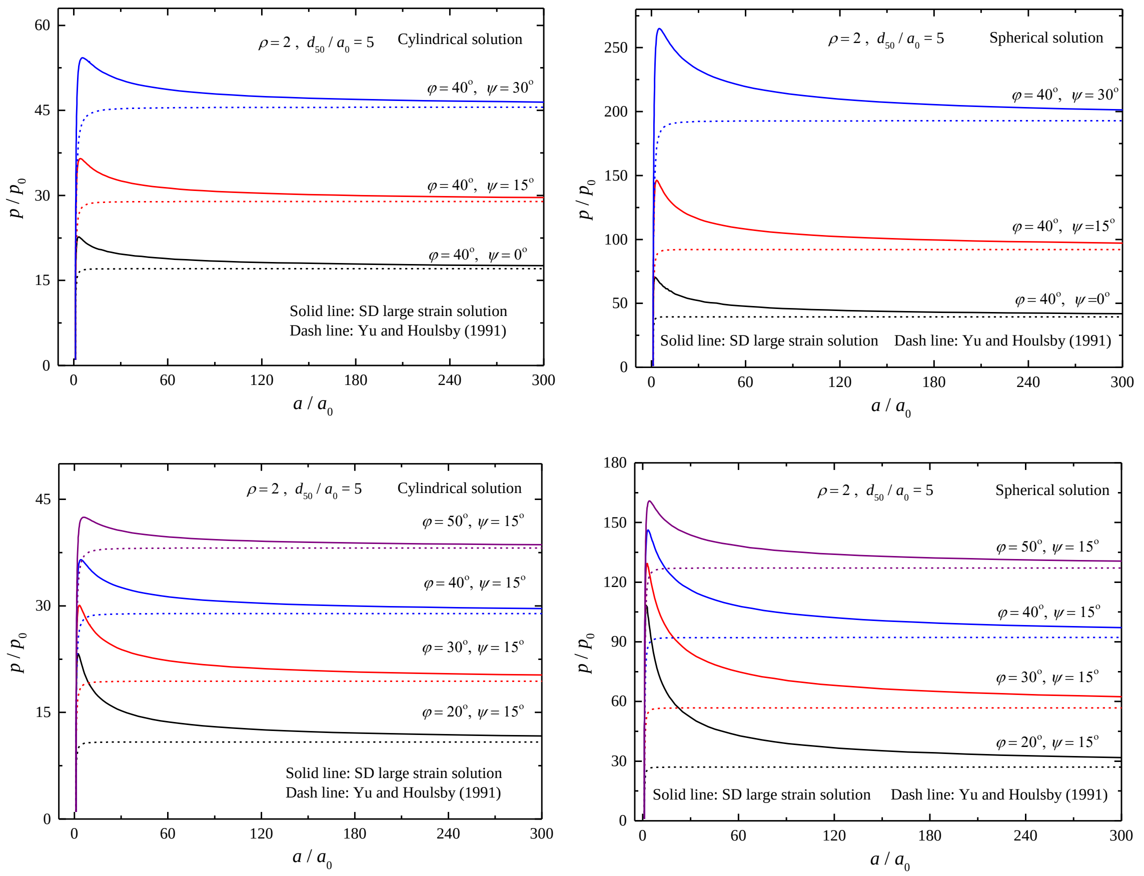

Fig. 3-8 Internal expansion pressure with varying friction and dilation properties

(2) Limit expansion pressure of a cavity with a given radius

The instantaneous cavity size (a) relates to the required expansion pressure in a non-dimensional manner in quasi-static solutions based on classical elastic-perfectly-plastic models as aforementioned, so the same expansion response will be predicted with the same value of a/a_0 no matter reached by increasing a or decreasing a_0 in these solutions. In other words, the constant limit expansion pressure will be reached as long as r_c/a gets close to its ultimate value either for cavities expanding from a given initial radius (Vesic, 1972; Yu and Houlsby, 1991) or in a self-similar manner (Carter et al., 1986; Hill, 1950; Yu and Carter, 2002). Contrarily, different performances are predicted by the present solution due to the inclusion of strain gradient terms. The pressure-expansion response with an increasing a from a given initial cavity radius has been discussed in above section. It showed that peak values of the required internal expansion pressure would be reached before the steady expansion state is reached, so results obtained in previous continuous pressure-expansion curves are not always the upper bound value for a cavity with a given size expands from any initial radius. In addition, it is not easy to determine the initial cavity radius in application to interpret *in-situ* tests. Hence the quasi-static expansion response of a cavity with a reversely decreasing a_0 is calculated as given in Fig. 3-9, Fig. 3-10 and Fig. 3-11.

It is shown that the required internal expansion pressure rapidly stabilises when the ratio of a/a_0 satisfied the requirement of steady expansions (approximately, $a/a_0 > 20$ and a bit quicker for cylindrical expansions). Hence, a limit expansion pressure for a cavity expands to a given radius also exists in the present size-dependent solution providing that the expansion degree is large enough to maintain the steady deformation happens before reaching the final cavity radius. This limit expansion pressure is cavity size-dependent (greater for smaller cavities) as shown in Fig. 3-9 and varies with the non-local property of H_g and the material characteristic length as shown in Fig. 3-10 and Fig. 3-11.

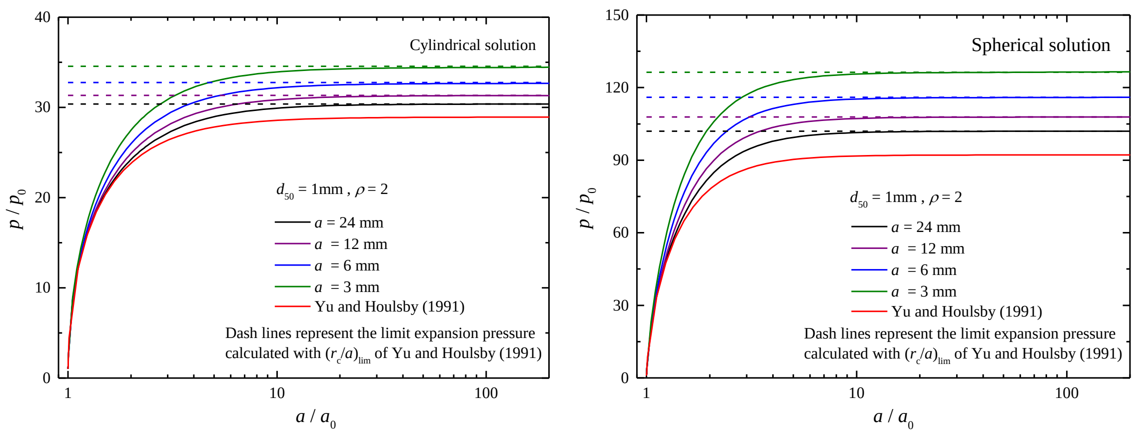

Fig. 3-9 Limit expansion pressure with varying final cavity radii

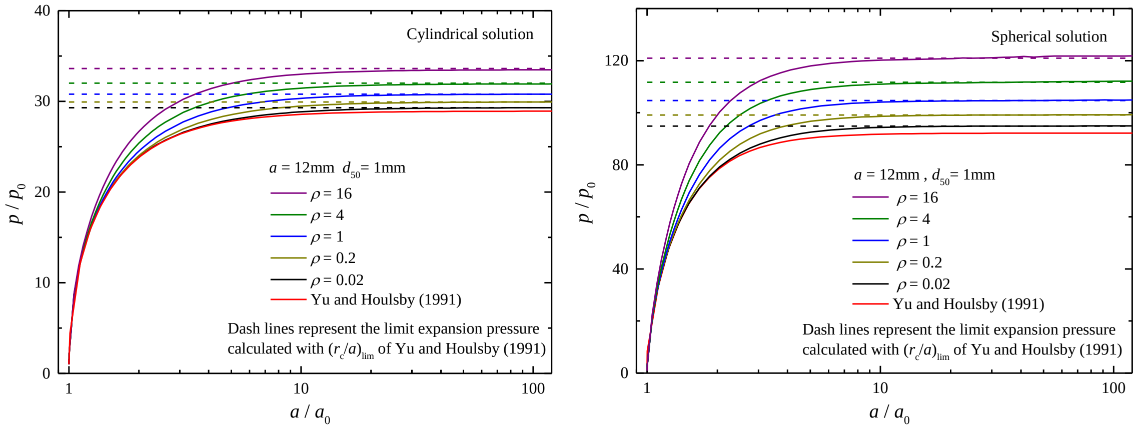

Fig. 3-10 Limit expansion pressure with different strain gradient coefficient

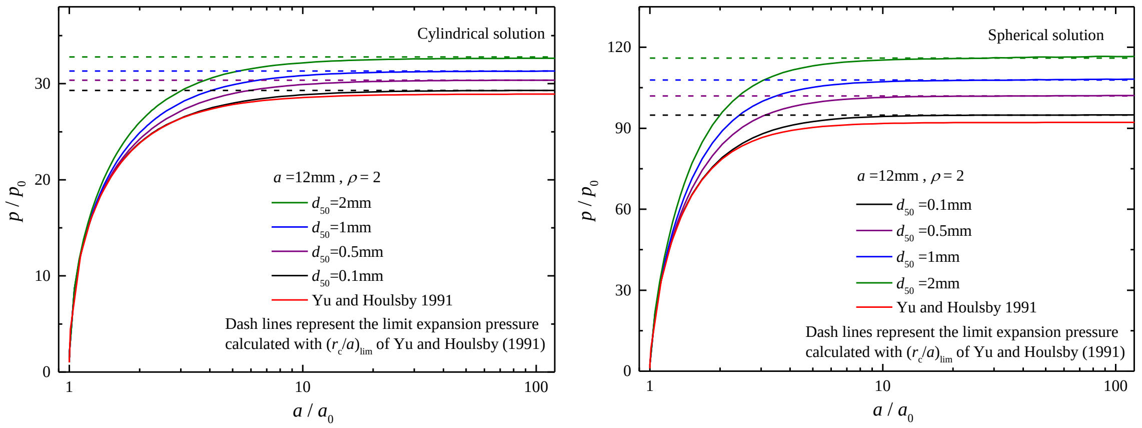

Fig. 3-11 Limit expansion pressure with different d_{50}

Alternatively, as demonstrated in Fig. 3-2, r_c / a rapidly gets close to the result calculated with the conventional solution of Yu and Houlsby (1991) in the steady state. Motivated by this finding, their analytical solution (as shown in Eq.(3-47)) is used to compute the relative position of the elastic-plastic boundary at the steady expansion stage (that is $(r_c / a)_{\lim}$) to reduce the computational cost. Results shown in Fig. 3-9-Fig. 3-11 demonstrated that this method gives almost the same limit expansion pressure as the continuous expansion solution. In this case, no iteration is required in predicting the limit expansion pressure, so the calculation procedure can be greatly simplified.

$$\Lambda_1(R_\infty, \xi_1) = (\eta_1 / \gamma_1)(1-\delta)^{(\beta+k)/\beta} \tag{3-47}$$

where $(r_c / a)_{\lim} = R_\infty^{\alpha/[k(\alpha-1)]}$, $\eta_1 = \exp\left\{\dfrac{(\beta+k)(1-2\nu)(\alpha-1)p_0[1+\nu(2-k)]}{E(\alpha-1)\beta}\right\}$,

$$\gamma_1 = \frac{\alpha(\beta+k)}{k(\alpha-1)\beta} \text{ , } \xi_1 = \frac{[1-\nu^2(2-k)](1+k)\delta}{(1+\nu)}\left[\alpha\beta + k(1-2\nu) + 2\nu - \frac{k\nu(\alpha+\beta)}{1-\nu(2-k)}\right].$$

and

$$\Lambda_1(R_\infty,\xi_1)=\sum_{n=0}^{\infty}A_n^1 \tag{3-48}$$

In which

$$A_n^1=\begin{cases}\dfrac{y^n}{n!}\ln x & ,\text{if} \quad n-\gamma_1 \\ \dfrac{y^n}{n!(n-\gamma_1)}[x^{(n-\gamma_1)}-1] & ,\text{otherwise}\end{cases}$$

In cone penetration tests, it was often observed that higher resistances are often experienced by smaller penetrometers (De Beer, 1963; Eid, 1987; Gao, 2006; Lima and Tumay, 1991; Wu and Ladjal, 2014), and the ratio of penetrometer diameter (final cavity size, e.g. a) over the median particle diameter (d_{50}) was commonly used to estimate if the size effect will be performing in these physical tests (Balachowski, 2007; Bolton et al., 1999). These findings coincide with the size effect predicted with the present solution in trend. Based on the analogy between the cone penetration test and the quasi-static cavity expansion process (Bishop et al., 1945; Yu, 2006), the present solution may provide a theoretical method to quantify those observed size-dependent behaviours (as applied later in Chapter 4). Or reversely, the data of cone penetration tests with varying sized penetrometers may be applicable to evaluate the introduced non-local property of the material (e.g. H_g).

(3) Pressure-expansion responses in small deformation levels

The radial pressure-expansion curve at initial expansion stages is also of practical use in interpretations of tests with small deformations, for example, pressuremeter tests (Hughes et al., 1977; Yu, 1990). Size-dependent behaviour at initial expansion stages (stiffer response) is also calculated with the present solutions as shown in Fig. 3-12. Naturally, almost the same results are given by the small strain solution and the large strain solution in small degrees of cavity expansions. Both these two solutions may be useful to describe the size-dependent behaviour in expansion problems with small deformations.

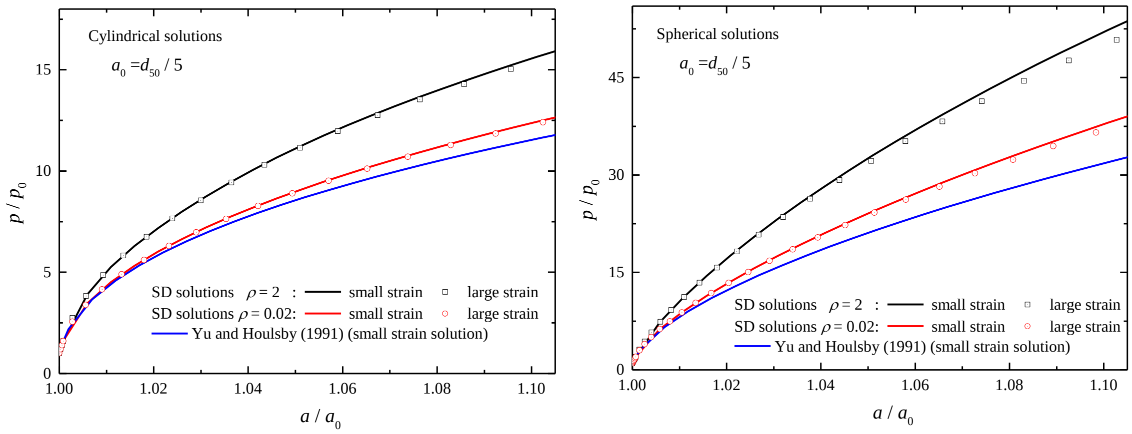

Fig. 3-12 Comparison of solutions in small deformations

3.6.3 Evaluation of the approximate size-dependent solutions

It was discussed by Bigoni and Laudiero (1989) that neglecting all the elastic deformations in the plastic region may lead to significant overestimations on the limit expansion pressure both in cylindrical and spherical cavity expansion solutions based the conventional Mohr-Coulomb criterion. Although part of the elastic strain in the plastic region has been considered in the present approximate solution, evident over-predictions are still produced with comparisons to the rigorous solutions as shown in Fig. 3-13 and Fig. 3-14, especially when the strain gradient effect performs. It is believed that the elastic increments of total strains in the plastic zone play an important role in a quasi-static cavity expansion analysis, but similar dependencies of the expansion pressure to the strain gradient effect performed by the rigorous size-dependent solutions and the approximate solutions in trend. Therefore, the analytical/semi-analytical approximate solutions can provide a more straightforward understanding of roles of the strain gradient effects in the present size-dependent model in spite of those obvious over-predictions.

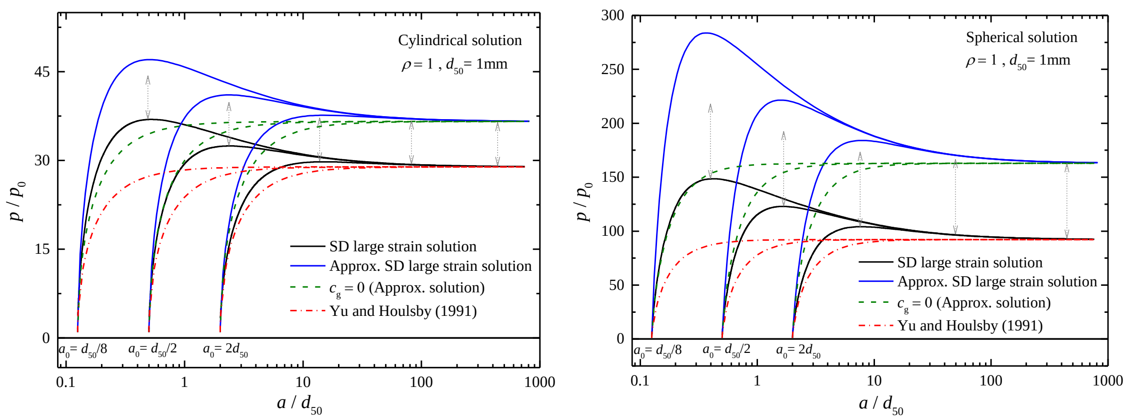

Fig. 3-13 Pressure-expansion behaviours during continuous finite deformations

In addition, Fig. 3-14 shows over-estimations on the required internal expansion pressure become more serious while describing the initial pressure-expansion response, and a stiffer initial soil strength is predicted while the approximate solutions are employed.

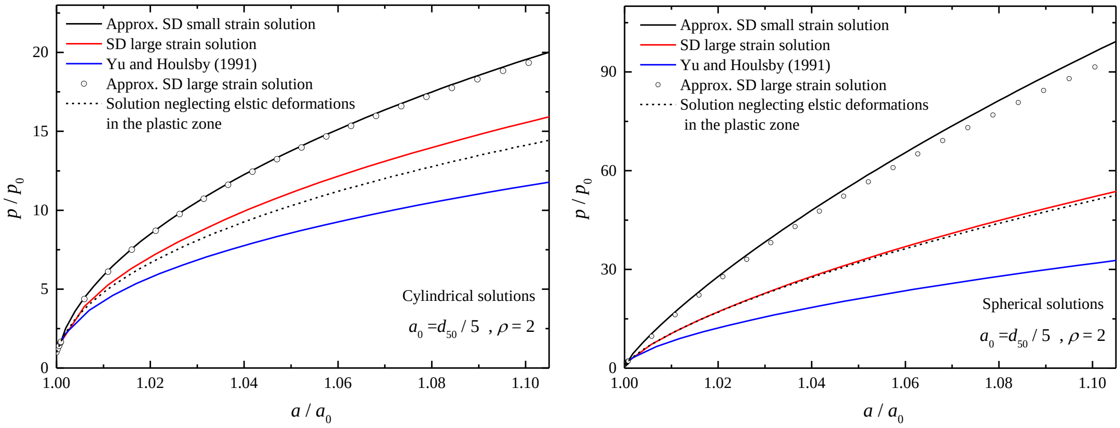

Fig. 3-14 Pressure-expansion response at small deformations

3.7 Chapter summary

Combined quasi-static cavity expansion solutions incorporating the size effect both for cylindrical and spherical cavities were presented and discussed in this chapter. In these solutions, the initial cavity radius, instantaneous cavity size and mean particle size all play independent roles in determining the continuous pressure-expansion response which cannot be modelled by solutions established within the framework of classical continuum mechanics. In addition to the method based on iteration technique, a simple approach to calculating the limit expansion pressure was proposed. This solution may be applicable to describe the widely observed size-dependent behaviours in cone penetration tests, bearing capacities of shallow and deep foundations. Applications to cone penetration tests will be presented in the next chapter.

The classical Mohr-Coulomb yield criterion was modified by incorporating a second-order strain gradient. Two new material parameters (H_g and l_g) were introduced in this model, but they have not been well defined and determined in physical tests until now. Therefore, the material characteristic length of sands was estimated by the mean particle size d_{50}, and H_g is approximately represented by $\rho(G/\sigma_{atm})$ in the development of present solutions. To better describe the size-dependent behaviours in cavity expansion problem, more experimental effort is needed to quantify these two parameters.

Chapter 4

Analysis and discussion of CPT results

4.1 Introduction

Mechanical impedance encountered by an advancing probe in soils generally consists of two parts: side friction and tip resistance. In general, they have different bearing mechanisms, and the proportion of their contributions to the total resistance varies with penetration depth, shape and surface conditions of the probe, soil response etc.. An advancing cone penetrometer usually displaces the surrounding soil in an analogous manner of a driven pile. Based on this analogy, methods used to estimate the bearing capacity of driven piles in sands are also commonly employed to interpret the present cone penetration tests, especially in estimations of the shaft friction capacity.

As suggested by Randolph et al. (1994), methods for estimating the capacity of driven piles in sands can be categorised into two broad groups: methods based on sand strength and deformation properties (friction angle, density, stiffness etc.) (API, 2000; Randolph et al., 1994; Toolan et al., 1990) and methods base on in-situ testing (CPT, standard penetration test (SPT), etc.) (Bustamante and Gianeselli, 1982; De Ruiter and Beringen, 1979; Kolk et al., 2005; Schmertmann, 1978). The tip resistance and side friction are often expressed as

$$q_b = N_b \sigma'_{v0} \quad \text{or} \quad q_b = k_c q_c \tag{4.1}$$

$$\tau_f = K_f \sigma'_{v0} \tan\delta_f = \beta \sigma'_{v0} \quad \text{or} \quad \tau_f = \bar{q}_c / \alpha \tag{4.2}$$

where q_b is the end-bearing resistance of a pile; N_b is a bearing capacity factor; σ'_{v0} is the effective vertical stress at depth *z*; k_c is a factor relating the pile end-bearing resistance and the cone resistance. K_f is a lateral earth pressure coefficient representing the ratio of the normal effective stress acting on the pile at failure to the in-situ effective overburden stress, which may significantly vary with the sand relative density (Alawneh et al., 1999; Kraft, 1990). α is a factor relating the cone tip resistance and the local shaft friction resistance, and $\bar{q}_c$ is usually taken as an equivalent average cone resistance over a specific range around the pile tip, but the suggested collecting range is not consistent in different design methods (Bustamante and Gianeselli, 1982; De Ruiter and Beringen, 1979).

The size effects both in the tip resistance and shaft capacity of cone penetration tests will be discussed based on available experimental data and theoretical analyses in this chapter. At first, empirical and theoretical methods commonly used to predict these two parts of soil resistance are briefly reviewed in the first section as follows. Then possible factors contributing the size-dependent behaviours in the shaft friction resistance are discussed, and the commonly used theoretical method to estimate changes in the lateral confining stress around a probe is improved with an additional consideration of the thickness of interface shear band in Section 4.2. Subsequently, the size effect on the cone tip resistance observed in the present tests and some other tests is theoretically analysed with the previously developed size-dependent spherical cavity expansion solution in the section of 4.3. Chapter conclusions are drawn in the final section.

4.1.1 Empirical methods for estimating the shaft friction

Specific theoretical methods for estimating the shaft friction of an advancing cone penetrometer are relatively scarce. Alternatively, design methods for the driven pile in sands will be employed to interpret the shaft frictional behaviour in present tests, which mainly depends on the Coulomb law as given in Eq.(4.3). Apart from the methods mentioned in Eq.(4.2), methods with combination uses of the CPT data and the intrinsic soil properties are increasingly popular for the driven pile design in sands, in particular, the method of ICP-05 (Jardine et al., 2005) and UWA-05 (Lehane et al., 2005c). A general expression of the shaft resistance for a close-ended pile in these two methods can be summarised as

$$\tau_f = (\sigma'_{hc} + \Delta\sigma_{rd})\tan\delta_f \tag{4.3}$$

$$\sigma'_{hc} = \frac{q_c}{a_e}\max\left(\frac{h}{D_{pile}}, e\right)^{-c} \tag{4.4}$$

$$\Delta\sigma_{rd} = 4\frac{G_m \Delta y}{D_{pile}} \tag{4.5}$$

where σ_{hc} is the normal stress acting on the pile surface after installation and equalisation, which is estimated by the cone tip resistance with consideration of the 'friction degradation effect'. $\Delta\sigma_{rd}$ is the change of radial stress during loading, which is often approximately calculated with a cavity expansion analogy as proposed by Boulon and Foray (1986). As discussed by Schneider et al. (2007b), parameter 'a_e' is to account for reduction of the radial stress behind the pile tip; exponent 'c' accounts for 'friction fatigue'; $h = |H - Z|$ (height above the pile tip), and parameter 'e' provides an upper limit of $(h/D)^{-c}$ near the pile tip since the existence of minimum shaft resistance. G_m is defined as the operational shear modulus of the sand; Δy is the normal displacement of sand at the pile interface. Different values of these parameters were recommended by methods of ICP-05 and UWA-05 based on different database and emphases (Lehane et al., 2005b).

4.1.2 Theoretical methods for predicting the tip resistance

Various theories with different merits and limitations have been developed to estimate the tip resistance in cone penetration tests (Yu, 2006; Yu and Mitchell, 1998), which are primarily based on the bearing capacity theory, cavity expansion theory, steady state approach and numerical simulation technique individually or in combination. Most commonly, methods based on the bearing capacity theory and the cavity expansion theory respectively will be employed to interpret our CPT results, and they are briefly introduced as follows.

(1) Bearing capacity approach

The bearing capacity theory is believed one of the first method applied in the analysis of cone penetration test (Meyerhof, 1951; Terzaghi, 1943). This class of methods are relatively easy to be accepted and employed by many engineers who are already familiar with the bearing capacity theory.

The cone resistance is estimated by the static failure load of equilibrium at a corresponding penetration depth, and a series of failure surfaces develops with the continuous penetration. Two theoretical approaches, limit equilibrium method and slip-line method, are usually applied to solve this simplified problem. In the limit equilibrium methods, the failure load is determined by the global equilibrium condition with a pre-assumed failure pattern. Therefore assumptions on the failure surface play a key role in this approach (Durgunoglu and Mitchell, 1975), and many types of failure patterns have been proposed (e.g. Fig. 4-1). In the slip-line approach, in general, a static slip-line network would be established based the plastic equilibrium and boundary conditions at first, and then the collapse load can be obtained based on the characteristics of slip lines. This method is relatively more rigorous than the former one because it satisfies both the equilibrium equations and the yield criterion everywhere within the slip-line network, but the velocity field usually cannot be exclusively determined and the stress field outside the plastic equilibrium zone is not clearly defined in this method. Furthermore, neither the deformation of soil nor further disturbances caused by the continuous penetration to the stress and strain distributions can be accounted by this branch of methods (Yu and Mitchell, 1998). Overall, these limitations may reduce the accuracy and reliability of these methods in predicting the tip resistance of a continuously moving penetrometer.

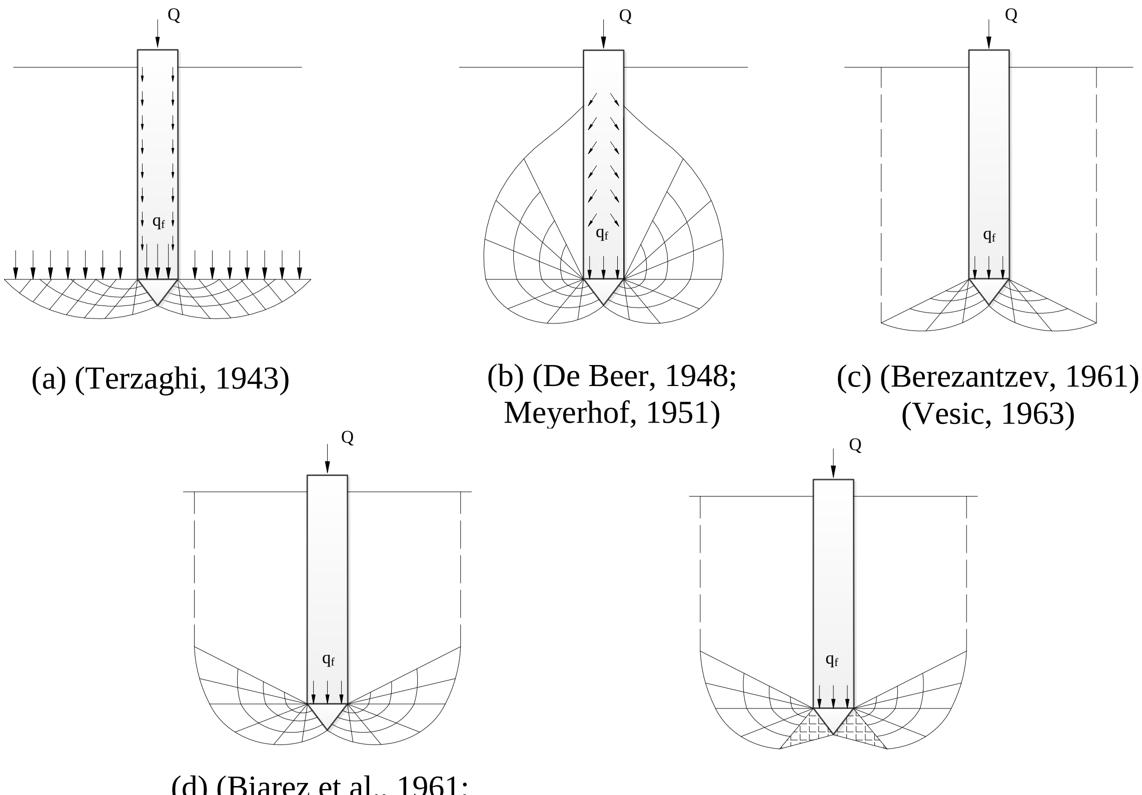

(a) (Terzaghi, 1943)

(b) (De Beer, 1948; Meyerhof, 1951)

(c) (Berezantzev, 1961) (Vesic, 1963)

(d) (Biarez et al., 1961; Hu, 1965)

(e) (Durgunoglu and Mitchell, 1973)

Fig. 4-1 Assumed failure mechanisms for a deep penetration

(2) Cavity expansion approach

Bishop, Hill, and Mott (1945) first demonstrated that the cone resistance with a deep indentation can be interpreted by an elastic-plastic quasi-static cavity expansion analysis. Then the analogy between cavity expansion and cone penetration greatly encouraged the development of cavity expansion theory and its applications to more penetration problems (Yu, 2000, 2006). In this approach, two key steps generally are required to be followed: ① obtain the limit expansion pressure based on appropriate cavity expansion solutions, and ② relate the limit expansion pressure to the tip resistance. Based on more and more realistic soil stress-strain models, great progress of the quasi-static elastic-plastic cavity expansion solutions (Baligh, 1976; Carter et al., 1986; Collins and Yu, 1996; Salgado et al., 1997; Vesic, 1972; Yu and Carter, 2002; Yu and Houlsby, 1991) has been made in the geotechnical field (e.g. reviewed in Section 1.2). Meanwhile, various relations connecting the cavity expansion pressure (either cylindrical or spherical solution, or in combination (Mo, 2014; Yu, 2006)) and the tip resistance have been proposed with different methods (e.g. Fig. 4-2).

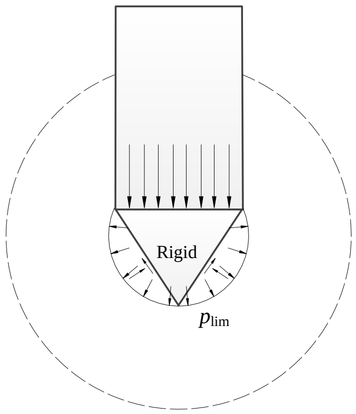

(a) (Ladanyi and Johnston, 1974; Randolph et al., 1994)

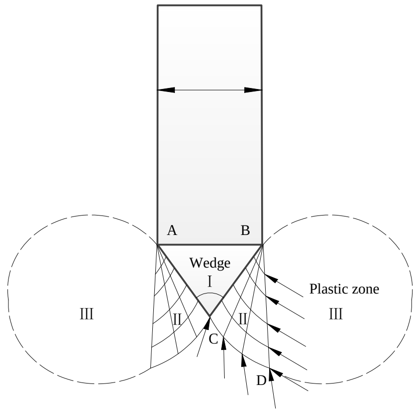

(b) (Vesic, 1977)

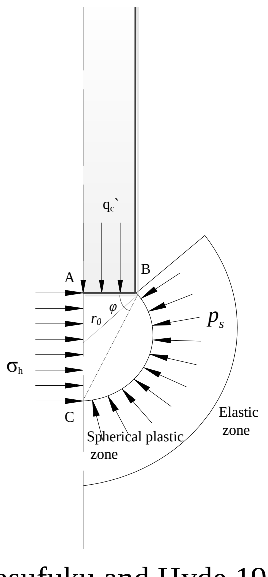

(c) (Yasufuku and Hyde 1995)

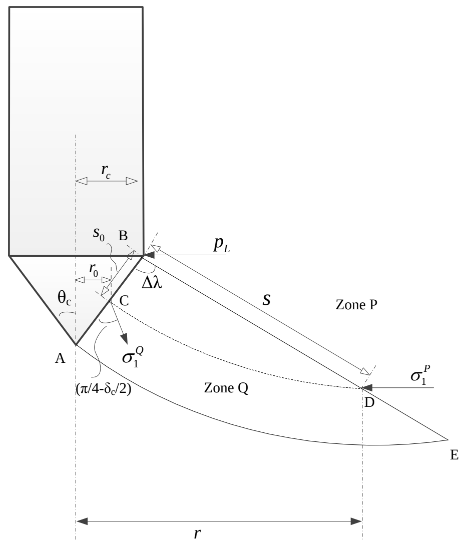

(d) (Salgado and Prezzi, 2007)

Fig. 4-2 Relations between cavity expansion pressure and end resistance

Although great simplifications are also assumed, especially in the relating process, this approach is widely regarded as one most tractable and reliable theoretical tool to interpreting the steady cone penetration problem. The bases or advantages of this method can be summarized as: (a) the stress and deformation fields ahead of an advancing cone are closely analogous to those described by the quasi-static cavity expansion solution, and (b) more realistic strength and deformation characteristics of soils can be taken into account by the cavity expansion theory.

4.2 Analysis on shaft friction

The Coulomb friction law as given in Eq.(4.3) has been widely employed to evaluate the shaft friction, which defines that the interface friction as the product of the experienced normal pressure and the mobilised interface friction strength. Specifically, the normal pressure acting on the shaft of a pressed-in pile is usually treated as the sum of the initial soil pressure at rest, the additional pressure caused by pile extrusion, and the shear-induced pressure due to interface dilation or contraction under loading (Lehane et al., 1993). Hence, the embedment depth, installation method, and soil stress history may all exert influences on the mobilisation of the confining soil pressure. The interface friction strength is predominantly determined by behaviours of soil in the localised shear zone formed in the close vicinity of the structure surface (named as interface shear band hereafter). In general, it is influenced by the independent or coupling effects caused by variations of the particle size, angularity, crushability, relative density of sand, roughness and hardness of pile surface and stress level (Frost et al., 2002; Jardine et al., 1993; Uesugi and Kishida, 1986a). The shaft friction capacity in our tests will be analysed with this method, and possible factors influencing the size-dependent behaviours in the interface frictional resistance will be discussed from these two aspects.

4.2.1 Back analysis of the shaft friction capacity in present tests

4.2.1.1 Characteristics of the shaft friction during penetrations

Among the aforementioned design methods for driven piles in sand, the CPT-based method (ICP-05) given by Jardine et al. (2005) is used to estimate the shaft friction capacity during cone penetrations, in which the local shaft resistance is computed by Eq.(4.3) with

$$\sigma_{hc}^{'} = A_{di} 0.029 q_c (\frac{\sigma_{v0}^{'}}{P_a})^{0.13} \max\left(\frac{h}{R_{pile}}, 8\right)^{-0.38} \tag{4.6}$$

where $G_m = q_c[0.0203 + 0.00125\eta - (1.216e-6)\eta^2]^{-1}$, $\eta = q_c(P_a\sigma_{v0}^{'})^{-0.5}$, $\Delta y = 2R_a$ .for parameters in Eq. (4.5). $P_a = 100\text{kPa}$, is the atmosphere pressure. A_{di} =1 in compression, and A_{di} =0.8 in tension.

Taking tests on the medium dense samples as examples, the measured and predicted shaft friction capacities are compared in Fig. 4-3. With interface friction angles of 10° and 20° respectively (Klotz and Coop, 2001), the ICP-05 method (Eqs.(4.3),(4.5), and (4.6)) gives good estimations for the shaft friction of cone penetrometers during continuous penetrations in relatively deep depths, but evident underestimations were made in relatively shallow depths. In addition, its accuracy may also vary with sand densities, which was also found by Mo (2014). Due to the pile size, typical embedment depths, and installation methods in their database for assessing these empirical formulas are more or less different to the present miniature cone penetration tests, so direct applications to interpretations of the present tests may inevitably lead to above deviations, and more discussions will be given later.

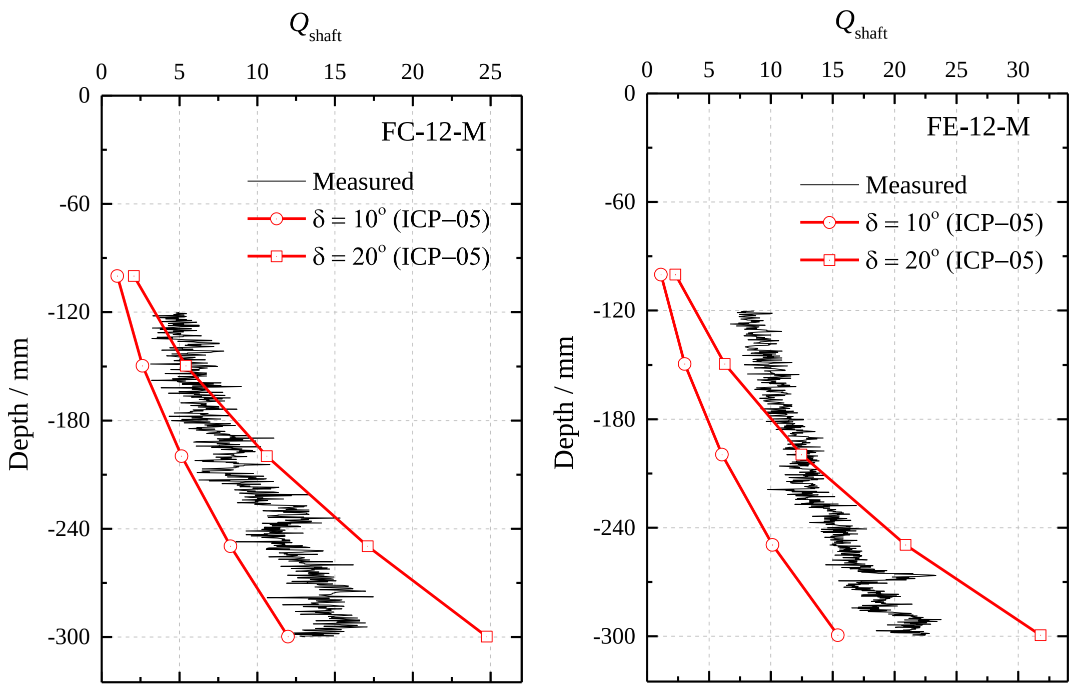

Fig. 4-3 Comparison of measured and predicted shaft friction capacity

Size effects have already been considered in above methods in terms of the interface friction strength and the lateral confining stress, but evident deviations still exist when they were directly applied to interpret the present tests. Therefore, the size-dependent shaft resistance in our tests is re-evaluated from these two aspects in the next section. In addition, it is found that the method for calculating of $\Delta\sigma_{rd}$ in Eq. (4.5) is greatly simplified, which was established based on a simple elastic cavity expansion solution. As a consequence, its accuracy strongly depends on the adopted value of G_m and Δy. However, so far, no widely-agreed method for determining these two fundamental parameters has been achieved (Schneider, 2007). For example, in aforementioned pile design methods (e.g. ICP-05 and UWA-05), the operational shear modulus G_m is assumed to be represented by the small strain shear moduli (G_0) with different empirical formulas. In fact, G_m may be smaller than G_0, which varies with the induced stress level and strain level (Fioravante et al., 2010b; Lehane et al., 2005a). In addition, Δy was estimated with two times of the average roughness of the interface ($\Delta y = 2R_a$) by the ICP-05 method, related to the pile diameter ($\Delta y / R_{pile} \approx 0.1\%$) by Lehane and White (2005), or expressed by the median particle diameter and R_a ($\Delta y \approx 2.5 {D_{50}}^{0.4} {R_a}^{0.6}$) by Schneider (2007). Therefore, to precisely quantify the change of lateral stress caused by pile installation (or probe penetration), more effort is still needed, and some attempts on this topic will be made as presented later in Section 4.2.2.2.

In addition, variations of the shaft friction during a continuous penetration is discussed with the averaged $\bar{\beta}$ (Eq.(4.2)) as plotted in Fig. 4-4 by following with Klotz and Coop (2001). $\bar{\beta}$ is the ratio of the average shaft friction resistance '$\bar{\tau}_{as}$' at a depth of H over the mean initial overburden earth pressure $\sigma'_{v0}\big|_{H/2}$. In Fig. 4-4, it shows that $\bar{\beta}$ rapidly decreases with an increasing depth at initial penetrations and then gradually approaches a relatively steady state, and higher values of $\bar{\beta}$ were obtained with tests on denser sand samples. In addition, the speeds of $\bar{\beta}$ approaching to the steady state in tests with the Fraction C sand are quicker than those in the Fraction E sand. Changes of $\bar{\beta}$ with the normalised depth ratio H/D are similar in values and trends to those observed by Klotz and Coop (2001) in centrifuge penetration tests with similar sand relative densities ($D_{pile} = 16mm$, $R_a = 1.1um \sim 1.5um$, maximum penetration depth is about 375mm, g-level: 50g~200g, Leighton Buzzard sand with particle sizes within 0.15-0.212mm). The stress level in these two series of tests are significantly different, but comparable curves were observed. This probably indicates that H/D plays a relatively dominant role in determining the distribution of $\bar{\beta}$ rather than the stress level, at least in relatively shallow depths. However, strong dependences of $\bar{\tau}_{as,t} / \sigma_{v0}^{'}$ on the stress level and the pile diameter were observed by Lehane et al. (2005a) in centrifuge pile tests under tension loading ($\bar{\tau}_{as,t}$ is the average side friction under tension). Therefore, the role of stress level in determining $\bar{\beta}$ needs to be figured out with more direct comparisons in future. Moreover, the observed trend of $\bar{\beta}$ coincides with some given distribution curves of the local β along the pile, for example, the curves changing with sand relative density for pile design by Toolan et al. (1990), and results from centrifuge pile loading tests with different pile surface roughness reported by Fioravante (2002).

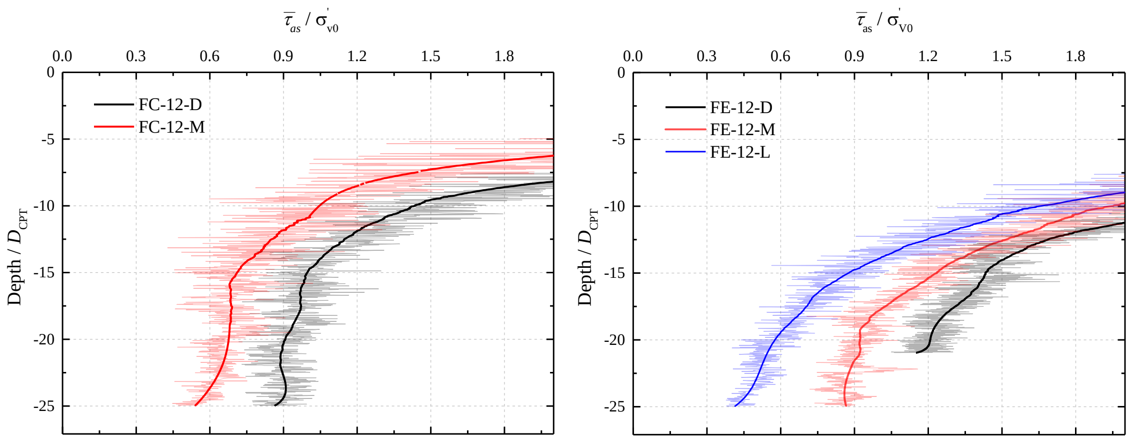

Fig. 4-4 Value of ‘ $\bar{\beta}$ ’ in cone penetration tests with the 12mm penetrometer

It also can be found from Fig. 4-4 that $\bar{\beta}$ obtained with tests in the Fraction E sand are always larger than those measured in the Fraction C sand with a similar relative density, which indicates that larger shaft frictions were experienced by the probe in the Fraction E sand. Based on the Coulomb friction law (Eq.(4.3)), this difference can be attributed to two aspects: Firstly, a higher penetration resistance was experienced by the moving penetrometer in the Fraction E sand under similar conditions. As a consequence, the confining pressure in these cases may be greater due to the induced soil stress level around the beneath of foundations closely relates to the experienced soil resistance (De Beer, 1970; Perkins and Madson, 2000). Secondly, the mobilised interface friction strength between the probe and the Fraction E sand may be higher than that with the Faction C sand since the difference in sand particle size, and this effect will be elucidated later.

4.2.1.2 Scale effect of side friction resistance under tension ($\bar{\tau}_{as,t}$)

Piles, soil nails and anchors are commonly used to resist uplift loads from superstructures, for example, transmission towers, mooring systems for ocean surface or submerged platforms, tall chimneys etc.(Chattopadhyay and Pise, 1986; Jones et al., 2007; Klinkvort et al., 2013). Size-dependent uplift shaft resistance was often observed in 1g model tests (Eid, 1987; Hettler, 1982; Turner and Kulhawy, 1994; Wernick, 1978), centrifuge tests (Balachowski, 2006; Fioravante, 2002; Foray et al., 1998; Garnier and König, 1998; Lehane et al., 2005a) and some full-scale pile tests (Sinnreich, 2011). In general, higher values of $\overline{\tau}_{as,t}$ would be mobilised by smaller piles or in coarser sands for cases with dilative interfaces, and a less pronounced size-strengthening effect or even size-reduction phenomenon would perform in loose sands or piles with smooth shafts (Balachowski, 2006). Similarly, significant size-dependent behaviours may also occur when pulling out plant roots due to their very small sizes (10^{-4}~10^{-1}m) (Mickovski et al., 2010). Hence, the uplift shaft capacity of probes after penetrations was also measured in present tests as illustrated in Section 2.5.

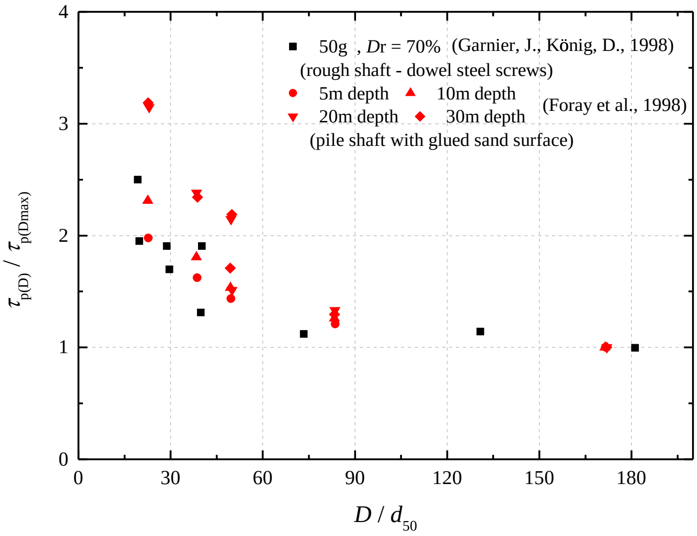

Fig. 4-5 Scale effect of the shaft friction under tension

Size-dependent influences to the shaft friction problems are usually named as the scale effect (Balachowski, 2006; Foray et al., 1998; Garnier and König, 1998; Lehane et al., 2005a), so it is followed in this research. Three typical geometry sizes (median particle diameter d_{50}, pile diameter D and surface roughness R_i) are often employed to evaluate the degree of the scale effect in interface friction problems (Garnier et al., 2007). Specifically, the dependence of the interface friction strength on R_i / d_{50} and the dependence of $\Delta\sigma_{rd}$ on D/d_{50} are usually regarded as the main reasons leading to the size-dependent behaviours, which are predominantly determined by the sand behaviour in the interface shear band and the confining stress level. Therefore, D/d_{50} was often used to indicate the potential influencing range of the scale effect to the shaft resistance, but different minimal values of D/d_{50} to get rid of this scale effect were reported, which may be 30-50 (Fioravante, 2002), 100 (Garnier and König, 1998), or 200 (Balachowski, 2006; Foray et al., 1998) in different conditions.

No base suction would contribute to the uplift capacity in present tests with dry sands, so the averaged maximum shaft friction resistances $\bar{\tau}_{f,t}$ is calculated by dividing the peak pull-out force by the embedded shaft area as plotted in Fig. 4-6. It shows that $\bar{\tau}_{f,t}$ gets larger with a decreasing probe diameter, and higher values of $\bar{\tau}_{f,t}$ were mobilised in tests with the Fraction E sand than those with the Fraction C sand of similar states. Subsequently, by normalising $\bar{\tau}_{f,t}$ with the value obtained with the corresponding largest probe ($\bar{\tau}_{f,t(D_{\max})}$), evident scale effect displays in Fig. 4-7, which shows that the scale effect becomes more significant with a decreasing D or an increasing d_{50}. The measured scale effects in present tests are comparable with those obtained by Lehane et al. (2005a) in tests with buried rough piles on the centrifuge platform but a bit smaller. In fact, unlike buried piles, the equilibrated stress fields ($\sigma_{hc}^{'}$) after penetration of different sized probes are not the same. No systematic change of the scale effect responding to the stress level has been found by Lehane et al. (2005a) in their tests. Therefore, the difference in $\sigma_{hc}^{'}$ arisen during the penetration process is not isolated here, which is approximately assumed to be producing a negligible influence on the normalised result. The shaft roughness in present tests is much smaller than that in tests of Lehane et al. (2005a) with piles of fully rough interfaces. This may explain why the observed scale effects in present tests are relatively smaller than theirs (Garnier and König, 1998). According to these experimental findings, potential reasons causing the size-dependent behaviour in shaft friction resistance are further discussed in detail as below.

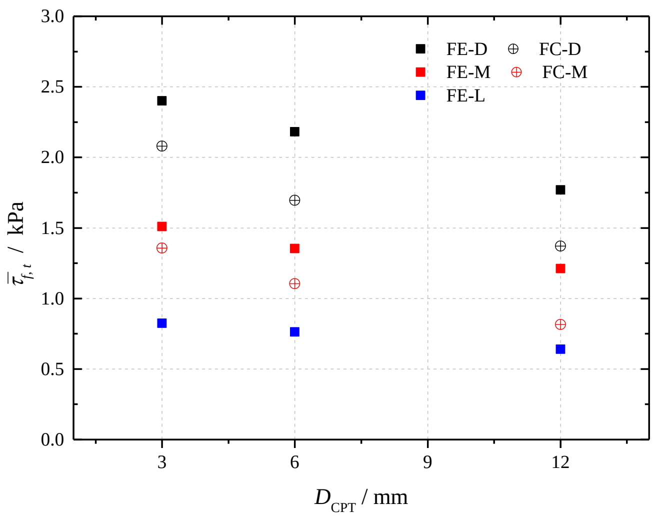

Fig. 4-6 Average tensile shaft friction resistance

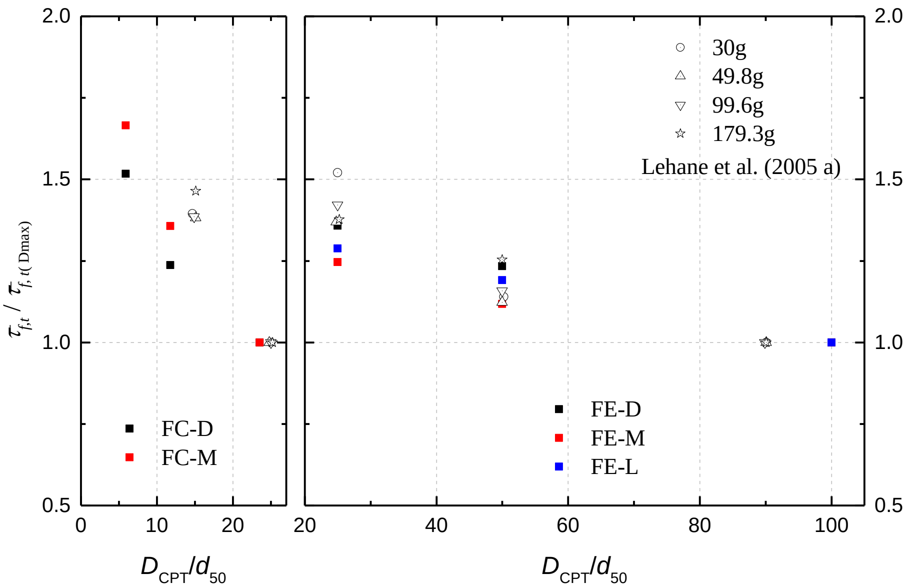

Fig. 4-7 Comparison of scale effect in $\bar{\tau}_{f,t}$

4.2.2 Explanations of scale effects in the shaft capacity

4.2.2.1 Size-dependent interface friction strength

The interface friction strength often plays an important role in determining the bearing capacity and stability of structures placing on or in soils. Therefore, the soil-structure interface friction property has been extensively investigated with several kinds of laboratory shear testing apparatuses (DeJong and Westgate, 2009; Ho et al., 2011; Kishida and Uesugi, 1987; Lings and Dietz, 2004; Paikowsky et al., 1995; Porcino et al., 2003). The interface friction coefficient, which is defined as the shear-to-normal stress ratio, is commonly employed to describe the interface friction strength in practice. In general, it is predominantly determined by the behaviour of materials in the narrow shear band around the interface as detailed below.

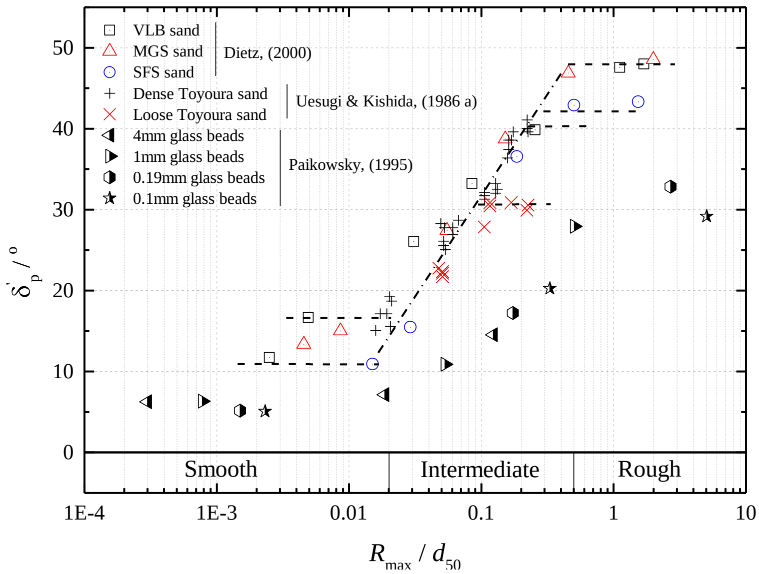

Fig. 4-8 Peak interface friction angle vs. normalised surface roughness

(VLB: Leighton Buzzard sand with d_{50}=0.78mm; MGS: medium golden sand with d_{50}=0.44mm; MGS: silver fine sand with d_{50}=0.13mm)

As found in extensive numbers of interface shear tests (Lings and Dietz, 2005; Paikowsky et al., 1995; Uesugi and Kishida, 1986a), the surface roughness and median particle size have significant influences on the coefficient of interface friction at yield. By expressing the maximum interface friction strength versus R_{max} / d_{50} (R_{max} is the surface roughness in terms of a maximum height within 0.2mm gauge length), three typical influencing stages varying with R_{max} / d_{50} on the soil-structure friction strength are generally defined (Garnier, 2002; Lings and Dietz, 2005; Paikowsky et al., 1995), which were termed as: ‘smooth’, ‘intermediate’ and ‘rough’ as recompiled in Fig. 4-8. Specifically, (1) when the interface is smooth (R_{max} / d_{50} is relatively small), the friction strength is low, and no dilatancy is expected to happen around the interface; (2) when the interface is rough enough (R_{max} / d_{50} is relatively large), the interface friction strength approximately approaches the sand friction strength, which means the overall interface friction strength no longer depends on the surface roughness. It implies the rupture or slippage surface forms inside of the deposit with little influence from the interface; (3) for the interface with a relative roughness falling in the intermediate zone, the mobilised friction strength, in general, proportionally increases with increasing relative roughness in the semilogarithmic scale. Note that two different roughness parameters, R_{max} and R_a, were often used to characterise the surface roughness in the interface friction problem. Although they were found to be equally good at unifying the data (Lings and Dietz, 2005), cautions should be taken while employing these empirical curves with different surface roughness parameters since they usually are in different orders of magnitudes.

The sand relative density influences the peak friction strength of sands, so it will impact the upper bound of the peak friction strength of a rough interface. It applies relatively little influence for interfaces lying in other zones although a decreasing density will push the trend line downwards slightly. Moreover, a different dependency of the interface friction on the confining stress level was reported (Dietz, 2000; Jardine et al., 1993; Uesugi and Kishida, 1986b), which may vary with the surface roughness and sand state (Dietz, 2000). In general, the interface friction angle slowly reduces with an increasing normal stress for a rough surface, and opposite trend may appear in a very smooth surface (Dietz, 2000). In addition, the sand type (compressibility, crushability etc.) also plays an important role in determining the interface strength (Balachowski, 2006; Uesugi and Kishida, 1986a).

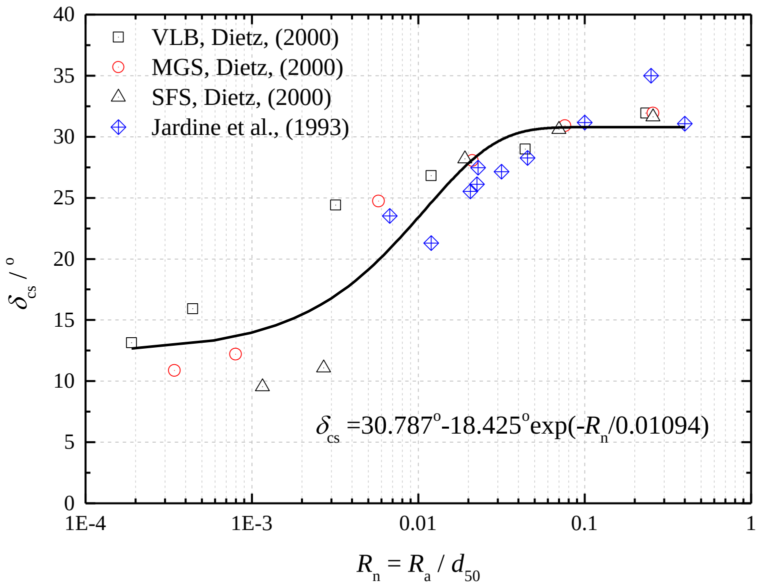

Fig. 4-9 Ultimate interface friction angle vs. normalised surface roughness

In determining the interface friction with large deformations (e.g. pile installation, CPT), the ultimate friction angle (or critical state), δ_{cs}, developed after a post-peak displacement was often recommended (Jardine et al., 1993). With a similar concept of the critical state friction angle in sands, the ultimate failure of the interface under shearing occurs when the interface's constituent sand grains became 'unlocked' from the rough structure surface which allows deformation to proceed without further volume change. Based on series of shearing tests on sands with different particle sizes, Jardine et al. (1993) summarised that δ_{cs} also highly depends on the normalised roughness (R_a / d_{50}), is independent of the initial sand relative density, and may depend on the effective stress level in some cases. Based on the data of shearing tests from Jardine et al. (1993) and Dietz (2000), a complication of δ_{cs} is given in Fig. 4-9. It shows that the trend of δ_{cs} against R_a / d_{50} is very similar to that happens to $\delta_p^{'}$ with varying normalised roughness (e.g. Fig. 4-8), and it also can be roughly divided into three roughness ranges. Specifically, the ultimate interface shearing friction angle is bonded with an upper limit (sand-sand critical state shearing angle φ_{cv}) for relatively rough surfaces, and a minimum value of δ_{cs} may practically exist for the interface with a very low value of R_a / d_{50}. Changes of φ_{cs} with R_a / d_{50} are very slight in these two zones, but a significant variation performs in the intermediate zone. An approximately exponential correlation between δ_{cs} and R_a / d_{50} is fitted. The sand-pile interface friction angle is also recommended with similar trends in some CPT-based pile design methods (e.g. ICP-05 and UWA-05). However, different upper limits were specified since the potential change of the surface roughness caused by abrasion during the large-displacement pile installation (Lehane et al., 2005b). However, a much lower sensitivity of δ_{cs} to the change of d_{50} was observed by Ho et al. (2011) in large-displacement ring shear tests due to the more significant particle breakage around the interface and interface smoothing effect. It was found that the ultimate interface friction angle varies in a very narrow range very close to that suggested value (e.g. 29°) by CUR (2001).

Above results can be employed to partly explain the measured results presented in Fig. 4-4. As defined in Eq.(4.2), $\beta = K_f \tan\delta$. Firstly, in tests with the same sand, the same value of R_a / d_{50} remains with the same penetrometer. Therefore, the difference of the initial sand relative density might not make any contribution to the difference of $\overline{\beta}$ in this case. Instead, it is mainly ascribed to changes of K_f caused by variations in the sand relative density as hypothesised by Kraft (1990). In addition, as measured, $R_a / d_{50} = 5.1 \times 10^{-3}$ between the penetrometer and the Fraction E sand, and

$R_a / d_{50} = 1.2 \times 10^{-3}$ with the Fraction C sand. These two values of the normalised interface roughness lie in the range of intermediate zone, and the estimated critical state friction angle is 19.2^o and 14.3^o for the Fraction E sand and the Fraction C sand respectively based on the fitted curve in Fig. 4-9. A higher interface friction strength may be mobilised in tests with the Fraction E sand than those in the Fraction C sand samples. This partly explains why higher values of $\bar{\beta}$ were obtained in tests on the Fraction E sand with comparisons of results measured within the Fraction C sand under similar relative densities and penetration depths as shown in Fig. 4-4.

4.2.2.2 Scale effect on the mobilised lateral stress

As defined in Eq.(4.3), the radial stress acting on the sand-pile interface at failure consists of the radial effective stress $\sigma_{hc}^{'}$ after equilibrium and the change of radial stress $\Delta\sigma_{rd}$ due to the interface dilation or contraction. $\sigma_{hc}^{'}$ is determined by the combination of the initial stress state of sand and the process of pile installation (or probe penetration). Specifically, it depends on the initial stress level, pile installation methods, sand relative density, and relative distance to the pile tip (h / D) etc. (Lehane et al., 1993; Lehane and White, 2005). For the currently concerned steady penetration problem, it can be roughly expressed as $\sigma_{hc}^{'} = f\left(D_r, \sigma_{v0}^{'}, h / D\right)$. Incorporating with readings of CPTs, these factors can be considered with the form of Eq.(4.4) (Schneider et al., 2007b). $\Delta\sigma_{rd}$ mainly arises from the volume change of the narrow interface along the pile under shearing, and it is often theoretically analysed with some elastic expansion/contraction solutions (Boulon and Foray, 1986; Sinnreich, 2011; Turner and Kulhawy, 1994; Wernick, 1978). Based on the postulation from Boulon and Foray (1986) as given in Eq.(4.7), the direct shear interface tests with constant normal stiffness (CNS) (as illustrated in Fig. 4-10) is increasingly employed to study the shaft interface friction behaviours (Balachowski, 2006; Foray et al., 1998; Lehane and White, 2005; Shahrour, 2013).

$$\Delta\sigma_{rd} = 4G_m \frac{\Delta y}{D_{pile}} = k_s \Delta y \tag{4.7}$$

where k_s is defined as the spring stiffness of surrounding soil, and other terms are the same as defined in Eq.(4.5). G_m is the operational shear modulus, which may depend on the sand packing conditions, confinement conditions (stress or stiffness), and pile installation methods (deformation history) etc. (Mitchell and Soga, 2005). It is often estimated by the small-strain modulus G_0 by multiplying an empirical constant less than unit due to the plastic deformations produced in this process. Consequently, the empirical constant may vary with the produced stress and strain level (Fahey and Carter, 1993; Fioravante, 2002; Lehane et al., 2005a). The incremental radial displacement (Δy) mainly depends on the pile surface roughness, mean particle size, confinement conditions and density of sand in the interface shear band, soil particle mineralogy and angularity, Poisson effect of the pile under loading etc. (DeJong and Westgate, 2009; Fioravante, 2002; Schneider, 2007).

In Eq.(4.7), it theoretically states that $\Delta\sigma_{rd}$ strongly depends on the confining soil stiffness and the volume change of the interface shear band and is inversely proportional to the pile radius. However, the effect of the median particle size (d_{50}) has not been taken into account in this solution, which also plays an important role in affecting the interface friction behaviour. Some improvements are made to address this problem as follows.

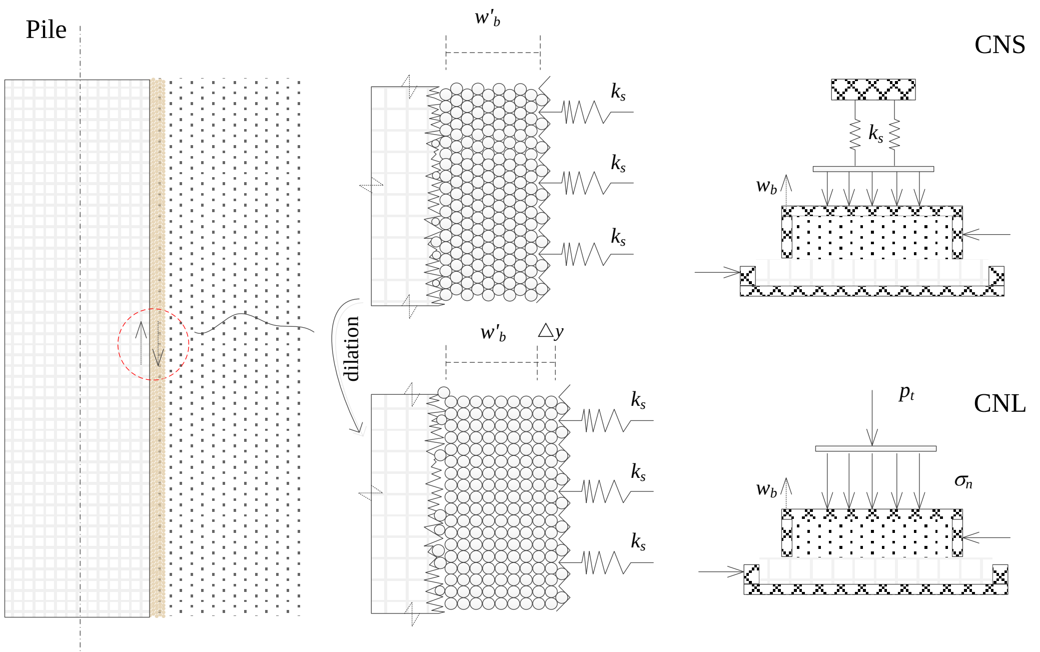

Fig. 4-10 Pile-soil interface model and direct shear interface tests (dilative interface)

In general, experimental observations reveal that the thickness of the mobilised interface shear band (w_b) along the pile surface distributes in a typical range of 2-15 times of d_{50}. It is usually independent of the pile diameter, but varies with the shaft surface roughness, sand relative density in the vicinity of the interface, confining conditions, and the sand crushability etc. (Balachowski, 2006; DeJong and Westgate, 2009; Fioravante, 2002; Ho et al., 2011; Lehane et al., 2005a; Martinez et al., 2015; Tehrani et al., 2016; Yang et al., 2010). In fact, Δy represents the degree of radial expansion or contraction of the narrow interface shear zone, and it may be also independent of the pile diameter (Lehane et al., 2005a). Following with Turner and Kulhawy (1994), the interface shear band is approximately regarded as an elastic, thick-walled cylinder with an inner radius a and an out radius b ($b = a + w_b$). In general, the shear-induced Δy is very small with the same magnitude of the surface roughness, d_{50} or less (Schneider, 2007). It is plausible to believe most parts of the outside soil mass may remain elastic under such amount of deformations. Therefore, the soil mass outside of the inner shear band is regarded as an infinite elastic medium subjecting to an incremental radial uniform pressure along its inner boundary. Under shear loading, uniform pressures on the internal and external boundaries of the inner thick-walled cylinder would be simultaneously mobilised due to dilation or contraction of the sand within the interface shear band. By assuming the pile is rigid, the inner boundary condition of the thick-walled cylinder is obtained, which restricts the radial displacement at the pile surface to be zero ($u_{s,p} = 0$). Then the interface pressure (p_s) along the outer surface of the interface shear band is derived based on the concept from a compound cylinder moulded with prestressing (Ugural and Fenster, 1995), and the radial displacement Δy is estimated by the shrinkage allowance. Specifically, Δy is the sum of the induced radial displacement of the inner cylindrical thick-walled shear zone and the radial displacement of the outer infinite soil mass under a uniform contacting pressure.

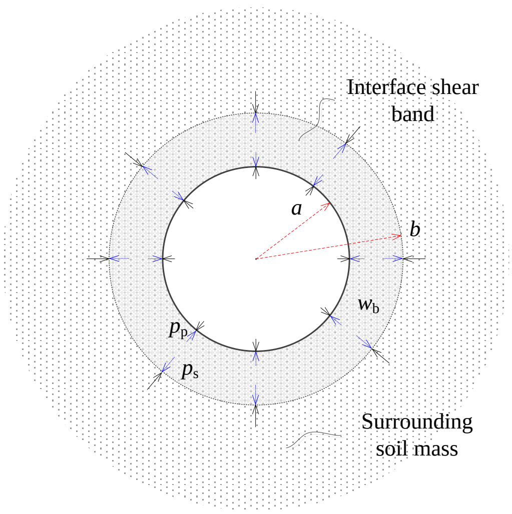

Fig. 4-11 Stress boundaries around the interface shear band

Based on the classical elastic cylindrical cavity solution given in Appendix B for plane strain problem, the incremental radial stress (p_p) acting on the pile surface can be obtained with the boundary condition at the pile surface ($u_{s,p}=0$) as

$$p_p = p_s \frac{2(1-\nu)}{(1-2\nu)(b/a)^2+1} = p_s \varpi \tag{4.8}$$

Radial displacements of the inner thick-walled shear zone ($u_{s,i}$) and the outer infinite soil mass ($u_{s,\mathrm{o}}$) caused by the mobilised contacting pressure p_s respectively are

$$u_{s,i} = \frac{p_s b}{2G_m}[2(1-\nu)(\varpi-1)\frac{a^2}{b^2-a^2}-(1-2\nu)] \tag{4.9}$$

$$u_{s,\mathrm{o}} = \frac{p_s b}{2G_m} \tag{4.10}$$

The induced total radial displacement Δy (positive for outwards displacement) is

$$\Delta y = u_{s,\mathrm{o}} - u_{s,i} = \frac{p_s b}{G_m}[(1-\nu)\frac{1-\varpi(a/b)^2}{1-(a/b)^2}] = \kappa(1-\nu)\frac{p_s b}{G_m} \tag{4.11}$$

Subsequently, the contacting pressing (p_s) is obtained as

$$p_s = \frac{1}{\kappa}\frac{G_m}{(1-\nu)}\frac{\Delta y}{b} \tag{4.12}$$

Then stress changes in the radial and circumferential direction respectively are

$$\Delta\sigma_r = -p_s + \frac{(\varpi-1)p_s}{[(b/a)^2-1]}(1-\frac{b^2}{r^2}) \tag{4.13}$$

$$\Delta\sigma_\theta = -p_s + \frac{(\varpi-1)p_s}{[(b/a)^2-1]}(1+\frac{b^2}{r^2}) \tag{4.14}$$

Distributions of the radial stress for cavities in different sizes are given in Fig. 4-12, the additional radial stress was assumed to be mobilised by the dilative or contractive displacement of the hollow cylindrical interface shear band. Therefore, the compressive radial stress is induced from the outer boundary of the shear band and then monotonically decreases to the pressure on the pile surface. The gap of $\Delta\sigma_r$ between these two positions decreases with increases of the cavity size, but it would disappear in incompressible soils.

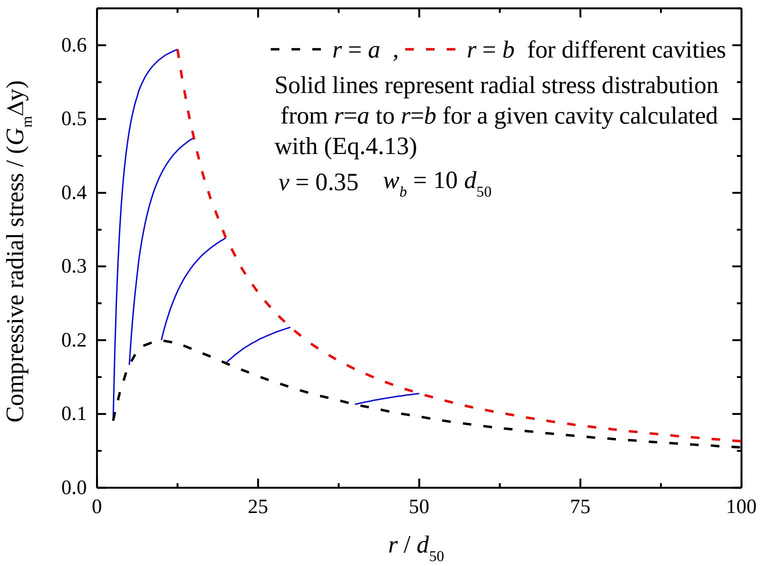

Fig. 4-12 Distribution of normalised radial stresses for cavities with different radii

In fact, the slippage or rupture surface under shearing around the interface would not ideally locate on the inner or outer boundary of the interface shear band in general cases. Therefore, $\Delta\sigma_{rd}$ is neither the induced radial pressure acting on the pile surface nor that on the outer boundary of the shear band. Instead, it may equal to the pressure on one ring within the thick-walled cylinder of the interface, but the exact position of this conceptual ring is not always fixed or clearly known. For simplicity, $\Delta\sigma_{rd}$ is approximated with p_s of the present solution.

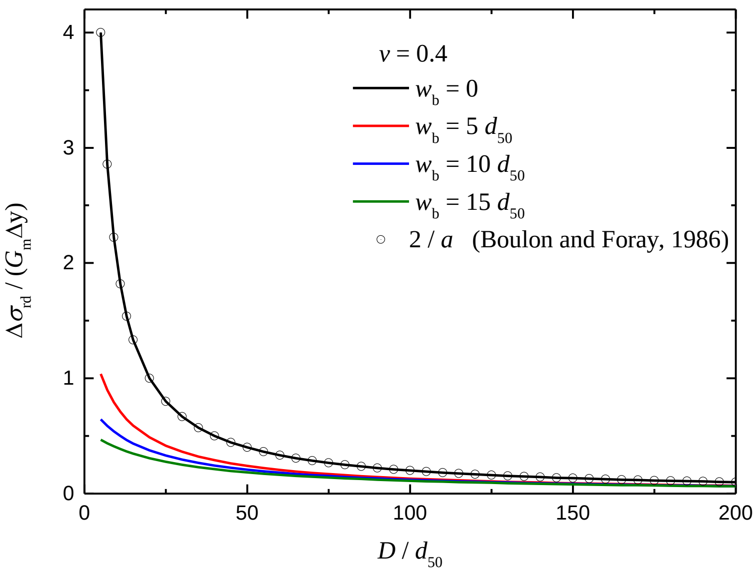

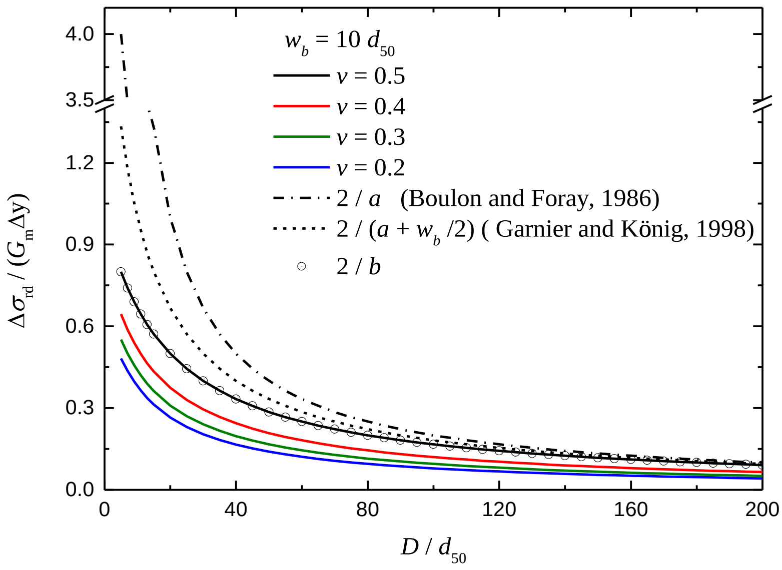

Fig. 4-13 $\Delta\sigma_{rd} / G_m \Delta y$ vs. D / d_{50} (different shear band thickness and Poisson's ratio)

Comparing with Eq.(4.7), two additional parameters, Poisson's ratio of soil and shear band thickness, were incorporated by the present solution (Eq. (4.12)), and G_m and Δy still play similar roles in determining $\Delta\sigma_{rd}$. In brief, G_m strongly depend on the confining stress level and the induced strain level and may reduce with increases of $\Delta y / D$ due to a relatively higher stress level and smaller strain level may be induced by a smaller pile. Δy is mainly caused by the deformation of the interface shear band, which may be independent of the pile size (Lehane et al., 2005a), but increases with the increasing sand particle size and pile surface roughness (Schneider, 2007). To express individual influences of the additional parameters, G_m and Δy remain unchanged in comparisons shown in Fig. 4-13. It shows that $\Delta\sigma_{rd} / G_m \Delta y$ decreases with increases of the shear band thickness (w_b) due to its inverse dependency on the nominal pile radius (b) and decreases of the Poisson's ratio. In addition, the scale effect also reduces with increases of w_b, but it slightly intensifies with decreases of the Poisson's ratio.

In addition, it is easy to find that the new expression of $\Delta\sigma_{rd}$ can exactly reduce to the solution given in Eq.(4.7) ($\Delta\sigma_{rd-1} = 2G_m \Delta y / a$) while omitting the thickness of the interface shear band for incompressible soil ($\nu = 0.5$). When w_b is taken into account, it will reduce to $\Delta\sigma_{rd-2} = 2G_m \Delta y / b$ for incompressible soils. Physically, these two special cases can be equivalently regarded as solutions derived with assumptions that $\Delta\sigma_{rd}$ is the mobilised radial stress acting on the pile surface and on the position with a nominal radius of $b = a + w_b$ respectively. Moreover, Garnier and König (1998) assumed that the shear rupture surface passes through the middle of the interface shear band, which gave a nominal pile radius of $(a + 0.5w_b)$. Accordingly, a new solution can be obtained as $\Delta\sigma_{rd-\mathrm{m}} = 2G_m \Delta y / (a + 0.5w_b)$. Performances of above assumptions are also compared in Fig. 4-13. It indicates that the inverse dependency of $\Delta\sigma_{rd}$ on the pile radius can be qualitatively captured by all these solutions, but different levels of the scale effect are predicted with them. For incompressible material, the gap between these methods gets smaller with increases of D / d_{50}, so no difference would be produced by them in practical pile designs (relatively large sizes). In addition, the scale effect attenuates with increases of D / d_{50} and almost vanishes when D / d_{50} gets close to 200 which coincides with some experimental findings (Balachowski, 2006; Foray et al., 1998). In addition, performances of these theoretical solutions are further evaluated with the results obtained by Lehane et al. (2005a) in tension tests with embedded rough piles in dense sand. In Fig. 4-14, it shows that the experimentally observed scale effect was better quantified by the present solution with a typical value of the interface shear band thickness while significant over-predictions were made by Eq.(4.7). More precise predictions can be made by taking into account the strain-level dependency of G_m. Based on these analyses, it is believed that Eq. (4.12) provides a more reliable solution to quantify the potential scale effect in the changes of the radial stress than the solution given in Eq.(4.7) without any loss of simplicity.

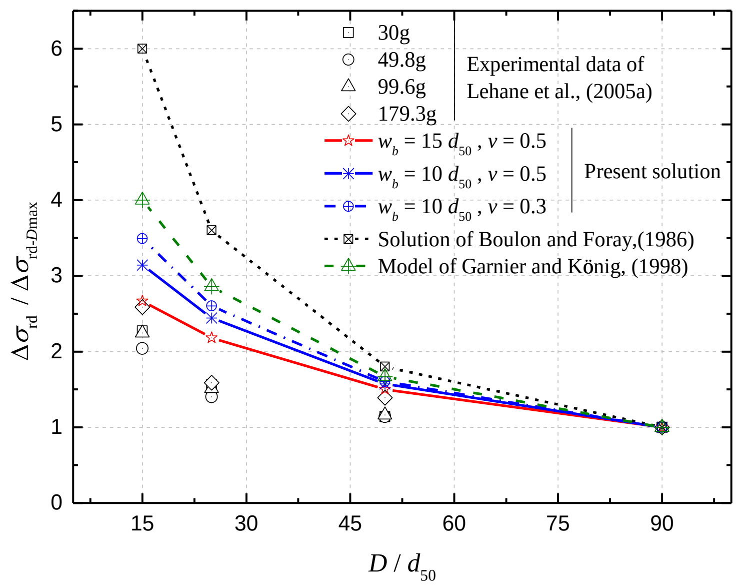

Fig. 4-14 Scale effect of $\Delta\sigma_{rd}$ with comparison to experimental results

To further examine the accuracy of Eq. (4.12), the measured and calculated shaft capacity of tests in tension and compression are compared in Fig. 4-15 and Fig. 4-16 respectively. The original ICP-05 method was given in Eq.(4.3)-Eq.(4.6), and the modified method is achieved only by replacing the expression of $\Delta\sigma_{rd}$ in Eq.(4.5) with Eq.(4.12). The experimental data was given in Tab. 2-7. All calculations are made with previously given parameters (R_a =0.607um, δ_{cs} =19.2° with FE sand and δ_{cs} =14.3° with FE sand). The interface shear band thickness is set in a typical range of 2-8 times of the mean particle size, which approximately varies with the sand relative density and confining stress levels (relatively higher in compression than those in tension). Additionally, considering the dependency of Δy on the particle size (Schneider, 2007), Δy=2R_a is set in predictions of shaft capacities in the Fraction C sand, and Δy=R_a for tests in the Fraction E sand. By comparing with the measured shaft capacities in present shallow penetration tests with miniature smooth-surfaced penetrometers, the modified method gives closer predictions than the original formulas which mainly serve for practical designs of large sized piles. In addition, by relating Δy with d_{50}, the difference between these two methods gets smaller with the increase of D/d_{50}. For example, the gap of predicted values with these two methods is obviously smaller in applications to tests with the Fraction E sand (d_{50} =0.12mm) than those with the Fraction C sand (d_{50} =0.51mm). Based on above analyses, the modified method may provide more reliable predictions of the experienced shaft resistance for applications to small sized model piles.

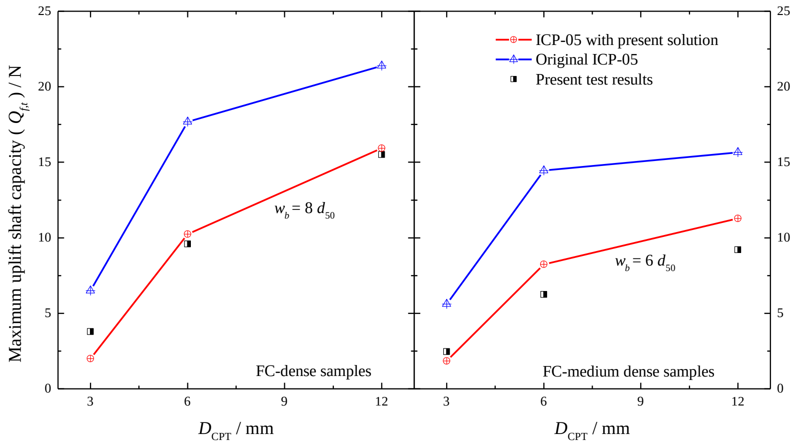

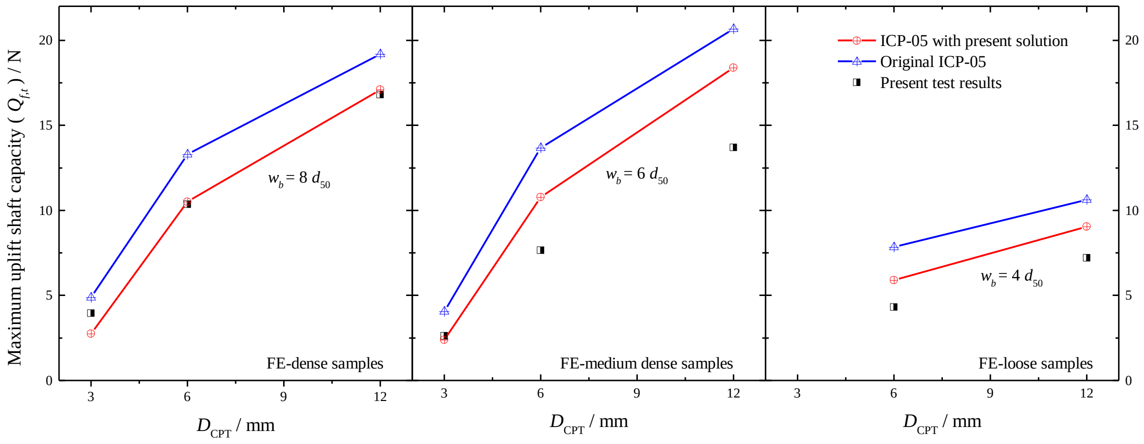

Fig. 4-15 Comparison of uplift shaft capacity

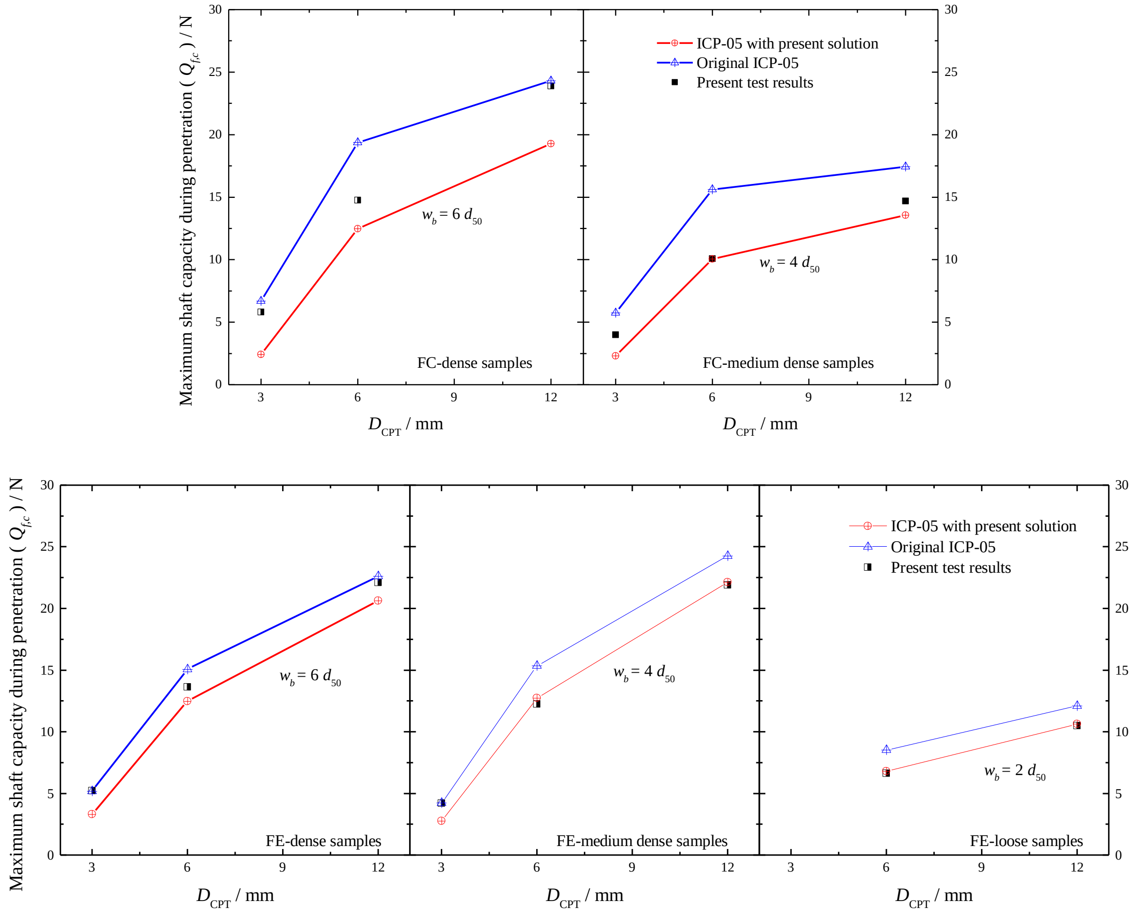

Fig. 4-16 Comparison of maximum shaft capacity during penetrations

In addition, as reported by Balachowski (2006), an opposite scale effect (size-softening phenomenon) was found in contractive interfaces (e.g. interface between loose sand and smooth plate), and the skin resistance reduces with decreasing D/d_{50}. In these cases, unloading may occur due to contraction of sand in the vicinity around the pile surface under shearing. The mobilised radial displacement Δy turns negative, and, consequently,

$\Delta\sigma_{rd}$ becomes negative (stress release). Therefore, the overall radial stress would reduce, and the reduction may increase with decreases of D/d_{50}. Similarly, the opposite scale effect observed in a contractive interface probably can be explained with the present solution with a negative interface displacement (Δy).

In the light of above discussions, it is concluded that the interface friction resistance may be greatly influenced by the aforementioned two scales, R_i/d_{50} and D/d_{50}, within certain ranges. Specifically, the interface friction strength significantly varies in proportion to changes of R_i/d_{50} for interfaces lying in the intermediate zone. Size-dependent responses will be performing in $\Delta\sigma_{rd}$ while D/d_{50} gets less than a limit value which may vary in the approximate range of 30 to 200 (Fioravante, 2002; Foray et al., 1998; Garnier and König, 1998). To avoid influences from these scale effects, ratios of R_i/d_{50} and D/d_{50} should be carefully designed in scaled model tests to simulate the field condition as realistic as possible. In addition, apart from these two main aspects, other factors may also contribute to the size-dependent performances of the shaft friction in some degrees. Among them, the potential stress level effect and H/D effect are emphasised here. Firstly, the Mohr-Coulomb strength envelope is usually approximated by a straight best-fitting line in a limited stress range. However, it is known that the friction angle of granular material more or less reduces with an increasing normal stress (Baligh, 1976; De Beer, 1963). So while the stress level induced by installations of different sized piles are significantly different, this effect also needs to be taken into account. Additionally, to maintain a same initial stress level, the same embedment depth may be required in 1g tests. Then different values of H/D will be produced with different sized piles. These two factors also deserve to be kept in mind to reduce their potential additional influences while evaluating the concerned scale effect in shaft friction.

4.3 Size-dependent cone tip resistance and analysis

As reviewed in Section 2.2, size-dependent behaviours of the end resistance have been extensively reported both in shallow and deep penetration tests. Penetration mechanisms of the shallow penetration and the deep penetration are significantly different (Durgunoglu and Mitchell, 1973; Meyerhof, 1951), so dominating size factors may vary with the penetration depth (Balachowski, 2007; De Beer, 1963). As previously concluded that the shallow penetration is highly influenced by the relative penetration depth, and the deep penetration mechanism is greatly determined by the local deformation characteristics. A critical penetration depth ratio ($(H/D)_{cr}$) was often defined in theoretical and empirical approaches interpreting the tip resistance of a static penetrometer (Durgunoglu and Mitchell, 1975; Kim et al., 2015; Meyerhof, 1983). In general, the normalised cone factor ($N_{q_c} = q_c / \sigma_{v0}$) increases with H/D almost linearly (Durgunoglu and Mitchell, 1975) in relatively shallow depths. While the critical relative depth is reached, q_c will be proportional to the increase in depth (Durgunoglu and Mitchell, 1973). The critical penetration depth varies with soil properties and penetrometer types, but Durgunoglu and Mitchell (1975) concluded that it should be on the order of 5-10 for loose sands and 20-25 for dense sands for normal cone penetrometers.

4.3.1 Size effect of the cone tip resistance in present tests

The tip resistances encountered by different sized probes are compared by conserving the initial vertical stress (σ_{v0}) level which has a significant influence on q_c . For the uniformly deposited sand samples, the initial vertical stress is assumed to linearly increase with the depth, so σ_{v0} can be directly represented by the penetration depth here. All results of the tip resistance and the cone factor ($N_{qc} = q_c / \sigma_{v0}$) in present tests are plotted in Fig. 4-17 and Fig. 4-18.

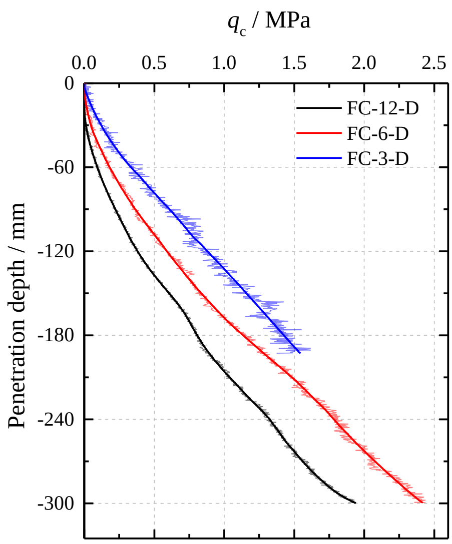

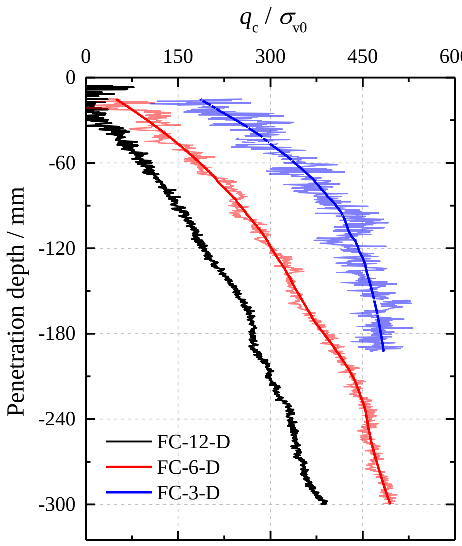

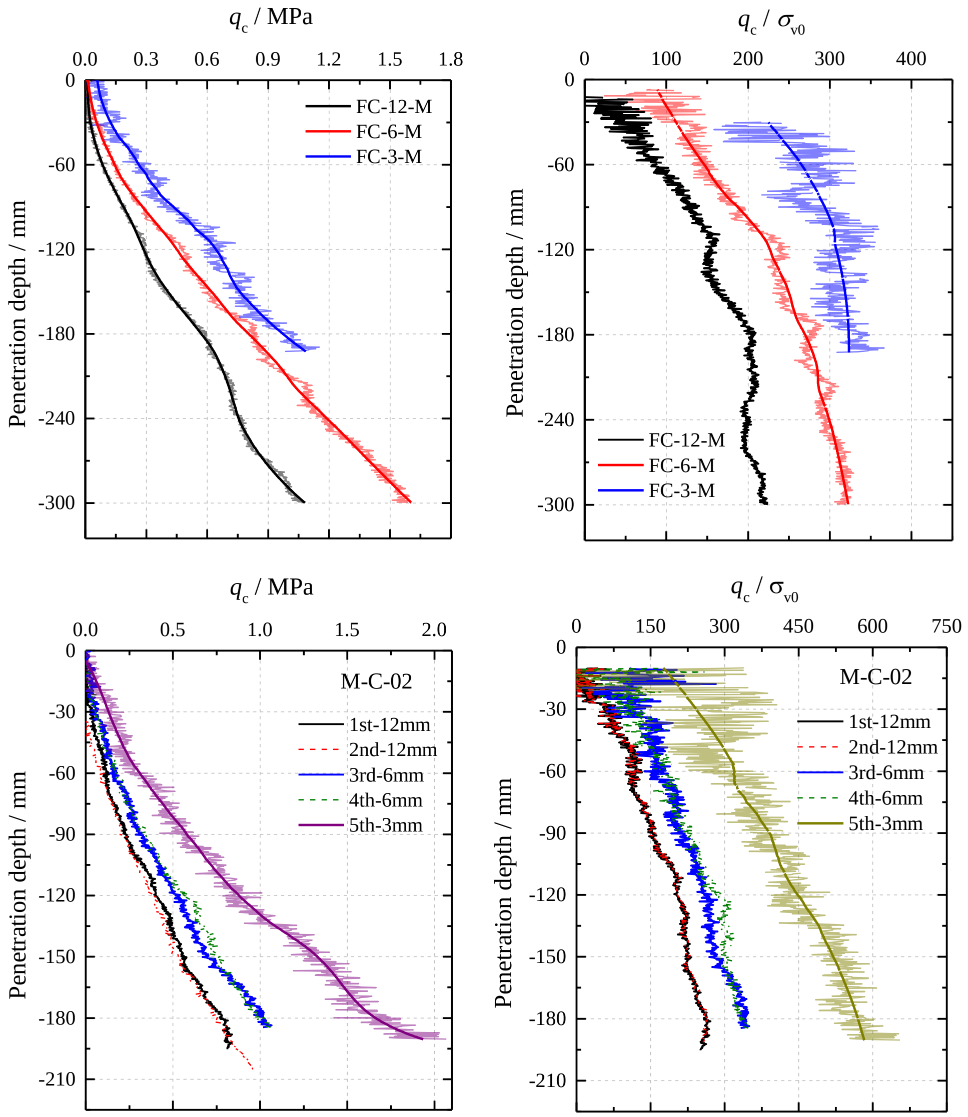

Fig. 4-17 q_c and q_c / σ_{v0} vs. penetration depth (FC sand samples)

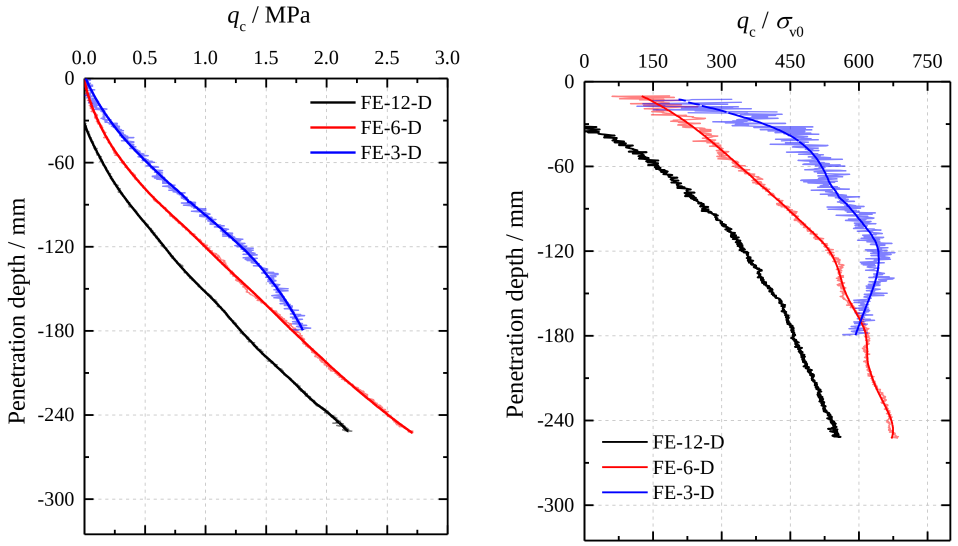

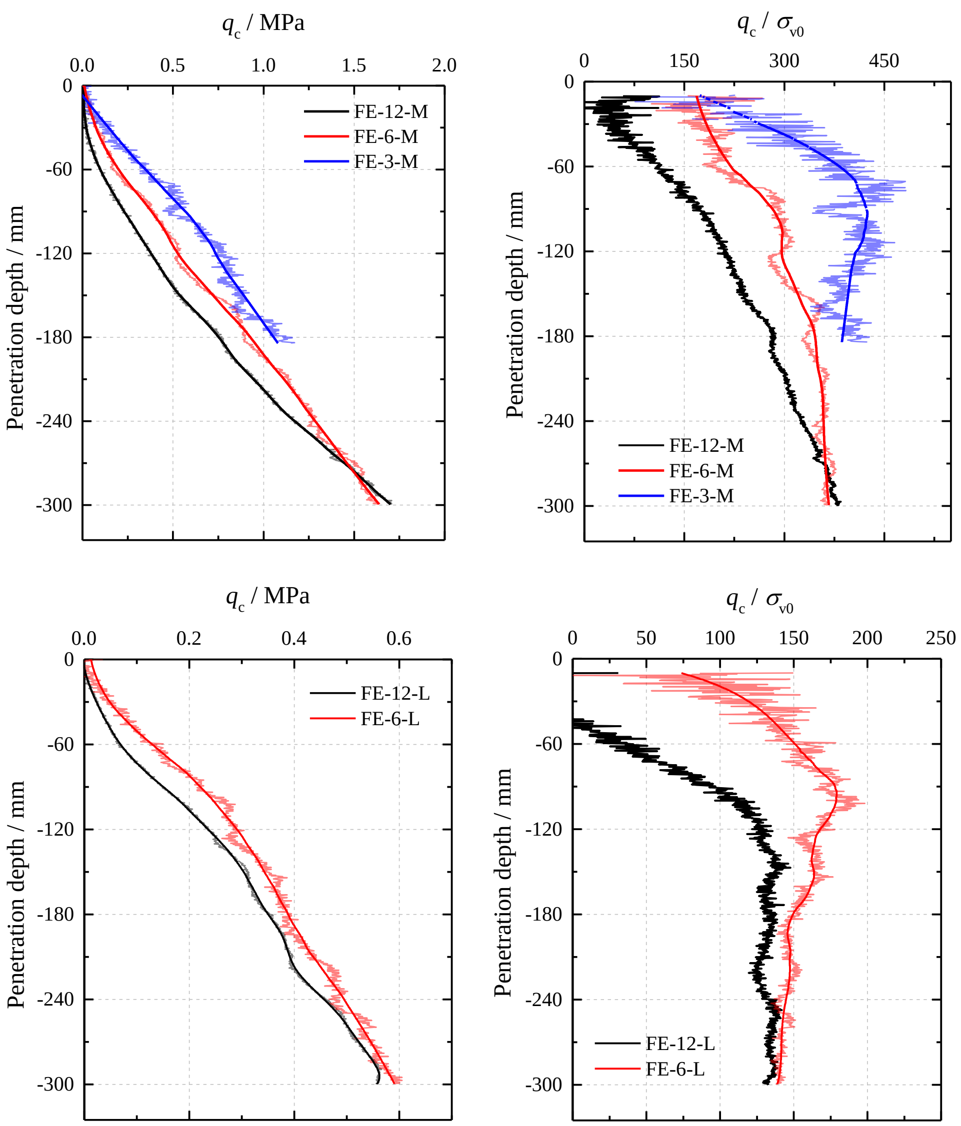

Fig. 4-18 q_c and q_c / σ_{v0} vs. penetration depth (FE sand samples)

Evident size differences of the measured tip resistance (and N_{qc}) were observed in results of the present 1g shallow penetration tests. At the same penetration depth (the same initial stress level), higher sand resistances were generally encountered by a smaller sized probe. The size effect seems less noticeable in loose sands as also observed by Balachowski (2007), but no obvious attenuation was found in present tests between the data obtained with dense samples and with medium dense samples.

As discussed in Chapter 2, present tests should immune from the side boundary effect. Even if the side boundary effect applied, above size-dependent behaviours of the tip resistance might not have been amplified. It is because more enhancements may be experienced by larger sized probes in that case because q_c would get higher while a greater side boundary effect is applying from a perfectly rigid lateral (Salgado et al., 1998). Therefore it is believed that the difference in ratios of the chamber size to the cone diameter ($R_d = B / D_{\mathrm{CPT}}$) is not the reason leading to the size-dependent differences of the tip resistances, and it may apply no additional effect on results of present tests. In addition, the rigid base boundary may exert influences in the process of sample preparation and test implementation. Similarly, the rigid base may also enhance the soil resistance more or less when this boundary effect works. Additional confining effects from the rigid base during penetrations may be eliminated by satisfying the requirements specified by Lee (1990) and Bolton and Gui (1993) as given in Fig. 2.15, but potential influences caused by the rigid base during sample preparations are not easy to be evaluated. Note that penetrations deeper than 250mm with the 12mm sized penetrometer in tests with dense samples of the Fraction C sand violated the minimum distance requirement from the bottom base, so data within this range will not be used in following comparisons.

4.3.2 Theoretical prediction of the size effect in cone tip resistances

In order to theoretically account for the observed size effect in the cone tip resistance, the classical bearing capacity theory based method from Durgunoglu and Mitchell (1975) and the size-dependent cavity expansion solution developed in Chapter 3 will be used to predict the tip resistance in present tests. In addition, performances of the later method in describing the concerned size effect in cone tip resistances will be further evaluated with some other available experimental CPT data. At first, the required strength and stiffness properties of sands used in present tests are estimated as follows.

(1) Sand friction and dilation angles

Basic sand parameters have been given in Tab. 2-3. The peak friction angle (φ_p) and dilation angle (ψ_p) of sands at different states are estimated based on the empirical formula proposed by Bolton (1986).

$$\varphi_p - \varphi_{cs} = B_\psi \psi_p = A_\psi I_R{}^o \tag{4.15}$$

where $B_\psi = 0.5$, $A_\psi = 3$ for triaxial conditions, and $B_\psi = 0.8$, $A_\psi = 5$ for plane strain conditions.

$$I_R = D_R(10 - \ln \frac{100 p_m'}{\sigma_{atm}}) - 1 \quad , \text{ for } p_m' \le 150\text{kPa} \tag{4.16}$$

$$I_R = 5D_R - 1 \quad , \text{ for } p_m' > 150\text{kPa} \text{ (Bolton, 1987)} \tag{4.17}$$

where $\sigma_{atm} = 100$ kPa. D_r is the relative density value, in % and p_m' is the mean effective confining stress at failure, in kPa. In shallow foundations, p_m' was often estimated by $p_m' = \frac{(q_c + 3\sigma'_{v0})}{4}(1 - \sin\varphi)$ suggested by De Beer (1970), or by $p_m' = q_c / 10$ suggested by Meyerhof in his doctor's thesis (De Beer, 1963). In deep penetrations, $p_m' = \sqrt{q_c \sigma'_{v0}}$ was often used (Bolton et al., 1993; Yu and Houlsby, 1991). According to these estimations, it is found that p_m' remains less than 150kPa in most cases of present tests. Therefore, Eq. (4.17) is used to predict the peak friction angle and dilation angle of sands in following calculations, and p_m' is estimated with $q_c / 10$.

Tab. 4-1 Estimated sand shear strength properties

Sand type	Sand state	φ_{cs} / °	Friction angle: Plane strain φ_{pp} / °	Friction angle: Triaxial φ_{pt} / °	Dilation angle (triaxial) ψ_p / °	Interface friction δ_{cs} / °
Fraction C	Dense	32	49.5	42.5	21.0	14.3*
	Medium dense		43.3	38.8	13.5	
Fraction E	Dense	32	49.5	42.5	21.0	19.2*
	Medium dense		43.3	38.8	13.5	
	Loose		37.0	35.0	6.0	

* Interface friction angle at the critical state, estimated from Fig. 4-9 as aforementioned.

Correlations for estimating parameters in Eq.(4.16) at low confining stresses were also suggested by Chakraborty and Salgado (2010) based on triaxial compression and plane-strain compression test data of Toyoura sand, which gives similar results for present tests.

It needs to point out that the same shear strength is approximately estimated for the Leighton Buzzard sands with different particle fractions in Tab. 2-3, and, as a consequence, the same plastic yield strength would be applied to them with the classical Coulomb yield criterion. However, the yield stress of the Leighton Buzzard sand may vary with the particle size distribution (increase with a decreasing particle size) as found by McDowell (2002). Similar grain size-dependent yield behaviours were also observed in other silica sands (Nakata et al., 2001; Zhang et al., 2016). Therefore, the yield stress of the Fraction E sand may be a bit higher than that of the Fraction C sand in nature, but this potential difference has not been taken into account in present calculations.

(2) Small strain shear modulus

The elastic soil stiffness (G_0) is generally evaluated from measurements of elastic wave velocities or use of local displacement transducers (Mitchell and Soga, 2005). It has been long recognised that the void ratio and confining stress level predominantly determine the stiffness of sands, and a number of empirical equations has been proposed with the form of Eq.(4.18) (Bui, 2009; Hardin and Black, 1966; Mitchell and Soga, 2005).

$$\frac{G_0}{\sigma_{atm}} = AF(e)(\frac{p_m}{\sigma_{atm}})^n \tag{4.18}$$

where $F(e)$ is a void ratio function, A and n are material constants. p_m is mean effective confining stress.

In specific, G_0 is often measured with resonant column or bender element tests in the laboratory (Bui, 2009; Lo Presti, 1987) and various in-situ devices in the field (Fahey et al., 2003; Schnaid et al., 2004; Schnaid and Yu, 2007). Among them, many empirical equations relating G_0 with the cone tip resistance (q_c) have been developed (Baldi et al., 1991; Lunne et al., 1997; Rix and Mayne, 1993; Rix and Stokoe, 1991; Schnaid et al., 2004). The empirical relationship suggested by Rix and Stokoe (1991) (given in Eq.(4.19)) based on several series of field and laboratory test data will be employed to estimate the small strain sand stiffness in following calculations.

$$(\frac{G_0}{q_c})_{ave} = 1634(\frac{q_c}{\sqrt{\sigma'_{v0}}})^{-0.75} \quad \text{(Uncemented quartz sands)} \tag{4.19}$$

Within this empirical equation, G_0 is determined by the cone tip resistance and initial soil stress level. Due to the size differences in the mobilised soil resistance (proportional to the confining pressure), the predicted values of G_0 also vary with the penetrometer size and sand types even at the same level of σ'_{v0}.

Note that the concerned particle size effect may also influence the small strain stiffness (G_0). For example, Bui (2009) found that G_0 significantly increase with increases of the particle size at the same confining pressure level based on a series resonant column tests with Leighton Buzzard sands. Slight increases of G_0 with increasing particle size were also reported by Menq et al. (2003). In contrast, it was observed that G_0 does not depend on d_{50} in the range of 0.1mm to 6mm in resonant column tests with a natural quartz sand but significantly decreases with an increasing coefficient of sand uniformity (Wichtmann and Triantafyllidis, 2009). Contradictory findings of the dependency of G_0 on the particle size were reported, therefore more effort is suggested to shed light on this phenomenon, and a better understanding of the particle size effect in cone penetration tests may be acquired then.

4.3.2.1 Estimation with method of Durgunoglu and Mitchell (1975)

The well-known bearing capacity theory-based method developed by Durgunoglu and Mitchell (1975) is briefly introduced before applications to interpret our test results. Durgunoglu and Mitchell (1975) studied the wedge penetration problem first to give a plane strain solution, and then the axisymmetric geometry of cone penetration was taken into account with an empirical shape factor. The cone tip resistance in sands was expressed as

$$q_c = \rho_s g D N_{\gamma q} \xi_{\gamma q} \tag{4.20}$$

where ρ_s is sand density. g is the gravity of earth. D is the diameter of the penetrometer. $N_{\gamma q}$ is the bearing capacity factor. $\xi_{\gamma q}$ is the shape factor.

In this method, the continuous penetration was separately analysed as a series of static equilibrium problems at different instants. Each failure surface corresponds to a certain penetration depth. At initial stages, the failure surface (represented by a logarithmic spiral) spreads out and intersects the ground surface before reaching vertical tangency. The critical relative depth was determined at the moment when the vertical tangential point just matches the ground level as given in Eq.(4.13). So $\beta_b \le \varphi$, $\theta_0 \le \theta_1$, in which equalities are taken when relative depths are equal or greater than the critical relative depth as depicted in Fig. 4-19.

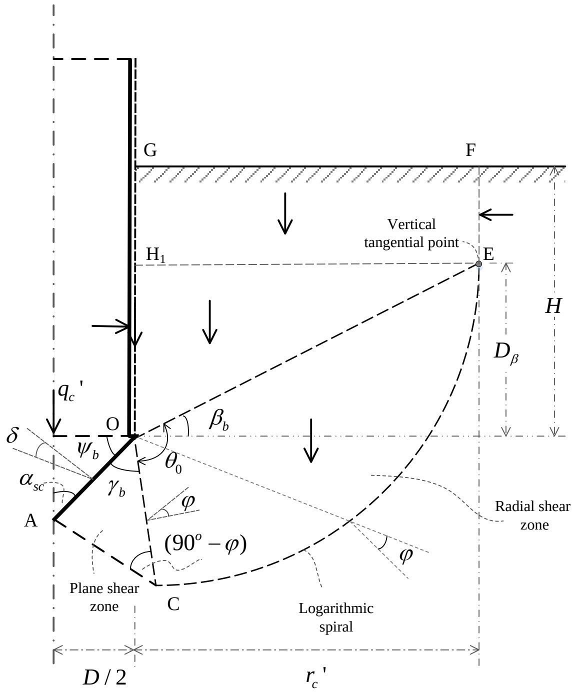

Fig. 4-19 Failure mechanism for wedge penetration at large relative depths (proposed by Durgunoglu and Mitchell (1975))

$$(H/D)_{cr} = \frac{\sin\varphi\cos(\gamma_b - \varphi)}{2\cos\varphi\cos\psi_b} e^{\theta_1 \tan\varphi} \tag{4.21}$$

and γ_b can be determined with Eq.(4.22).

$$\tan\delta[1 + \sin\varphi\sin(2\gamma_b - \varphi)] - \sin\varphi\cos(2\gamma_b - \varphi) = 0 \tag{4.22}$$

where $\theta_1 = 180^o - (\psi_b + \gamma_b) + \varphi$, $\psi_b = 90^o - \alpha_{\mathrm{sc}}$. For penetrometers with a rough surface, a rigid wedge (or cone) will be developed in front of the tip with a base angle of $45^{\mathrm{o}} + \varphi/2$.

The bearing capacity factor is

$$\begin{aligned} N_{\gamma q} = {} & \frac{\cos(\psi_b - \delta)}{\cos\delta} \frac{[1 + \sin\varphi\sin(2\gamma_b - \varphi)]}{\cos\varphi\cos(\gamma_b - \varphi)} \left\{ \frac{\cos^2(\gamma_b - \varphi)}{4\cos^2\psi_b\cos^2\varphi} I_\theta \right. \\ & + \frac{3\cos(\gamma_b - \varphi)\cos^2\beta_b}{4\cos\psi_b\cos\varphi} e^{2\theta_0\tan\varphi} (m_1 - \frac{2}{3}m') - K_D \frac{\cos\psi_b\cos\varphi}{\cos(\gamma_b - \varphi)} \cdot \\ & \left. (m_1 + 2m')(m_1 - m')^2 + K_D \frac{\cos\psi_b\cos\varphi}{\cos(\gamma_b - \varphi)} m_1^3 \right\} - \frac{\tan\psi_b}{4} \end{aligned} \tag{4.23}$$

where $m_1 = H/D$, $\theta_0 = 180^o - (\psi_b + \gamma_b) + \beta_b$,

$$m' = \frac{D_\beta}{D} = \frac{\sin\beta_b \cos(\gamma_b - \varphi)}{2\cos\psi_b \cos\varphi} e^{\theta_0 \tan\varphi} \quad , \quad \beta_b = \sin^{-1}\left\{ \frac{2m_1 \cos\varphi \cos\psi_b}{\cos(\gamma_b - \varphi) e^{\theta_0 \tan\varphi}} \right\} ,$$

$$I_\theta = \frac{1}{1+9\tan^2\varphi}\left\{3\tan\varphi\left[e^{3\theta_0\tan\varphi}\cos\beta_b - \cos(\theta_0 - \beta_b)\right] + \left[e^{3\theta_0\tan\varphi}\sin\beta_b + \sin(\theta_0 - \beta_b)\right]\right\} ,$$

K_D is the lateral earth pressure coefficient, and it is estimated with $(1-\sin\varphi)$ here.

Iterations are required to determine β_b in relative depths less than $(H/D)_{cr}$. The shape factor in Eq.(4.24) was adopted for penetrations of circular cone penetrometers.

$$\xi_{\gamma q} = 0.6 + \frac{1.5}{D/H + 1.5/(0.6+\tan^6\varphi)} \tag{4.24}$$

The sand resistance is entirely characterised by the sand shear strength and interface friction angle in this method, so the calculated cone tip resistance is very sensitive to these two parameters. The interface friction angle is taken as estimated in Tab. 2-3. The peak friction angle was adopted by Durgunoglu and Mitchell (1973) in their predictions with this method, so peak values of the friction angle were also first attempted in following calculations. Relatively satisfactory predictions were obtained with $(\varphi_{pp} + \varphi_{pt})/2$ to tests with dense sand samples, and with φ_{pp} for medium dense sand samples as shown in Fig. 4-20. It is shown that results predicted by this method compare well with data obtained by the 12mm sized penetrometer in relatively shallow depths, and relatively better performances it has in applications to tests on the dense sand samples. Evident underestimations were made in relatively deep depths, which is more serious in predictions to tests with the medium dense sand samples even the plane strain peak friction angle was employed.

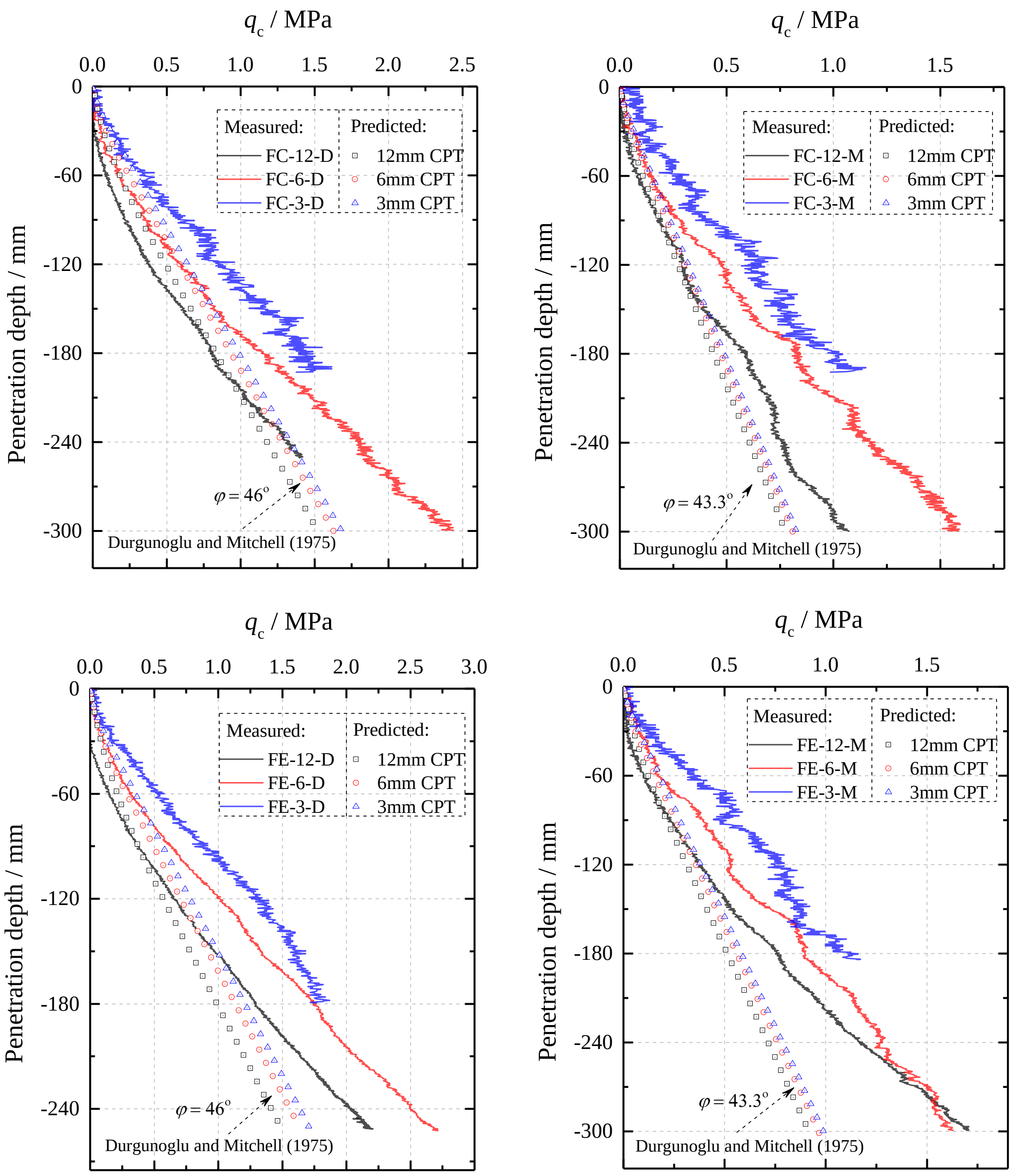

Fig. 4-20 Comparison of q_c with present tests(experimental data vs. D-M solution)

In this solution, the normalised cone tip resistance (cone factor q_c / σ_{v0}) strongly depends on the value of H / D regardless of the real cone size as demonstrated in Fig. 4-21. Therefore, higher resistances are predicted for tests with smaller sized penetrometers at the same penetration depth due to greater values of H / D. However, the observed size effect in the cone tip resistance cannot be sufficiently accounted for just with consideration of the H / D effect, in which it was obviously underestimated as shown in Fig. 4-20. By considering the stress dependency of the sand friction angle, the size effect in shallow penetrations was studied by De Beer (1963) on the basis of another classical bearing capacity theory based method from Meyerhof (1951). To put it simply, the same value of H / D would be reached by smaller sized penetrometers in relatively shallower depths where lower initial soil stresses exist. The sand friction angle increases with decreases of the confining stress, in particular at low-stress levels. Therefore, a higher soil resistance may be experienced by a small penetrometer with the same value of H / D as assumed in De Beer's solution. More pronounced size effect in shallow penetrations can be predicted with this method, but a calculation of trial and error must be performed since the mutual dependency of the sand friction angle and the penetration resistance. The bearing capacity based method is very sensitive to the variation of sand friction angle, so this method is not attempted in this research due to lack of precise measurement of the sand friction angle under varying confining pressures. In addition, the progressive failure mechanism (strain level dependent strength) discussed in the previous section of 2.2.1 may also play roles in determining this size effect at shallow depths.

Above discussion reveals that the size difference of cone tip resistances within shallow penetrations may be explained by the H / D effect and the associated stress-dependent or strain-dependent internal friction strength of sands. The H / D effect may dominate the change of q_c / σ_{v0} in relatively shallow penetrations (e.g. as indicated in Fig. 4-22), but better predictions of the size dependency of cone tip resistances in shallow penetrations may be achieved with simultaneous considerations of the other two factors in bearing capacity theory-based approaches.

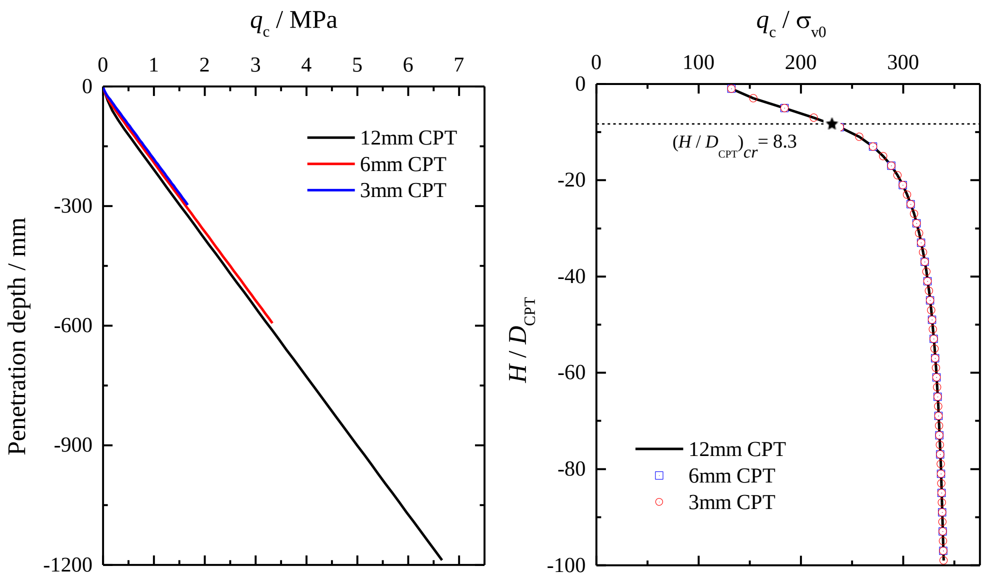

Fig. 4-21 q_c and q_c / σ_{v0} with parameters used in predictions of dense sand samples

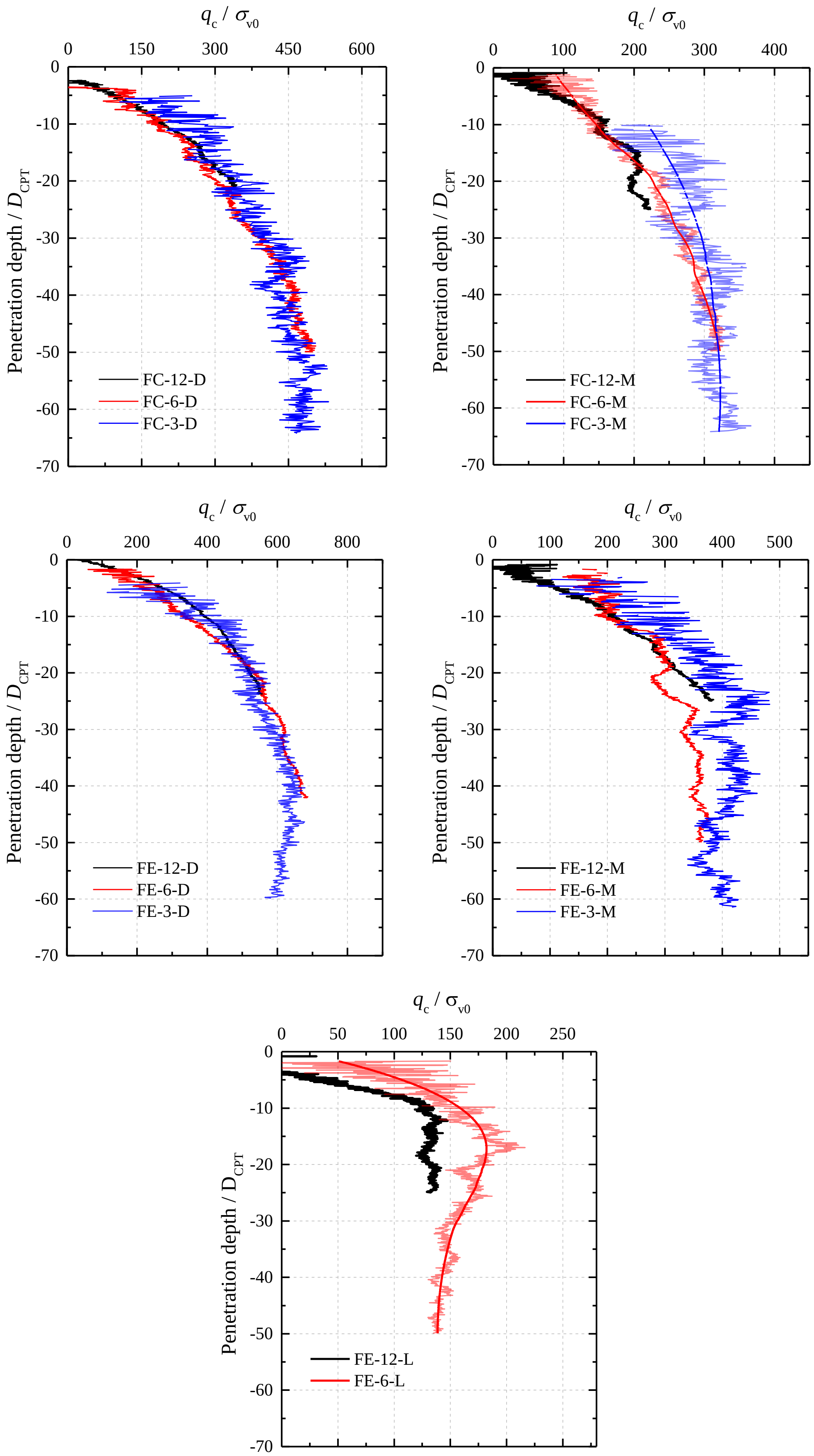

Fig. 4-22 q_c / σ_{v0} vs. normalised penetration depth

4.3.2.2 Applications of the size-dependent cavity expansion solution

As reviewed in Section 4.1.2, due to the analogy between cavity expansion and cone penetration, cavity expansion theory has been widely adopted to interpret the cone penetration test as a simple theoretical tool in addition to the above bearing capacity theory. To account for the observed size effect in cone tip resistances, a size-dependent cavity expansion solution for sands was developed in the previous chapter. To relate the cavity expansion pressure with the cone tip resistance, the simple relationship given in Eq.(4.25) will be employed in following interpretations.

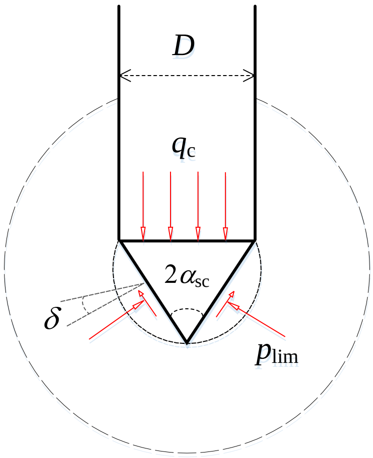

Fig. 4-23 Schema for transformation of a cavity expansion to a deep cone penetration

$$q_c = [1 + \tan\delta_{cv} \cot\alpha_{sc}]p_{\lim} \tag{4.25}$$

where $p_{\lim}$ is the required quasi-static expansion pressure of a spherical cavity (Ladanyi and Johnston, 1974; Randolph et al., 1994). It is calculated with the limit expansion pressure for a cavity expanding to a given radius (i.e. $D_{\mathrm{CPT}}/2$ (Mo et al., 2016)) in following calculations.

(1) Application to the present tests

Soil failures caused by a static penetrometer at shallow depths are usually in the type of general shear failure. The soil bearing capacity is usually estimated with the assumption that the soil is incompressible (Durgunoglu and Mitchell, 1975; Meyerhof, 1951). In relatively deep penetrations, local shear failure takes place around the cone tip, and the deformation characteristics of the material become of greater importance. The displaced soil deforms more analogous to that caused by a cavity expansion, therefore better predictions may be made with methods based on the cavity expansion theory in deep penetrations (Yu and Mitchell, 1998). Based on the data availability of present tests, tip resistances in two relatively deep depths (180mm and 240mm) are selected (as tabulated in Tab. 4-2) for comparisons with the theoretical results. These two depths are deeper than the defined critical depth by Eq.(4.21), so deep penetration behaviours are expected.

Tab. 4-2 Cone tip resistance at given penetration depths

Test ID	At 180mm depth		At 240mm depth	
	q_c / MPa	Size effect*	q_c / MPa	Size effect
FE-12-D	1.296	1.00	2.031	1.00
FE-6-D	1.755	1.35	2.509	1.24
FE-3-D	1.823	1.41		
FE-12-M	0.754	1.00	1.167	1.00
FE-6-M	0.924	1.23	1.286	1.10
FE-3-M	1.089	1.45		
FE-12-L	0.356	1.00	0.457	1.00
FE-6-L	0.398	1.12	0.495	1.08
FC-12-D	0.806	1.00	1.326	1.00
FC-6-D	1.155	1.43	1.812	1.37
FC-3-D	1.427	1.77		
FC-12-M	0.582	1.00	0.765	1.00
FC-6-M	0.824	1.42	1.187	1.55
FC-3-M	0.972	1.67		

* The size effect is defined as q_{c-xmm} / q_{c-12mm} for tests with a similar relative density.

It can be found from Tab. 4-2 that: (1) the defined size effect is more significant in relatively shallow penetration depths; (2) the size effect vanishingly decreases with the decrease of sand relative density; (3) the defined size effect is greater in tests within the Fraction C sand than those within the Fraction E sand.

As aforementioned, the general size effect consists of grain size effect and geometry size effect (H / D_{CPT} effect) (Balachowski, 2007). The H / D_{CPT} effect mainly behaves in relatively shallow depths, and it mostly depends on the initial stress level and sand relative density (Kim et al., 2015). In relatively deep penetration, soil failure around the cone is predominantly determined by the local deformation characteristics (characterised as the D / d_{50} effect). The strain-level dependent difference of sand behaviours between the peak state and ultimate state attenuates with decreases of the sand relative density. So the former two trends can be explained with above reasons. The third observation is mainly attributed to the grain size effect because the same conditions of penetration depths (initial stress levels) and sand relative density are conserved in comparisons.

As suggested by Collins et al. (1992); Randolph et al. (1994), the friction angle and dilation angle in the present cavity expansion theory-based approach are represented by the average values between the peak state and the ultimate state, which equal to $\varphi_{av} = (\varphi_p + \varphi_{cs})/2$, $\psi_{av} = \psi_p/2$ (for triaxial conditions). The sand friction angle and sand-penetrometer interface friction angle were given in Tab. 4-1.The penetrometer sizes and mean particle sizes were given in Tab. 2-4. The initial soil stress is estimated with $p_0 = (1+2K_0)\sigma_{v0}/3$ and $K_0 = 1-\sin\varphi_{av}$. The elastic shear modulus is estimated with Eq.(4.19). The Poisson's ratio is set as 0.3 in estimations for tests with the Fraction C sand and 0.35 for tests with the Fraction E sand. With above parameters, tip resistances calculated with the size-dependent spherical cavity expansion solution are compared with the experimental results as shown in Fig. 4-24.

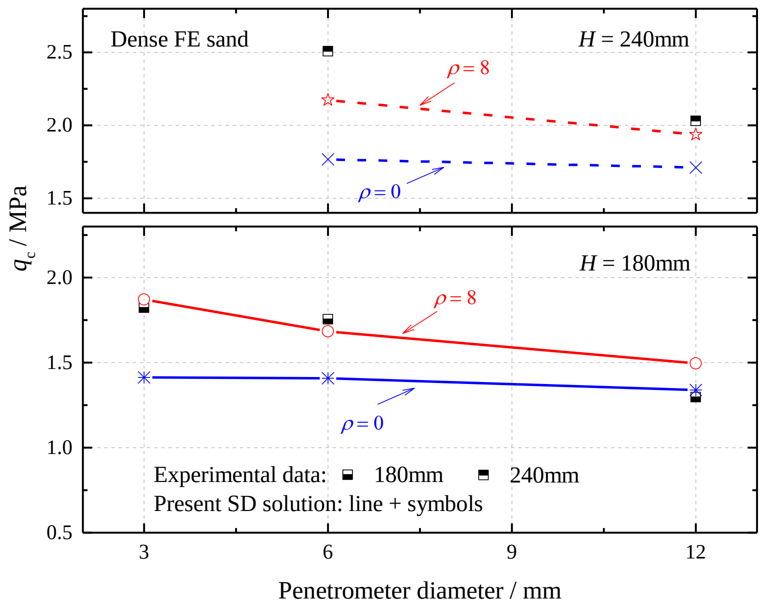

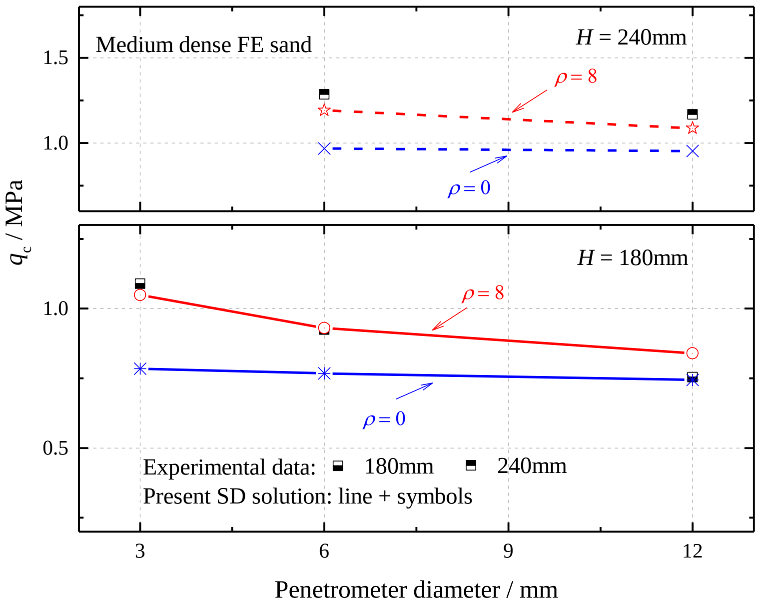
Medium dense FE sand
H = 240mm
ρ = 8
ρ = 0
H = 180mm
ρ = 8
ρ = 0
Experimental data: 180mm 240mm
Present SD solution: line + symbols
q_c / MPa
Penetrometer diameter / mm

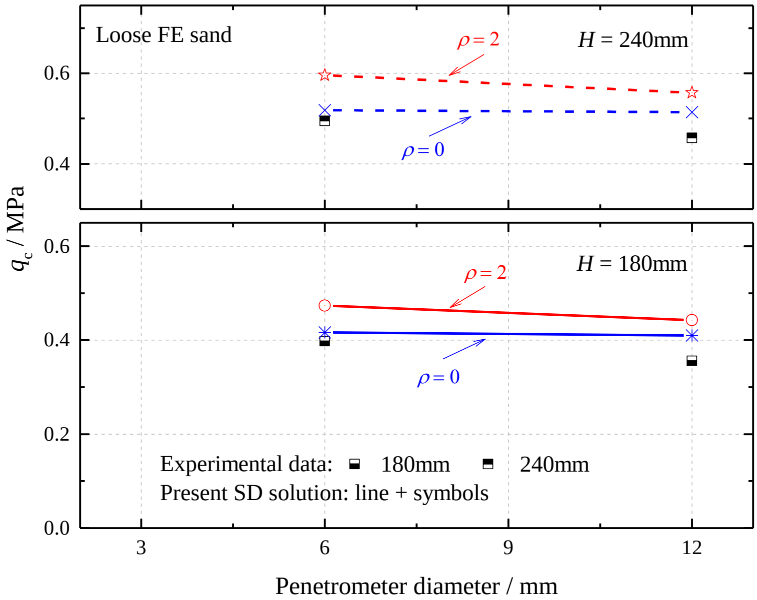
Loose FE sand
H = 240mm
ρ = 2
ρ = 0
H = 180mm
ρ = 2
ρ = 0
Experimental data: 180mm 240mm
Present SD solution: line + symbols
q_c / MPa
Penetrometer diameter / mm

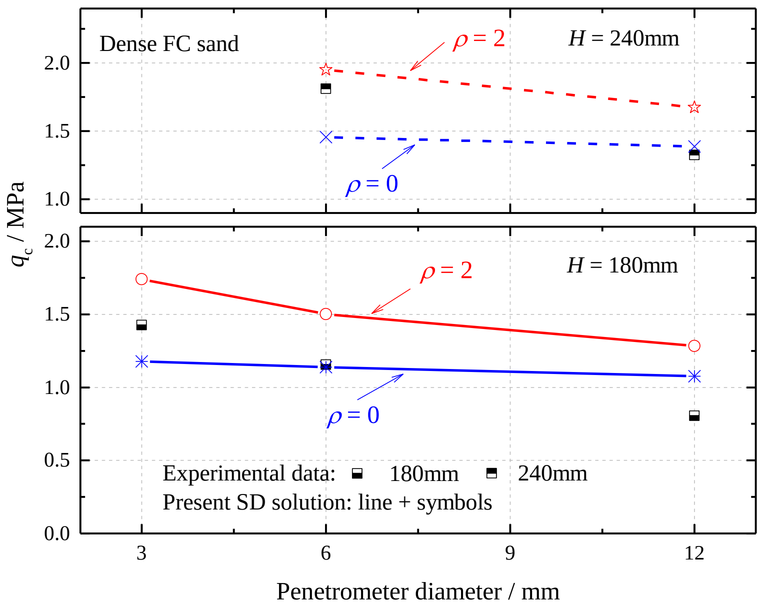
Dense FC sand
H = 240mm
ρ = 2
ρ = 0
H = 180mm
ρ = 2
ρ = 0
Experimental data: 180mm 240mm
Present SD solution: line + symbols
q_c / MPa
Penetrometer diameter / mm

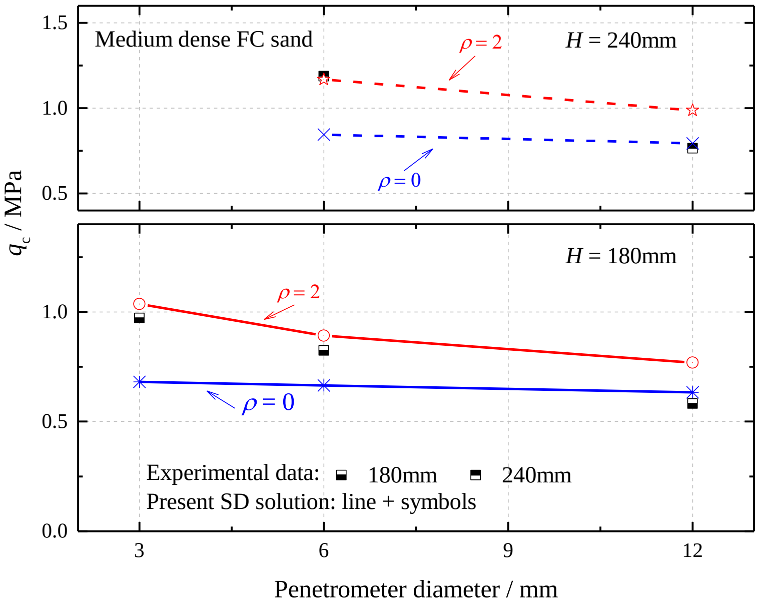

Fig. 4-24 Comparison of cone tip resistances (experimental data vs. SD solution)

As demonstrated in Chapter 3, Yu and Houlsby's (1991) solution (elastic-perfectly-plastic quasi-static model) will be recovered by the present size-dependent solution with $\rho = 0$. Figure 4-24 shows that this conventional solution can give comparable predictions of the tip resistance measured in the present tests, but it fails to capture the observed size effect. These size differences can be reflected by the previously developed size-dependent cavity expansion solution with suitable gradient coefficients (represented by ρ). It is found that ρ may increase with decreases of the sand particle size and reduce with decreases of the sand relative density. Better predictions of the size effect can be achieved by varying ρ with the penetrometer size. Taking data in the first graph as an example, with $\rho = 0$ for the 12mm sized penetrometer and $\rho = 8$ for the 6mm and 3mm sized penetrometer, the predicted tip resistances closely agree with the experimental data. Overall, the developed SD solution in Chapter 3 can predict the size effects in tip resistances of the present tests as expected. It demonstrated that the introduced parameter H_g $(=\rho(G/\sigma_{atm}))$ in the SD solution, describing the non-local behaviours of sands, may be strain-level dependent (D/d_{50} effect) and vary with the sand state, and better predictions of the size-dependent behaviours can be made by considering these dependencies in the theoretical model. Or reversely, the cone penetration test with variable penetrometer sizes may provide a simple experimental method to quantify this micro-structure-involved material property in the employed phenomenal strain gradient plasticity model.

(2) Applications to other cone penetration tests

This approach is also validated by comparing with results of other cone penetration tests which studied the concern size effect. Firstly, the results of cone penetration tests in a large calibration chamber from Eid (1987) are compared with the present theoretical solution as given in Fig. 4-25. As presented in Tab. 2-1, to get rid of the potential influences of side boundary effect in their tests, only the data of tests with loose sand samples are used.

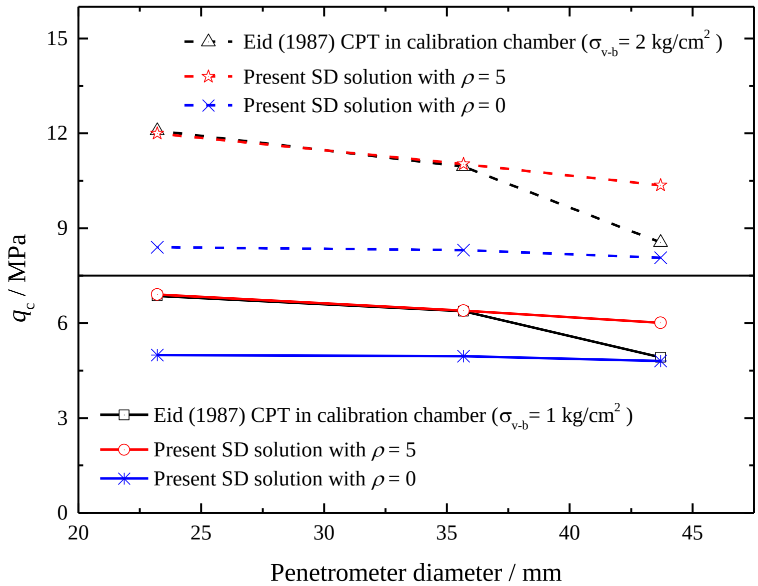

Fig. 4-25 Comparison with CPT data of Eid (1987)

In calculations with the present SD spherical solution, the friction angle of the loose sand is set as 33^{o} as given by Eid (1987); the sand-penetrometer interface friction angle is set as half of the sand-sand friction strength; the elastic shear modulus is estimated with Eq.(4.19), and the inputted Poisson ratio is 0.35. It can be found that the observed size effects can also be well predicted by the present theoretical solution with values of ρ varying from 0 to 5.

In addition, based on a series of needle penetration tests with penetrometers of sizes ranging from 1mm to 2mm, Whiteley and Dexter (1981) proposed an empirical formula to describe the size effect in the cone tip resistance as given in Eq.(4.26). x_e with a range of 0-0.6 was observed with soil textures ranging from sand to clay, which may be greatly affected by the soil structural condition as suggested.

$$q_c = q_{c-\text{large}}(1+\frac{x_e}{D_{\text{CPT}}})^2 \tag{4.26}$$

where x_e was defined as the effective diameter of the penetrometer.

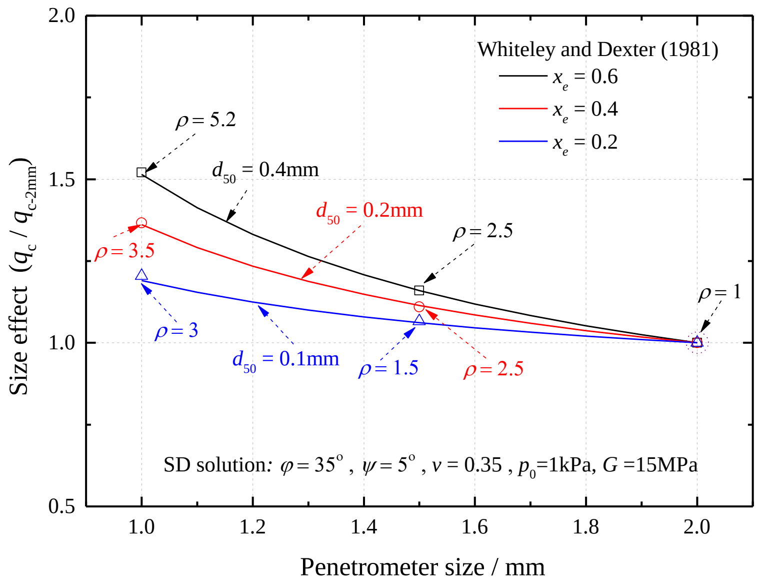

Fig. 4-26 Comparison with the empirical formula proposed by Whiteley and Dexter (1981)

Size effects predicted by equation (4.26) are calculated with typical values of x_e (0.6, 0.4 and 0.2 respectively). As given in Fig. 4-26, they are compared with those predicted by the size-dependent spherical cavity expansion solution. For penetrometers in this size range, it is shown that the empirical relationship given in Eq.(4.26) can be matched by the present theoretical model with roughly estimated values of d_{50} and ρ. However, it needs to be pointed out that a much more significant size effect of the cone tip resistance with penetrometers around this size range was reported by Wu and Ladjal (2014). The present size-dependent solution is not good at describing such significant size effects, and better predictions may be obtained with different inclusion methods of the strain gradient term.

4.4 Discussion and summary

Influences of the particle size and the penetrometer size in cone penetration tests were discussed both experimentally and theoretically in this chapter.

In section 4.2, scale effect in the shaft frictional resistance was studied. At first, the dependency of the interface friction strength on the particle size and surface roughness was summarised based on available experimental data from interface shear tests. Then an improved elastic cavity expansion solution with an additional consideration of the interface shear band thickness was established to better quantify changes of the radial confining stress under shear loading, and good performances were obtained with this solution in estimations of the shaft capacity experienced by small sized piles/probes by comparing with experimental results.

Subsequently, the size-dependent cone tip resistances measured in present tests were analysed in the section of 4.3. Reasons leading to these size-dependent differences were summarised and discussed, and the observed size effect in the cone tip resistance was estimated with two theoretical methods. By comparing with experimental results, it was found that the method based on the size-dependent spherical cavity expansion solution can provide a good theoretical tool to quantify the concerned size effect but more effort is still required to more further clarify the roles of the additionally introduced material properties (H_g and l_g) in the present model.

In the light of discussions presented in this chapter, the size-dependent behaviours in the cone penetration test were mainly attributed to the following aspects:

(1) It was found that the sand-structure friction strength may be significantly influenced by the normalised surface roughness (R_a / d_{50}). Specifically, when sand particles pass around the cone tip, an intensified shear zone will be formed in a localised region close to the interface (shear band). The strength and deformation behaviours in this narrow zone highly depend on the sand particle size and structure surface roughness. For example, in the present tests, R_a / d_{50} is about 5.06e-3 and 1.19 e-3 for the penetrometer within the Fraction E sand and the Fraction C sand respectively. As discussed in the section of 4.2.2.1, these two values lie in the intermediate roughness zone, in which the interface friction angle greatly changes with the variation of R_a / d_{50}. Based on the results of interface shear tests compiled in Fig. 4-9, the estimated critical state interface friction angle is 19.2^{o} and 14.3^{o} for tests within the Fraction E sand and Fraction C sand respectively ($\tan\delta_{cs-E} / \tan\delta_{cs-C} = 1.37$). The higher sand resistances measured in tests with the Fraction E sand than those with the Fraction C sand is partly due to this effect.

(2) When a probe penetrates into sands, rupture surfaces might be formed in the sand at failure. The sand strength and deformation (dilatation or contraction) characteristics along the slip surface greatly depend on the induced stress level and strain level which are closely related to the probe size and particle size (e.g. d_{50}). In a relatively shallow penetration depth, a rupture surface stemming from below the cone tip to the ground

surface will be developed (Durgunoglu and Mitchell, 1975), and the fact of non-uniformly distributed friction strength along the developed slip lines (caused by its stress-level or strain-level dependency or progressive failure) can be applied to explain the general size effect. In addition, the geometry size effect (H / D_{CPT} effect) also plays a significant role in leading to these size-dependent differences of the cone tip resistance in relatively shallow penetrations. For deep penetration problems, the tip penetration is greatly determined by the local deformation. The stress-level and strain-level dependent strength and deformation features of sands may also contribute to the observed size-dependent behaviours when the ratio of D_{CPT} / d_{50} is sufficiently small. In addition, the H / D_{CPT} effect gradually attenuates with increases of the penetration depth, so the difference of the sand response detected by different sized cone tip at relatively deep depths are smaller than that in shallow depths.

(3) The penetrometer size and particle size also exert influences on the mobilised lateral confining stress during the insertion and extraction process when the ratio of D / d_{50} is relatively small as quantified in Eq.(4.12), which may also contribute to the size-dependent behaviour of the shaft frictional resistance. This size-dependent influence closely depends on the structure surface conditions (e.g. roughness, hardness), confinement conditions and sand properties in/around the interface shear band.

Chapter 5

Elastic solutions for expanding ellipses and application to root-soil interaction

5.1 Introduction

In modern agriculture, soil compaction is becoming more serious than ever before because of the intensive cropping/grazing system and overuse of heavy agricultural machineries (Hamza and Anderson, 2005; Nawaz et al., 2013). It has even been described as the most serious environmental problem caused by conventional agriculture with soil erosion (McGarry, 2003). Compaction exerts influences on physical, chemical, and biological properties of the soil, and the response of plant growth to these alterations is the consequence of a complex interplay (Gregory and Nortcliff, 2013; Tracy et al., 2011).

Physically, compaction directly applies influences on the soil structure and texture (e.g. porosity, pore connectivity), soil strength, aeration condition, hydraulic properties and soil fertility (Gregory and Nortcliff, 2013). Light or moderate soil compaction might be beneficial for plants growing in some types of soils since it increases root-soil contact, especially in coarse-textured soils (Bouwman and Arts, 2000; Sharma et al., 1995). However excessive compaction usually deteriorates these physical conditions for the root and shoot growth and consequently results in detrimental influences on agriculture production (Bengough et al., 2006; Lipiec and Hatano, 2003; Lipiec et al., 2003). Therefore, there must be an optimum range of soil compaction for the maximum plant growth. This is of great importance for soil management, and a deeper understanding of the root-soil mechanical interaction will be of great helpful for seeking this optimum range. Among these mentioned physical degradations, the increased mechanical impedance is often regarded as a major limitation to root growth (Bengough et al., 2011; Whalley et al., 2008). Therefore, mechanical analysis on the soil-root interaction is selected as one of the main research objects of this chapter.

Roots grow by a continuous process of cell division in the apical meristem and cell expansion in the region of elongation just behind the apex. Its elongation rate is a consequence of the dynamic balance between the generated growth pressure (cell turgor pressure with removal of the cell wall yield pressure) and the external constraints (e.g. soil resistance, matric potential) (Bengough et al., 2006; Greacen and Oh, 1972; Hallett and Bengough, 2013). Therefore the surrounding soil environment is of great importance for root morphological development. Due to the spatial and temporal heterogeneity of soil (especially in structure/texture and strength), the interaction models between a growing root-tip and the ambient soil mass are complex. According to whether or not pre-existing channels (or gaps) appear in the growth pathway, the typical interaction models are roughly categorised into two broad groups (Bengough, 2012; Jin et al., 2013) as follows

(1) Pre-existing channels (or gaps) exist in the growth path of roots. In mechanically impeded conditions, roots prefer to exploit pores and cracks existing in the soil to effectively evade the higher resistance (Dexter, 1986; Landl et al., 2016). This might be one of the main reasons why macropores (60um-300um) volume could be closely related to root elongation rate in field soils (Valentine et al., 2012). Specifically, since root elongation is relatively insensitive to the radial pressures (Kolb et al., 2012), its axial growth along an ideal channel is not likely to be restricted unless it reaches the end of the channel or additional axial pressure is applied. When pre-existing pores or cracks are much narrower than the nominal root tip diameter, the root tip has to displace the surrounding soil particle to enlarge the channel for accommodation. Even so, Whiteley and Dexter (1983) found roots were able to elongate more rapidly in the narrower cracks than those in undisturbed clods without cracks. In addition, while the crack is oriented at an oblique angle to the preferential growth direction (tropistic growth), the likelihood of root buckling to cracks is predominantly determined by the gap width, insertion angle, physical stresses (e.g. effective soil stress, water stress) of the soil to be penetrated and the root growth pressure (Whiteley and Dexter, 1983, 1984; Whiteley et al., 1982). Smaller gap width, more perpendicular to the soil surface, lower soil strength of the next layer and thicker root diameter all can produce positive contributions to resist root buckling at the gap.

(2) No continuous pores/cracks (comparing with the size of the root tip) appear. In this case, the root tip must exert pressure to deform the soil for growth. Benefiting from its flexibility, it is able to take advantage of the relatively weak regions existing in the soil with a tortuous growth path (Bengough and Mullins, 1990). Though a certain degree of bending resistance is also necessary to maintain its ability to deeply penetrate into strong layers for seeking more mechanical support, water and nutrients (Jin et al., 2013).

In general, the elongation rate of mechanically impeded roots would be inevitably slowed (Bengough and Mullins, 1991; Goss, 1977; Schmidt et al., 2013; Taylor and Gardner, 1963), which is usually accompanied by thickening in width (Abdalla et al., 1969; Materechera et al., 1992; Materechera et al., 1991) and shortening in length (Atwell, 1993; Jin et al., 2013). Although there are species and cultivar differences (Clark et al., 2003), the penetration ability of root tips to strong soils generally depends on the soil strength to be penetrated, the magnitude of generated growth pressure, the lubricating effect of root surface caused by mucilage excretion and sloughing off of border cells, the mechanical support from root hair anchorage and radial constraints, the bending resistance of roots, the growth direction and tip shapes from the physical point of view (Atwell, 1993; Bengough et al., 2011; Bengough and Mullins, 1990; Hettiaratchi et al., 1990). Their influences are briefly summarised in turn in the following part, and, as one of the major response, the mechanism and benefits of root swelling are emphasised in part of 5.1.2.

5.1.1 Traits of the root tip that influence root penetration

(1) Soil strength and root growth pressure

The root elongation rate (dl/dt) in response to soil physical stresses is empirically expressed with the modified Lockhart equation (Hallett and Bengough, 2013) as given in Eq.(5-1). The root growth pressure (Q_{root}) is usually defined as Eq.(5-2) (Greacen and Oh, 1972).

$$(dl/dt) = l_r \cdot m_r(Q_s, \Psi_s) \cdot [P_r - Y_r(Q_s, \Psi_s) - Q_s(\Psi_s)] \tag{5-1}$$

$$Q_{root} = P_r - Y_r(Q_s, \Psi_s) \tag{5-2}$$

where l_r is the length of the zone of elongating root tissue, $[\mathrm{L}]$. m_r is the wall extensibility of cells, $[\mathrm{M^{-1}LT}]$. P_r is the turgor pressure, $[\mathrm{ML^{-1}T^{-2}}]$. Y_r is the cell wall yield threshold, $[\mathrm{ML^{-1}T^{-2}}]$. Q_s is the root penetration resistance in soil, $[\mathrm{ML^{-1}T^{-2}}]$. Ψ_s is the soil matric potential, $[\mathrm{ML^{-1}T^{-2}}]$.

It is described that the maximum soil resistance the root tip can withstand and is determined by the maximum turgor pressures generated and constraining stresses from the cell wall. The typical turgor pressures in rapidly growing plant cells range from 0.1MPa to 1MPa (Cosgrove, 1993; Mirabet et al., 2011), varying with species and growing conditions. There is no consensus on the turgor pressures' response to the mechanical impedance experienced (Tracy et al., 2011), but it is believed that the potential changes in P_r might not be central for root growth in stress adaptation (Clark et al., 2003). Instead, changes in the orientation of cell expansion might play a crucial role in the response to mechanical impedance (Atwell and Newsome, 1990; Croser et al., 2000; Hettiaratchi et al., 1990). Regulated by the orientation of microfibril (or microtubules), the cell wall stiffness differs in directions (Bengough et al., 2006). Specifically, when the longitudinal elongation is hampered by the axial soil resistance, growth polarity of cells in the root apex will gradually alter to radial expansion in which requires less pressure for enlargement (Hettiaratchi et al., 1990). In addition, Eq.(5-1) shows that the cell wall extensibility and yield threshold as two aspects of cell wall stiffness are both influenced by soil strength and matric potential (Hallett and Bengough, 2013). This provides more evidence demonstrating the importance of cell wall properties in responding to soil physical stresses.

Furthermore, quantitative measurements of the growth pressure and the encountered soil resistance may provide more precise and more practical information for evaluating the response of root growth to soil compaction. Several methods were developed to directly measure the maximum axial growth pressures of root tips (Clark et al., 1999). However, due to the great variation in measuring methods, species (or cultivars) and growing conditions, more efforts are necessarily demanded in standardising the measurement and establishing a high-quality database, especially in in-situ conditions. Alternatively, cone penetrometers have been widely used to estimate the soil resistance that roots may encounter and evaluate the degree of soil compaction (Bengough and Mullins, 1991; Cockroft et al., 1969; Greacen et al., 1968; Whiteley et al., 1981). However, variations in equipment (penetrometer size, tip shape, shaft type etc.) and testing procedure (e.g. penetration rate), also exist (Bengough et al., 2000; Bengough and Mullins, 1990), and great discrepancy has been found in direct comparisons of the soil resistance encountered by a growing root and an advancing penetrometers as detailed in Chapter 1. So more effort is needed for improving this promising method for applications on this topic.

(2) Interface friction properties between root cap and soil

The root cap provides protection on the apical meristem from abrasion by soil particles. By secreting mucilage and sloughing off border cells, the root cap is able to significantly reduce the friction resistance encountered by the root tip while penetrating into soil layers (Bengough and McKenzie, 1997; Iijima et al., 2003; Mckenzie et al., 2013). For example, Iijima et al. (2003) observed that the penetration resistance of intact root tips of Maize (Zea mays L.) increased 68% ($(Q_{\text{intact}} - Q_{\text{decapped}}) / Q_{\text{decapped}}$) due to the removal of root cap. The contribution of mucilage to this lubricating effect approximately takes 43% (Iijima et al., 2004). In addition, with increasing soil strength, the number of detached border cells and quantity of mucilage exudation may increase (Boeuf-Tremblay et al., 1995; Iijima et al., 2000). For instance, Iijima et al. (2000) estimated that the number of detached border cells is sufficient to cover the shorter elongation zone of an impeded root tip which only covers 7% of the surface area of roots growing in loose sand.

One significant aim of research on this specific topic is to quantify the interface friction coefficient (μ_r) between a growing root and the soil. As discussed in Chapter 4, the interface friction properties are greatly determined by the shear failure mode and the location where it takes place. In the close vicinity of the contacting area, variations in particle size, angularity, crushability, soil state (relative density of sand, saturation of clay etc.), surface adhesion, roughness and hardness of the object and normal stress level would result in some changes of μ_r . In particular, the small size, the irregular geometry of the root cap and the environment-dependent root exudation make direct and precise measurements of the root tip-soil interface friction property more difficult to operate. Even so, several attempts have also been made (Barley, 1962; Bengough and Kirby, 1999; Mckenzie et al., 2013). The methods from Barley (1962) and Bengough and Kirby (1999) are, more or less, akin to the conventional interface friction tests, which measured the slip resistance by moving the vertically loaded roots. By moving a 1cm length of excised maize roots close to the tip at a speed of 1cm/min, Barley (1962) obtained the average values of μ_r for a root/nylon interface and a root/porous stone interface are 0.20 and 0.31 respectively. Though the measured μ_r between hydrated root caps of maize and peas with ground glass surfaces by Bengough and Kirby (1999) was in the range of 0.02-0.04 which is an order of magnitude lower. Presumably, this large discrepancy resulted from their main differences in the measured position of roots, failure mode of the root surface, moving speed, level of vertical stress and interface conditions. Alternatively, Mckenzie et al. (2013) proposed an approximate method to estimate the interface friction coefficient directly from readings of penetration tests. μ_r is defined with Eq.(5-3) which has been widely used both in geotechnical and agricultural fields (Bengough and Mullins, 1991; Randolph et al., 1994).

$$\mu_r = \frac{Q - \sigma_n}{A(\sigma_n - \chi\psi_m)} \tag{5-3}$$

$$Q_s = \sigma_n(1 + A\tan\delta) + c_a \cot\alpha_s \tag{5-4}$$

where Q is the soil resistance encountered by roots or penetrometers. σ_n represents the normal stress acting on the surface of the object. $\chi\psi_m$ represents the additional contribution of surface adhesion to the normal stress. A is a defined shape factor, which equals to $\cot\alpha_s$ for a cone tip and $\pi a/2r$ for an elliptical half- spheroid tip (Mckenzie et al., 2013). α_s is the semi-angle of tip cone. a and r length parameters of an elliptical half-spheroid as shown in Fig. 5.1.

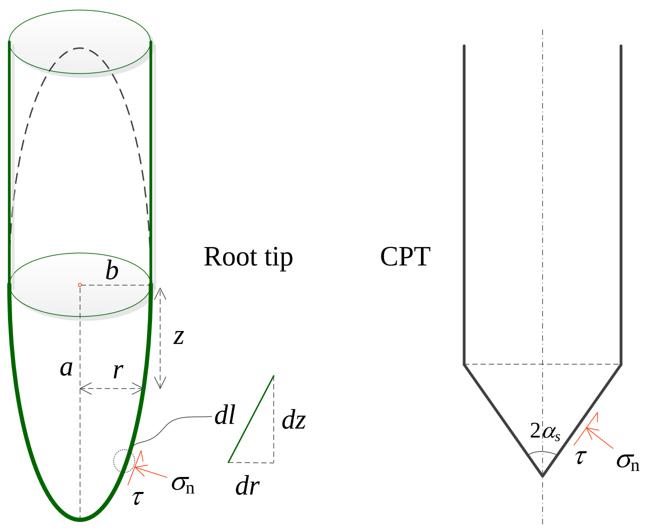

Fig. 5.1 Diagram of root and cone penetrometer geometries

The key of this method is to determine the normal stress σ_n. Mckenzie et al. (2013) proposed to use the resistance of a rotating probe (Q_{rotation}) $\times 0.986$ as the estimate of σ_n based on the work from Bengough et al. (1997). With the use of this assumption, they calculated the interface friction coefficient of soil-metal (stainless steel and silt loam topsoil with a bulk density of 1.2Mgm^{-3} and water content 223 ± 6 g/kg) ranges from 0.79 to 0.97. However, the typical value of soil-steel interface friction coefficient under similar condition would be less than 0.6 (Stafford and Tanner, 1983; Tsubakihara et al., 1993). So an overestimation may be made with this method, which probably results from several aspects: (1) underestimation of σ_n. σ_n is not the same for the case with or without rotation. As noticed by Bengough et al. (1997), the additional influence of rotation-induced shear stress will contribute to the plastic failure of soil, and this is theoretically proven in Chapter 6 of this thesis. It is found that the additional shear stress may lead to 6% decrease of the required expansion pressure in undrained saturated clay and this decrease would rise with an increase of the soil shear stress hold capacity; (2) Eq.(5-3) was established on the basis of stress equilibrium along the contact surface by ideally assuming the normal stresses acting on the interface are uniform. In the limit equilibrium method, the failure pattern is pre-assumed, and it is not able to take the soil stress-strain behaviour into account (Yu and Mitchell, 1998). In addition, the size and shape of the penetrometer tip and speed also affect the relationship of σ_n and Q_{rotation}. Therefore, certain differences may also be caused because these parameters in tests of Mckenzie et al. (2013) are different to those used by Bengough et al. (1997). In fact, this method can be readily evaluated by directly comparing the estimated μ_r with the corresponding data from direct interface shear tests.

This promising method opened up a new way to estimate μ_r between growing root and soil. It estimated the soil-root interface friction coefficient under similar conditions lies in the range of 0.21-0.26. However, considering its overestimation of the soil-steel friction coefficient, this estimated range is also possibly a bit higher than the real value. In addition, assumptions on the shape factor (A) which depend on the real size and shape of the root cap have a large influence on the calculation of μ_r, so great care should be taken in estimating this parameter.

(3) Longitudinal supports for root penetration

As the balancing force of penetration pressure, it is no doubt that the obtained reaction force partly determines the root axial penetration ability. As illustrated in Fig. 5.2, the anchorage of root tips can be generally classified into two typical conditions (Bengough et al., 2011), and reaction forces for root elongation mainly come from three sources: anchorage effect of root hairs, side friction due to soil-root contact (in particular from the maturation zone) and the potential longitudinal reaction force at an adjacent bend.

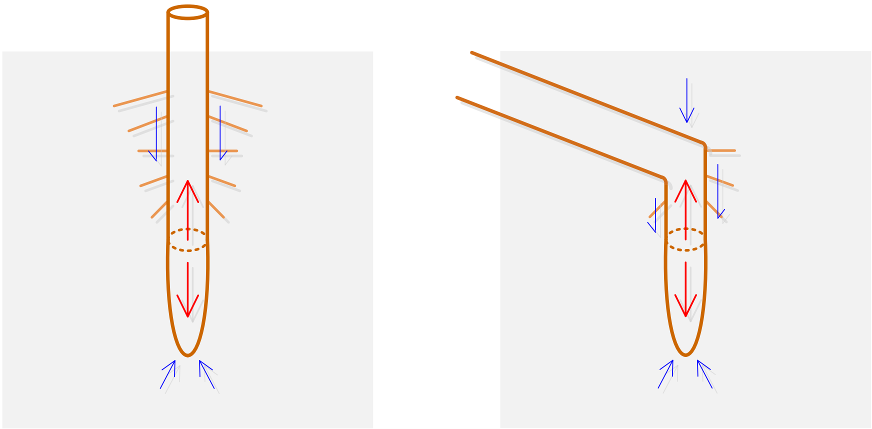

Fig. 5.2 Schematic diagrams illustrating reaction forces for root growth

Contributions of the anchorage effect from root hairs to root penetration have been experimentally confirmed by Bengough et al. (2016) and Haling et al. (2013) in recent years. They found that the presence of root hairs, in general, can significantly increase the penetration ability of root, and this contribution would be more important in relatively loose seed beds. To theoretically estimate the anchorage effect of root hairs, Bengough et al. (2011) calculated the stress required to break all the root hairs (by multiplying the tensile strength with the cross-sectional area of root hairs). However, the anchorage mechanism of root hairs has not been clearly identified. In other words, no solid evidence has been presented to directly confirm the real failure mode or the most probable mode to happen between root hairs and the surrounding soil. The maximum anchorage effect is probably either determined by the tensile strength of root hairs or the shear resistance between the anchored zone and surrounding soil or both of them. So confirming the failure mode can enable us to better quantify this anchorage effect.

Apart from above anchorage effect of root hairs, the mobilised side friction resistance may also provide reaction forces for facilitating root penetrations. It is known the friction forces are greatly determined by the magnitude of confining stresses from the surrounding soil. The magnitude of the confining soil stress is positively proportional to the root diameter before the surrounding soil reaches a steady plastic deformation stage. Therefore, thicker roots could get higher side frictions. Probably, this is another benefit of root swelling to the root tip penetration, and this will be further discussed later.

Lastly, the reaction force from a bend can be easily distinguished, and the mobilised magnitude of this force may depend on the distance of the bend to the apex, the bending angle, soil strength and possible reverse displacement in the longitudinal direction.

(4) Bending resistance and radial support

The flexibility of roots enables them to take advantage of the pre-existing cracks, pores and weakening zones in the soil. However, if they are too flexible they would lose the ability to penetrate into strong layers (Jin et al., 2013). Therefore sufficient bending resistance is necessary for the root penetration, which mainly depends on the root bending stiffness and radial confining stresses. Clark et al. (2008b) demonstrated that good root penetration was consistently associated with greater root diameter and bending stiffness. Regarding the root tip as a cylinder of a simple material, the bending stiffness is a function of the elastic modulus and the area moment of inertia of its cross section. Therefore a gradient of 4 should be expected on a log–log plot of bending stiffness against diameter. However, a slope being near 3.5 was found in their tests. Two direct conclusions can be drawn from this finding: (1) the bending stiffness of root is highly related to root diameter; and (2) the elastic modulus of roots may slightly decrease with the increase of the root diameter. In addition, with a given diameter, they found the bending stiffness of roots that had penetrated into a strong layer is lower than those had not, and it is ascribed to the cell-wall relaxation which usually happens in impeded roots. Furthermore, the presence of radial stresses can facilitate root axial elongation with a significant increase of the axial penetration ability (Bengough, 2012; Bizet et al., 2016). The confining soil stresses motivated by a thick root is usually higher than those received by a thin one and also depends on the strength of surrounding soil as indicated in Fig. 5.3. The results are calculated by the widely used cylindrical cavity expansion solution from Yu and Houlsby (1991) (initial cavity diameter a_0 = 0.5mm; Poisson's ratio v = 0.35; friction angle 30^o; dilation angle 5^o; soil cohesion 10 kPa; far-field is set zero; two values of the shear modulus are used).

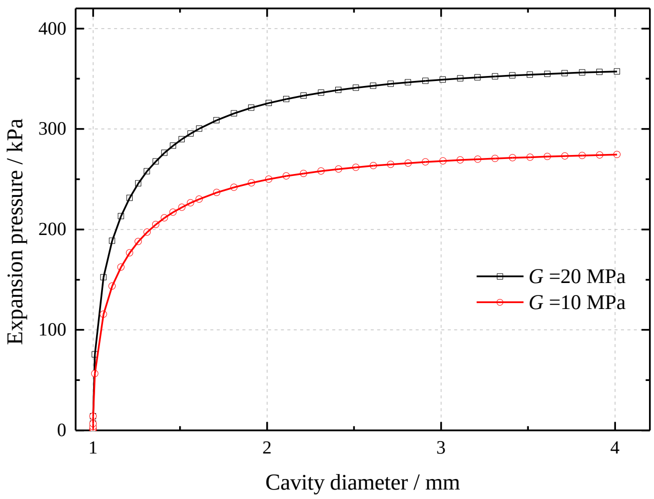

Fig. 5.3 Radial confining stresses vs. root diameter

Confining stresses of the surrounding soil to the root not only resists the root tip to deflect and also determines the magnitude of the reverse side friction for anchorage. This explains, at least partly, that a stronger upper layer or a gradient increase of soil strength can considerably increase the percentage of roots that are able to penetrate into deeper strong layers (Clark et al., 2008a; Jin et al., 2013).

(5) Growth model of the root tip

As one of the most active parts of living plants, the root tip can sense, adapt and even change its related growing environment (Carminati et al., 2010; Clark et al., 2003; Jin et al., 2013). Although the morphologic development of plant roots are greatly determined by their tropistic growth (e.g. gravitropism, chemotropism, hygrotropism), the root tip is also able to effectively evade higher soil resistance by altering its growing pathway or expansion model. The ability of root tips to take advantages of relatively weak zones has been discussed in above parts, therefore the attention will focus on the latter characteristics here. The growth model of roots would greatly determine how the root-tip to interact with the surrounding medium. Specifically, dynamic changes of the root tip (or to put it simply, the sequence of root elongation and radial expansion) determine the soil particles moving trajectories, and consequently, determine the required pressure to displace these particles. For example, it is known that the required pressure for spherically displacing the soil is much higher than that required by a cylindrical expansion (Greacen et al., 1968; Hettiaratchi et al., 1990; Yu and Houlsby, 1991). The resistance encountered by an advancing root cap of an approximately ellipsoidal shape must lie somewhere between those required by a cylindrical expansion and a spherical expansion, and it will change with root growth models. Even though many experimental findings demonstrated that the deformation pattern around the root tip is closer to a cylindrical expansion (Bengough and Mullins, 1991; Cockroft et al., 1969; Greacen et al., 1968), quantitative analysis is scarce, and especially developments of relevant theoretical analyses are lagging far behind. Several growth models were proposed to explain the above problem (Abdalla et al., 1969; Faure, 1994; Kirby and Bengough, 2002; Richards and Greacen, 1986). For example, Abdalla et al. (1969) proposed an inverse-peristalsis model (detailed later). Richards and Greacen (1986) assumed that the roots can elongate by entering an existing pore, crack or interaggregate space and then deform the soil like a cylindrical cavity expansion.

Above discussion deliberately focuses on the physical interactions between the root tip and the surrounding soil. In fact, these responses of root growth to the mechanical impedance are predominantly regulated by several phytohormones (Ubeda-Tomás et al., 2012), especially the ethylene, auxin, abscisic acid (ABA) (Okamoto et al., 2008; Tracy et al., 2015). In addition, these physical responses may be accompanied by some chemical and biological changes and consequently cross influences will further affect the physical interactions.

5.1.2 Root thickening with response to mechanical impedance

Root swelling behind the apex in response to high soil resistance has been widely observed in a number of species (Abdalla et al., 1969; Atwell, 1990; Clark et al., 2008b; Iijima et al., 2003; Kirby and Bengough, 2002; Materechera et al., 1992; Materechera et al., 1991; Misra and Gibbons, 1996). It is found that a thick root usually has higher penetration ability into strong soils than a thin one under similar conditions (Abdalla et al., 1969; Hettiaratchi et al., 1990; Kirby and Bengough, 2002; Materechera et al., 1992). According to the previously summarised influencing factors on the root penetration, possible benefits resulted from root thickening are attributed to:

(1) higher bending resistance of the root with a greater diameter.

(2) higher radial stress constraints due to more radial compression, which are beneficial to resist root buckling and provide more reaction forces.

(3) stress relief or loosening of soils ahead of the root tip due to the radial expansion.

In addition, Materechera et al. (1992) put forward that higher axial growth pressure (Q_{root}) may be exerted by thicker roots based on the experimental finding from Misra et al. (1986a) which gave that Q_{root} is proportional to $D_{root}^{0.94}$ (D_{root} is the root diameter). However, conflicting results were obtained by Whalley and Dexter (1993) and Clark et al. (1999) with similar apparatuses. Clark et al. (1999) concluded that the apparatus used to measure Q_{root} may apply significant influences on the results, and Q_{root} might not increase with increases of the root diameter. And Clark and Barraclough (1999) even found that the roots of dicotyledons (dicots) did not systematically generate higher Q_{root} than those of monocotyledons (monocots) based on a series tests with young seedlings of Maize, wheat, barley, rice, albus lupin, pea and sunflower. Therefore, as suggested, this factor is not included here as a general benefit caused by root thickening.

Contributions of the first two aspects of above benefits are relatively straightforward and have been elucidated in the previous section. Hence, the following study will mainly focus on the third benefit to shed some lights on its mechanism. This hypothesis was first proposed by Abdalla et al. (1969) to account for the root thickening caused by mechanical impedance. They roughly validated this root growth model with a penetration simulator, which is capable of radial expansion and axial penetration separately, and an elastic cavity expansion solution. Subsequently, Hettiaratchi and Ferguson (1973) advanced these validations, and Hettiaratchi et al. (1990) enriched this theory with some new assumptions later. Taking these works into consideration, this named inverse-peristalsis root growth model is briefly summarised here.

According to experimental findings, responses of root growth to the mechanical impedance were generally divided into three conditions (Abdalla et al., 1969). If the soil resistance is lower than the first threshold (Q_{th-1}), the root will grow with normal diameters in normal elongation rates. When the encountered resistance of root tips exceeds the upper threshold (Q_{th-2}), the root tip thickens without further axial elongation. In a stress range of $Q_{th-1} < Q_{soil} < Q_{th-2}$, the root tends to be thicker and then elongates as illustrated in Fig. 5.4. Steps of this growth circle were summarised as

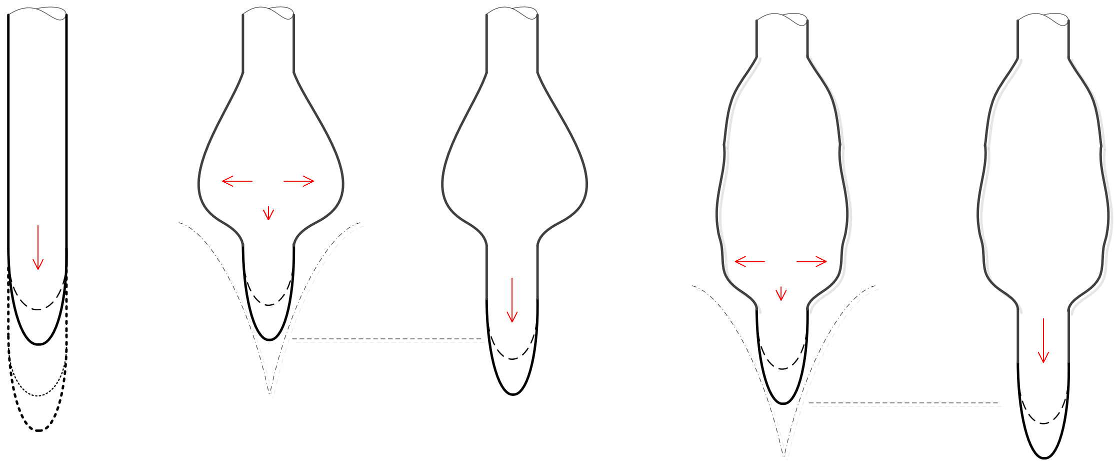

Fig. 5.4 Growth steps of impeded roots in the inverse-peristalsis model (after Hettiaratchi et al. (1990))

ⅰ) The axial elongation of root tip is inhibited due to soil resistance.

ⅱ) Enlargement of cells in the elongation zone gradually alters from longitudinal elongation to radial expansion.

iii) Radial thickening of root aids to relieve the resisting stress field ahead of the root cap.

iv) When the root tip is able to overcome the soil resistance ahead, the axial elongation will resume until the root cap enters a zone of soil would inhibit its axial elongation again.

In strong soil layers, the growth of root tips is achieved with continuous repeats of this growth cycle until it is no longer triggered. As a consequence, the elongation rate will be significantly reduced.

Two basic prerequisites were included in this growth model, which are

1) The axially impeded root tip tends to and is able to radially thicken.

As aforementioned, by altering the orientation of microfibrils, roots can reorient the cell growth direction to adapt the stress variation around the root tip (Bengough et al., 2006; Hettiaratchi et al., 1990). It confirmed that the root tip has the ability to alter the growth orientation. In addition, Kolb et al. (2012) recorded that the radial expansion pressure of chick pea (Cicer arietinum L.) seedlings reached approximate 0.30 ± 0.15MPa, which is in a comparable level of the turgor pressure, and the root growth is more easy to be hampered by the axial resistance other than the radial confinement (Bengough, 2012).

Moreover, to identify the difference of the encountered soil resistances between the radial expansion and the axial elongation, results calculated with cylindrical and spherical cavity expansion solutions were often compared (Abdalla et al., 1969; Greacen et al., 1968; Hettiaratchi and Ferguson, 1973; Hettiaratchi et al., 1990). As known, two kinds of expansion pressures are usually concerned in conventional quasi-static cavity expansion solutions, including the pressure of a cavity expanding from the initial radius a_0 to a given radius a and the limit expansion pressure $P_{\lim}$ (as discussed in Chapter 3). For illustration, the closed-form solution from Yu and Houlsby (1991) (large displacement solution with the non-associated Mohr-Coulomb yield criterion) was employed the calculated these two kinds of pressures as shown in Fig. 5.5.

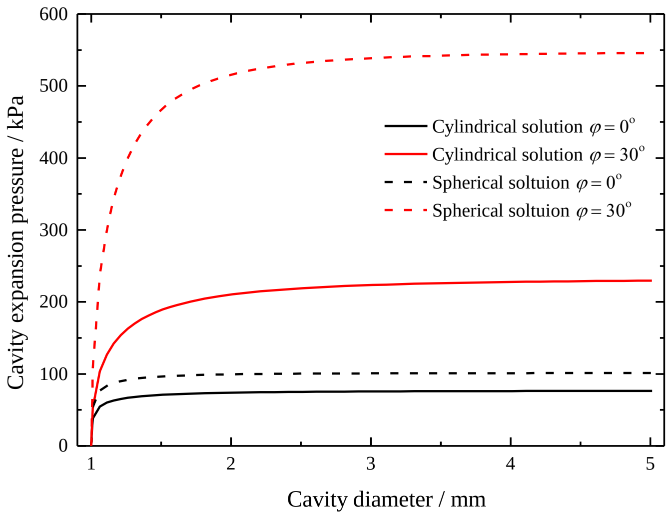

Fig. 5.5 Cavity pressure-expansion response
(a_0= 0.5mm; v = 0.35; ψ = 0^o; c = 10 kPa; p_0 = 0; G = 10MPa)

It is shown the required expansion pressure rapidly increase with increasing a/a_0 at initial expansion stages (roughly $a/a_0 < 2$), and a relatively steady expansion state is reached afterwards. The process of continuous cavity expansion is analogous to that of root enlargement displacing the surrounding soil. For roots growing in an existing pore, the initial pressure-expansion response may be more suitable to model the root-soil interaction. More commonly, the limit expansion pressure $P_{\lim}$ was used to compare the aforementioned difference. Numbers of analytical solutions are available to identify this difference as summarised by Yu (2000), and the analytical elastic-perfectly-plastic solution from Yu and Carter (2002) is employed here. This combined solution was established for cohesive-frictional soil with non-associated Mohr-Coulomb yield criterion. The convected part of the stress rate is neglected in formulas of Eq.(5-5) and Eq.(5-6) for simplicity, and they give the same results as another widely-used cavity expansion solution from Carter et al. (1986).

$$P_{\lim} = \eta'(\frac{r_c}{a})^{k\frac{(\alpha-1)}{\alpha}} - \frac{Y}{\alpha-1} \tag{5-5}$$

$$1 = \gamma'(\frac{r_c}{a})^{k\frac{(\alpha-1)}{\alpha}} + [\delta(1+k) - \gamma'](\frac{r_c}{a})^{1+\frac{k}{\beta}} \tag{5-6}$$

$\alpha = (1+\sin\varphi)/(1-\sin\varphi)$, $\beta = (1+\sin\psi)/(1-\sin\psi)$, $Y = 2c\cos\varphi/(1-\sin\varphi)$

$\delta = \dfrac{Y+(\alpha-1)p_0}{2G(\alpha+k)}$, $\gamma' = \dfrac{\alpha\beta s'}{k\alpha - k\beta(\alpha-1)+\alpha\beta}$, $M = \dfrac{E}{1-v^2(2-k)}$

$$s' = -\frac{\chi'\eta' k(\alpha-1)}{\alpha\beta} \;,\; \eta' = \frac{\alpha(1+k)[Y+(\alpha-1)p_0]}{(\alpha-1)(\alpha+k)}$$

$$\chi = \frac{1}{M}[\beta - \frac{k\nu}{1-\nu(2-k)}] + \frac{1}{M\alpha}[k(1-2\nu)+2\nu - \frac{k\beta\nu}{1-\nu(2-k)}]$$

where definitions of the above soil properties are re-expressed here. $k=1$ for the cylindrical cavity and $k=2$ for the spherical cavity. c, φ and ψ are cohesion force, friction angle and dilation angle of soil respectively. E is Young's modulus, and $G=E/2(1+\nu)$ stands for the shear modulus of the material. ν is Poisson's ratio.

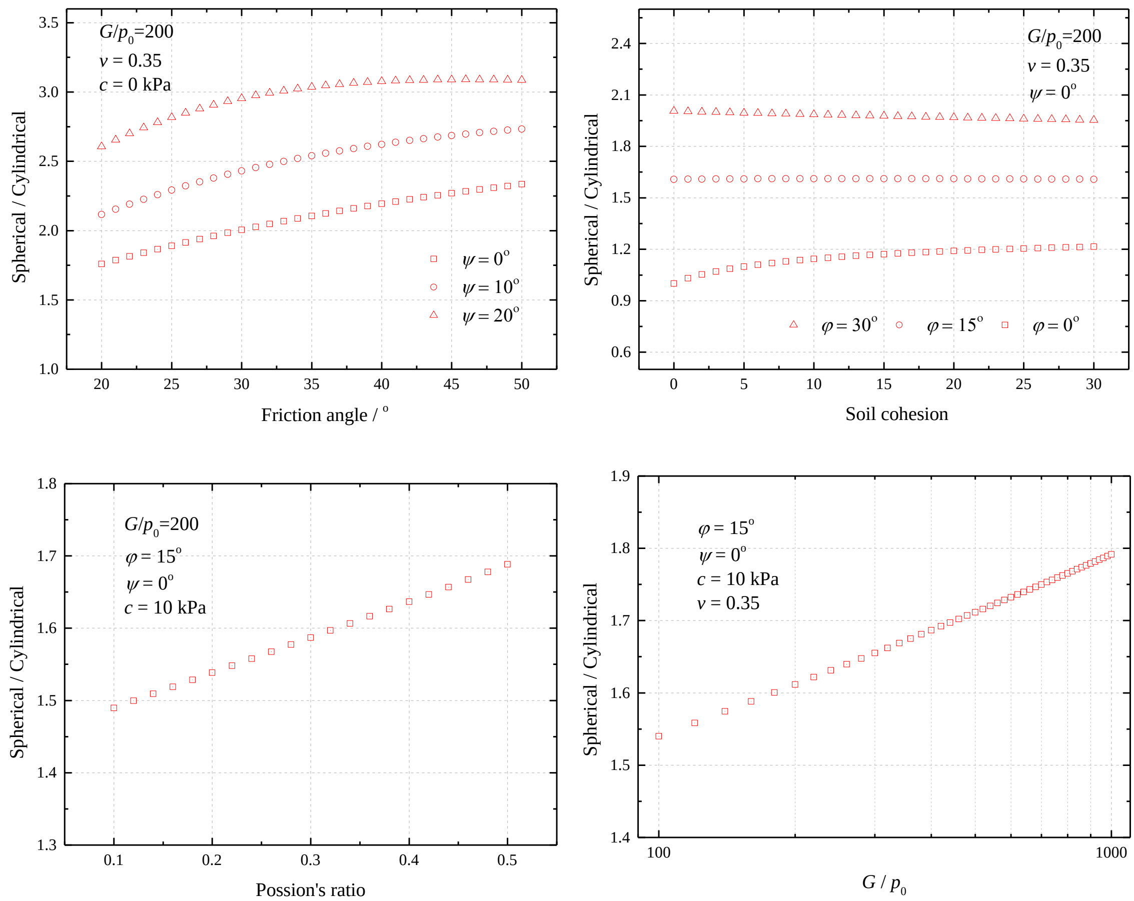

Fig. 5.6 Comparison of the limit expansion pressures (spherical /cylindrical solution)

It is shown that the ratio of limit expansion pressures (spherical/cylindrical) is influenced by soil friction angle, dilation property, soil cohesion, Poisson's ratio and soil stiffness (G/p_0) in the adopted solution. Within a very broad range of soil properties (Yu and Houlsby, 1991), this ratio normally lies in a range of 1.1 (soft clay) to 3 (dense sand, would be higher with a greater G/p_0), and this range is compatible with that given by Nguyen (1977) (1.3 for frictionless cohesive soil to 2.5 for a frictional soil with a high modulus of rigidity as summarised by Hettiaratchi et al. (1990)). It approximately demonstrated that the required expansion pressure for a radial expansion is lower than that required by an axial elongation, and it was also demonstrated in the punch test with a flat-end probe with inflatable rubber sleeve by Hettiaratchi and Ferguson (1973).

2) Radial expansion of cells just behind the root apex can facilitate its axial penetration.

To account for the contributions of radial expansion to axial penetration, some investigations have been carried out in the last several decades. A relief effect on the front stress field caused by the radial expansion was usually expected (Abdalla et al., 1969; Richards and Greacen, 1986; Whalley and Dexter, 1993), and this hypothesis has been roughly demonstrated in some experimental investigations (Abdalla et al., 1969; Hettiaratchi and Ferguson, 1973) and numerical simulations (Kirby and Bengough, 2002; Richards and Greacen, 1986). By using a penetration simulator (a flat-end probe with inflatable rubber sleeve), Hettiaratchi and Ferguson (1973) quantified the radial enlargement was able to effectively reduce the encountered axial resistance which even became lower than the required radial pressure. They contributed this reduction effect due to the increase of shear stresses under the punch which brings the underlying material closer to failure. Differently, Richards and Greacen (1986) found a tensile strain region immediately ahead of the root would always be caused due to the radial expansion based on numerical analysis. The confining stresses in the front of the cylindrical 'root' were relieved and, as a consequently, it facilitates the axial elongation of the root tip. In addition, in contrast to these methods focusing on the radial expansion, this problem was studied by assuming the root grows as a moving rigid body with a constant shape in the soil (Kirby and Bengough, 2002). It was found that thicker roots may experience smaller axial resistance than thin roots while the soil-root interface friction presents. Otherwise, the stress relief effect caused by thickening would be greatly diminished. However, the assumed pattern of surface movement is not similar to the root thickening process (no radial change in shape). And different conclusions may be produced with different constitutive models or simulation tools. Specifically, due to the moving rigid body has a comparable size of soil particle, evident size effect would display by adopting non-local constitutive models (e.g. the model adopted in Chapter 3) or different numerical methods (e.g. with DEM simulations (Lin and Wu, 2012)). So this method probably is not a good approach to account for the size-related root thickening effect. In the light of above discussions, the advantage of thickening on relieving the front stress field was more or less agreed, but much more quantitative analyses, both experimentally and theoretically, are necessarily needed to describe this process. Hence, a new simple theoretical method attempting to approximately address this problem will be given as follow.

5.2 Elastic analysis of stress and displacement fields around an ellipse

In order to deal with the preceding problem, solutions for an elliptic cavity deforming in the linear elastic material will be presented in this section. Considering the shape-shifting of the longitudinal cross-section of root tip during growth, both stress-type boundary conditions and displacement-type boundary conditions will be considered in developing these solutions.

5.2.1 Definition of coordinate system

For convenience, the orthogonal curvilinear coordinates presented by Unger (2005, 2010) is employed to describe the geometry positions around an ellipse in the physical plane as depicted in Fig. 5.7. The orthogonal curvilinear coordinates consist of a series of naturally orthogonal oval shape lines, paralleling to the innermost ellipse, and radial lines, perpendicular to the innermost cavity, (Lawrence, 1972).

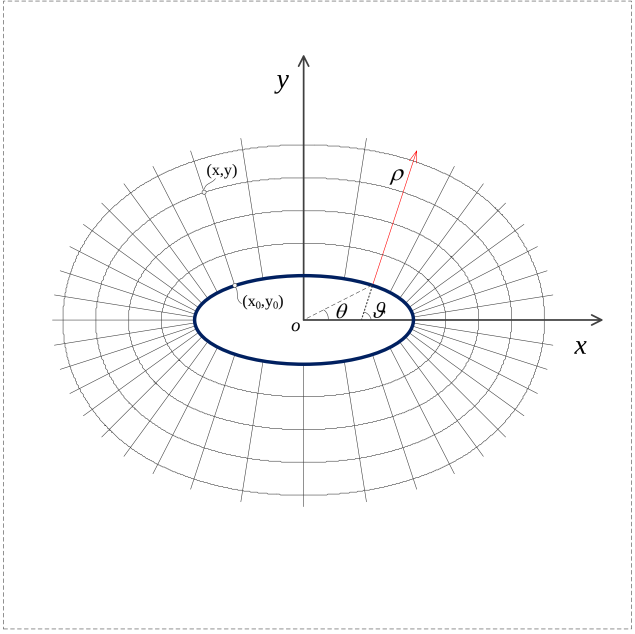

Fig. 5.7 Stress boundaries and coordinate systems

Points in the new coordinates system can be expressed as

$$x = x_0 + \rho \cos \vartheta \quad , \quad y = y_0 + \rho \sin \vartheta \tag{5-7}$$

where (x_0, y_0) represents points on the inner ellipse. ρ shows the distance from the hole surface to a particular point along the normal direction. ϑ is the angle that normal to the inner elliptic boundary, which is counted anti-clockwise from the positive x-axis direction.

Both the Cartesian coordinates and the paralleled elliptic coordinates, of which have the same origin in the centre of the ellipse, are employed. In the Cartesian coordinates, points (x_0, y_0) on the surface of inner ellipse can be described as

$$\frac{{x_0}^2}{a^2} + \frac{{y_0}^2}{b^2} = 1 \quad (x_0 = a\cos t \ , \ y_0 = b\sin t \ \text{and} \ a \neq 0 \ , \ b \neq 0) \tag{5-8}$$

where 't' represents the eccentric angle of an ellipse. 'a' and 'b' are semi-major axis and semiminor axis respectively. Two coordinates can be linked with $\tan\vartheta = \frac{a}{b}\tan t$. So the inner ellipse can be described in the curvilinear coordinates as

$$x_0 = a^2 \cos\vartheta \big/ \sqrt{H} \quad , \quad y_0 = b^2 \sin\vartheta \big/ \sqrt{H} \quad (H = a^2\cos^2\vartheta + b^2 \sin^2\vartheta) \tag{5-9}$$

Spatial directions of points in these two coordinate systems are linked now, but how to measure the vector length is not clearly defined. To complete the transformation between them, the concept of the metric coefficient (Love, 1927; Saada, 1974) is applied. Let us refer a region of space to the Cartesian coordinates, and the coordinates of any points in this region are (x_1, x_2, x_3). Then they are transformed to points (y_1, y_2, y_3) belonging to the curvilinear coordinate system by following one-to-one corresponding relations.

$$y_1 = f_1(x_1, x_2, x_3) \quad , \quad y_2 = f_2(x_1, x_2, x_3) \quad , \quad y_3 = f_3(x_1, x_2, x_3) \tag{5-10}$$

These relations are single valued and continuously differentiable. Then an arc length in the curvilinear coordinates can be expressed as

$$(ds)^2 = g_{ij} dy_i dy_j \tag{5-11}$$

where g_{ij} is called 'metric coefficient'. The scalar factor is defined as $h_i^2 = g_{ii}$ (no sum). The coefficients for each axis direction of the curvilinear coordinate system are readily obtained with Eq.(5-7) and Eq. (5-10).

$$g_{11}{}^2 = (\frac{\partial x}{\partial \rho})^2 + (\frac{\partial y}{\partial \rho})^2 + (\frac{\partial z}{\partial \rho})^2 = 1 \tag{5-12}$$

$$g_{22}{}^2 = (\frac{\partial x}{\partial \vartheta})^2 + (\frac{\partial y}{\partial \vartheta})^2 + (\frac{\partial z}{\partial \vartheta})^2 = [\rho + F(\vartheta)]^2 \tag{5-13}$$

$$g_{33}{}^2 = (\frac{\partial x}{\partial z})^2 + (\frac{\partial y}{\partial z})^2 + (\frac{\partial z}{\partial z})^2 = 1 \tag{5-14}$$

With these coefficients, the strain tensor, strain-displacement relations and equilibrium equations in the paralleled elliptic coordinate system can be readily established with the general relations for orthogonal curvilinear coordinate systems, for example, those presented by Saada (1974).

$$\varepsilon_{\rho\rho} = \frac{\partial u_\rho}{\partial \rho} \quad , \quad \varepsilon_{\vartheta\vartheta} = \frac{1}{\rho + F(\vartheta)}[\frac{\partial u_\vartheta}{\partial \vartheta} + u_\rho] \quad , \quad \varepsilon_{\rho\vartheta} = \frac{1}{2}[\frac{1}{\rho + F(\vartheta)}\frac{\partial u_\rho}{\partial \vartheta} + \frac{\partial u_\vartheta}{\partial \rho} - \frac{u_\vartheta}{\rho + F(\vartheta)}] \tag{5-15}$$

where $F(\vartheta) = a^2b^2 / H^{3/2}$. u_ρ and u_ϑ are displacement components in the radial and tangential directions of the parallel-elliptic coordinates respectively. $\varepsilon_{\rho\rho}$, $\varepsilon_{\vartheta\vartheta}$ and $\varepsilon_{\rho\vartheta}$ are strain components in the radial, tangential, and axial directions of the parallel-elliptic coordinates respectively. In fact, $F(\vartheta)$ represents the radius of curvature of the corresponding point at the cavity wall.

The stress equilibrium equations along the normal and tangential directions with absence of the body force for plane strain problem are

$$\frac{\partial \sigma_{\rho\rho}}{\partial \rho} + \frac{1}{\rho + F(\vartheta)}\frac{\partial \sigma_{\rho\vartheta}}{\partial \rho} + \frac{\sigma_{\rho\rho} - \sigma_{\vartheta\vartheta}}{\rho + F(\vartheta)} = 0 \tag{5-16}$$

$$\frac{1}{\rho + F(\vartheta)}\frac{\partial \sigma_{\vartheta\vartheta}}{\partial \vartheta} + \frac{\partial \sigma_{\rho\vartheta}}{\partial \rho} + \frac{2\sigma_{\rho\vartheta}}{\rho + F(\vartheta)} = 0 \tag{5-17}$$

where $\sigma_{\rho\rho}$, $\sigma_{\vartheta\vartheta}$ and $\sigma_{\rho\vartheta}$ are stress components in the radial, hoop, and axial directions within the parallel-elliptic coordinates respectively.

5.2.2 Elastic stress and displacement solutions

In linear elasticity theory, three groups of boundary-value problems are broadly categorised, which generally include stress boundary-value problem, displacement boundary-value problem, and mixed boundary-value problem. With unremitting efforts for centuries, lots of analytical solutions are available for a wide range of elastic boundary-value problems (Love, 1927; Muskhelishvili, 1963; Saada, 1974; Selvadurai, 2000; Timoshenko and Goodier, 1970). The govern equations to these problems generally consist of equilibrium equations, compatibility equations, and constitutive equations. In linear elastic materials, the complexity of solving these problems largely depends on the concerned geometric boundary conditions and applied stress boundary conditions. Based on this, they can be broadly categorised into two groups in term of the types of potentials (Chou and Pagano, 2013; Saada, 1974):

(a) potentials related to displacements (by solving the Navier's equation), for example, the scalar and vector potentials, the Galerkin vectors, and the Neuber-Papkovich functions;

(b) potentials that generate systems of equilibrating stresses, namely, Maxwell's stress functions, the Morera's stress functions. In particular, when a plane problem with absence of body force is under consideration, these two stress potential methods will be particularised to the Airy's stress function.

Medium around the ellipse is assumed homogeneous and isotropic. With a small amount of deformation, the pressure-expansion response is characterised with a linear elastic model. By using this simplified model, the number of unknown variables is greatly reduced, and it is mainly determined by the boundary conditions. Specifically, if the stresses uniformly distribute along the axes directions of a simple rectangular or polar coordinates, the elastic problem usually can be reduced to be a one-dimensional problem even without need of assumptions on the stress/strain potentials, for example a cylindrical/spherical cavity deforms in a uniform stress field (Yu, 2000). Furthermore, when the initial stress field becomes not that uniform, some analytical solutions can also be obtained within the simple rectangular or polar coordinate system by properly setting the forms of stress/strain potentials, for example, the well-known Kirsch formulas. Many forms of displacement and stress functions corresponding to different typical types of boundary conditions were suggested in many treatises of elasticity theory (Chou and Pagano, 2013; Saada, 1974). More generally, when more types of geometry boundaries (for example ellipsoid, pyramid, triangles, ellipses, hyperbolas) are considered, the complexity of analytical analysis will dramatically increase. General approaches for three-dimensional analytical analysis are very rare, but some advanced analytical techniques for plane elastic problems were well developed, especially the methods based on the complex variable theory (Muskhelishvili, 1963). Sometimes, suitable curvilinear coordinate systems may be adequate to reduce the complexity caused by geometry variations in some special cases (Timoshenko and Goodier, 1970), but it is believed that the conformal mapping technique is a more powerful and efficient tool in dealing with the problem of geometric transformation. And its advantage will be more evident while being used in combination with the complex variable theory. Therefore, the complex potential method with the conformal mapping technique will be employed in this research, and they are briefly introduced as follows.

5.2.2.1 Kolosov-Muskhelishvili complex potentials

The complex variable theory provides a powerful theoretical tool in dealing with a broad class of two-dimensional boundary-value problems in elasticity (England, 2003). From its first systematic use in elasticity by Kolossof as early as 1909, this method experienced great developments and improvements in both theory and application, due greatly to a group of Russian mathematicians (Muskhelishvili, 1963; Savin, 1970; Sokolnikoff, 1956).

As known, stress components can be expressed by means of a stress function (Airy's stress function) in the plane theory of elasticity when no body forces are considered. The stress function satisfies the biharmonic equation ($\nabla^2\nabla^2 U = 0$), and it is biharmonic mathematically. The real and imaginary parts of an analytic function in complex variable theory also satisfy the Laplacian equation ($\nabla^2 U = 0$), and solutions of the Laplacian equation must be biharmonic. Meanwhile, the real and imaginary parts of an analytic function satisfy the Cauchy-Riemann condition. Based on these mathematical characteristics, it was found that the stress function can be generally represented by two analytic functions of one complex variable (as in Eq.(5-18)).

$$2U = \bar{z}\varphi(z) + z\overline{\varphi(z)} + \chi_1(z) + \overline{\chi_1(z)} \tag{5-18}$$

This is the well-known Goursat formula (found in 1898)(Sokolnikoff, 1956). The derivation process is not repeated here, and two different methods are available in the monograph of Muskhelishvili (1963). Based on relationships between the stress function and the stress components and the stress-strain relationships, the stress components and displacement components (free of body forces) can be represented by the first-order and second-order derivatives of these two analytic functions as

$$\sigma_x^e + \sigma_y^e = 4\,\mathrm{Re}[\Phi(z)] \tag{5-19}$$

$$\sigma_y^e - \sigma_x^e + 2i\tau_{xy}^e = 2[\bar{z}\Phi'(z) + \Psi(z)] \tag{5-20}$$

$$2G(u_x^e + iu_y^e) = [\chi\varphi(\mathrm{z}) - z\overline{\varphi'(\mathrm{z})} - \overline{\psi(\mathrm{z})}] \tag{5-21}$$

where σ_x^e , σ_y^e and τ_{xy}^e are elastic stress components, and u_x^e and u_y^e are elastic displacement components. $\Phi(z)$ and $\Psi(z)$ are usually referred to as the Kolosov-Muskhelishvili complex potentials. $z = x + iy$, $\bar{z} = x - iy$, $i = \sqrt{-1}$. $\varphi(\mathrm{z}) = \chi_1'(\mathrm{z})$, $\Phi(z) = \varphi'(\mathrm{z})$, $\Psi(z) = \psi'(\mathrm{z})$. $\chi = (3-v)/(1+v)$ for plane stress problem; $\chi = 3-4v$ for plane strain problem. G is elastic shear modulus, and v is Poisson's ratio.

Both stress boundary conditions and displacement boundary conditions can be readily represented by the Kolosov-Muskhelishvili complex potentials. Therefore, above relations can be directly applied to aforementioned three kinds of boundary-value problems. Based on the complexity of boundary conditions, different methods are required to derive the complex potentials. Three basic methods of solution are generally used, which include the series method of solution, the direct method of solution based on Cauchy integrals and the method based on stress and displacement continuation as summarised by England (2003). Moreover, above formulas also can be established by solving the govern equations with representations of displacement variables, which also demonstrates that there is no difference between the stress function method and displacement function method in this branch of elasticity theory. In addition, formulas with consideration of the body force (gravitational or centrifugal type) were given by Stevenson (1945), and expressions for an anisotropic medium refer to Savin (1970).

5.2.2.2 Conformal mapping

There is a single-valued transformation relation (as shown in Eq.(5-22)) which maps points of a region in the physical plane (z-plane) into points of a region in the phase plane (ζ -plane). The transformation between these two planes is one-to-one and invertible (corresponding inverse transformation $\zeta = \omega^{-1}(z)$), and it preserves angles locally. A conformal mapping relation will be built when these requirements are completely satisfied. More relevant discussions refer to the monograph of Muskhelishvili (1963) and England (2003).

$$z = x + iy = \omega(\zeta) \tag{5-22}$$

where $\zeta = \xi + i\eta = \rho e^{i\phi}$ describing the position vectors in the phase plane as shown in Fig. 5.8.

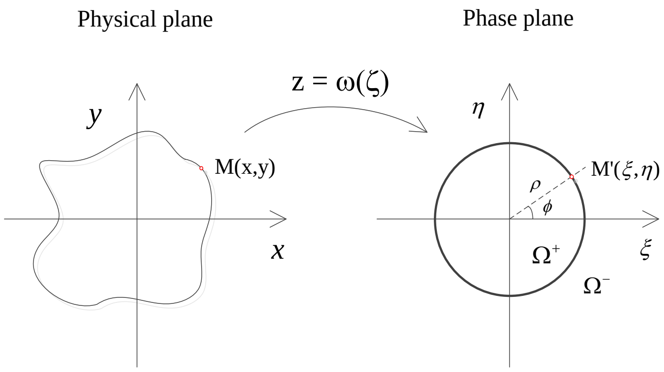

Fig. 5.8 Sketch of conformal mapping

As emphasised by England (2003), the usefulness of conformal transformations for these problems stems not only from the fact that they are a wide class of transformations, but also that they enable us to extend the basic complex variable formulation to the transformed problems. Hence, this technique is adopted in this research. Focusing on the problem of an infinite region with a simple contour inside, the conformal mapping technique is able to convert the region with a contour in various shapes in the physical plane to the region bounded by the unit circle with origin in the centre of the phase plane. Specifically, for the currently concerned cavity problem in an infinite plane, it is convenient to map the exterior of the hole in the physical plane onto the exterior region of the unit circle in the phase plane. Both of these two regions are infinite, and points at infinite are also related by the one-to-one correspondence. The general form of conformal mapping function for this problem is

$$\omega(\zeta) = \alpha'\zeta + \alpha'_0 + \sum_{n=1}^{\infty} \frac{\alpha'_n}{\zeta^n} \tag{5-23}$$

For an infinite plane with an elliptic hole, the conformal mapping function is well known as given in Eq.(5-24). As illustrated in Fig. 5.9, Eq.(5-24) is a function to conformally map the exterior of an elliptic cavity in the physical plane onto the exterior region of the unit circle ‘ γ ’ in the phase plane.

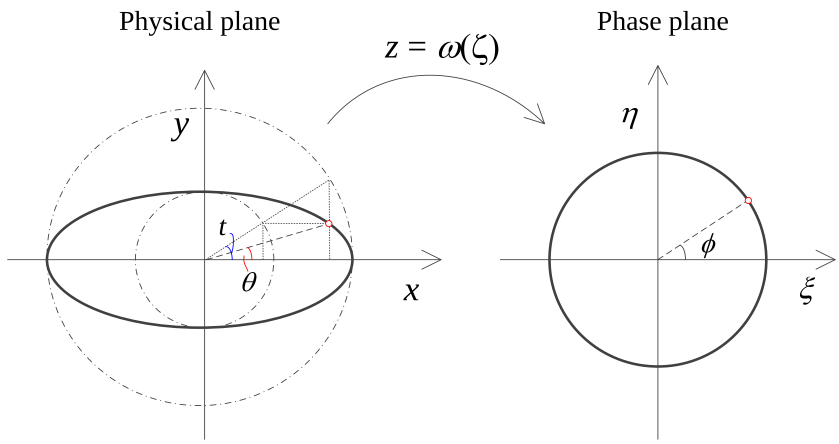

Fig. 5.9 Mapping function for an ellipse

$$z = x + iy = \omega(\zeta) = R(\zeta + \frac{m}{\zeta}) \tag{5-24}$$

where $R = \frac{a+b}{2}$, $m = \frac{a-b}{a+b}$. a and b is the semi-major and semi-minor of given ellipse respectively. By relating to the previously defined curvilinear coordinates, the corresponding positions of points in the phase plane and the physical plane can be linked with

$$x = x_0 + \rho\cos\vartheta = R(r + \frac{m}{r})\cos\phi \tag{5-25}$$

$$y = y_0 + \rho\sin\vartheta = R(r - \frac{m}{r})\sin\phi \tag{5-26}$$

5.2.2.3 Representation of boundary conditions

Both the stress and displacement boundary conditions can be expressed in terms of the Kolosov-Muskhelishvili complex potentials with the formulas from Eq.(5-19) to Eq.(5-21). Moreover, for convenience, the stress boundary conditions sometimes are dealt with in the form of Eq.(5-27).

$$f(x,y) = \frac{\partial U}{\partial x} + i\frac{\partial U}{\partial y} = \varphi(z) + z\overline{\varphi'(z)} + \overline{\psi(z)} \tag{5-27}$$

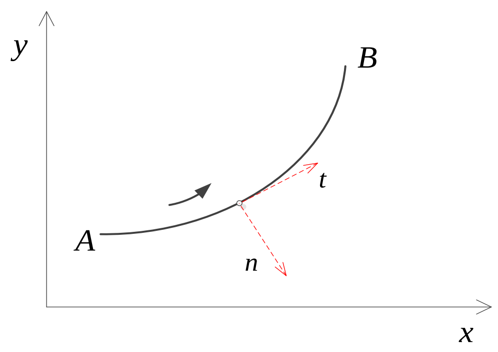

Fig. 5.10 Definition of positive directions

The mechanical definition of function $f(x,y)$ can be found by seeking the resultant stress vector applied on the concerned arc in the region occupied by the body. Specifically, we define an arbitrary arc $\widehat{\mathrm{AB}}$ in the concerned region, and its positive direction is set along the direction from point *A* to point *B*. The positive normal direction oriented to right when looking along the positive advancing direction of $\widehat{\mathrm{AB}}$. The concerned region is kept on its left side, which means that tensile stress is taking as positive. If the force $(X_n ds, Y_n ds)$ acts on one element 'ds' of the arc $\widehat{\mathrm{AB}}$ (*A* is a fixed point, and *B* is a movable point) from the side of positive normal, the function $f(x,y)$ can be expressed as

$$f(x,y) = i\int_{AB} (X_n + iY_n)ds + \text{const.} = i(X + iY) + \text{const.} \tag{5-28}$$

where X and Y represent components of the resultant stress vector in x-axis and y-axis directions respectively. Accordingly, the complex potentials are related to the stress boundary conditions.

Based on the determinacy analysis of these complex potentials within a given stress state and/or an admissible displacement field, the general forms of the Kolosov-Muskhelishvili for multiple-connected regions and single-connected regions were given by Muskhelishvili (1963). For addressing the currently concerned problem, the general solutions for an infinite plane with a single hole are followed here, which are

$$\varphi(\zeta) = \Gamma R\zeta - \frac{X + iY}{2\pi(1+\chi)}\ln\zeta + \varphi_0(\zeta) \tag{5-29}$$

$$\psi(\zeta) = \Gamma' R\zeta + \frac{\chi(X - iY)}{2\pi(1+\chi)}\ln\zeta + \psi_0(\zeta) \tag{5-30}$$

$$\Gamma = (N_1 + N_2)/4 \quad , \quad \Gamma' = -(N_1 - N_2)e^{-2i\Lambda}/2 \tag{5-31}$$

where N_1 and N_2 represent the principal stresses at infinity (tension for positive). Λ is the angle between N_1 and x-axis direction and takes the x-axis direction to the direction of N_1 of anticlockwise rotation as positive. $\varphi_0(\zeta)$ and $\psi_0(\zeta)$ are holomorphic in the whole concerned region.

5.2.2.4 Complex potentials for ellipse with different boundary conditions

Developments of elastic solutions for an elliptical cavity with different kinds of boundary conditions are briefly reviewed before the derivation. Elastic solutions for an infinite plate with an elliptical hole were first given by Kolosoff and Inglis (1913) around a century ago (Timoshenko and Goodier, 1970). The solution of Inglis (1913) provided a theoretical basis for the development of the famous Griffith's energy criterion (1921) in fracture mechanics. Stevenson (1945) independently carried out some two-dimensional analyses on similar problems in curvilinear coordinate systems later. The elliptic coordinate system and the complex variable theory were used in these solutions more or less, and judicious selection of the complex potentials is necessarily required and greatly determines the accuracy of these methods (Timoshenko and Goodier, 1970). Contrarily, a more powerful and general method was developed by deducing the potentials directly from the boundary conditions, as elaborated in the monograph of Muskhelishvili (1963). Based on the complex variable theory and some more advanced mathematic techniques, this branch of methods is not only capable of dealing with problems with complex stress boundary conditions but also can be extensively applied in analyses of cavities with various shapes. Overall, lots of analytical solutions for elastic analysis of the elliptical cavity problem in an infinite or a semi-infinite plane were developed over the past century, and they provided important and solid theoretical foundations in many areas, for example, analyses of crack propagation, calculation of stress redistribution/concentration (Atroshchenko, 2010; Maugis, 1992; Savin, 1970; Wu and Chang, 1978; Zhou et al., 2015).

5.2.2.4.1 An ellipse subjecting to given stress boundary conditions

The studied stress boundaries are depicted in Fig. 5.11. According to the superposition principle in linear elasticity, the concerned stress boundary conditions are studied separately for illustration.

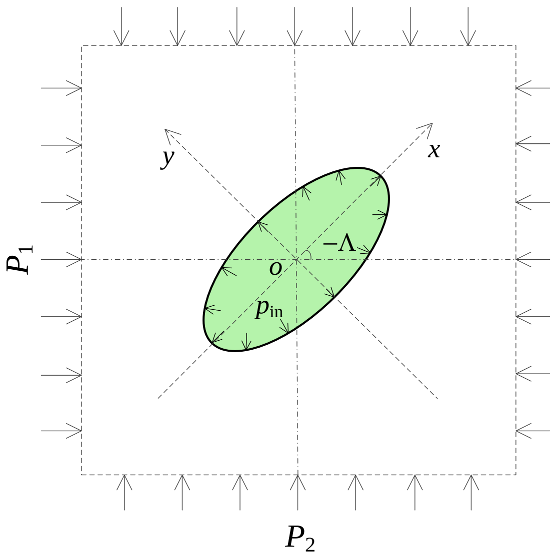

Fig. 5.11 Stress boundary conditions

(a) An ellipse with a uniform normal stress applying on the inner boundary

Taking this case as an example, application of the complex potential method to addressing the stress boundary-value problem of an infinite plane with an elliptical hole is illustrated by following with Muskhelishvili (1963).

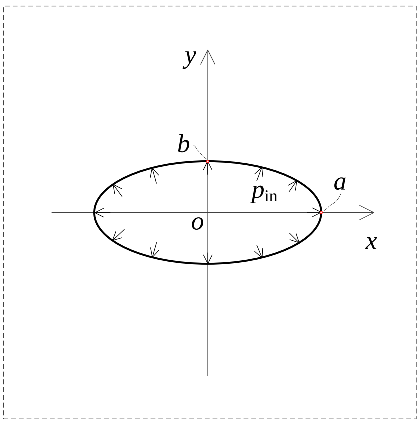

Fig. 5.12 Definition of stress boundary condition (case 1)

As defined in Fig. 5.12, no stress is applied at infinity, so $N_1 = N_2 = 0$. A uniform compression stress in the normal direction is applied on the whole contour 'L' (the elliptical cavity). Since $X_n = -p_{in}\sin(n,x)$, $Y_n = -p_{in}\sin(n,y)$, the stress boundary condition can be expressed by components as

$$(X_n + iY_n)ds = -p_{in}(d_y - id_x) = p_{in}id_z \qquad (5\text{-}32)$$

Subsequently, the stress boundary condition can be expressed as

$$f = i\int_{z_1}^{z_2}(X_n + iY_n)ds = -p_{in}z = -p_{in}R(\sigma + \frac{m}{\sigma}) \tag{5-33}$$

where 'σ' is a complex variable on the unit circle in the phase plane, which represents the boundary value of 'ζ'.

Based on the given general forms of complex potentials and properties of the holomorphic functions $\varphi_0(\zeta)$ and $\psi_0(\zeta)$, general expressions for the stress boundary and complex potentials of stress-boundary problem for the infinite plane with an elliptic hole were established by Muskhelishvili (1963) as

$$f_0 = f - \Gamma R[\sigma + \frac{\sigma^2 + m}{\sigma(1 - m\sigma^2)}] - \frac{\overline{\Gamma'}\mathrm{R}}{\sigma} + \frac{X + iY}{2\pi}\ln\sigma + \frac{X - iY}{2\pi(1+\chi)}\frac{\sigma^2 + m}{(1 - m\sigma^2)} \tag{5-34}$$

$$\varphi_0(\zeta) = -\frac{1}{2\pi i}\int_\gamma \frac{f_0}{\sigma - \zeta}d\sigma \tag{5-35}$$

$$\psi_0(\zeta) = -\frac{1}{2\pi i}\int_\gamma \frac{\overline{f_0}}{\sigma - \zeta}d\sigma - \zeta\frac{1 + m\zeta^2}{\zeta^2 - m}\varphi_0'(\zeta) \tag{5-36}$$

There is no stress or rotation at infinity, so $\Gamma = \overline{\Gamma'} = 0$. The resultant stresses (X, Y) of the uniformly applied normal stress on the whole cavity wall is equal to zero because the stress boundary at cavity wall is continuous and single-valued. The complex potentials were given by Muskhelishvili (1963) as

$$\varphi_1^e(\zeta) = -\frac{mRp_{in}}{\zeta} \tag{5-37}$$

$$\psi_1^e(\zeta) = -\frac{Rp_{in}}{\zeta} - \frac{mRp_{in}}{\zeta}\cdot\frac{1 + m\zeta^2}{\zeta^2 - m} \tag{5-38}$$

(b) An ellipse with non-equal biaxial far-field stresses

In this case, biaxial compression stresses (P_1 and P_2) are applied at infinity (far away from the cavity comparing with the cavity size), and the semi-major axis direction of the ellipse takes a clockwise angle Λ to the direction of the principal stress P_1.

$$X_n = Y_n = 0 \quad \text{(at inner cavity wall)} \tag{5-39}$$

$$\Gamma = -(P_1 + P_2)/4 \quad , \quad \Gamma' = (P_1 - P_2)e^{-2i\Lambda}/2 \quad \text{(at infinity)} \tag{5-40}$$

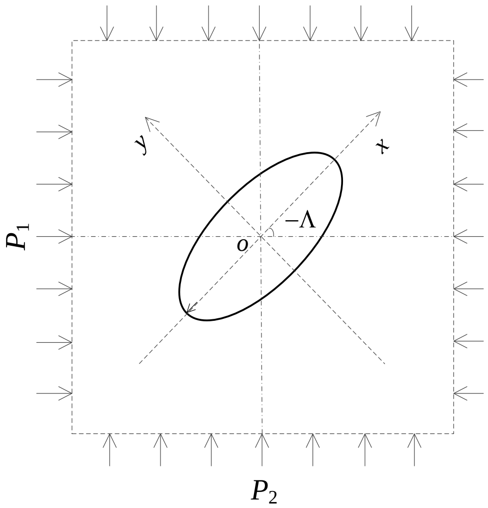

Fig. 5.13 Definition of stress boundary condition (case 2)

The solution can be found with the same procedure as above. It also can be solved by superposing the well-known solution for the problem of 'a stretched plate weaken by an unstressed elliptical hole' which is widely available in many treatises (Muskhelishvili, 1963; Savin, 1970; Sokolnikoff, 1956; Timoshenko and Goodier, 1970). The complex potentials are

$$\varphi_2^e(\zeta) = -\frac{R}{4}[(P_1+P_2)(\zeta-\frac{m}{\zeta})+2(P_1-P_2)\frac{e^{2i\Lambda}}{\zeta}] \tag{5-41}$$

$$\psi_2^e(\zeta) = \frac{R}{2}\left\{(P_1-P_2)(e^{-2i\Lambda}\zeta+\frac{e^{2i\Lambda}}{m\zeta})-\frac{(1+m^2)[(P_1-P_2)e^{2i\Lambda}-(P_1+P_2)m]}{m}\frac{\zeta}{(\zeta^2-m)}\right\} \tag{5-42}$$

Based on the superposition principle in linear elasticity, the resultant complex potentials for the problem defined in Fig. 5.11 are

$$\varphi^e(\zeta) = \varphi_1^e(\zeta)+\varphi_2^e(\zeta) \tag{5-43}$$

$$\psi^e(\zeta) = \psi_1^e(\zeta)+\psi_2^e(\zeta) \tag{5-44}$$

5.2.2.4.2 An ellipse deforms with given inner displacements

1. Inner displacement boundary conditions

The displacement boundary condition consists of two basic parameters which are the magnitude and the direction of movement of each point. The initial ellipse is described with known semi-major axis length a_0 and semi-minor axis length b_0 as

$$\frac{x_0^{\ 2}}{a_0^{\ 2}}+\frac{y_0^{\ 2}}{b_0^{\ 2}}=1 \tag{5-45}$$

It is assumed that the cavity after deformation is still in an elliptic shape, and its axes directions coincide with the initial ellipse. So the geometry of the deformed cavity can be expressed as

$$\frac{x_1^{\ 2}}{a_1^{\ 2}}+\frac{y_1^{\ 2}}{b_1^{\ 2}}=1 \tag{5-46}$$

(1) Inner boundary displacements being normal to the initial surface (the first displacement-controlled solution)

In this case, it is assumed that points on the inner ellipse move outwards in the direction perpendicular to the initial cavity wall, and the magnitude of boundary displacements is determined by the given initial and final position of the cavity. As illustrated in Fig. 5.14, apart from the assumed inner displacement boundary condition, non-equal biaxial stresses are applied at infinity. For convenience, a combination use of the Cartesian coordinate system and the orthogonal curvilinear coordinates defined in Section 5.2.1 is adopted in this analysis.

$$x=x_0+\rho\cos\vartheta \quad , \quad y=y_0+\rho\sin\vartheta \tag{5-47}$$

where x_0 and y_0 are given in Eq.(5-9).

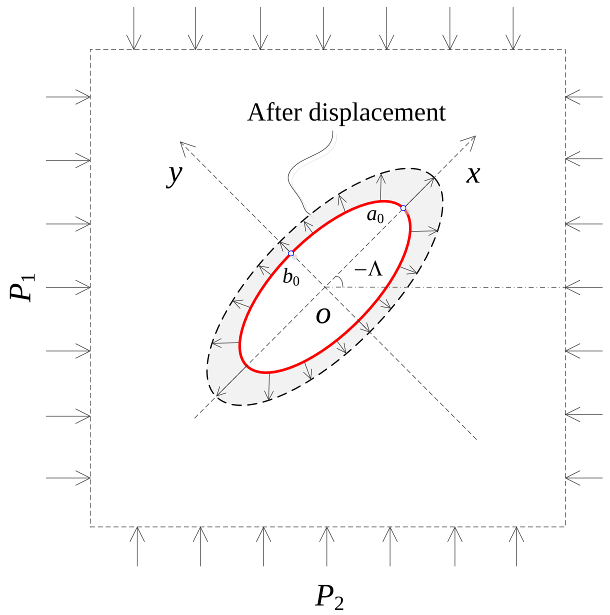

Fig. 5.14 Schematic diagram of the boundary conditions (case 1)

The displacement components can be obtained with

$$u_x^e + iu_y^e = \rho(\vartheta)\cos\vartheta + i\rho(\vartheta)\sin\vartheta = \rho(\vartheta)e^{i\vartheta} \tag{5-48}$$

In the orthogonal parallel-elliptical coordinates, the normal distance ($\rho(\vartheta)$) from the initial cavity rim to the ellipse after deformation varies with angle because the deformed ellipse circumference does not parallel to the original ellipse. It can be obtained by solving Eq.(5-47) and Eq.(5-46).

$$\rho(\vartheta) = \frac{\begin{bmatrix} -(x_0 b_1^2\cos\vartheta + y_0 a_1^2\sin\vartheta) + \\ \sqrt{(x_0 b_1^2\cos\vartheta + y_0 a_1^2\sin\vartheta)^2 - (a_1^2\sin^2\vartheta + b_1^2\cos^2\vartheta)(x_0^2 b_1^2 + y_0^2 a_1^2 - a_1^2 b_1^2)} \end{bmatrix}}{(a_1^2\sin^2\vartheta + b_1^2\cos^2\vartheta)} \tag{5-49}$$

As given in Eq.(5-21), the relation between the complex potentials and the displacement boundary is rewritten as

$$2Gg(x,y) = 2G(u_x^e + iu_y^e)\Big|_\gamma = \chi\varphi(\sigma) - \frac{\omega(\sigma)}{\overline{\omega'(\sigma)}}\overline{\varphi'(\sigma)} - \overline{\psi(\sigma)} \tag{5-50}$$

To transform the displacement boundary in Eq.(5-48) which in terms of ϑ to the phase plane, ϑ is related to the argument ϕ of the phase plane on the basis of Eq.(5-25) and Eq.(5-26).

$$\tan\vartheta = \frac{a_0^2(1-m)}{b_0^2(1+m)}\tan\phi \tag{5-51}$$

All the trigonometric function can be expressed with above tangent function, so Eq.(5-48) becomes a function of the variable of argument ϕ. The resultant displacement boundary function $g(\phi)$ is continuous in the range of $0 \le \phi \le 2\pi$ along the circumference of the unit circle γ in the phase plane and satisfies the Dirichlet conditions. Therefore, it is convenient to re-express it based on the expansion of Fourier series in terms of σ ($\sigma = e^{i\phi}$) (Muskhelishvili, 1963; Zhou et al., 2015). The series-type representation is

$$g(\phi) = g_1(\phi) + ig_2(\phi) = u_x^e + iu_y^e = \sum_{-\infty}^{+\infty} A_n e^{in\phi} = \sum_{-\infty}^{+\infty} A_n\sigma^n = \sum_{n=1}^{+\infty}\frac{A_{-n}}{\sigma^n} + A_0 + \sum_{n=1}^{+\infty} A_n\sigma^n$$

$$(n = 1,2,3,\cdots) \tag{5-52}$$

where $A_n = \dfrac{1}{2\pi}\int_0^{2\pi}[g_1(\phi)+ig_2(\phi)]e^{-in\phi}d\phi$ which are the coefficients of the Fourier series. $g_1(\phi)$ is an even function, and $g_2(\phi)$ is an odd function. Consequently, A_n are real numbers based on the property of Fourier series. Furthermore, based on the consistency requirement of Eq.(5-48) and Eq.(5-52) in parity with respect to the variable of σ, it can be concluded that the even terms of the Fourier series in Eq.(5-52) should equal to zero. So $g(\phi)$ can be simplified to

$$g(\phi)=\sum_{n=1}^{+\infty}\frac{A_{-(2n-1)}}{\sigma^{2n-1}}+\sum_{n=1}^{+\infty}A_{2n-1}\sigma^{2n-1} \tag{5-53}$$

- **Special case:** Points of the cavity deform with the same normal displacements

In this special case, points on the initial cavity wall move outwards in the normal direction with the same distance. In another word, a constant value of ρ is assumed. So the boundary condition becomes

$$u_x^e+iu_y^e=\rho\cos\vartheta+i\rho\sin\vartheta=\rho e^{i\vartheta} \qquad (\rho=\text{const.}) \tag{5-54}$$

The same procedure can be followed as above to transform this boundary condition to Fourier series, and the same form of representation as Eq.(5-53) can be obtained but with different coefficients.

(2) Inner boundary displacements pointing outwards from the centre of the initial ellipse (the second displacement-controlled solution)

In this case, the points on the initial ellipse move outwards along the radial direction of the cylindrical coordinate system. Therefore, a combination use of the Cartesian coordinate system and the cylindrical coordinate system is adopted in this analysis. Similarly, the coordinate positions can be expressed in terms of the centre angle θ as

$$x=x_0+l\cos\theta \quad , \quad y=y_0+l\sin\theta \tag{5-55}$$

where $x_0=ab\cos\theta\big/\sqrt{T}$, $y_0=ab\sin\theta\big/\sqrt{T}$ $(T=b^2\cos^2\theta+a^2\sin^2\theta)$. l represents the distance from one given point to the corresponding point on the inner ellipse along the radial axis direction.

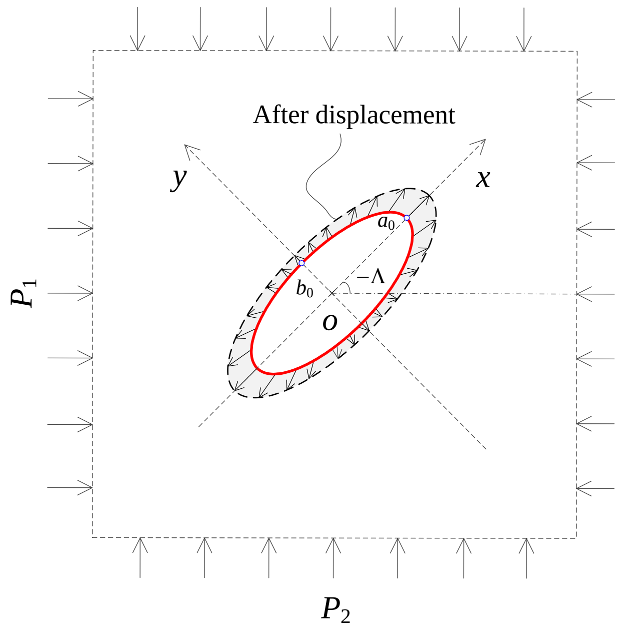

Fig. 5.15 Schematic diagram of the boundary conditions (case 2)

Subsequently, the given boundary conditions can be expressed as

$$u_x^e + iu_y^e = l(\theta)\cos\theta + il(\theta)\sin\theta = l(\theta)e^{i\theta} \tag{5-56}$$

And, similarly

$$l(\theta) = \frac{\begin{bmatrix} -(x_0 b_1^2\cos\theta + y_0 a_1^2\sin\theta) \\ +\sqrt{(x_0 b_1^2\cos\theta + y_0 a_1^2\sin\theta)^2 - (a_1^2\sin^2\theta + b_1^2\cos^2\theta)(x_0^2 b_1^2 + y_0^2 a_1^2 - a_1^2 b_1^2)} \end{bmatrix}}{(a_1^2\sin^2\theta + b_1^2\cos^2\theta)} \tag{5-57}$$

Then the centre angle is related to the variable ϕ belonging to the phase plane with

$$\tan\theta = \frac{(1-m)}{(1+m)}\tan\phi \tag{5-58}$$

Then following the same procedure, the displacement boundary conditions can be expressed in the same form as Eq.(5-53) with different coefficients.

2. Far-field stress boundary conditions

Biaxial compression stresses (P_1 and P_2) are applied at infinity (far away from the cavity comparing with the cavity size), and the semi-major axis direction of the ellipse takes a clockwise angle Λ to the direction of the principal stress P_1.

$$\Gamma = -(P_1 + P_2)/4 \quad , \quad \Gamma' = (P_1 - P_2)e^{-2i\Lambda}/2 \qquad \text{(at infinity)} \tag{5-59}$$

3. Derivation of the complex potentials

To represent the given type of displacement boundary conditions in terms of the complex potentials, Eq.(5-21) is rewritten as

$$2Gg(x,y)=2G(g_1+ig_2)=\chi\varphi(\zeta)-\frac{\omega(\zeta)}{\omega'(\zeta)}\overline{\varphi'(\zeta)}-\overline{\psi(\zeta)} \tag{5-60}$$

With this representation and general forms of $\varphi(\zeta)$ and $\psi(\zeta)$ (Eq.(5-29) and Eq.(5-30)), Muskhelishvili (1963) gave the general representations for the complex potentials with the displacement-type boundary conditions for the problem of an elliptic hole in an infinite plane.

$$\varphi_0(\zeta)=-\frac{2G}{\chi}\frac{1}{2\pi i}\int_\gamma\frac{g}{\sigma-\zeta}d\sigma+(m\Gamma+\bar{\Gamma}')\frac{R}{\chi\zeta} \tag{5-61}$$

$$\psi_0(\zeta)=\frac{G}{\pi i}\int_\gamma\frac{\bar{g}}{\sigma-\zeta}d\sigma+\Gamma R(\frac{\chi}{\zeta}-\zeta\frac{1+m^2}{\zeta^2-m})+\frac{X+iY}{2\pi(1+\chi)}\frac{1+m^2}{(\zeta^2-m)}-\zeta\frac{1+m\zeta^2}{\zeta^2-m}\varphi_0{}'(\zeta)+\psi_0{}'(\infty) \tag{5-62}$$

$$\psi_0(\infty)=-\frac{G}{\pi i}\int_\gamma\frac{\bar{g}_0}{\sigma}d\sigma=-\frac{G}{\pi i}\int_\gamma\frac{\bar{g}}{\sigma}d\sigma+\frac{m(X+iY)}{2\pi(1+\chi)} \tag{5-63}$$

Based on these formulas and the given boundary conditions, complex potentials for the defined problem can be obtained by using the Cauchy integral method.

$$\varphi_0(\zeta)=\frac{2G}{\chi}\sum_{n=1}^{+\infty}\frac{A_{-(2n-1)}}{\zeta^{2n-1}}+[-m\frac{(P_1+P_2)}{4}+\frac{(P_1-P_2)e^{2i\Lambda}}{2})\frac{R}{\chi\zeta} \tag{5-64}$$

$$\begin{aligned}\psi_0(\zeta)=&-2G\sum_{n=1}^{+\infty}\frac{\bar{A}_{2n-1}}{\zeta^{2n-1}}+R\frac{(P_1+P_2)}{4}(\frac{\chi}{\zeta}-\zeta\frac{1+m^2}{\zeta^2-m})\\&-\zeta\frac{1+m\zeta^2}{\zeta^2-m}\left\{-\frac{2G}{\chi}\sum_{n=1}^{+\infty}(2n-1)\frac{A_{-(2n-1)}}{\zeta^{2n}}+[m\frac{(P_1+P_2)}{4}-\frac{(P_1-P_2)e^{2i\Lambda}}{2}]\frac{R}{\chi\zeta^2}\right\}\end{aligned} \tag{5-65}$$

$$\varphi(\zeta)=-\frac{(P_1+P_2)}{4}R\zeta+\frac{2G}{\chi}\sum_{n=1}^{+\infty}\frac{A_{-(2n-1)}}{\zeta^{2n-1}}+[-m\frac{(P_1+P_2)}{4}+\frac{(P_1-P_2)e^{2i\Lambda}}{2})\frac{R}{\chi\zeta} \tag{5-66}$$

$$\begin{aligned}\psi(\zeta)=&\frac{(P_1-P_2)e^{-2i\Lambda}}{2}R\zeta-2G\sum_{n=1}^{+\infty}\frac{\bar{A}_{2n-1}}{\zeta^{2n-1}}+R\frac{(P_1+P_2)}{4}(\frac{\chi}{\zeta}-\zeta\frac{1+m^2}{\zeta^2-m})\\&-\zeta\frac{1+m\zeta^2}{\zeta^2-m}\left\{-\frac{2G}{\chi}\sum_{n=1}^{+\infty}(2n-1)\frac{A_{-(2n-1)}}{\zeta^{2n}}+[m\frac{(P_1+P_2)}{4}-\frac{(P_1-P_2)e^{2i\Lambda}}{2}]\frac{R}{\chi\zeta^2}\right\}\end{aligned} \tag{5-67}$$

5.2.2.5 Formulas for stress and displacement components

By expressing the formulas from Eq.(5-19) to Eq.(5-21) in terms of ζ, the stress and displacement components can be expressed with

$$\sigma_x^e + \sigma_y^e = 4\,\mathrm{Re}[\Phi(\zeta)] \tag{5-68}$$

$$\sigma_y^e - \sigma_x^e + 2i\tau_{xy}^e = 2[\frac{\overline{\omega(\zeta)}}{\omega'(\zeta)}\Phi'(\zeta) + \Psi(\zeta)] \tag{5-69}$$

$$2G(u_x^e + iu_y^e) = [\chi\varphi(\zeta) - \frac{\omega(\zeta)}{\overline{\omega'(\zeta)}}\overline{\varphi'(\zeta)} - \overline{\psi(\zeta)}] \tag{5-70}$$

where $\Phi(\zeta) = \dfrac{\varphi'(\zeta)}{\omega'(\zeta)}$, $\Psi(\zeta) = \dfrac{\psi'(\zeta)}{\omega'(\zeta)}$.

Points between the physical plane and the phase plane can be correspondingly related by Eq.(5-25) and Eq.(5-26). In addition, based on the mapping function, required functions in the above representations are obtained as

$$\overline{\omega(\zeta)} = \bar{\omega}(\bar{\zeta}) = R(\bar{\zeta} + \frac{m}{\zeta}) = R(\frac{\rho^2}{\zeta} + \frac{m\zeta}{\rho^2}),\ \omega'(\xi) = R(1 - \frac{m}{\zeta^2}),\ \overline{\omega'(\zeta)} = R(1 - \frac{m\zeta^2}{\rho^4})$$

where $\zeta \cdot \bar{\zeta} = \rho^2$ in the phase plane ($\bar{\zeta}$ is the conjugate complex of ζ).

5.2.3 Results analysis

For application to the root-tip growth model, elastic solutions with different types of boundary conditions have been presented in the above part. The first type of solution assumes that a uniform internal pressure is applied on the inner boundary, so the cavity deforms in a pressure-controlled manner. The second type of solutions is for displacement-controlled ellipses which deform with given boundary displacements. They will be validated by comparing with some other available solutions first in this section, and their performances will be briefly discussed at the end.

5.2.3.1 Comparison with solution for pressure-controlled circular cavity

With the stress boundary conditions defined in Fig. 5.11, the stress and displacement fields around a circular cavity also can be obtained with the conventional potential-based method. Specifically, the influence of far-field stress boundary conditions can be calculated with the Kirsch (1898) equations, and the uniform pressure applied on the cavity wall can be easily taken into account by solving the equilibrium equation and compatibility equation. Solutions given by Yu (2000) for this problem are followed as shown in Eq.(5-71)- Eq.(5-75).

$$\sigma_r = P_\infty(1-\frac{R_0^{\ 2}}{r^2}) - \tau_\infty(1+\frac{3R_0^{\ 4}}{r^4} - \frac{4R_0^{\ 2}}{r^2})\cos 2\theta - p_{in}\frac{R_0^{\ 2}}{r^2} \tag{5-71}$$

$$\sigma_\theta = P_\infty(1+\frac{R_0^{\ 2}}{r^2}) + \tau_\infty(1+\frac{3R_0^{\ 4}}{r^4})\cos 2\theta + p_{in}\frac{R_0^{\ 2}}{r^2} \tag{5-72}$$

$$\tau_{r\theta} = \tau_\infty(1-\frac{3R_0^{\ 4}}{r^4} + \frac{2R_0^{\ 2}}{r^2})\sin 2\theta \tag{5-73}$$

$$\begin{aligned} u_r = &\frac{1-\nu}{2G}\left[P_\infty(r-\frac{R_0^{\ 2}}{r}) - \tau_\infty(r-\frac{R_0^{\ 4}}{r^3} - + \frac{4R_0^{\ 2}}{r})\cos 2\theta\right] \\ &-\frac{\nu}{2G}\left[P_\infty(r-\frac{R_0^{\ 2}}{r}) + \tau_\infty(r-\frac{R_0^{\ 4}}{r^3})\cos 2\theta\right] + \frac{p_{in}R_0^{\ 2}}{2Gr} \end{aligned} \tag{5-74}$$

$$u_\theta = \frac{\tau_\infty}{2G}\left[(1-\nu)(r+\frac{2R_0^{\ 2}}{r}+\frac{R_0^{\ 4}}{r^3}) + \nu(r-\frac{2R_0^{\ 2}}{r}+\frac{R_0^{\ 4}}{r^3})\right]\sin 2\theta \tag{5-75}$$

with $P_\infty = (\sigma_y|_{y\to\infty} + \sigma_x|_{x\to\infty})/2 = -(P_1+P_2)/2$, $\tau_\infty = (\sigma_y|_{y\to\infty} - \sigma_x|_{x\to\infty})/2 = (P_1-P_2)/2$.

In fact, the presented pressure-controlled solution for elliptical cavity has been commonly accepted in elasticity theory (Muskhelishvili, 1963; Savin, 1970; Sokolnikoff, 1956; Timoshenko and Goodier, 1970). So the comparison with above solution for a circular cavity ($a = b = R_0$) is just to double-check and validate the employed calculation method. It is shown in Fig. 5.16 that the stress and displacement results computed with these two solutions are exactly the same in this case.

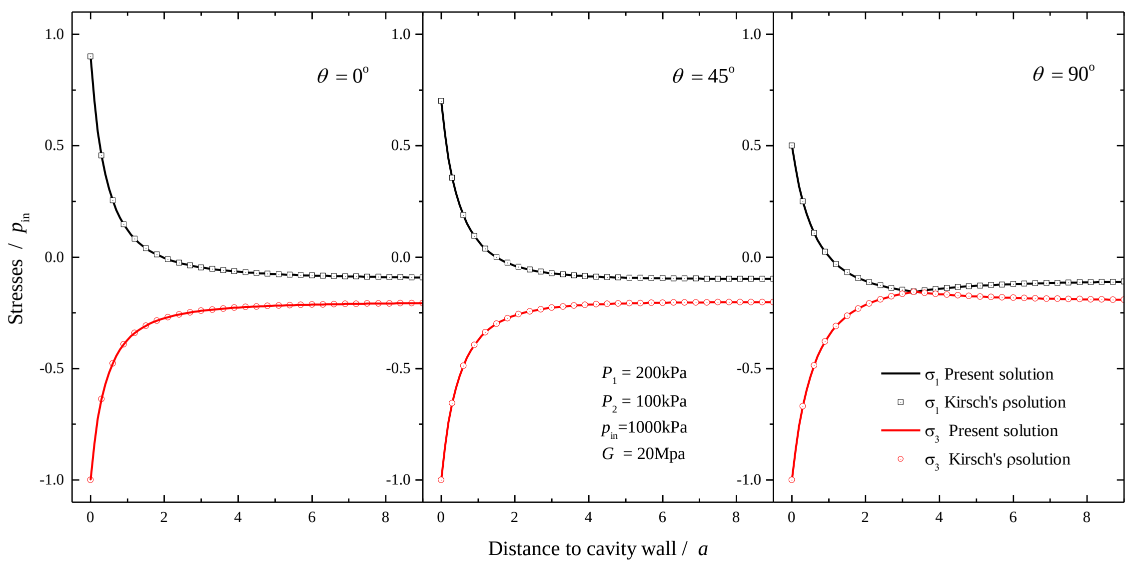

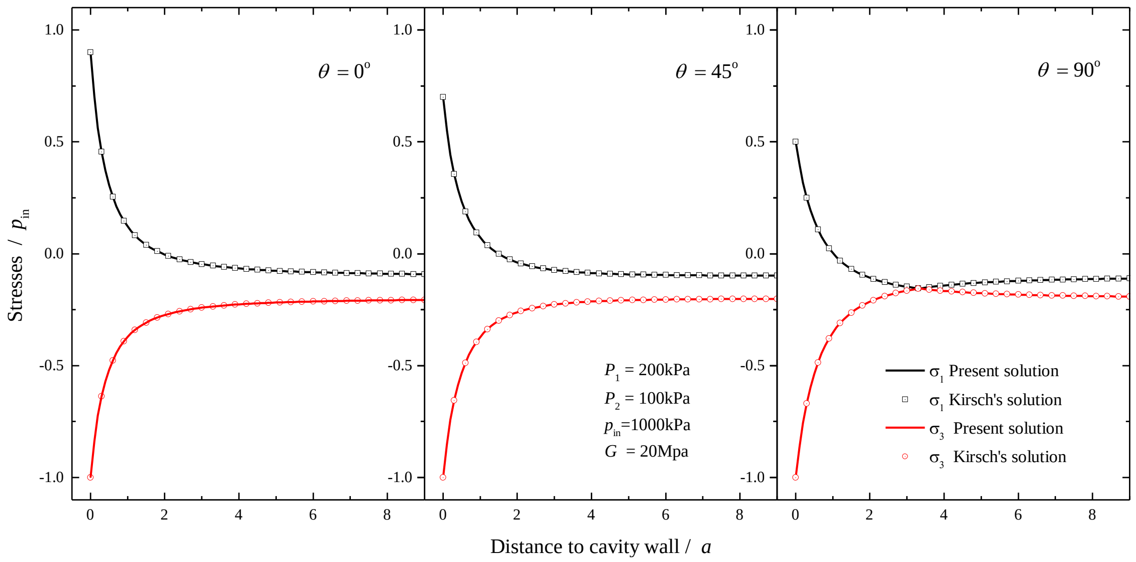

Fig. 5.16 Validation of the pressure-controlled solutions (for a circular cavity)

5.2.3.2 Validation of solutions for the displacement-controlled ellipse

(1) Comparison with the solution for a flat cavity

The first displacement-controlled solution for an ellipse (boundary displacement normal to the initial cavity wall) is validated with the solution proposed by Zhou et al. (2015). Their solution was designed for a flat elliptic cavity undergoing small displacements in the direction parallel to one coordinate axis, and the given final shape of the inner cavity is still in an elliptic shape. The boundary condition is defined in Eq.(5-76). In fact, the defined moving directions of boundary points in this solution are not exactly the same as that in present solution in general cases, but it is anticipated that they could give approximately the same results when the ellipse is very flat. As illustrated in Fig. 5.17, the normal directions of the inner flat ellipse are almost parallel to the axis direction in a large angular scope.

$$u_x^e + iu_y^e\Big|_\gamma = \frac{-ia(b-b_0)\sin\phi}{\sqrt{\beta^2 b_0{}^2 + (a^2 - \beta^2 b_0{}^2)\sin^2\phi}} \tag{5-76}$$

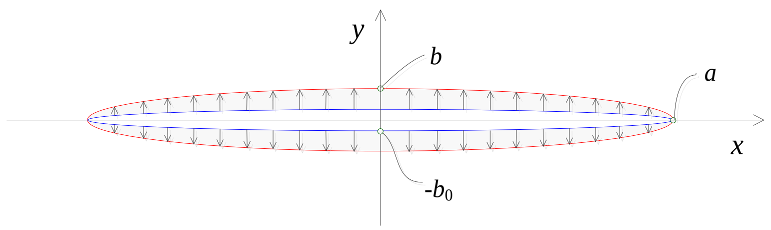

Fig. 5.17 Normal directions of points on a flat cavity

Taking the elastic modulus as 15MPa and Poisson's ratio as 0.5, comparisons of these two solutions are carried out as shown in Fig. 5.18. With the given geometry parameters, the normal direction of the inner flat ellipse just rotated 1° away from the direction of y-axis even when $x_0 = 0.9927a$. Not surprisingly, these two solutions gave almost the same results in a wide range as demonstrated in Fig. 5.18. This comparison well corroborated our first displacement-controlled solution.

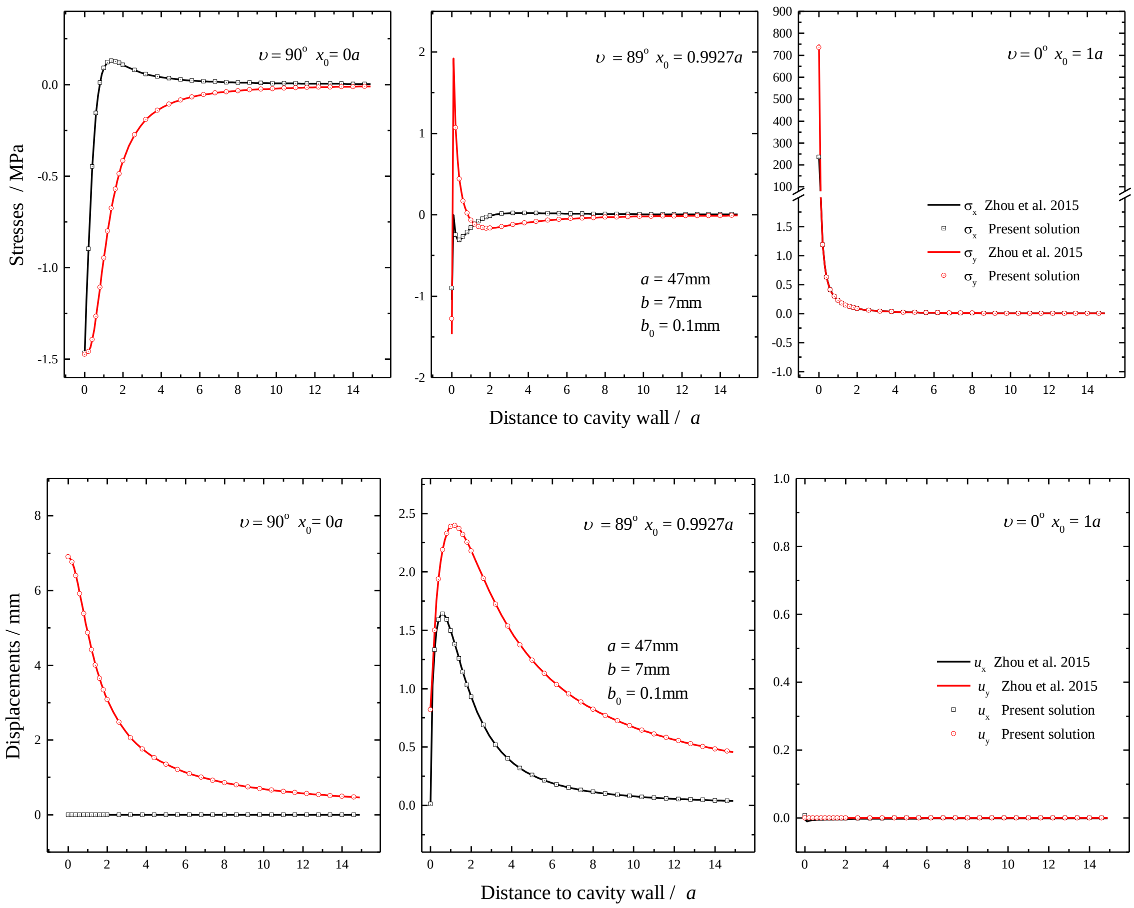

Fig. 5.18 Validation of the solution with displacement boundary

(2) Comparison with solution for circular cavity

With axisymmetric stress and geometry conditions, the pressure-type and displacement-type boundary conditions will lead to the same expansion process in linear elastic materials. In other words, providing that the initial and final shapes of the inner cavity are both circular ($a_0 = b_0 = R_0$) and the far-field stress conditions are hydrostatic, the presented displacement-controlled solutions can give the same results as the conventional stress-controlled solution, and the first and the second displacement-controlled solution will become the same in this case. The conventional elastic stress and displacement solution are followed by Yu (2000) as given in Eq.(5-77) to Eq.(5-79). As demonstrated in Fig. 5.19, results calculated with these three solutions agree well within the aforementioned conditions.

$$\sigma_r = -P_\infty - (p_{in} - P_\infty)\frac{R_0^{\ 2}}{r^2} \tag{5-77}$$

$$\sigma_\theta = -P_\infty + (p_{in} - P_\infty)\frac{R_0^{\ 2}}{r^2} \tag{5-78}$$

$$u_r = \frac{-(p_{in} - P_\infty)}{2G}\frac{R_0^{\ 2}}{r}r \tag{5-79}$$

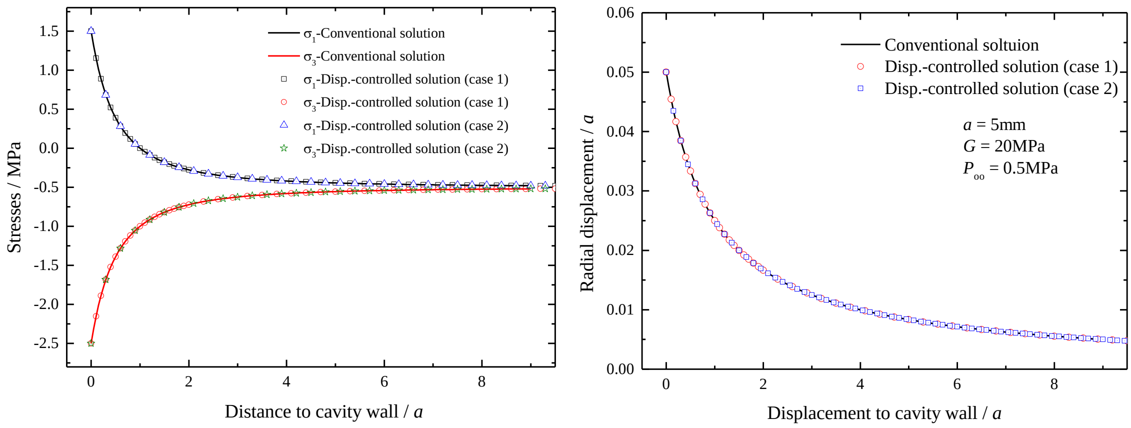

Fig. 5.19 Comparison with conventional solution for circular cavity

5.2.3.2 Stress and displacement fields around ellipses with given stress boundaries

The stress and displacement fields around ellipses with varying axis ratios are calculated with the presented solutions as shown in Fig. 5.20 to Fig. 5.24. The individual influence of the far-field stresses on the stress and displacement fields around an ellipse were elaborated by Maugis (1992), so the present calculations mainly focused on the influence of the internal pressure alone and their combination effects respectively. Lengths of the displacement vectors are magnified 10 times to more clearly illustrate the displacement fields.

(1) Ellipses only under internal pressure

The principal stress fields around ellipses with different axis ratios are given in Fig. 5.20, and corresponding displacement fields are shown in Fig. 5.21. In these calculations, the material properties and stress boundaries were set as: $p_{in}/G = 1/20$, Poisson's ratio $\nu = 0.4$.

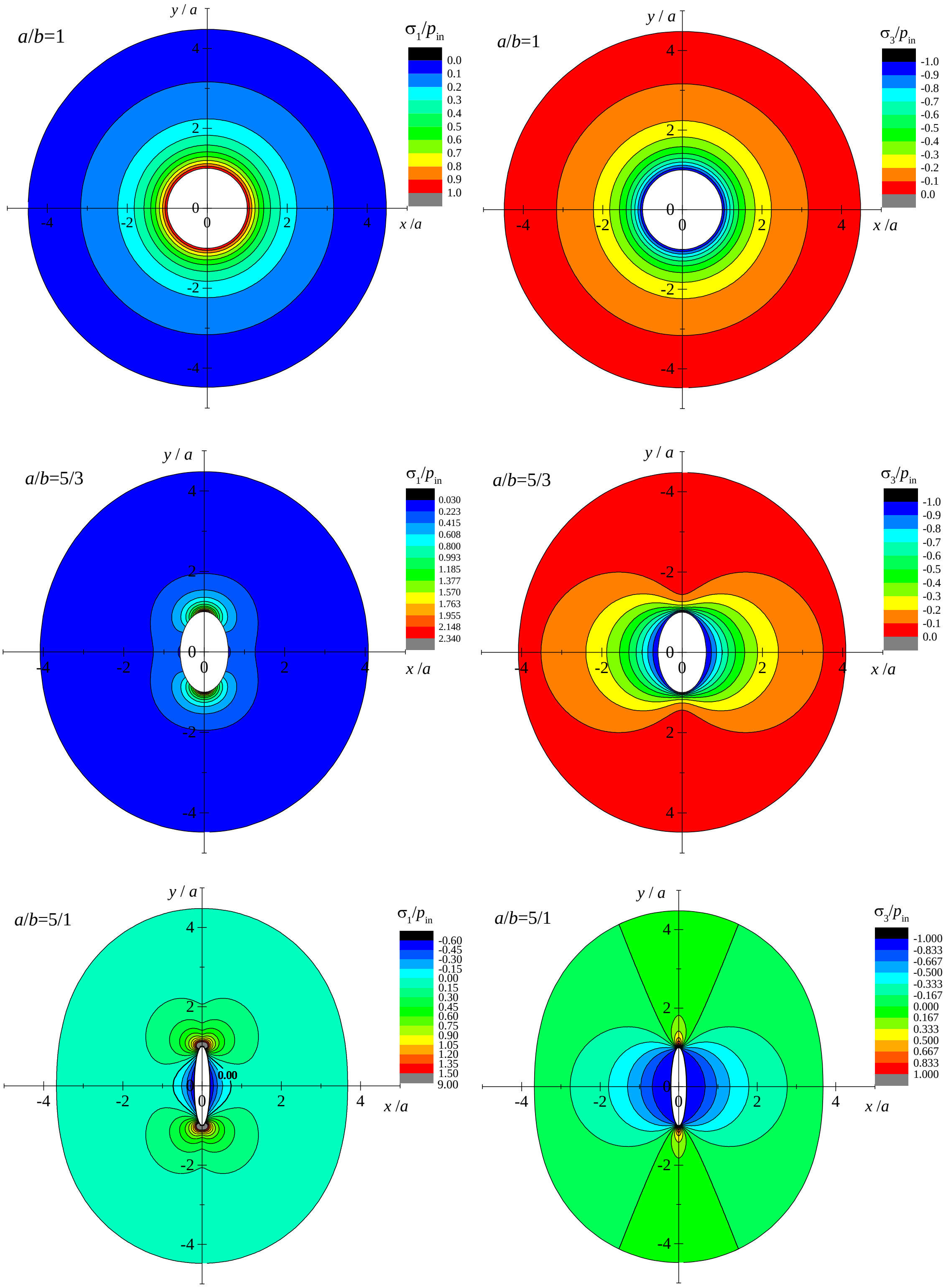

Fig. 5.20 Stress fields around ellipses with varying axial ratios

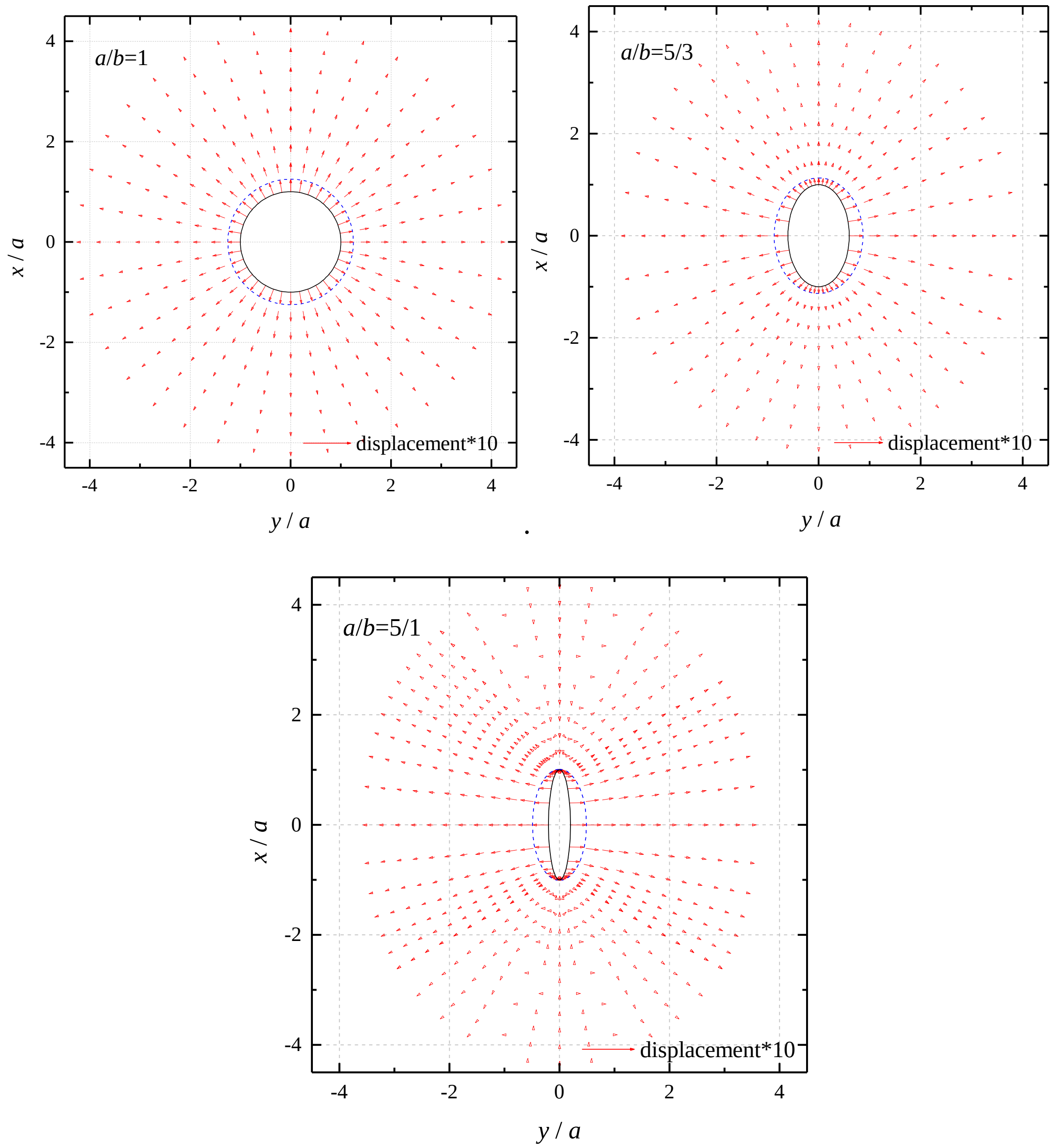

Fig. 5.21 Displacement fields around ellipses with varying axial ratios

Subjecting to a uniform internal pressure, the stress and displacement fields are axisymmetric while the inner cavity is in a circular shape. However, with increases of the axis ratio of the ellipse, the axial symmetry would fade away and stress concentrations appear and get intensified around vertices of the major axis instead. Even tensile regions will be formed around the vertices of the major axis under uniform compression pressure, for example, in the case of an ellipse with $a/b = 5/1$ (like a tearing crack). Additionally, directions of the displacements gradually turn towards the direction of the minor axis with increases of the axis ratio (a/b), and displacements at vertices of the minor axis are always the largest in length.

(2) Ellipses with combination effect of the internal pressure and far-field stresses

With the same amount of internal pressure, redistributions of stress and displacement fields caused by the changes of far-field stresses are presented in Fig. 5.22 and Fig. 5.23. The results are calculated by taking ellipses of $a/b=5/3$ as example. Stress boundary conditions are given in the graphs, and material properties are the same as given above.

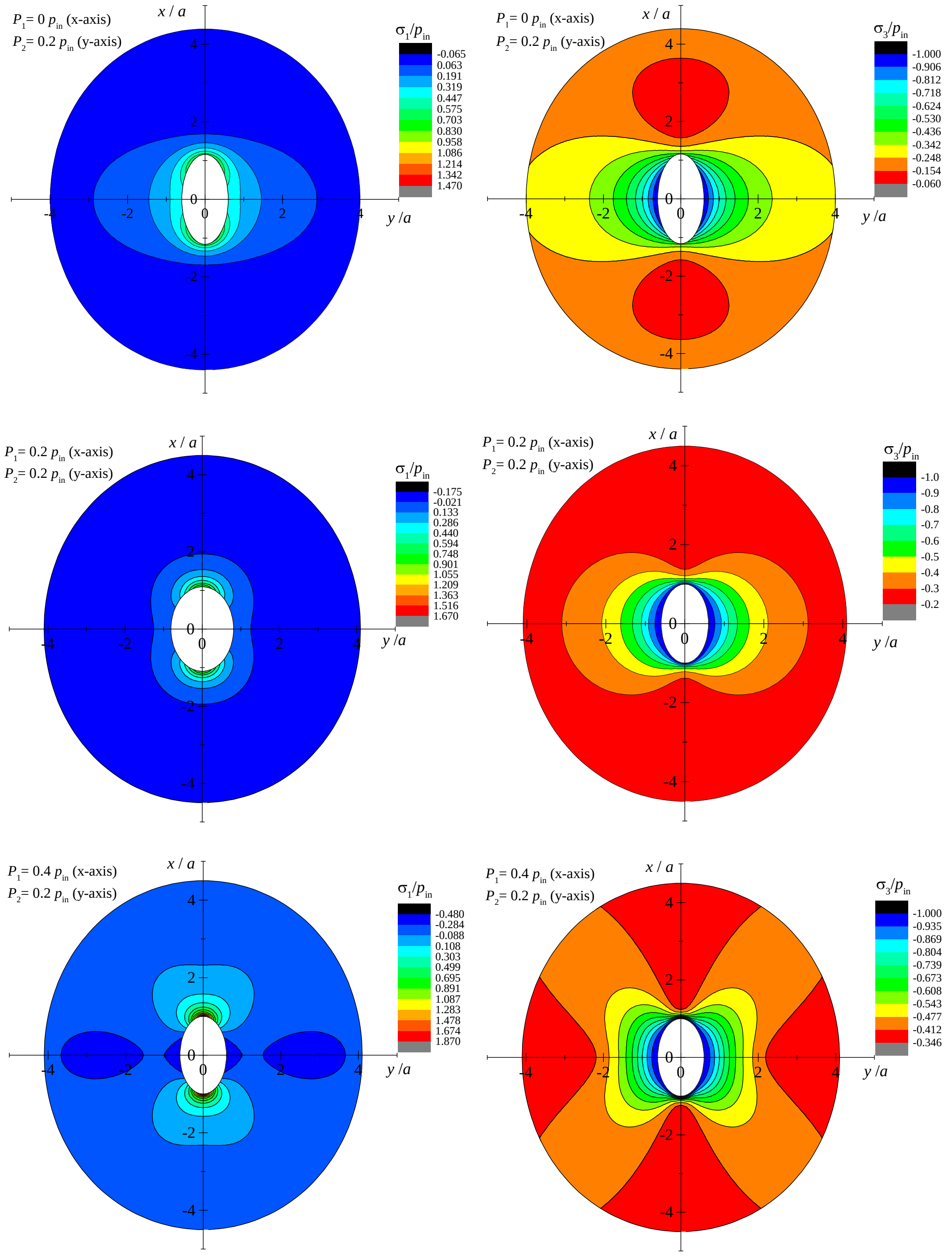

Fig. 5.22 Stress fields with different far-field stresses

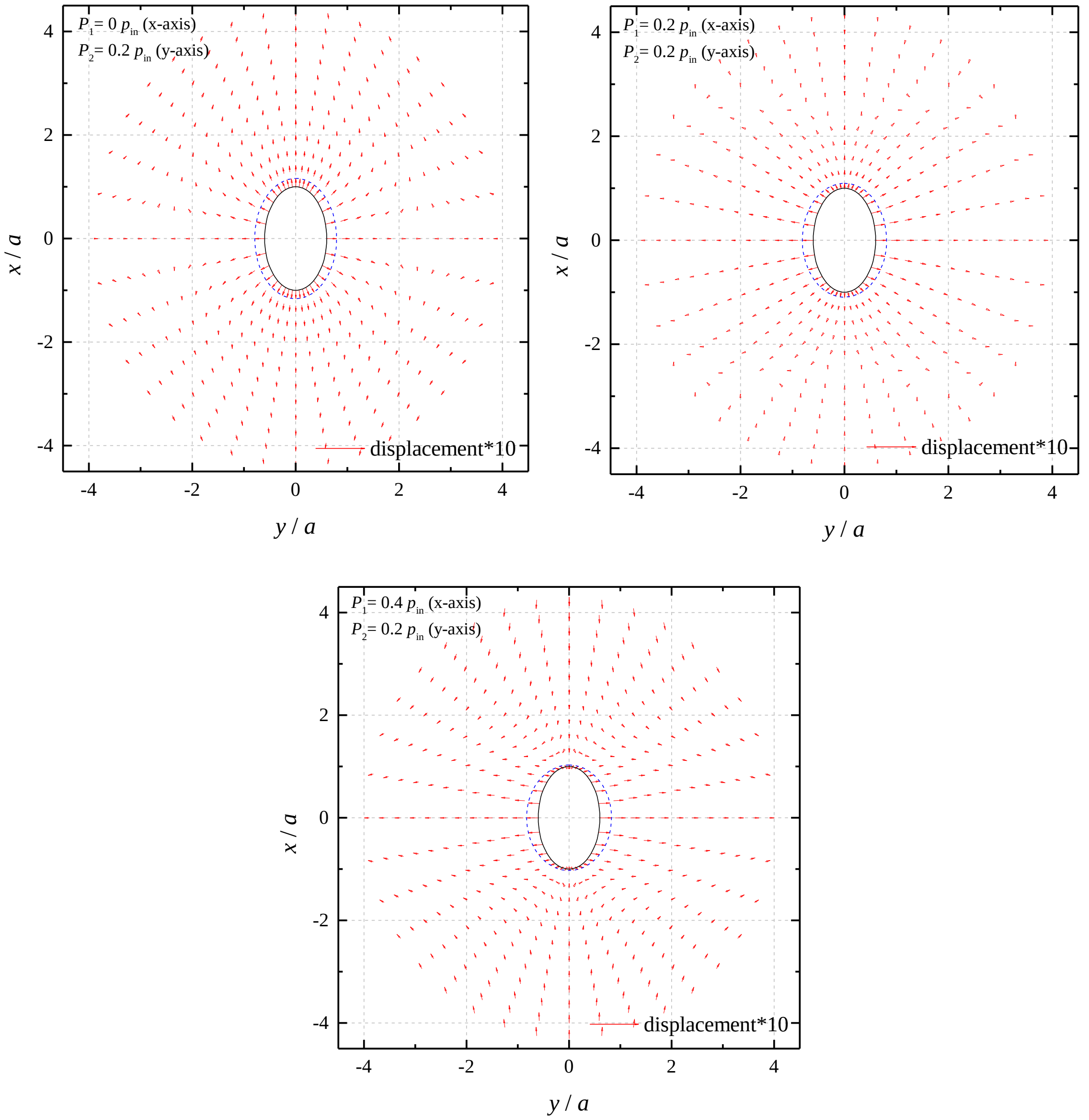

Fig. 5.23 Displacement fields with different far-field stresses

By setting $\Lambda = 45^{\mathrm{o}}$ (P_1 takes a clockwise angle of 45° to the major axis of the ellipse), the influence of far-field stresses on the stress and displacement fields are presented in Fig. 5.24. It is shown that the stress concentration region is inclined to the direction of largest compression stress at infinity, and, contrarily, the largest cavity deformations occur in its perpendicular direction.

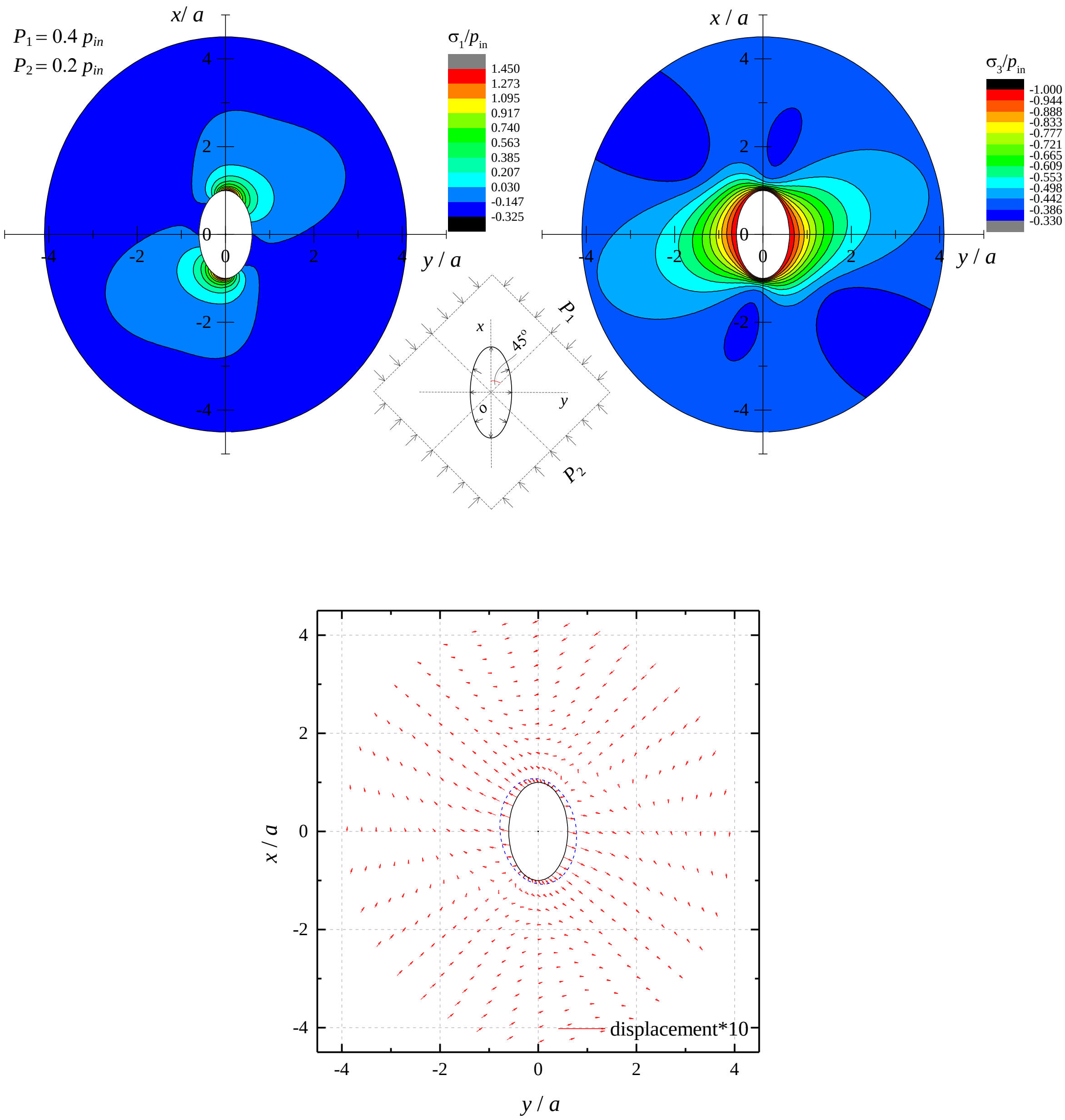

Fig. 5.24 Stress and displacement fields around an ellipse under oblique far-field stresses

5.2.3.4 Stress and displacement fields resulted by given displacement boundaries

Except at the vertices, the radial direction of points on an ellipse does not coincide with the normal direction, and this difference would be intensified with increases of a/b. Therefore, the formed stress field around the ellipse calculated with the previously developed two displacement-controlled (D-C) solutions would be different. Taking $a/b = 5/3$ as an example, with the same soil properties and cavity positions (initial and final), results calculated with these two solutions are presented in Fig.(5-25) and Fig.(5-26) respectively ($G = 20\text{MPa}$, Poisson's ratio $\nu = 0.4$).

(1) Solution with given displacements normal to the initial ellipse

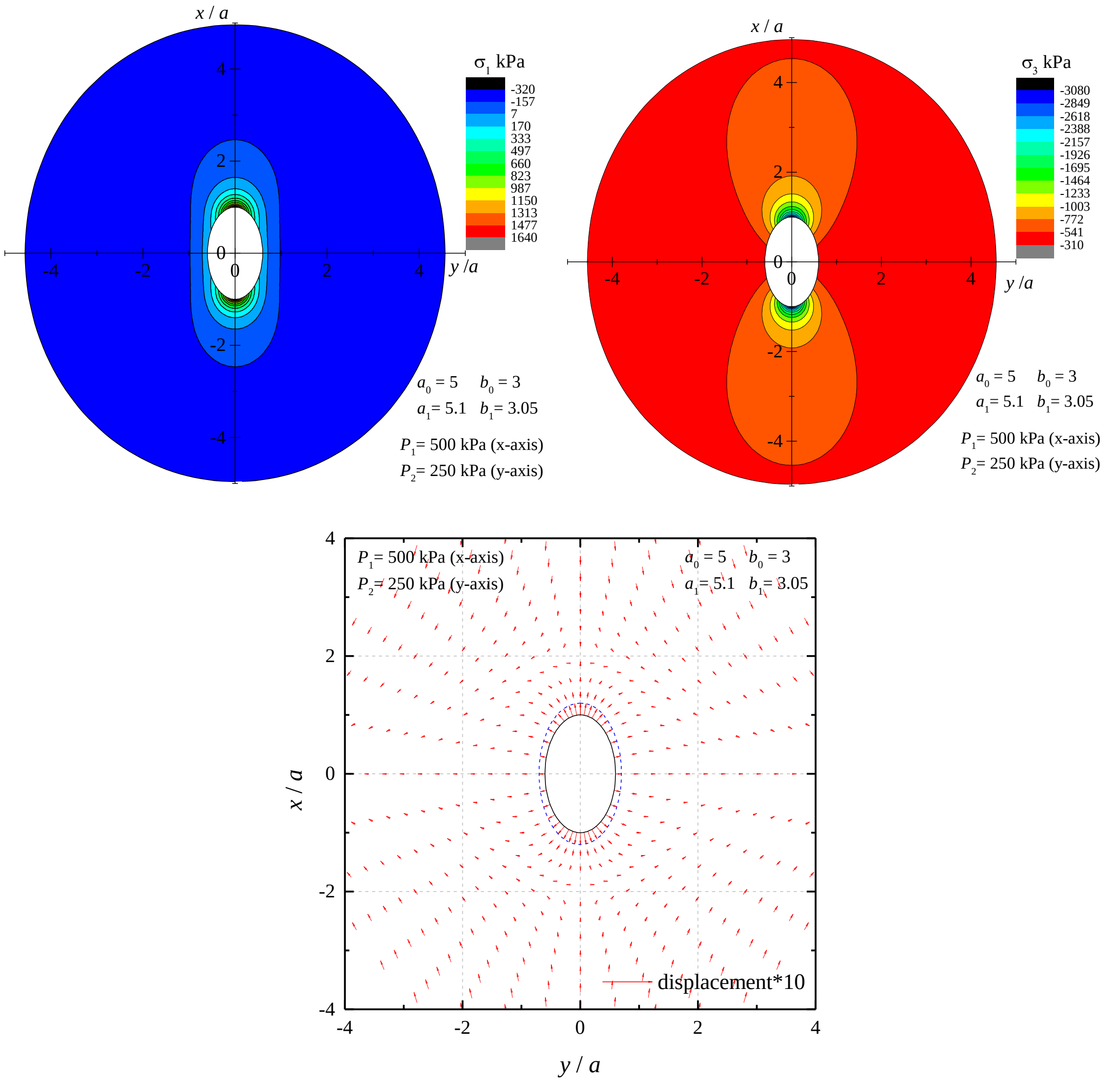

Fig. 5.25 Stress and displacement fields around an ellipse (first D-C solution)

(2) Solution with given displacements pointing out from the centre (case 2)

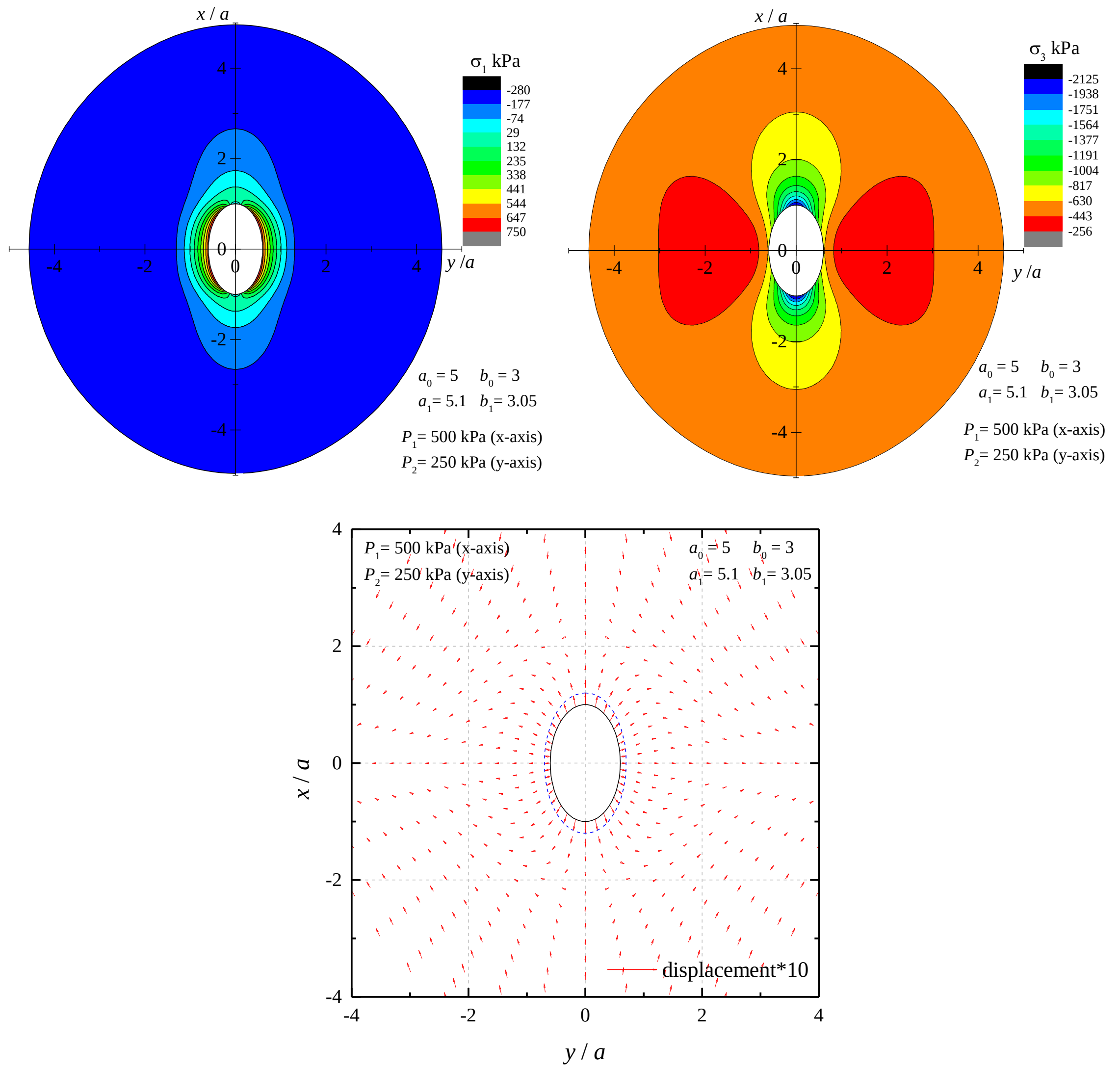

Fig. 5.26 Stress and displacement fields around an ellipse (second D-C solution)

The assumed displacement directions of boundary points in the first displacement-controlled solution are more paralleling to the major axis direction of the ellipse than the second solution. This difference leads to significant variations of the surrounding stress fields although the initial and final positions of the ellipse were set as the same in these two solutions. Specifically, with given displacements normal to the initial ellipse, tensile zones concentrated around vertices of the major axis. Medium around the ellipse seems to be stretched in the direction paralleling to the minor axis of the ellipse. On the contrary, tensile zones emerged from vertices of the minor axis when the boundary points were set to move along radial directions. The medium seems to be stretched in the direction paralleling to the major axis of the ellipse. In addition, the magnitude and concentration degree of the stresses caused by different types of displacement boundary conditions are distinctly different as well.

5.3 Mechanical analysis of root growth models

As reviewed in Section 5.1, several growth models were proposed to study the mechanical interaction problem between the root tip and the surrounding soil, but related theoretical analyses are relatively scarce. Based on the preceding elastic solutions, some theoretical investigations will be presented in this section in order to provide a simple approximate method to study the root tip-soil mechanical interaction during a short-term growth.

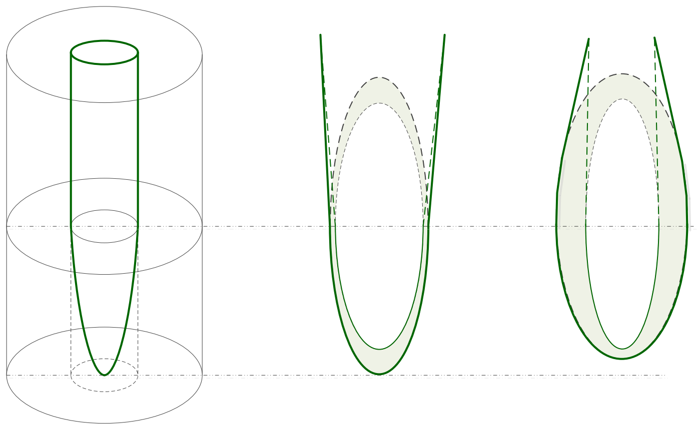

Fig. 5.27 Assumptions on the root apex geometry

As illustrated in Fig. 5.27, the extending part of the root tip is approximately represented with a half-spheroid (Mckenzie et al., 2013), and its longitudinal section, therefore, becomes in a half-elliptic shape. Analytical three-dimensional analysis on an expanding spheroid would be extremely complicated, if possible. Alternatively, the three-dimensional penetration or bearing problems were usually analysed in the plane strain condition which is much easier to be dealt with, and then they can be associated with empirical shape factors (De Beer, 1970; Durgunoglu and Mitchell, 1975; Hansen, 1970; Lyamin et al., 2007; Vesic, 1973). Similarly, for the present problem, by multiplying a shape factor, the real soil resistance encountered by the root tip may also be approximately obtained from a reasonable two-dimensional analysis. Accordingly, the mechanical interaction of a root tip with the surrounding soil caused by a short-term growth under the plane strain condition is approximately modelled with one-half part of an expanding ellipse. It is assumed that the longitudinal section of the concerned part of the root tip is still in an elliptical shape with an unchanged origin position after a short-term growth. With a sufficient small displacement increment, deformations of the displaced soil may mainly stay in an elastic stage (or at least in a large extent). In addition, the possible influence of stress and strain history is neglected in the current static elastic analysis.

Based on these assumptions, the preceding closed-form displacement-controlled solutions become capable of calculating the incremental elastic stress and displacement fields caused by a short-term root growth as discussed in the following parts.

5.3.1 Mechanical analysis on axial growth of root tips

5.3.1.1 Incremental stress and strain fields caused by axial root growth

Two displacement-controlled elastic solutions have been developed in the above section. It showed that assumptions on the displacement vectors (magnitude and direction) played key roles in quantifying the produced stress and strain fields. Unfortunately, so far direct observation on this information is really rare except the work presented by Vollsnes et al. (2010). As shown in Fig. 5.28, they obtained some displacement patterns of sand around primary root tips by means of the GeoPIV technique (White et al., 2003).

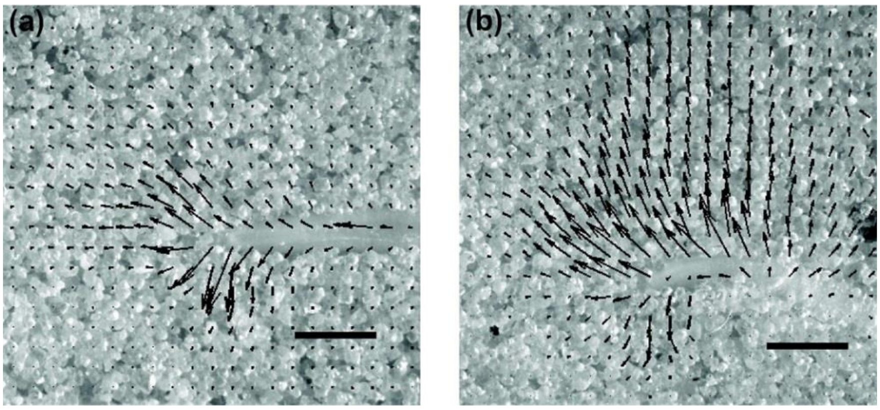

Fig. 5.28 Sand displacement patterns for KYS maize roots
grown in (a) medium dense (straight root) and (b) compact sand (curved root).
Displacement vectors have been magnified 100× in (a) and 200× in (b) for clarity.
Horizontal bars=2mm. After Vollsnes et al. (2010).

It is shown that the sand particles displaced by a normally growing root rip move more paralleling to the axial direction (e.g. Fig. 5.28 (a)), so the second displacement-controlled solution (surface displacements direct outwards from the origin) is used to model the interaction of root apex with surrounding soil for roots with dominant axial elongation. The half-ellipse has the same size as the front part of the root tip of an approximately elliptical longitudinal section, and the caused sand displacements in a short-term growth interval (about 5-minute) were approximated from their experimental data. An initial half ellipse of $a_0 = 2mm$ and $b_0 = 0.5mm$ is set, and the semi-axes of the half-ellipse after displacement are $a_1 = 2.006mm$ and $b_1 = 0.503mm$ (the maximum elongation length is $6\mu m$, and maximum radial expansion is $3\mu m$). The required elastic properties of the used growing sand have not been given, and the calculation was conducted with estimated parameters of $G = 10\text{MPa}$ and $\nu = 0.35$ (the used growing sand samples are relatively loose).

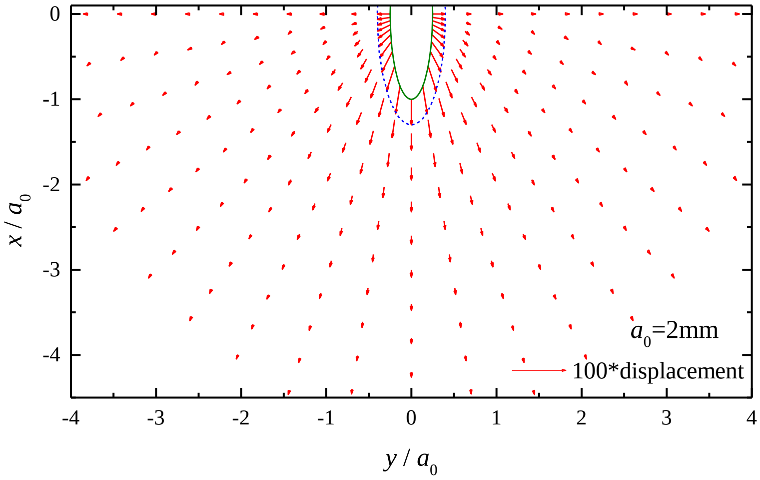

Fig. 5.29 Sand displacement pattern calculated with the second D-C solution

As shown in Fig. 5.29, idealised sand displacement vectors with a similar magnitude of lengths as that observed in the experiments were given by the theoretical calculation. The displacement directions were not attempted to be exactly consistent at every point due to their great sensitivity and variations to the root surface conditions and anisotropic properties of the local soil. By using this model, the incremental stress and strain fields around a half-elliptical root tip were calculated as below.

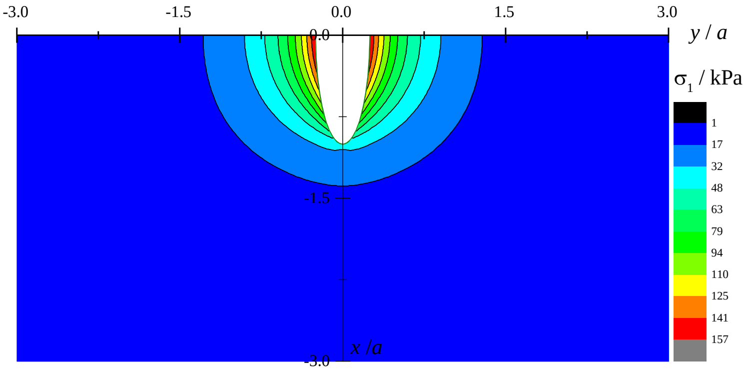

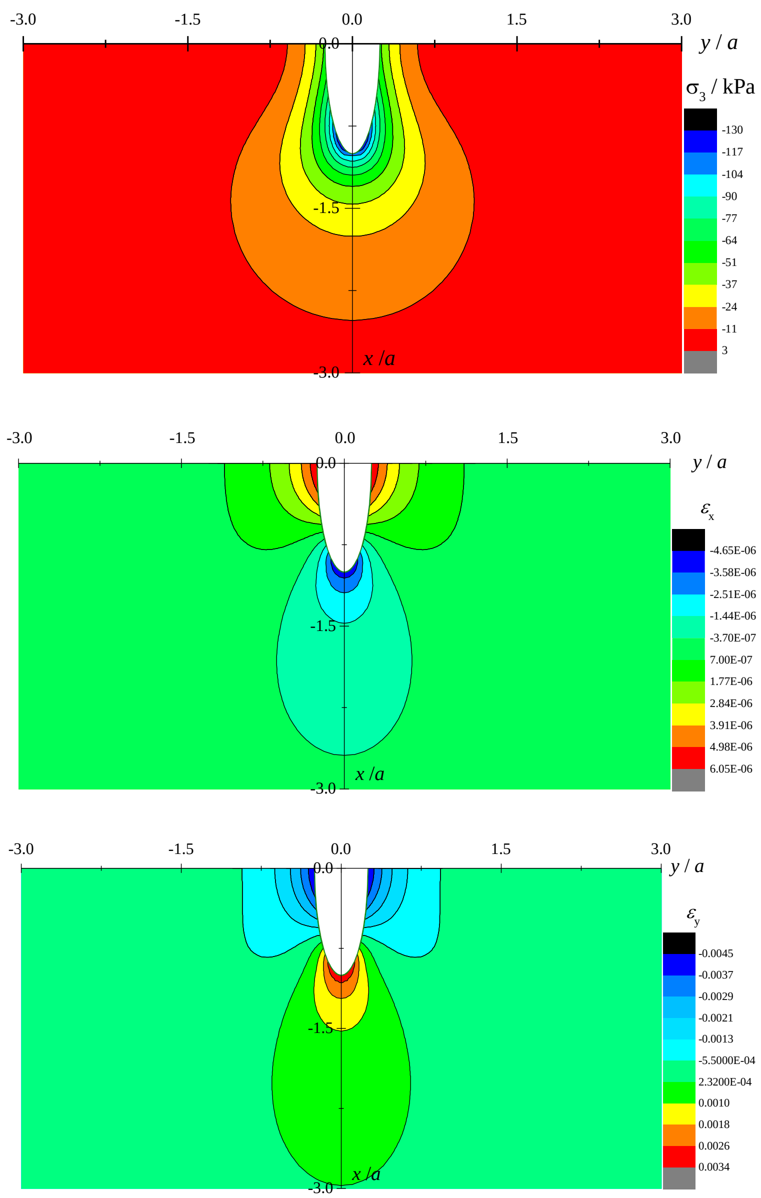

Fig. 5.30 Stress and strain fields calculated with the second D-C solution

With given enlargements of the root tip (maximum elongation: $6\mu m$, maximum radial expansion: $3\mu m$), Figure 5.30 indicates that the soil ahead of the root apex is predominantly compressed in the growing direction. Therefore, ε_x is compressive (negative), and ε_y is tensile (positive) in this zone. Contrarily, the soil on the sides is mainly under tension during the ellipse expansion. The side tensile zones are mainly due to the stretching stresses existing between the upper and lower half of the calculated ellipse. This loading condition of the side zones is different from those in the real penetration problem which is mainly under shear due to the interface friction. However, the axial resistance mainly arose from the compression deformation of front soil (Palmer et al., 2009), so the relatively slight influence of the side soil on the axial resistance was neglected.

The largest compressive stress is produced in a narrow vicinity around the root apex, which is about 130kPa representing the maximum soil resistance in the present two-dimensional growth model. To estimate the real soil resistance encountered by a half-spheroidal root tip, the aforementioned shape factor is required, which varies with the probe geometry, soil properties and stress environments (e.g. Eq.(4.24)) (Durgunoglu and Mitchell, 1975). Detailed analysis of the shape factors is out of the scope of this research, but a rough approximation may be made based on the difference between the elastic displacement solutions for spherical (3-D) and cylindrical (2-D) cavities (given in Eq.(5-80) (Yu, 2000)). In this greatly simplified approach, the required stress of a sphere is 2 times of that by a cylinder with the same wall displacement. Accordingly, the estimated resistance in the calculated relatively loose soil for a three-dimensional root tip may be around 260kPa. This level of resistance is a bit lower than the typical maximum root growth pressure and within the same magnitude of that experimentally measured (Clark et al., 1999). So this solution may provide a simple way to estimate of soil resistance encountered by axial root elongation.

$$u_e = \frac{p_{in} - p_0}{2kG}\left(\frac{a}{r}\right)^{1+k} r \quad (k = 1 \text{ for cylindrical, } k = 2 \text{ for spherical}) \tag{5-80}$$

5.3.1.3 Definition of the root growth pressure

The thrust pushing the root cap into the soil is mainly made of the individual forces generated by the elongating cells in the elongation zone just behind the apex. In general, the cells in the upper part of the elongation zone gradually get matured with fully extension, and continuous fresh supplies advance to its lower part from the meristem zone to maintain the normal growth. This driving force is usually regarded as the growth pressure generated by a root tip (Hettiaratchi et al., 1990), and it, therefore, can be estimated by the resultant force transmitting in the transverse section between the elongation zone and the meristem zone. As illustrated in Fig. 5.31, an averaged longitudinal stress (p_{av}) is defined to quantify this growth pressure.

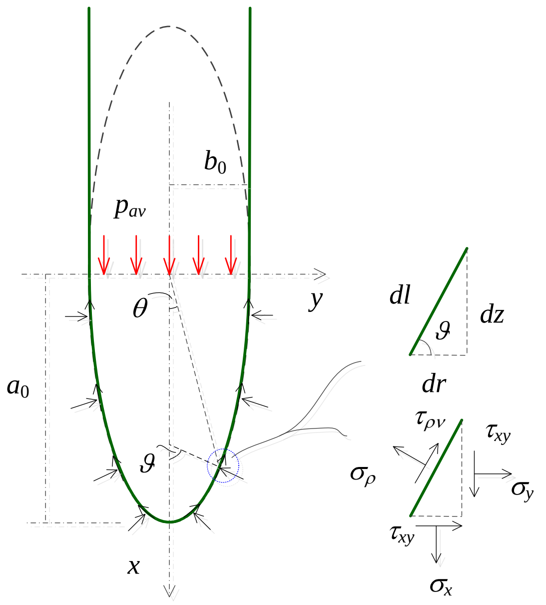

Fig. 5.31 Definition of the average longitudinal stress

Due to the encountered stresses around the surface root tip are usually non-uniform, p_{av} is calculated with Eq.(5-81) (Palmer et al., 2009).

$$p_{av}b_0 = \int_0^{b_0} \sigma_x d_r = \sum_{i=1}^{n} \sigma_{xi} d_{ri} \tag{5-81}$$

As usually assumed in the application of cavity expansion theory to penetration problems, we took the half part of an expanding ellipse to model the growth of the root tip. In fact, it is not the same as the real process of root-soil interaction in which no expansion would happen in the upper half. As a consequence, the calculated stress and deformation fields on the side soil of an elongation root were inevitably distorted as previously discussed, and its relatively slight influence to the axial resistance was neglected. Hence, only the soil resistance on the front compression zone is calculated to approximately estimate the defined averaged longitudinal stress. Subsequently, the required growth pressure (p_{root}) is available by taking the average of the produced compressive stresses in the front soil with Eq.(5-82). b_c is the transverse width of the front root tip encountering compression.

$$p_{root} = -\int_0^{b_c} \sigma_x d_r / b_c = -\sum_{i=1}^{n} \sigma_{xi} d_{ri} / b_c \tag{5-82}$$

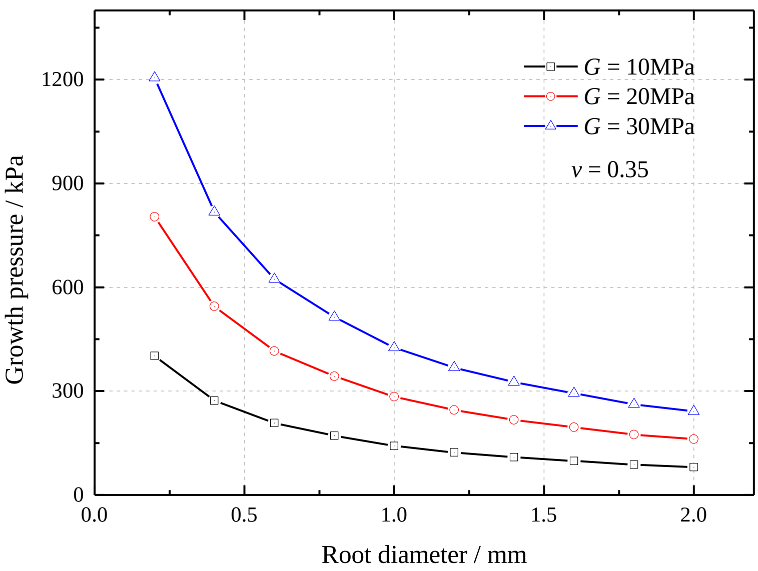

Fig. 5.32 Calculated growth pressure with the second displacement-controlled solution

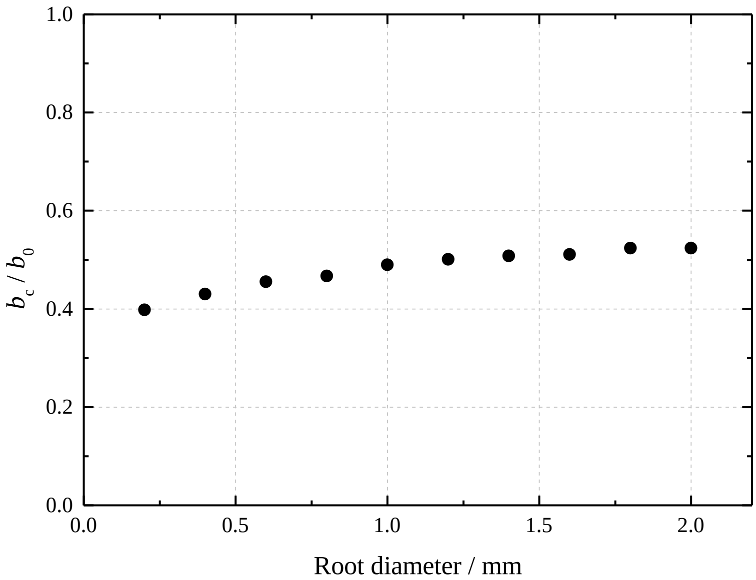

Fig. 5.33 Ratio of the width of root experiencing compression to the root diameter

With an axial elongation length of $5\mu m$ ($a_0 = 2mm$, $a_1 = 2.005mm$), the defined growth pressures (p_{root}) were calculated with varying root sizes in soils of different strengths as shown in Fig. 5.32. The length of the short axis of each ellipse was kept unchanged ($b_0 = b_1$) in these calculations to reduce the number of variables. It showed that the required growth pressure for the axial advancement increases with increases of the soil strength, but less soil resistance was encountered by relatively thicker roots. The higher soil resistance encountered in strong soils has also been widely observed in cone penetrations tests (Jamiolkowski et al., 2003; Rix and Stokoe, 1991). The observed size-dependent behaviour is due mainly to the greater stress concentration happened around the thinner cavities in the present model. Additionally, b_c / b_0 (the width ratio of the front root surface under compression to the root diameter) slightly increases with the root diameter as shown in Fig. 5.33, which may also contribute to the above size-dependent differences. This behaviour may partly account for the higher penetration ability of thicker roots (Materechera et al., 1992; Materechera et al., 1991).

5.3.2 Theoretical analysis on root thickening effect

As reviewed in Section 5.1, several growth models were proposed to study the root-soil interaction, especially roots with strong soils. Among them, the inverse-peristalsis root growth model proposed by Abdalla et al. (1969) has been widely adopted to explain the root swelling phenomenon in response to mechanical impedance. However, no theoretical basis was presented for this hypothesis (Kirby and Bengough, 2002) although it has been roughly validated in some model tests (Abdalla et al., 1969; Hettiaratchi and Ferguson, 1973). Hence, we aim to do some further theoretical investigations on this topic. Firstly, the tendency of deformation of a uniformly pressurized elliptical cavity is studied based on the previously introduced pressure-controlled cavity expansion solution. After that, the developed first displacement-controlled solution is employed to quantify the influence of the radial thickening on the stress and strain redistributions around the root tip.

5.3.2.1 Ellipse with a uniform internal pressure

(1) Deformation tendency of a uniformly pressurised ellipse

In Fig. 5.6, based on the differences of the required expansion pressures for a cylindrical cavity and a spherical cavity, the reason why the root cells still can swell radially when the axial elongation is halted was qualitatively explained, but further details about the influences associated with the variation of cavity geometry cannot be quantified with that method. Alternatively, the preceding pressure-controlled solution is employed to fill up this gap. Similar to the above approximate method, a uniform internal pressure is applied on the inner cavity wall. Displacements of two representative points of the ellipse (vertices) were recorded with the varying ellipticity (a/b) as shown in Fig. 5.34. It indicates that for a free cavity under uniform internal pressure always tends to be circular in deformation. In other words, the displacements at the vertices of the short axis are the largest along the whole cavity wall, and, on the contrary, vertices on the long axis have the smallest deformation. For a half-elliptical root tip, the longitudinal direction usually lies in the major axis direction, therefore radial swelling is more likely to happen if the same amount of constraints from the cell wall and external pressure was received by the cavity along the whole inner rim.

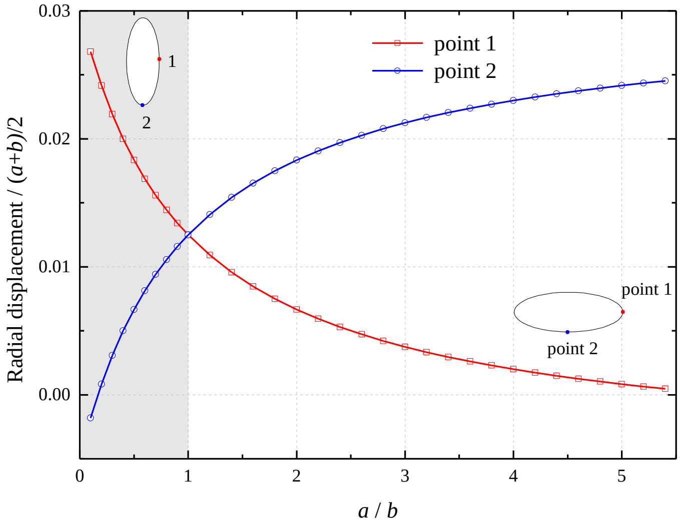

Fig. 5.34 Displacements of cavity vertices with changing shapes

($p_{in} = 500\text{kPa}$, $G = 20\text{MPa}$, $\nu = 0.4$)

(2) Stress and strain fields around a half-ellipse-shaped root tip

With this pressure-controlled solution, the stress and strain distributions around a half-ellipse with a typical size of the root tip $a = 2mm$ and $b = 0.5mm$ (Kirby and Bengough, 2002) are calculated as presented in Fig. 5.35. As previously demonstrated, the ellipse tends to be thicker with a uniform internal pressure. A tensile stress/strain region (positive for tensile) perpendicular to the axial growth direction appeared just ahead of the root apex. This is consistent with the finding of Richards and Greacen (1986), and may partly account for the benefit of the radial thickening to the axial elongation. Providing that the constraints from microfibrils within cell walls or the stimuli from phytohormones apply non-directional influences on the cell expansion, this pressure-type boundary can approximately represent the boundary condition of the root tip. It may occur sometimes, but it is not always the case since the nature of tropistic growth of roots and anisotropic strength of the surrounding soil. Alternatively, with a precise control of the root tip geometry and size, more analysis about the root-soil interaction will be carried out in the next part by using the previously developed displacement-controlled solution.

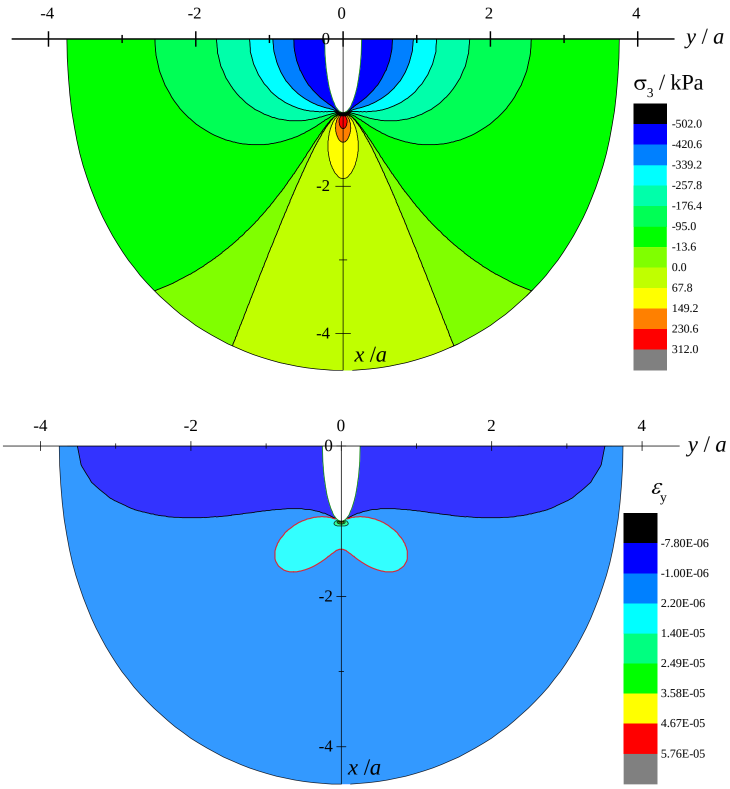

Fig. 5.35 Stress and strain fields around the root tip with stress-controlled solution

5.3.2.2 Purely radial thickening with given normal displacements

When the axial elongation is halted ($Q_{th-1} < Q_{soil} < Q_{th-2}$), the roots would tend to grow radially as assumed in the inverse-peristalsis root growth model (introduced in Section 5.1.2). Consequently, movements of the displaced soil would reorient more radially in this case. As previously discussed, the assumed boundary condition on the cavity wall in the first displacement-controlled solution is more paralleling to the direction of the minor axis of an ellipse. Therefore, it is employed to study the concerned root swelling problem. In this solution, it assumed that points on the inner ellipse move outwards along the normal directions of the initial cavity surface. The root tip is approximately modelled as a half-elliptical cavity with $a = 2$mm and $b = 0.5$mm (d_{rt} = 1mm). Its axial elongation is fully impeded by the high soil resistance, then it ideally thickens to another ellipse with a larger minor axis length $b_1 = 0.505$mm ($a_1 = 2$mm). In this case, the maximum swelling happened along the minor axis of the assumed half-ellipse (approximately in the elongation zone), and a smooth thickening growth is applied along the root longitudinal section. The amplified displacement vectors ($100\times$) around the root tip are given in Fig. 5.36. ($G = 10$MPa , $\nu = 0.35$).

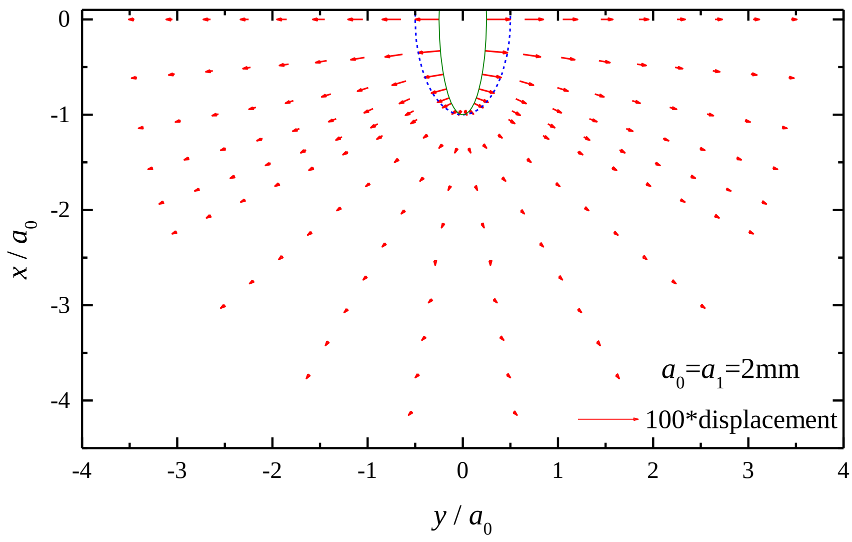

Fig. 5.36 Displacement vectors field around a thickening root tip

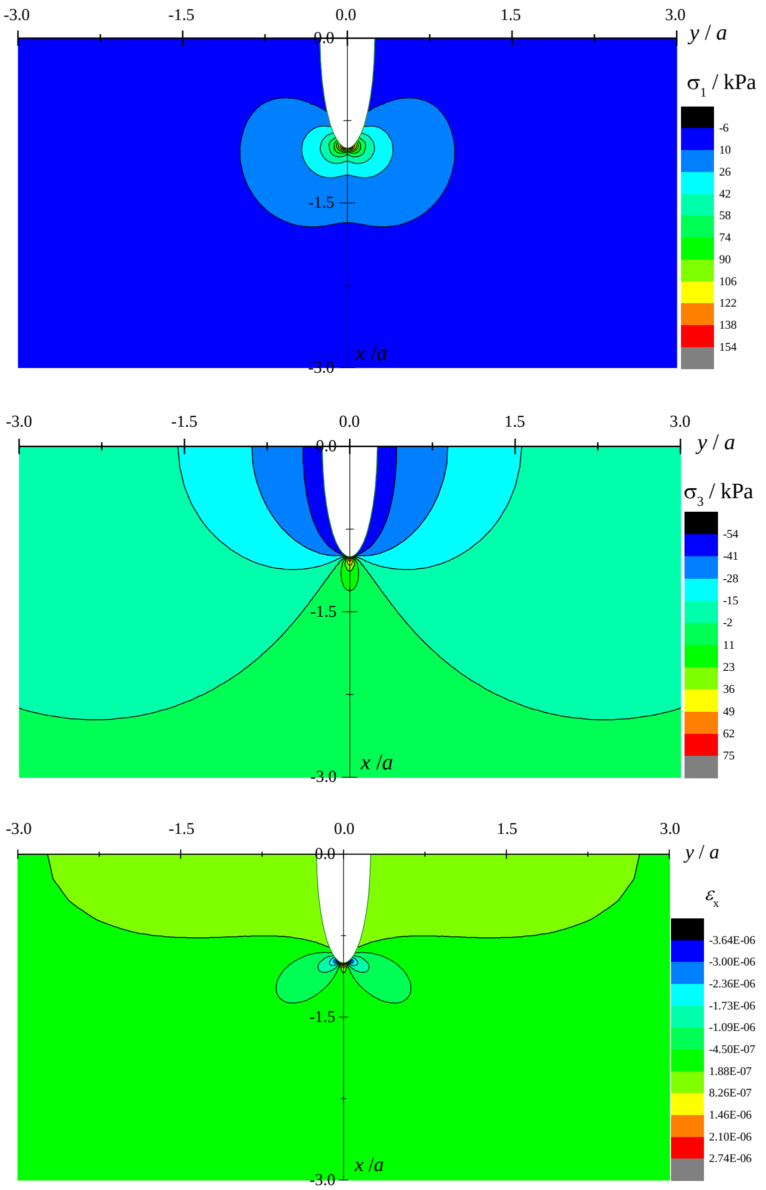

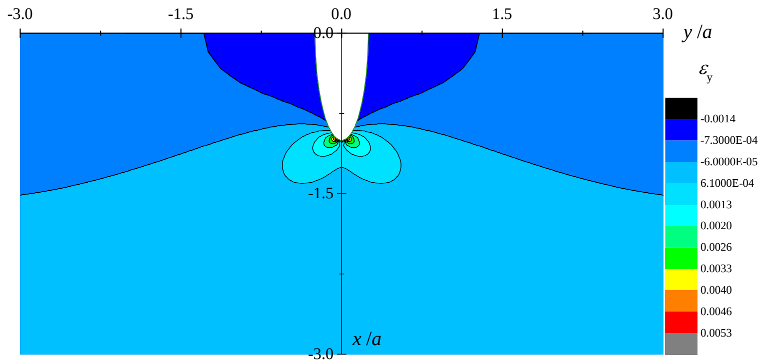

Fig. 5.37 Stress and strain fields around a thickening root tip

The initial stress field is assumed to be equilibrated before the root thickening. So the stress and strain fields shown in Fig. 5.37 are the incremental values calculated with the first elastic displacement-controlled solution. It demonstrated that significant stress and strain concentration took place in the immediate front of the root apex due to a small amount of radial swelling (maximum incremental thickness is $1/200d_{rt}$). In this immediate front zone, the soil is mainly subject to tensile stresses and accompanied by concentrated tensile strains tending to the transversal direction. As a consequence, it will lead to a reduction of the axial resistance due to the release of the radial confining stress, and the soil may even be teared, leading to some micro-cracks initiate or grow in the immediate vicinity of the root apex. These consequences will effectively facilitate subsequent root axial elongation. As aforementioned, similar findings were also found with other approximate methods, and they provide a theoretical explanation for the hypothesised stress relief effect caused by radial thickening which is one important basis of the inverse-peristalsis root growth model proposed by Abdalla et al. (1969).

5.4 Chapter summary

Factors influencing the root penetration ability was summarised, and studies on the root radial thickening phenomenon with response to the mechanical impendence were reviewed in the first section. In the second section, three closed-form elastic solutions for ellipses with different types of boundary conditions were presented for later applications to model the root tip-soil mechanical interaction. The complex variable theory and conformal mapping technique were employed to develop these solutions. For a pressure-controlled ellipse, the solution of Muskhelishvili (1963) was followed. Solutions for displacement-controlled ellipses were derived by means of expressing the displacement boundary conditions with the Fourier series method. Subsequently, these solutions were validated with other available analytical solutions in some special cases, and their performances were briefly discussed in the end part of this section.

In Section 5.3, the second displacement-controlled solution (given displacements directing outwards from the centre of the ellipse) was employed to estimate the axial soil resistance encountered by an elongating root tip in a small growth interval. The calculated soil resistance was in the same magnitude of the experimentally measured growth pressure of root tips. However the present solution was derived based on the plane strain assumption, so reliable shape factors are required to estimate the real soil resistance encountered by a three-dimensional root tip growth. Subsequently, the stress-controlled solution and the first displacement-controlled the solution (displacement normal to the initial cavity surface) were employed to evaluate contributions of the radial thickening to the subsequent axial elongation. Evident transverse tensile strain zone immediately ahead of the root apex was predicted in both methods. These theoretical findings directly supported the hypothesis that root radial thickening has a relief effect on the front soil, and tension failure in the transverse direction even may occur, which can further reduce the required axial elongation pressure.

Chapter 6

Static and quasi-static analysis of cavity expansion under shear stress in compressible Tresca materials

6.1 Introduction

Stress and displacement analyses around a cylindrical or spherical cavity deforming in static states (Detournay and Fairhurst, 1987; Savin, 1970), in quasi-static processes (Bishop et al., 1945; Hill, 1950), or during dynamic expansions (Durban and Masri, 2004; Forrestal and Tzou, 1997) have been widely investigated by researchers in many areas (as reviewed in Section 1.2). Among them, due to the successful applications in the interpretation of in-situ tests (e.g.cone penetration tests, pressuremeter tests), prediction of bearing capacity of foundations, estimation of tunnel deformation, and analysis of stress redistribution around piles or excavations etc., analytical static and quasi-static cavity expansion solutions experienced a great deal of developments and played an important role in the geotechnical field (Yu, 2000, 2006). In general, most of them were established based on the assumption that a uniform normal stress is applied on the inner cavity wall without consideration of the shear stress. However, a great amount of surface shear stress may also be applied or generated in some analogous cases, for example, in the process of rotary drilling/excavation, accommodation of screw piles, rotary penetration tests (Bengough et al., 1997; Bishop et al., 1945; Mckenzie et al., 2013; Sadeghi et al., 2014; Whalley et al., 2005; Zhou et al., 2014a). In view of these practical problems, by assuming an additional uniform shear stress on the cavity wall, a few pioneering studies considering the influence of the inner shear stress on the static stress distribution or quasi-static pressure-expansion response have been presented (Muskhelishvili, 1963; Parasyuk, 1948; Zhou et al., 2014a). However, some imperfections still exist in some cases (elaborated later), which more or less limited their applications. Therefore, a complete static stress solution is developed in this chapter, which describes an embedded circular cavity under loading of uniform normal pressure and shear stress at the inner cavity wall and non-equal biaxial stresses at infinity.

Subsequently, a large deformation displacement analysis is carried out for the cavity deforming in a hydrostatic stress environment. Based on them, the continuous quasi-static expansion process of a cavity deforming in compressible Tresca materials can be modelled without limit of deformation level.

In a static stress analysis, the governing equation system usually consists of constitutive models and equilibrium equations, which fundamentally determines the mathematical tractability as well as the boundary conditions, particularly in analytical derivations. For a cavity with axisymmetric geometry and stress conditions, it generally can be simplified to a one-dimensional equilibrium problem, which greatly facilitates the development of a number of analytical elastic, elastic-plastic solutions (Yu, 2000). However for problems involving a non-symmetrical geometry and/or stress boundary conditions, more advanced mathematical techniques are usually required, such as the complex variable theory (Muskhelishvili, 1963; Stevenson, 1945), perturbation methods (Ivlev, 1959; Kuznetsov, 1972), variational approaches (Kerchman and Erlikhman, 1988) or some other numerical techniques (Bradford and Durban, 1998; Huang, 1972). Among them, the complex variable theory with conformal mapping technique (Muskhelishvili, 1963) provides a very powerful analytical tool for calculating the elastic stress and displacement fields around a cavity with various shapes and stress boundaries (it is noteworthy that the compatibility condition with small deformation is included in the complex potential-based method). To be specific, in purely elastic materials, numerous solutions have been proposed by using this method (Savin, 1970). For elastic-perfectly plastic materials, Galin (1946) creatively proposed an analytical solution for a circular cavity embedded in an infinite plate under non-equal biaxial remote stretching loading. Both constant and polynomial types of far-field stress conditions were discussed, and the Tresca yield criterion was employed to describe the plastic deformation. Although some deficiencies existed as found and improved by Tokar (1990) and Ochensberger et al. (2013), it is generally believed that this method yields a lot of developments of analytical solutions for this specific static cavity problem (Yarushina et al., 2010). For example, Cherepanov (1963) extended it to address plane stress problems, Detournay (1986) developed it into applications on the Mohr-Coulomb material. In addition, similar to the complex variable theory in linear elasticity, a few analytical solutions for hardening material have also been derived by means of constructing two unified pseudo-stress functions (Gao et al., 1991; Lee and Gong, 1987).

Due to additional consideration of the shear stress at the inner cavity wall, the formed plastic region cannot be characterised with a biharmonic stress function, which results in Galin's method is not applicable to the present problem. Parasyuk (1948) proposed another analytical approach to determine the shape of the formed elastic-plastic boundary (hereinafter referred as EP boundary) based on the Cauchy integral method and the conformal mapping technique. However, the size of the EP boundary and the elastic stress field have not been given in Parasyuk's paper. To address this problem, by using the Laurent decomposition theorem and the Liouville's theorem, an explicit expression of the mapping function and analytical elastic complex potentials are obtained. Furthermore, taking into account the material compressibility, a large strain displacement solution for a circular cavity continuously expanding in a uniform stress environment is developed, and then it is combined with the developed static stress solution for conducting a quasi-static cavity expansion analysis. Subsequently, the admissible application range of present solution and influences of the shear stress on the stress distribution and quasi-static expansion response are discussed in Section 6.5 and Section 6.6 respectively. Finally, conclusions are drawn in the last section.

6.2 Problem definition

A sufficiently large and thick plane (in comparison with the cavity size) with a cylindrical inner cavity is considered, which allows the plane strain assumption to be adopted in the stress and deformation analysis. As illustrated in Fig. 6.1, non-equal biaxial stresses are applied at infinity, and normal and shear pressures uniformly act on the inner cavity wall. For convenience, both Cartesian coordinates and cylindrical polar coordinates with the same origin at the centre of the cavity are utilised. It is worth pointing out that the defined remote stress conditions are sufficiently general because we always can set a coordinate system with axes parallel to the directions of the principal stresses at infinity. Within the cylindrical polar coordinates, the stress equilibrium equations in axes directions are

$$\frac{\partial \sigma_r}{\partial r} + \frac{1}{r}\frac{\partial \tau_{r\theta}}{\partial \theta} + \frac{\sigma_r - \sigma_\theta}{r} = 0 \tag{6-1}$$

$$\frac{1}{r}\frac{\partial \sigma_\theta}{\partial \theta} + \frac{\partial \tau_{r\theta}}{\partial r} + \frac{2\tau_{r\theta}}{r} = 0 \tag{6-2}$$

Taking tension as positive for normal stresses and rotation in the counterclockwise direction to the object as positive for shear stresses, the stress boundary conditions can be expressed as

$$\sigma_r\big|_{r=R_0} = -p_{in}\ ,\ \ \tau_{r\theta}\big|_{r=R_0} = mk\ \ \ (-1 \le m \le 1) \tag{6-3}$$

$$P_\infty = (\sigma_y\big|_{y\to\infty} + \sigma_x\big|_{x\to\infty})/2 = -(\sigma_{v0}+\sigma_{h0})/2\ ,\ \tau_\infty = (\sigma_y\big|_{y\to\infty} - \sigma_x\big|_{x\to\infty})/2 = (\sigma_{h0}-\sigma_{v0})/2 \tag{6-4}$$

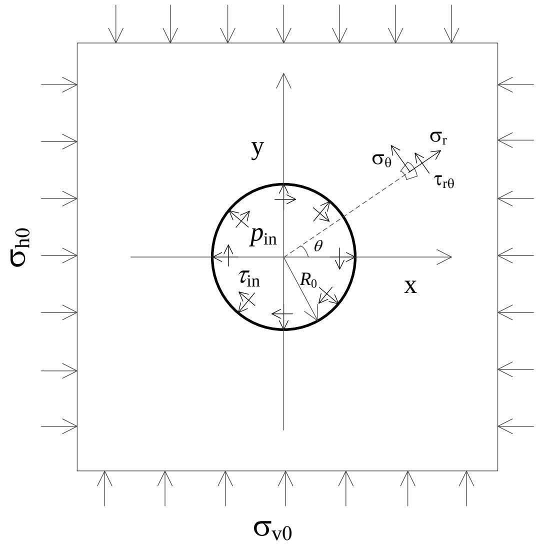

Fig. 6.1 Stress boundaries and coordinate systems

A homogenous and isotropic plane is under consideration. The material behaviour is described with an elastic-perfectly plastic model. Specifically, the elastic response is characterised with the generalised Hooke's law until the onset of yielding which obeys the Tresca yield criterion as Eq.(6-5).

$$\left(\sigma_r - \sigma_\theta\right)^2 + 4{\tau_{r\theta}}^2 = 4k^2 \tag{6-5}$$

where k is the yield stress in pure shear loading.

6.3 Static stress analysis

6.3.1 Plastic region

To determine the surrounding plastic stress field, three basic assumptions are adopted as suggested by Galin (1946) and Detournay (1986), which include: (1) the inner cavity is fully enclosed by a continuous plastic region, and the plastic stress field is statically determined; (2) the plastic zone is formed under monotonic loading, and there is no elastic unloading occurring in any cases; (3) the vertical stress component, σ_{zz}, always remains as the intermediate principal stress regardless of other stresses. Firstly, static determinacy of the plastic stress field implies that the plastic stresses can be completely determined by the inner boundary conditions (Detournay, 1986; Hill, 1950). Then according to the axisymmetric nature of the geometry and stress boundaries at the inner cavity wall, it is reasonable to assume

$$\frac{\partial \sigma_r^p}{\partial \theta} = 0\ ,\ \ \frac{\partial \sigma_\theta^p}{\partial \theta} = 0\ ,\ \ \frac{\partial \tau_{r\theta}^p}{\partial \theta} = 0 \tag{6-6}$$

Subsequently, the plastic stress components are directly obtained by solving the preceding stress equilibrium equation and yield criterion with given stress boundaries, which were known as the Mikhlin's solution (Parasyuk, 1948; Zhou et al., 2014a).

$$\sigma_r^p = k\left\langle \ln\left[\frac{(r/R_0)^2 + \sqrt{(r/R_0)^4 - m^2}}{1+\sqrt{1-m^2}}\right] - \sqrt{1-m^2(\frac{R_0}{r})^4} + \sqrt{1-m^2}\right\rangle - p_{in} \tag{6-7}$$

$$\sigma_\theta^p = k\left\langle \ln\left[\frac{(r/R_0)^2 + \sqrt{(r/R_0)^4 - m^2}}{1+\sqrt{1-m^2}}\right] + \sqrt{1-m^2(\frac{R_0}{r})^4} + \sqrt{1-m^2}\right\rangle - p_{in} \tag{6-8}$$

$$\tau_{r\theta}^p = mk\frac{R_0^{\ 2}}{r^2} \tag{6-9}$$

Two corresponding solutions exist to describe different failure models, which are the active model (when $\sigma_\theta^p < \sigma_r^p$) and the passive model (when $\sigma_\theta^p > \sigma_r^p$) (Detournay, 1986), of the surrounding material. Only the loading condition (passive model) is considered in this research. According to the elastic solution in Appendix C, the requirement that a plastic zone starts forming from the cavity rim under loading can be found as

$$(p_{in} + P_\infty) \geq k\sqrt{1-m^2} - 2\left|\tau_\infty\right| \tag{6-10}$$

6.3.2 Determination of the elastic-plastic interface

Although the plastic stress components are assumed independent of the centre angle, the EP boundary will no longer be in a circular shape because of the non-axisymmetrical far-field stresses. Several methods have been developed to determine the EP boundary which is of critical importance in addressing the present problem. Specifically, Galin (1946) first developed an approach to obtain the EP boundary by constructing a biharmonic stress function crossing the elastic-plastic surface based on the stress continuity condition. Subsequently, Parasyuk (1948) developed a method (as in Appendix D) for cases with a non-biharmonic plastic stress state, and this method was also used by Savin (1970) in dealing with Galin's problem. Cherepanov (1963) introduced Laurent's theorem to deal with the stress continuity conditions at the EP boundary and gave a solution for the Tresca material under the plane stress condition. For materials obeying the Mohr-Coulomb criterion, Detournay (1986) built an approximate mapping function in the series form for describing the EP boundary based on the Schwarz's reflection principle and Laurent's decomposition theorem. Overall, these methods provided valuable references for further exploration of the present problem. Partly based on Parasyuk's derivation (1948) as presented in Appendix D, an explicit expression of the mapping function for predicting the EP boundary is firstly derived with Laurent's decomposition theorem.

Stress components in the plastic region were given in Eqs. (6-7), (6-8) and (6-9). The elastic stresses can be expressed with the Kolosov-Muskhelishvili complex potentials, $\Phi(\zeta)$ and $\Psi(\zeta)$, (Muskhelishvili, 1963). Therefore, stress continuity conditions along the EP boundary (corresponding to the unit circle γ centred at the origin of the phase plane) and their boundary values at infinity can be expressed as

$$\Phi(\zeta)+\overline{\Phi(\zeta)}=\frac{(\sigma_x^e+\sigma_y^e)}{2}=\frac{(\sigma_r^e+\sigma_\theta^e)}{2}$$
$$=\begin{cases} k\left\langle \ln\left[\dfrac{\omega(\sigma)\overline{\omega(\sigma)}/R_0{}^2+\sqrt{[\omega(\sigma)\overline{\omega(\sigma)}]^2/R_0{}^4-m^2}}{1+\sqrt{1-m^2}}\right]+\sqrt{1-m^2}\right\rangle-p_{in} & \text{, at } \gamma \quad \text{(a)} \\ P_\infty & \text{, } \zeta\to\infty \; (b) \end{cases} \tag{6-11}$$

$$\frac{\overline{\omega(\zeta)}}{\omega'(\zeta)}\Phi'(\zeta)+\Psi(\zeta)=\frac{(\sigma_y^e-\sigma_x^e+2i\tau_{xy}^e)}{2}=\frac{(\sigma_\theta^e-\sigma_r^e+2i\tau_{r\theta}^e)}{2}e^{-2i\theta}$$
$$=\begin{cases} k\left\langle \dfrac{\sqrt{[\omega(\sigma)\overline{\omega(\sigma)}]^2-m^2R_0{}^4}+mR_0{}^2 i}{\omega(\sigma)\overline{\omega(\sigma)}}\right\rangle\dfrac{\overline{\omega(\sigma)}}{\omega(\sigma)} & \text{, at } \gamma \quad \text{(a)} \\ \tau_\infty & \text{, } \zeta\to\infty \; \text{(b)} \end{cases} \tag{6-12}$$

where $i=\sqrt{-1}$ and σ represents points on the unit contour of γ in the phase plane, hence $\bar{\sigma}=1/\sigma$. The function of $\omega(\zeta)$ conformally maps the exterior of the EP boundary in the physical plane onto the exterior region of the unit circle in the phase plane.

Boundary conditions in Eq.(6-11)$_{(b)}$ and Eq. (6-12)$_{(b)}$ specified the behaviour of elastic complex potentials at infinity as

$$\Phi(\infty)=\frac{P_\infty}{2}+O(\zeta^{-2}) \quad , \quad \Psi(\infty)=\tau_\infty+O(\zeta^{-2}) \tag{6-13}$$

Given by Parasyuk (1948) (see Appendix D), the mapping function is in the form of

$$\omega(\zeta)=\alpha(\zeta+\frac{\beta}{\zeta}) \tag{6-14}$$

where $\zeta=\xi+i\eta=\rho e^{i\phi}$. $\beta=\tau_\infty/k$. Parameter ' α ' determines the size of the EP boundary, but it has not been given by Parasyuk (1948). The far-field stress conditions bound the behaviour of the right-hand side of Eq.(6-11)$_{(a)}$ at infinity (Chakrabarty, 2006; Savin, 1970), therefore continuity condition of the mean stress across the elastic-plastic surface is reconstructed as

$$\Phi(\sigma)+\overline{\Phi(\sigma)}=k\left[\frac{1}{2}\ln[F(\sigma,\bar{\sigma})]+\sqrt{1-m^2}\right]-p_{in} \tag{6-15}$$

where $F(\sigma,\bar{\sigma})=\left\{\dfrac{\omega(\sigma)\overline{\omega(\sigma)}/R_0{}^2+\sqrt{[\omega(\sigma)\overline{\omega(\sigma)}]^2/R_0{}^4-m^2}}{(1+\sqrt{1-m^2})\sigma\bar{\sigma}}\right\}^2=\dfrac{f(\sigma)}{\sigma}\dfrac{\bar{f}(\bar{\sigma})}{\sigma^{-1}}$.

An elliptic EP boundary is predicted based on the prior assumptions, which is a closed smooth contour in the physical plane. And equation (6-15) implies that $\ln[F(\sigma,\bar{\sigma})]$ continues analytically on both sides of γ in an annulus ($0\le|\zeta-\sigma|\le\infty$). Based on the Laurent decomposition theorem (Gamelin, 2001), $\ln[F(\sigma,\bar{\sigma})]$ can be decomposed as a sum of two functions, $d(\zeta)$ and $\bar{d}(\zeta^{-1})$, which are analytic in Ω^+ ($|\zeta|<1$) and Ω^- ($|\zeta|>1$) respectively. Then by multiplying $\dfrac{1}{2\pi i}\dfrac{d\sigma}{\sigma-\zeta}$ on both sides of Eq.(6-15) and integrating it along γ, it gives

$$F^+(\zeta)=\bar{d}(\zeta^{-1})-\overline{\Phi(\zeta)} \tag{6-16}$$

$$F^-(\zeta)=\Phi(\zeta)-d(\zeta)-(k\sqrt{1-m^2}-p_{in}) \tag{6-17}$$

where $d(\zeta)=k\ln[f(\zeta)/\zeta]$ and $\bar{d}(\zeta^{-1})=k\ln[f(\bar{\zeta})/\zeta^{-1}]$. $F^+(\zeta)$ is analytic everywhere within the region of Ω^+, and $F^-(\zeta)$ is analytic everywhere in the region of

Ω^{-}. Now the continuity conditions of mean stress across the unit circle γ can be expressed as $F^{+}(\sigma)=F^{-}(\sigma)$.

The parameter α can be determined based on the Liouville's theorem, which states $F^{+}(\zeta)$ and $F^{-}(\zeta)$ are identically equal to one and same constant due to the complex potentials are bounded at infinity. It is noteworthy that the boundary value of $d(\zeta)$ and $\bar{d}(\zeta^{-1})$ should be studied in the extend complex plane and the variable of ζ (and $\bar{\zeta}$) should be replaced by $1/\bar{\zeta}$ (and $1/\zeta$) in analysing $\bar{d}(\zeta^{-1})$ due to it is the reflection of $d(\zeta)$ in γ (where $\bar{\sigma}=1/\sigma$). Therefore,

$$-\frac{P_{\infty}}{2}+\frac{1}{2}k\ln[\frac{2\alpha^{2}/R_{0}^{2}}{1+\sqrt{1-m^{2}}}]=\frac{P_{\infty}}{2}-\frac{1}{2}k\left[\ln(\frac{2\alpha^{2}/R_{0}^{2}}{1+\sqrt{1-m^{2}}})-2\sqrt{1-m^{2}}\right]+p_{in} \tag{6-18}$$

Finally, the undetermined parameter α in the above mapping function is obtained.

$$\alpha=\delta R_{0}\,\mathrm{e}^{\frac{1}{2k}[p_{in}+P_{\infty}-k\sqrt{1-m^{2}}]} \qquad (\text{with } \delta=\left[(1+\sqrt{1-m^{2}})/2\right]^{1/2}) \tag{6-19}$$

By now the conformal mapping function is completely confirmed, and a new parameter δ is included due to the additional consideration of the shear stress, comparing with the Galin's mapping function. It is shown that the non-dimensional size and axes directions of the elliptical EP boundary entirely depend on the far-field stress boundary conditions, and its size in the physical plane can be expressed with lengths of the semi-major axis, $a_{ep}=\alpha(1+|\beta|)$, and the semi-minor axis, $b_{ep}=\alpha(1-|\beta|)$.

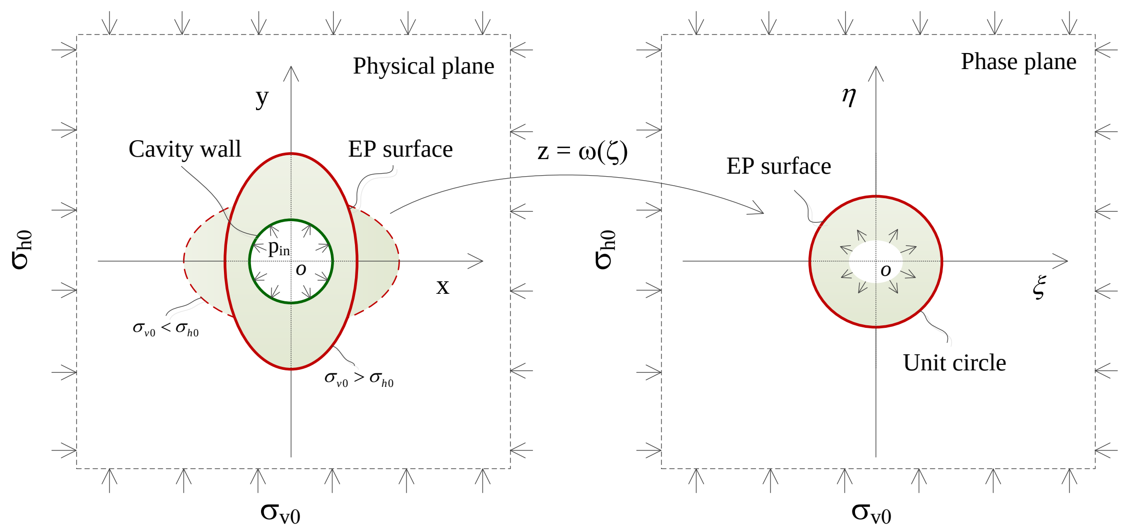

Fig.6.2 Mapping relations between planes

6.3.3 Elastic stress analysis

The determined EP boundary and plastic stresses provide the inner geometry and stress boundaries for calculation of the external elastic field. In fact, a typical elastic stress boundary value problem is constructed, which is equivalent to an elliptical inner cavity embedded in an infinite plane subjecting to non-uniform stresses at the inner cavity wall and non-equal biaxial stresses at infinity. Therefore, a two-dimensional stress analysis is necessarily required, and the complex potential method given by Muskhelishvili (1963) is employed. In view of the stress boundary conditions at the EP boundary given in Eq.(6-11) and Eq.(6-12), it is impracticable to directly derive the elastic complex potentials with simple algebraic transformations. Alternatively, the inner stress boundaries are transformed into Fourier series form. At fist, the elastic complex potentials, $\Phi(\zeta)$ and $\Psi(\zeta)$, in general forms (Muskhelishvili, 1963) are

$$\Phi(\zeta)=\Gamma-\frac{X+iY}{2\pi(1+\chi)}\frac{1}{\zeta}+\Phi_0(\zeta) \tag{6-20}$$

$$\Psi(\zeta)=\Gamma'+\frac{\chi(X-iY)}{2\pi(1+\chi)}\frac{1}{\zeta}+\Psi_0(\zeta) \tag{6-21}$$

where $\Phi_0(\zeta)=\sum_{n=1}^{\infty}\frac{a_n}{\zeta^{n+1}}$, $\Psi_0(\zeta)=\sum_{n=1}^{\infty}\frac{b_n}{\zeta^{n+1}}$, which are holomorphic in the whole elastic region. $\Gamma=P_\infty/2$ and $\Gamma'=\tau_\infty$, which describe the stress conditions at infinity. X and Y are components of the resultant vector of forces acting on the EP boundary from the plastic deformation side. $\chi=3-4\nu$ for the plane strain problem. ν is Poisson's ratio.

The complex potentials are first sought with the assumption that both the stress and displacement components remain bounded at infinity, which implies that the resultant stresses vanish at infinity (Muskhelishvili, 1963). Mathematically, it requires $\Gamma=\Gamma'=0$, $X=Y=0$. In this case, the complex potentials $\Phi(\zeta)$ and $\Psi(\zeta)$ remain holomorphic in the outside region of contour γ. In fact, $\Phi_0(\zeta)$ and $\Psi_0(\zeta)$ fully satisfy above requirements. Hence, the inner stress boundary condition, Eq.(6-11)$_{(a)}$, becomes

$$\Phi_0(\sigma)+\overline{\Phi_0(\sigma)}=k\left\langle \ln\left[\frac{(x_{ep}{}^2+y_{ep}{}^2)/R_0{}^2+\sqrt{(x_{ep}{}^2+y_{ep}{}^2)^2/R_0{}^4-m^2}}{1+\sqrt{1-m^2}}\right]+\sqrt{1-m^2}\right\rangle-p_{in}-P_\infty$$

$$=G(\phi)=\sum_{-\infty}^{+\infty}A_n e^{in\phi}=\sum_{-\infty}^{+\infty}A_n\sigma^n \tag{6-22}$$

where $A_n=\dfrac{1}{2\pi}\int_0^{2\pi}G(\phi)e^{-in\phi}d\phi$. $x_{ep}=\alpha(1+\beta)\cos\phi$ and $y_{ep}=\alpha(1-\beta)\sin\phi$.

In Eq.(6-22), an even function of $G(\phi)$ is formed, which is a continuous real function in terms of the argument ϕ within the interval of $0\le\phi\le 2\pi$. It states that $A_n=A_{-n}$ (real numbers) and coefficients of the odd terms in $\Phi_0(\sigma)$ are infinitesimal. Due to $A_{-n}=\overline{A}_n$ and $\bar{\sigma}=\sigma^{-1}$, it is obvious that both sides of the above equation consist of two conjugate parts. As a result,

$$\Phi_0(\sigma)=A_0/2+\sum_{n=1}^{+\infty}A_{-2n}/\sigma^{2n} \tag{6-23}$$

Calculation shows A_0 naturally is a small value who applies little influence on the result. Hence the requirement of $\Phi_0(\sigma)$ at infinity, $\Phi_0(\infty)=O(\zeta^{-2})$, is basically fulfilled. More strictly in mathematical formulation, the terms with coefficients of A_0 are equivalently modified at the unit circle as

$$\Phi_0(\sigma)+\overline{\Phi_0(\sigma)}=\sum_{n=1}^{+\infty}A_{-2n}\frac{1}{\sigma^{2n}}+\frac{A_0}{2|\sigma|^2}+\frac{A_0}{2}|\sigma|^2+\sum_{n=1}^{+\infty}A_{2n}\sigma^{2n} \tag{6-24}$$

By multiplying both sides with $\dfrac{1}{2\pi i}\dfrac{d\sigma}{\sigma-\zeta}$ (here ζ is a point within ‘ Ω^- ’), and integrating it along the circumference of γ, Eq.(6-24) gives

$$\Phi_0(\zeta)=\frac{A_0}{2|\zeta|^2}+\sum_{n=1}^{+\infty}\frac{A_{-2n}}{\zeta^{2n}} \tag{6-25}$$

Then the general form of $\Phi(\zeta)$ can be recovered by releasing the previous assumption in the process of deriving $\Phi_0(\sigma)$. The resultant vectors still equal to zero ($X=Y=0$) because of the continuous distribution of stresses along the EP boundary. Based on Eq.(6-13), the first complex potential goes to

$$\Phi(\zeta) = \frac{P_\infty}{2} + \Phi_0(\zeta) \tag{6-26}$$

Instead of transforming the second stress continuity condition (Eq.(6-12)$_{(a)}$) into a Fourier series, the second complex potential is obtained by directly integrating it along γ from the Ω^- side with the Cauchy integral method. As discussed in Appendix D, all parts in Eq.(6-12)$_{(a)}$ are holomorphic in Ω^-, therefore it gives

$$\Psi(\zeta) = k\frac{(\beta\zeta^2+1)}{(\zeta^2+\beta)}\left\langle \frac{\sqrt{\hat{r}^4 - m^2R_0{}^4} + mR_0{}^2 i}{\hat{r}^2} \right\rangle - \frac{\zeta(\beta\zeta^2+1)}{\zeta^2-\beta}\Phi'(\zeta) \tag{6-27}$$

where $\hat{r}^2 = \alpha^2(1+\beta^2+\beta\zeta^2+\beta\zeta^{-2})$. $\Phi'(\zeta)$ is the derivative of the complex potential $\Phi(\zeta)$ with respect to ζ, which can be easily calculated with $|\zeta|^2 = \xi^2+\eta^2$ and $\frac{\partial}{\partial\zeta} = \frac{1}{2}(\frac{\partial}{\partial\xi} - i\frac{\partial}{\partial\eta})$.

$$\Phi'(\zeta) = -\frac{A_0}{2\zeta|\zeta|^2} - \sum_{n=1}^{+\infty} 2n\frac{A_{-2n}}{\zeta^{2n+1}} \tag{6-28}$$

A method based on combination use of the Cauchy integral method and Fourier series was presented to solve the encountered stress boundary value problem. More generally, it is capable of dealing with similar elastic problems with a various shaped geometry boundary and arbitrary stress boundaries. Without any difficulties, the elastic stress field can be calculated with Eqs. (6-26), (6-27), (6-29) and (6-30) by separating the real and imaginary parts, but explicit expressions for each stress components are very cumbersome and, therefore, not attempted in this work.

$$\sigma_x^e + \sigma_y^e = 4\,\mathrm{Re}[\Phi(\zeta)] \tag{6-29}$$

$$\sigma_y^e - \sigma_x^e + 2i\tau_{xy}^e = 2[\frac{\overline{\omega(\zeta)}}{\omega'(\zeta)}\Phi'(\zeta) + \Psi(\zeta)] \tag{6-30}$$

6.4 Quasi-static expansion analysis in hydrostatic far-field stresses

When a uniform far-field stress environment is considered, the mapping function of the elastoplastic interface will reduce to $\omega(\zeta) = \alpha\zeta$. The inner pressure during expansion can be expressed as

$$\frac{p_{in}+P_{\infty}^{h}}{k}=2\ln[\frac{r_c}{\delta R_0}]+\sqrt{1-m^2} \tag{6-31}$$

where P_{∞}^{h} is the hydrostatic far-field stress.

Based on Eq.(6-31), providing that the radius ratio (r_c / R) of the EP boundary to the current cavity radius at any expansion moment is known, the quasi-static expansion process under a monotonically increasing expansion pressure p_{in} can be readily modelled. In this special case, the displacement field will remain axisymmetric, therefore the continuous displacement analysis can be conducted as a one-dimensional problem. A small strain theory is adopted in the calculation of the elastic displacement, and a large deformation analysis is carried out for determination of the plastic deformation (Chadwick, 1959; Yu and Houlsby, 1991). The radial elastic displacement is found as

$$u_r=r-r_0=\frac{p_{in}+P_{\infty}^{h}}{2G}(\frac{R}{r})^2 r \tag{6-32}$$

Displacement at the EP boundary should be continuous, and it can be calculated with above elastic solution by replacing p_{in} with p_{r_c} and R with r_c. p_{r_c} is the compression pressure at the EP boundary, which is available by substituting the elastic stress solution in Appendix C (ignoring the angle-dependent terms) into the yield criterion.

$$p_{r_c}=k\sqrt{1-m^2(\frac{R}{r_c})^4}-P_{\infty}^{h} \tag{6-33}$$

When $p_{in}\geq k\sqrt{1-m^2}-P_{\infty}^{h}$, a plastic zone starts forming from the inner cavity wall. Then the radial displacement at the EP boundary becomes

$$u_r\big|_{r=r_c}=\frac{kr_c}{2G}\sqrt{1-m^2(\frac{R}{r_c})^4}=Mr_c \quad (M=\frac{k}{2G}\sqrt{1-m^2(\frac{R}{r_c})^4}) \tag{6-34}$$

Due to the plastic volumetric strain rate is zero for Tresca materials, the compressibility equation (Yu, 2000) in the plastic region becomes

$$\dot{\varepsilon}_r+\dot{\varepsilon}_\theta=\frac{1-2v}{2G}[\dot{\sigma}_r+\dot{\sigma}_\theta] \tag{6-35}$$

With the initial stress boundary conditions, integrating above equation gives

$$\varepsilon_r+\varepsilon_\theta=\frac{1-2v}{2G}[\sigma_r+\sigma_\theta-2P_{\infty}^{h}] \tag{6-36}$$

With use of the definition of logarithmic strain to characterise the accumulative deformation, the radial strain and circumferential strain respectively are

$$\varepsilon_r = \ln\frac{dr}{dr_0} \quad , \quad \varepsilon_\theta = \ln\frac{r}{r_0} \tag{6-37}$$

By substituting the plastic stresses and Eq.(6-37) into Eq.(6-36), it gives

$$\ln[\frac{r}{r_0}\frac{dr}{dr_0}] = \varpi \ln\left[\frac{r^2+\sqrt{r^4-m^2R^4}}{r_c^{\,2}+\sqrt{r_c^{\,4}-m^2R^4}}\right] \quad (\varpi = \frac{(1-2v)k}{G}) \tag{6-38}$$

With use of Eq.(6-34), Eq.(6-38) can be integrated over the interval $[r,\ r_c]$, leading to

$$(1-M)^2 r_c^{\,2} - r_0^{\,2} = \frac{1}{\varpi^2-1}\left[\left(\frac{r_c^{\,2}+\sqrt{r_c^{\,4}-m^2R^4}}{r^2+\sqrt{r^4-m^2R^4}}\right)^{\varpi}(r^2+\varpi\sqrt{r^4-m^2R^4})-(r_c^{\,2}+\varpi\sqrt{r_c^{\,4}-m^2R^4})\right] \tag{6-39}$$

Letting $r = R$ and $r_0 = R_0$, the relation of the radius ratio of r_c / R is finally obtained.

$$\begin{aligned}&(1-M)^2(\frac{r_c}{R})^2-(\frac{R_0}{R})^2\\ &=\frac{1}{\varpi^2-1}\left[\left(\frac{(r_c/R)^2+\sqrt{(r_c/R)^4-m^2}}{1+\sqrt{1-m^2}}\right)^{\varpi}(1+\varpi\sqrt{1-m^2})-[(\frac{r_c}{R})^2+\varpi\sqrt{(\frac{r_c}{R})^4-m^2}\,]\right]\end{aligned} \tag{6-40}$$

So far all stress and deformation information at any expansion stage are available by calculating Eq.(6-31) and Eq.(6-40). While regarding the material as incompressible solution of Zhou et al. (2014a) can be reduced by Eq.(6-40) as

$$\frac{r_c}{R} = \sqrt[4]{\left[\frac{G}{k}[(1-(\frac{R_0}{R})^2]\right]^2+m^2} \quad (\text{case with } v = 0.5) \tag{6-41}$$

It is well-known a limit ratio of r_c / R exists in the continuous displacement analysis, which leads to a limit value of the required expansion pressure. This feature in quasi-static cavity expansion analysis is of great interest in many practical applications. The limit value of r_c / R can be approached by putting $R_0 / R \to \infty$ in Eq.(6-40). When the inner shear stress vanishes, $m = 0$, the limit ratio derived by Yu (2000) for a cavity expanding from zero radius is recovered as shown in Eq.(6-42), if neglecting the small quantities. With further simplification, the well-known limit expansion pressure for a cavity in undrained clays without the shear stress found by Gibson and Anderson (1961) can be recovered as well by substituting the limit 'r_c / R' into Eq.(6-31) as shown in Eq.(6-43).

$$\frac{r_c}{R}=\left[(\varpi-1)(1-\frac{k}{2G})^2+1\right]^{\frac{1}{2(\varpi-1)}} \quad \text{(case with } m=0\text{)} \tag{6-42}$$

$$p_{\mathrm{limit}}=k[1+\ln(\frac{G}{k})]-P_\infty^h \tag{6-43}$$

6.5 Range of admissible applicability of the static stress solution

The closed-form two-dimensional stress solution was achieved based on the aforementioned three fundamental assumptions. These prior assumptions determine that this static stress solution is only rigorously valid within a limited stress range. The admissible application range is discussed with references to the methods of Detournay (1986) and Yarushina et al. (2010).

(1) The cavity is fully enclosed by a plastic region

This restriction is to ensure the cavity is fully encompassed by the plastic region, and the limit condition will be approached once the EP boundary touches the cavity wall at its vertices on the minor axis direction. That is

$$b_{ep}=\alpha(1-|\beta|)\geq R_0 \tag{6-44}$$

(2) Intermediate principal stress

A prior assumption on the principal stresses in the plastic region was applied, which requires the major and minor principal stresses distribute within the studied plane. This assumption can be completely fulfilled for analyses in incompressible materials. While the material compressibility is taken into account, some restrictions will be produced by this assumption. It is known that the plastic principal stresses monotonically increase from the inner cavity wall to the EP boundary. Therefore, it just needs to ensure that values of the out-of-plane stress, σ_{zz}, at the inner cavity wall and the vertices on major axes of the EP boundary always remain as the intermediate principal stress (Yarushina et al., 2010). The principal stresses are calculable with

$$\sigma_1=\frac{\sigma_r+\sigma_\theta}{2}+\left[(\frac{\sigma_r-\sigma_\theta}{2})^2+{\tau_{r\theta}}^2\right]^{1/2} \tag{6-45}$$

$$\sigma_3 = \frac{\sigma_r + \sigma_\theta}{2} - \left[(\frac{\sigma_r - \sigma_\theta}{2})^2 + \tau_{r\theta}{}^2 \right]^{1/2} \tag{6-46}$$

$$\sigma_2 = \nu(\sigma_1 + \sigma_3) \tag{6-47}$$

With Eq.(6-7) Eq.(6-8) and Eq.(6-9), two inequalities are established.

$$\sqrt{1-m^2} - \frac{1}{1-2\nu} \le \frac{p_{in}}{k} \le \sqrt{1-m^2} + \frac{1}{1-2\nu} \tag{6-48}$$

$$\sqrt{1-m^2} - \frac{1}{1-2\nu} + \ln(\Theta) \le \frac{p_{in}}{k} \le \frac{1}{1-2\nu} + \sqrt{1-m^2} + \ln(\Theta) \tag{6-49}$$

where $\Theta = \frac{[\alpha(1+|\beta|)/R_0]^2 + \sqrt{[\alpha(1+|\beta|)/R_0]^4 - m^2}}{1+\sqrt{1-m^2}} > 1$. Furthermore, this restriction can be combined into one inequality as

$$\sqrt{1-m^2} - \frac{1}{1-2\nu} + \ln(\Theta) \le \frac{p_{in}}{k} \le \sqrt{1-m^2} + \frac{1}{1-2\nu} \tag{6-50}$$

(3) Requirement for static determinacy of the plastic zone

A statically determined plastic region is pre-defined before seeking the EP boundary. Theoretically, it implies that every point in the plastic region can be connected to the cavity rim by two characteristic lines (slip-lines) of different families, and every slip-line cuts the EP boundary only once (Hill, 1950). Therefore, a limit condition is reached when there is one, and only one, characteristic line being tangent to the elastic-plastic interface within one quadrant.

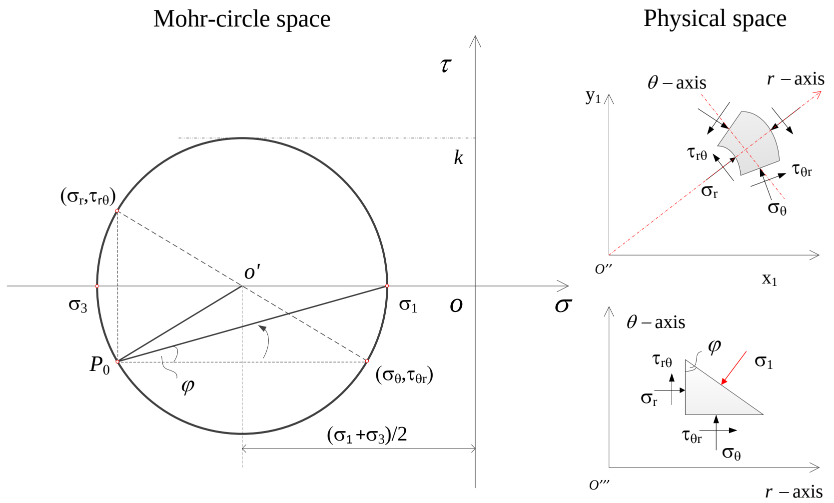

Fig.6.3 Direction of principal stresses

It is known that directions of the slip-lines take an angle of $\pi/4$ with the principal stress directions in the Tresca material. When an inner shear stress is applied, the radial and tangential directions are no longer the principal stress directions. As shown in Fig.6.3, the radial direction of polar coordinates takes a counterclockwise rotation angle to the major principal surface when a positive inner shear stress applied. On the contrary, a clockwise rotation will be caused by a negative inner shear stress. Here taking the clockwise direction of φ as positive, the geometry relation in Fig.6.4 requires

$$|\lambda-\theta| \leq \frac{\pi}{4} \mp \varphi \tag{6-51}$$

where the sign of negative for $\beta \geq 0$, and positive for $\beta \leq 0$.

Angles in above relationship can be uniformly expressed in terms of the variable of σ.

$$e^{2i(\lambda-\theta)} = \sigma^2 \frac{\omega'(\sigma)}{\overline{\omega'(\sigma)}} \frac{\overline{\omega(\sigma)}}{\omega(\sigma)} = \frac{(\sigma^2-\beta)}{(1-\beta\sigma^2)} \frac{(1+\beta\sigma^2)}{(\beta+\sigma^2)} \ ; \ 2\varphi = \arcsin\left[m \frac{R_0^{\ 2}}{\omega(\sigma)\overline{\omega(\sigma)}}\right] \tag{6-52}$$

where $\omega(\sigma) = \alpha(\sigma + \beta/\sigma)$, $\overline{\omega(\sigma)} = \alpha(\sigma^{-1} + \beta\sigma)$.

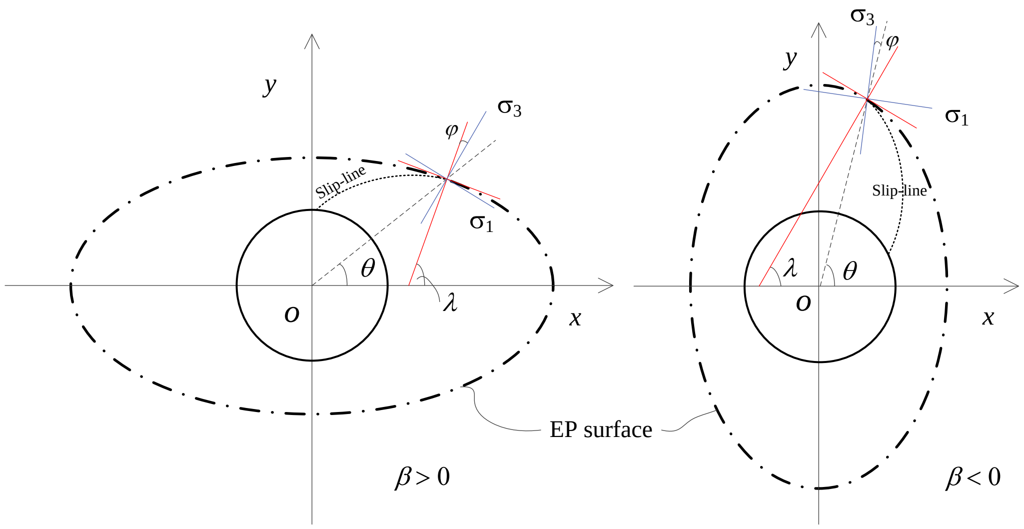

Fig.6.4 Typical conditions for slip-line intersecting with the EP boundary (positive shear stress)

In addition, to guarantee that only one characteristic line reaches the limit condition within the first quadrant, it restricts the equality condition holds only when the function $g(\sigma)$, $g(\sigma) = |\lambda-\theta| \pm \varphi$, reaches its extremum (Detournay, 1986). The extremum values of $g(\sigma)$ lie at the zero points of its derivative. If no shear stress is applied, this restriction can be explicitly expressed as $|\beta| \le (\sqrt{2}-1)$ (Detournay, 1986; Yarushina et al., 2010).

6.6 Results analysis

6.6.1 Calculation procedure of the static stress solution

If the experienced stress conditions lie in the permissible range specified by Eqs. (6-10), (6-44), (6-50), (6-51), the present solution can be employed. With all required formulas presented, results can be calculated with the following procedure.

① Calculate the EP boundary with the known mapping function. Then the plastic stress field can be obtained directly with Eq.(6-7) Eq.(6-8) and Eq.(6-9).

② Calculate the coefficients of the established Fourier series, which stay the same values in the whole elastic filed. ($n=5$ is set in Eq.(6-25) in the following calculation).

③ To get the elastic stresses at one particular point, a one-to-one corresponding relationship between the physical plane and the phase plane is required first, which is available with Eq.(6-53). Accordingly, all elastic stresses are calculable with the derived elastic complex potentials, Eq.(6-26) and Eq.(6-27).

$$x = r\cos\theta = \alpha(\rho + \frac{\beta}{\rho})\cos\phi \ , \ y = r\sin\theta = \alpha(\rho - \frac{\beta}{\rho})\sin\phi \tag{6-53}$$

6.6.2 Verification for stress solution

The present closed-form solution is verified with Galin's solution (1946) first in cases without the internal shear stress. Further validation is carried out by comparing it with results obtained with the finite element method (FEM). The FEM simulations are implemented in Abaqus /Standard 6.12 with the model shown in Fig.6.5. An 8-node biquadratic plane strain quadrilateral element is utilised for meshing, and material properties are set as $\nu = 0.4$, $G/k = 200$.

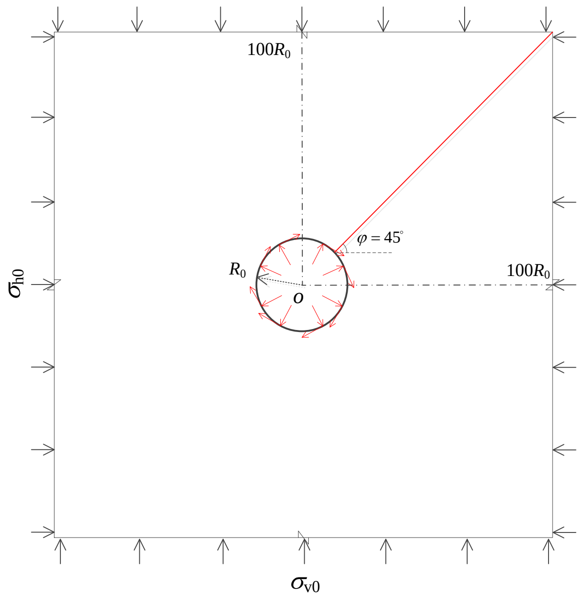

Fig.6.5 Boundary conditions in the FEM model

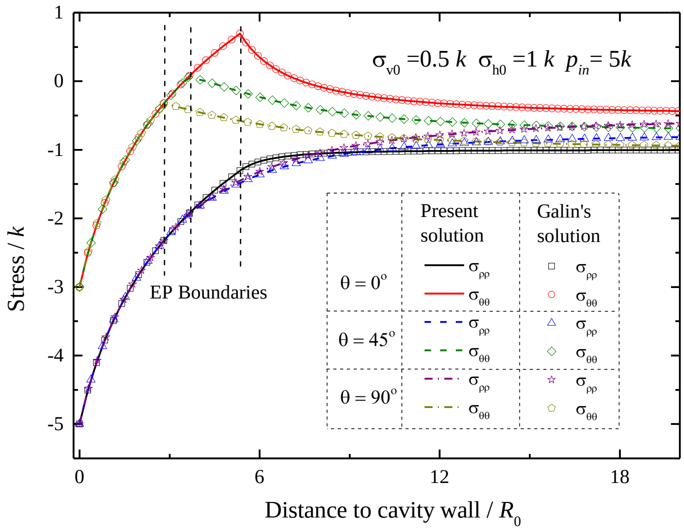

Fig.6.6 Comparison with Galin's solution

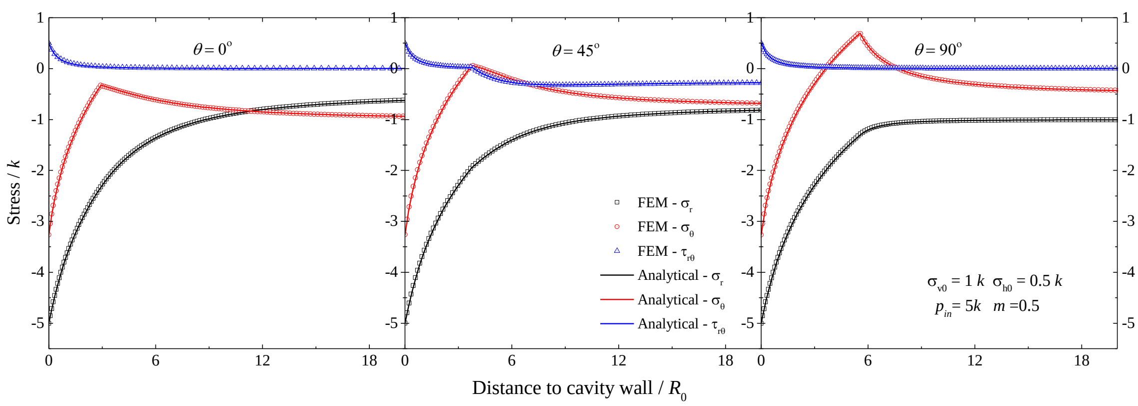

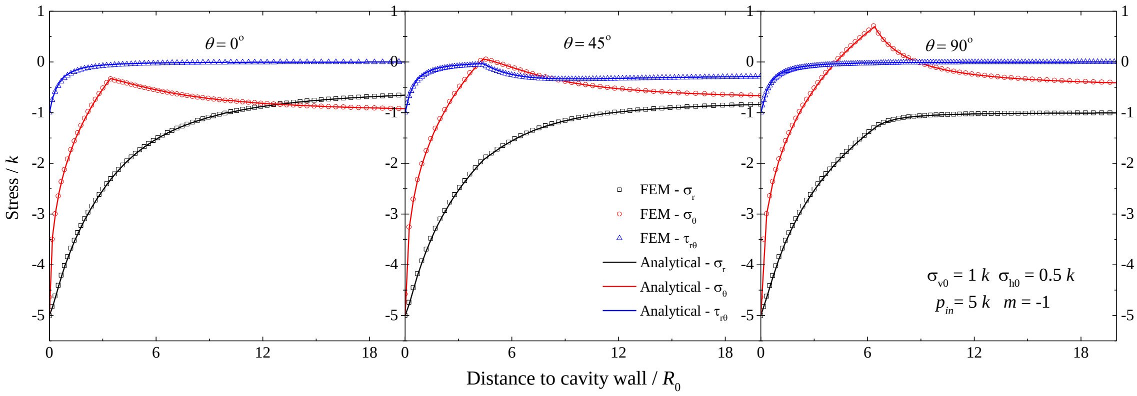

Fig.6.7 Comparison of stress components with FEM results

The problem studied will reduce to the Galin's (1946) problem when no shear stress is present. In this case, it is found that the plastic stress solution and the mapping function of the EP boundary are exactly the same as given by Galin's (1946) solution. Although the elastic complex potentials are not in the same form due to the difference in the method decomposing the stress continuity conditions, figure 6.6 demonstrated the calculated results with them are identical. Furthermore, the calculated stress fields with the present solution are perfectly consistent with the FEM simulation results as presented in Fig.6.7. Additionally, it is proved that the developed series-form elastic complex potentials have good convergence precision and speed.

6.6.3 Influence of inner shear stress on the admissible application range of present solution

With the defined stress boundary conditions, formed stress fields around the inner cavity can be generally categorized into three states, a purely elastic state (zone A), a state when the cavity is partially surrounded by plastic regions (for example, zone B), and a state when the cavity is fully encompassed by a plastic zone (for example, zone C and zone D). The stress field in the purely elastic state can be readily calculated with the solution given in Appendix C. For other two states, the distribution and shape of the formed plastic zones are various (Yarushina et al., 2010), depending on the stress boundary conditions. Some analytical solutions for parts of problems staying in the second state are derived based on the perturbation theory (Bykovtsev and Tsvetkov, 1987; Lozhkin, 2001) or approximate methods (Leitman and Villaggio, 2009). The present stress solution is specifically derived for problems with stress conditions belonging to the Zone C.

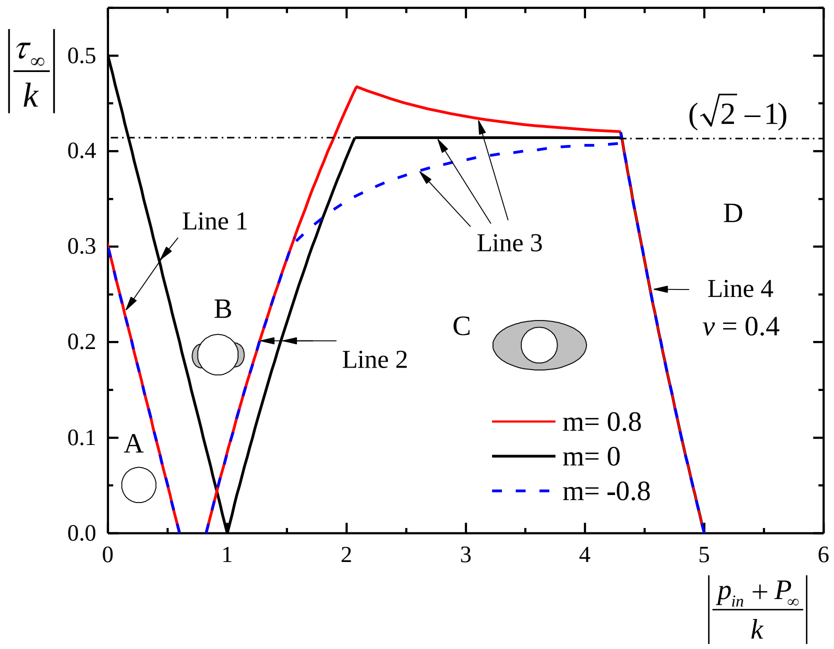

Fig.6.8 Permissible range of stress boundary conditions ($\nu = 0.4$)

Fig.6.8 depicts an admissible application range of the present solution (in zone C) which is calculated with equations (6-10), (6-44), (6-50) and (6-51). For cases without the inner shear stress, the results (black lines) are the same as given by Yarushina et al. (2010). With additional consideration of the shear stress, the permissible range of stress boundaries changes with the applied quantity and direction of the shear stress. Specifically, the stress range of purely elastic deformations shrinks when a shear stress is involved no matter it is positive or negative. Additionally, line 2 determined by Eq.(6-44) moves left with an increasing level of the shear stress. Line 3 represents the static determinacy requirement of the plastic region. For problems without externally applied shear stresses, this dividing line is horizontal with a constant value of $\left|\tau_\infty / k\right| \leq (\sqrt{2}-1)$. However, it becomes curved while a shear stress is applied, which gradually approach to $\left|\tau_\infty / k\right| = (\sqrt{2}-1)$ with increasing $\left|P_\infty + p_{in}\right| / k$. Due to the direction of the applied shear stress determines the rotation direction of principal stresses, opposite influences will be produced by the shear stress with different directions. Consequently, limit bounds of this requirement distribute in oppose sides of the mentioned horizontal line for cases without inner shear stress. Finally, line 4 reflects the requirement of intermediate principal stress as specified by Eq. (6-50). As an example, a line calculated with $p_{in} = 0$ and $\nu = 0.4$ is shown here, and line 4 moves rightwards with an increasing Poisson's ratio and moves left with decreasing values. It is shown the additional shear stress has little impact on this restriction, and it will be released for incompressible materials as previously discussed.

6.6.4 Influence of the inner shear stress on stress distributions

Within above permissible stress conditions, stress redistributions caused by different levels of stresses applied to the cavity wall are presented in Fig.6.9 and Fig.6.10. It illustrates that influences of the additional shear stress mainly concentrate in the plastic region, and the shear stress rapidly attenuates from the applied value at the cavity wall to the stable level that produced by the remote-field stresses.

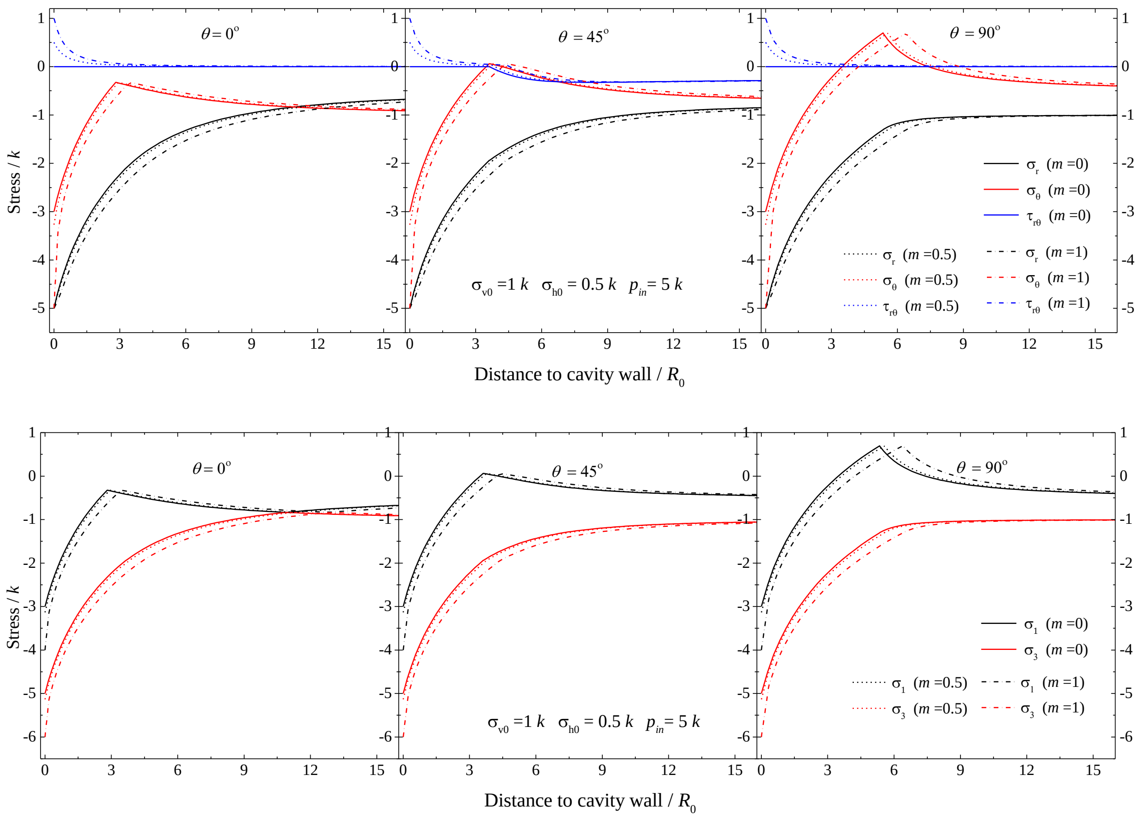

Fig.6.9 Stress distributions changing with the inner shear stress

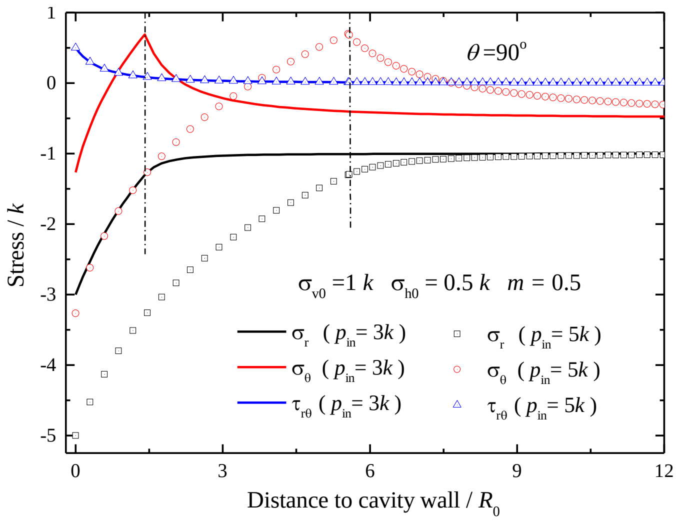

Fig.6.10 Stress distribution changing with internal compression stress

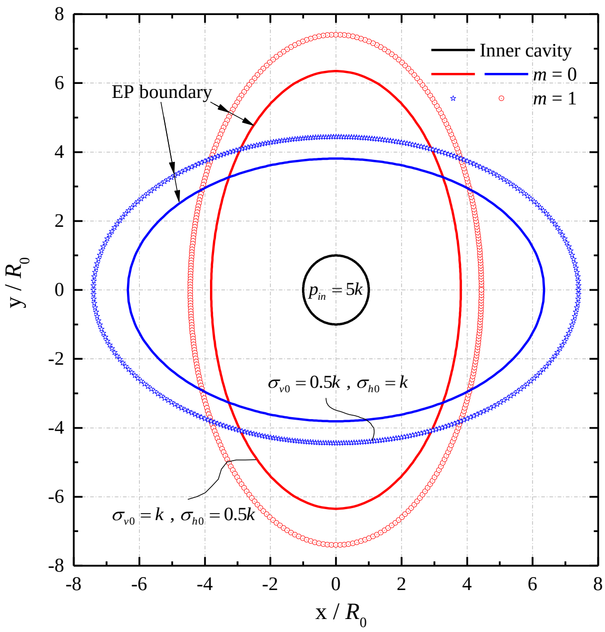

Fig.6.11 Influences of the shear stress on EP boundaries

As shown in Fig.6.11, the additional shear stress at the inner cavity wall extends the range of plastic zone since it increases the principal stresses (as shown in Fig.6.9). But it imposes no influence on the shape of the EP boundary which has a same major to minor axis ratio as $a_{ep}/b_{ep} = (1+|\beta|)/(1-|\beta|)$, and the direction of the major axis of the EP boundary coincides with the direction of minor principal stress at infinity. Specifically, its major axis lies on the defined x-axis direction when $\beta > 0$, and in the direction of y-axis when $\beta < 0$. In addition, the additional shear stress induces continuous rotation of the principal stresses, which must cause differences in the deformation or failure mode of the surrounding material.

6.6.5 Continuous pressure-expansion response

In a quasi-static analysis, both the continuous pressure-expansion curve and the limit expansion pressure are of great interests to engineers (Yu, 2000). The influence of the additionally applied shear stress on these two responses are shown in Fig.6.12 and Fig.6.13. It shows that the required normal pressure during a continuous expansion gets smaller with an increasing shear stress as well as an evident decline of the limit expansion pressure with increases of the applied shear stress. The required limit expansion pressure increases with increases of the Poisson's ratio and the soil shear modulus. With a fully mobilised shear stress (e.g. slip interface), a reduction of 6% of the limit expansion pressure may be produced within the Tresca material, and this influence would be intensified within in materials with higher interface strength.

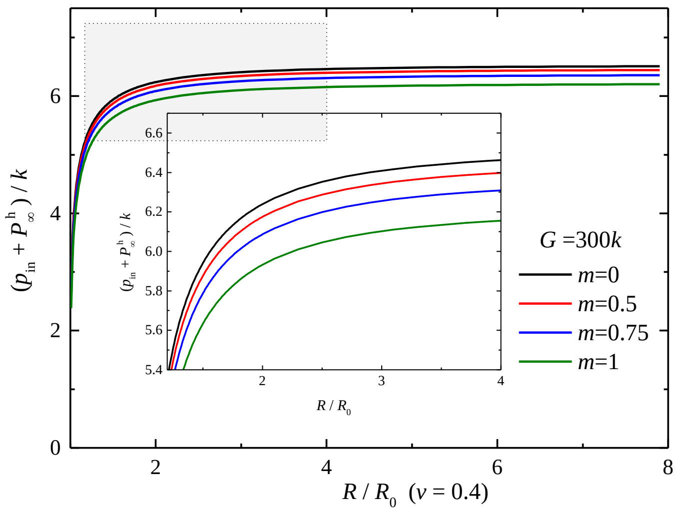

Fig.6.12 Continuous pressure-expansion curves

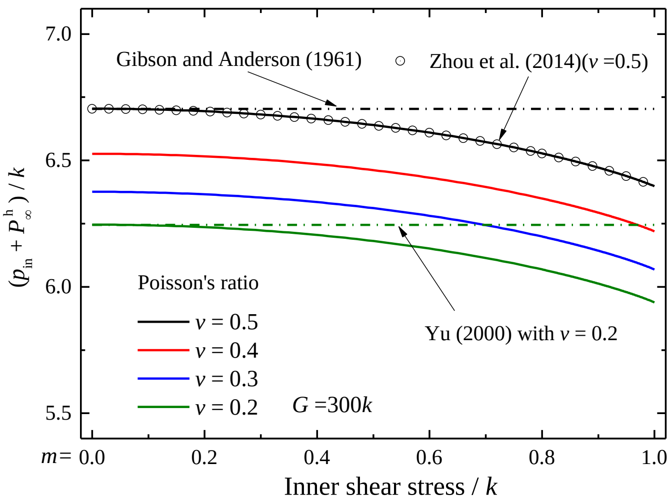

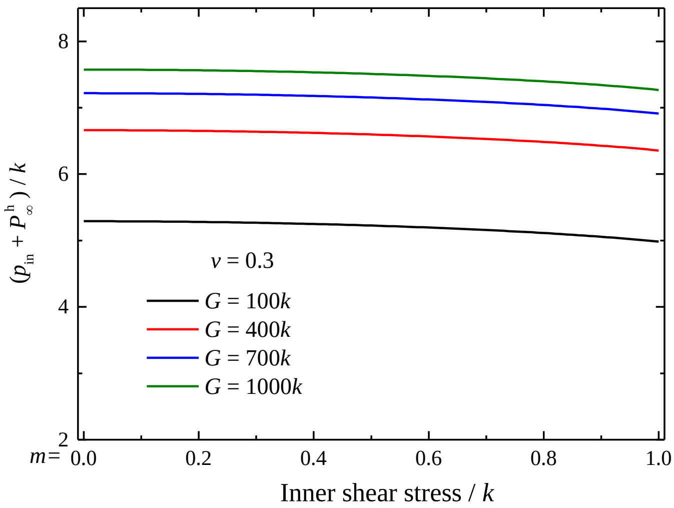

Fig.6.13 Influences of the shear stress on the limit expansion pressure with varying material properties

Quasi-static cylindrical cavity expansion solutions have been successfully applied in many engineering practices, for example, estimation of soil confining pressure along the pile shaft (Turner and Kulhawy, 1994), prediction of tip resistance in cone penetration test (Salgado et al., 1997; Salgado and Prezzi, 2007). With additional consideration of the internal shear stress, the present solution may also be useful in applications to similar problems, for example, estimation of the shaft confining pressure of piles under torsion (Garnier and König, 1998) and interpretation of rotary cone penetration tests (Bengough et al., 1997). Taking the penetration tests (stainless cone with a apex angle of 19^{o} and 2mm in diameter) conducted by Mckenzie et al. (2013) with rotating penetrometers as an example, it was observed that the encountered soil resistance by a rotated probe may even be only 1/(6.7±0.6) of that by the probe without rotation. This significant decrease of the axial soil resistance may be explained from two key aspects. Firstly, the rotation reoriented the vector of surface friction away from the axial direction, so its contribution to the axial cone tip resistance would greatly reduce. This factor may take a relatively large portion of the above resistance decrease, but the influence of the shear stress to the required normal expansion pressure still needs to be taken into account, which is the second factor. In specific, by estimating the cavity expansion pressure with the measured soil resistance with a rotary probe, an obvious overestimation of soil-metal interface friction strength was made by comparing with the normal values (as discussed in the second part of Section 5.1.1). In fact, the required cavity expansion pressure would be reduced due to the mobilised interface shear stress during rotations. Consequently, the soil-metal interface friction strength was overestimated while this reduction was neglected. It demonstrated the necessity of consideration of the mobilised surface shear stress in rotary cone penetration tests. In addition, the soil deformation model triggered by a rotated probe is increasingly cylindrical, especially for the probe with a sharp cone (Bengough et al., 1997). Therefore, the present quasi-static cylindrical cavity expansion solution may be more suitable for interpretation of the rotary cone penetration test in undrained clay.

6.7 Chapter summary and conclusion

A uniform inner shear stress was additionally considered to the classical Galin's problem in this chapter. An explicit mapping function of the EP boundary and closed-form elastic complex potentials to the present problem were completely derived partly based on Parasyuk's (1948) work. An analytical approach for confirming the EP boundary was developed by utilising Laurent's decomposition theorem and Liouville's theorem. With known stress and geometry boundary conditions at the EP boundary, a general approach to calculating the elastic stress field was developed with the Fourier series method and conformal mapping technique. This method can be readily applied to other similar elastic stress analyses for problems of different cavity shapes and various stress boundary conditions. Good agreements were achieved by the present solution in comparison with the Galin's solution and FEM simulation results. It is found the additional shear stress will extend the plastic region, and it has a notable influence on the permissible application range of the present solution. With a large value of $|P_\infty + p_{in}|/k$, the permissible range may be roughly judged with $|\tau_\infty / k| \le (\sqrt{2}-1)$ in practical applications, for example, in controlled laboratory loading tests and in-situ soil or rock mass. Therefore, the static stress solution can be applied to estimate the extent of plastic failure zone and calculate the stress fields around some shear stress involved cavity expansion problems.

In addition, taking the soil compressibility into account, a rigorous large strain displacement analysis of plastic deformation was carried out for a cavity deforming in a hydrostatic initial stress field. With a combination use of the static stress solution and displacement analysis, an analytical quasi-static cavity expansion solution with consideration of the interface shear stress was established. It showed that the interface shear stress has an evident effect on the continuous pressure-expansion response, and it may cause reduction of the limit normal expansion pressure. This solution may be useful in some bearing capacity analyses of rotation involved structures in practice.

Chapter 7

Two-dimensional elastoplastic cavity analysis in Mohr-Coulomb material

7.1 Introduction

Cavity expansion/contraction solutions have been extensively applied in a variety of geotechnical engineering fields (Yu, 2000). Among them, elastic-plastic analyses take up a large proportion due to the high tendency of granular materials to plastic yielding under pressure, especially for soil. In analytical approaches dealing with the cavity expansion/contraction problem, elastic-plastic solutions are often achieved by assuming the cavity (cylindrical or spherical) deforms in a hydrostatic stress environment, which makes a one-dimensional analysis feasible. However, in fact, the earth pressure at rest (e.g. in-situ stress state) is usually non-hydrostatic (Mayne, 2001; Mesri and Hayat, 1993), which is more realistic to treat it as non-equal, at least between the horizontal direction and the vertical direction in engineering practices. For a circular cavity deforming in such initial stress conditions, a two-dimensional elastic-plastic analysis is necessary. This case widely exists in many stress controlled laboratory tests and, more importantly, is increasingly experienced in fast-growing explorations and utilizations of the underground space, for example, deep excavation problems, soil-structure interaction problems etc. (Detournay and John, 1988; Zhou et al., 2016). As known, static stress solutions are able to provide quick and effective methods for calculating stress redistributions and predicting plastic failure ranges around the cavity, which is of great significance in practice. Therefore, a two-dimensional elastic-plastic stress analysis for a circular cavity under loading or unloading condition is carried out in this chapter.

For the sake of simplicity, it is assumed that the circular cavity is embedded in an infinite plane with non-equal biaxial far-field stresses. Depending on the constitutive model of material, the loading path, and the applied stress level, several stress states may occur around the cavity. Specifically, in a linear elastic material, several classical analytical solutions for various stress boundaries were developed, which can be found in many treatises (Muskhelishvili, 1963; Timoshenko and Goodier, 1951). Analytical solutions were also available for power-law materials by constructing a complex pseudo-stress function (Gao et al., 1991; Lee and Gong, 1987). Although non-linear responses of the material were characterised in them, only one stress-strain relation exists in the constitutive model, which determines that the stress and strain components therein can be uniformly expressed with unified biharmonic stress functions. However, in an elastic-perfectly plastic material, different constitutive equations are incorporated to describe the elastic and plastic behaviour separately. So they cannot be physically modelled with one stress function. Alternatively, Galin (1946) first developed an analytical approach for calculating the stress field around an expanding circular cavity based on the Tresca yield criterion. By assuming the plastic state is statically determined, the formed plastic zone was directly obtained by a one-dimensional analysis due to the axisymmetric internal boundary conditions. External elastic stresses were expressed by means of the Kolosov-Muskhelishvili complex potentials (Muskhelishvili, 1963), and the elastic-plastic boundary (EP boundary) was described with the conformal mapping technique. Inspired by this ingenious approach, a large amount of solutions dealing with similar problems within different stress states (Cherepanov, 1963; Leitman and Villaggio, 2009; Parasyuk, 1948; Tokar, 1990), or in different materials (Detournay, 1986; Detournay and Fairhurst, 1987; Tokar, 1990) has been proposed. More detailed information about these developments is available in recent papers from Yarushina et al. (2010) and Ochensberger et al. (2013).

Within the framework of Galin's problem, rigorous analytical stress solutions for a cavity under loading or unloading conditions in the Tresca material were already available (Galin, 1946; Yarushina et al., 2010). However, it is believed that solutions based on the Mohr-Coulomb criterion may be more general and applicable for analyses on granular materials, and main contributions to this specific problem were largely due to Detournay (1986) and Detournay and Fairhurst (1987). As known, the critical step in analytically solving this problem is to determine the EP boundary. As demonstrated by Detournay (1986), a closed-form expression of mapping function for describing the EP boundary in the general case of Mohr-Coulomb material is not readily achievable, if possible. Alternatively, an asymptotic form of mapping function was given by Detournay and Fairhurst (1987) and successfully employed in an unloading analysis. Based on the asymptotic form of mapping function, a combined static solution both for expanding and contracting cavities is developed in Section 7.3. The admissible application range of the developed solution is discussed in the last part of Section 7.3, and both the loading and unloading solutions are evaluated and validated in Section 7.4. Finally, discussions and conclusions about potential applications of the present solution are presented in the end.

7.2 Problem definition

In a homogenous and isotropic infinite plate, an embedded circular cavity is subject to non-equal-biaxial stresses at infinity and a uniform pressure at the inner cavity wall as shown in Fig.7.1. The inner pressure is monotonically loaded or unloaded with a slow enough speed which allows the potential dynamic effect to be ignored. It is assumed that the medium around the cavity deforms in the manner of plane strain. For convenience, both Cartesian coordinates and cylindrical polar coordinates are employed in the stress analysis. The stress boundaries applied at the cavity wall and at infinity are expressed in Eq.(7-1) and Eq.(7-2) respectively.

$$\sigma_{rr}\big|_{r=a} = -p_{in}\ ,\ \sigma_{r\theta}\big|_{r=a} = 0 \tag{7-1}$$

$$P_\infty = (\sigma_y\big|_{y\to\infty} + \sigma_x\big|_{x\to\infty})/2 = -(\sigma_{v0}+\sigma_{h0})/2\ ,\ \tau_\infty = (\sigma_y\big|_{y\to\infty} - \sigma_x\big|_{x\to\infty})/2 = (\sigma_{h0}-\sigma_{v0})/2 \tag{7-2}$$

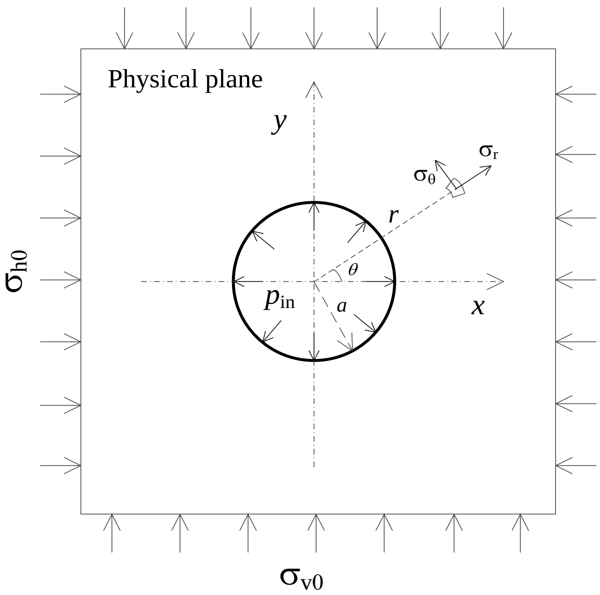

Fig.7.1 Stress boundaries and coordinates

For abbreviation, some functions recurring in the derivation process are expressed first:

$$K_p = (1+\sin\varphi)/(1-\sin\varphi)\ \ ,\ \ Y = 2c\cos\varphi/(1-\sin\varphi)$$

$$\delta = (1-K_p)/(1+K_p) \quad , \quad S_p = \frac{[(1-K_p)P_\infty + Y]}{K_p + 1}$$

where c and φ are cohesion force and friction angle of the Mohr-Coulomb material respectively.

Physical properties of the surrounding material are described with an elastic-perfectly plastic model. Specifically, the elastic response is governed by the generalised Hooke's law, and the plastic behaviour is characterised with the Mohr-Coulomb yielding criterion as in Eq.(7-3).

$$K_p\sigma_1 - \sigma_3 = Y \tag{7-3}$$

where σ_1 and σ_3 are the major and minor principal stress respectively.

7.3 Stress analysis

Due to the non-axisymmetrical nature of the defined stress boundaries, the induced stress field is inevitably non-axisymmetrical, at least partly. So the stress equilibrium condition cannot be solely studied in one direction with a simple coordinate transformation. As first proposed by Galin (1946), a two-dimensional elastic-plastic analysis of the plate in a specific state can be analytically achieved based on some restrictive assumptions. As elaborated by Detournay (1986), the *a priori* assumptions can be briefly expressed as: (1) a plastic zone is developed under pressure, and it is statically determined; (2) the inner cavity is fully encircled by the formed plastic zone.

The first assumption confirmed the necessity of plastic analysis and theoretically postulated that the plastic stress state is completely determined by the inner stress boundary condition (Detournay, 1986; Hill, 1950). The second assumption is to guarantee the elastic field to be bounded internally with a closed simple contour. In this case, calculation of the plastic stress field naturally reduces to a one-dimensional static stress equilibrium problem, and the elastic field becomes an infinite region bounded by the EP boundary, which can be computed with the complex variable theory in elasticity.

7.3.1 Static plastic stress field

With a uniform normal pressure on the cavity rim, the statically determined stress components in the plastic region do not vary with the central angle, and the equilibrium equation in the radial direction can be expressed as

$$\frac{\partial \sigma_r}{\partial r} - \frac{\sigma_\theta - \sigma_r}{r} = 0 \tag{7-4}$$

where σ_r and σ_θ are the radial stress and circumferential stress respectively. Taking tension as positive, the hoop direction is the major principal stress direction for loading cases, and on the contrary, the major principal stress orients in the radial direction for unloading cases. It is assumed that the axial stress (out-plane) always remains as the intermediate stress, which would be satisfied for most of soils (Yu and Houlsby, 1991).

By solving the yielding criterion and equilibrium equation with given inner stress boundaries, the plastic stress components can be obtained (Yu, 2000) as

$$\sigma_r^p = \frac{Y}{K_p - 1} - (p_{in} + \frac{Y}{K_p - 1})(\frac{r}{a})^{(1/K-1)} \tag{7-5}$$

$$\sigma_\theta^p = \frac{Y}{K_p - 1} - \frac{1}{K}(p_{in} + \frac{Y}{K_p - 1})(\frac{r}{a})^{(1/K-1)} \tag{7-6}$$

where r represents the centre radius of one material point. $K = K_p$ for loading cases and $K = 1/K_p$ for unloading cases, which coincides with definitions of the passive model and active model described by Detournay (1986) based on the concept from Rankine's theory.

7.3.2 Elastic-plastic boundary

Confirming the EP boundary is a vital step in current two-dimensional elastic-plastic stress analysis. It determines the outer margin in the calculation of plastic stresses and simultaneously provides the inner boundary for calculating the elastic stress field. In general, the EP boundary is obtained based on the stress continuity conditions of elastic stresses and plastic stresses at the interface. However, the elastic stress field is not available prior to confirming its inner stress and geometry boundaries. Alternatively, the elastic stresses are expressed with the Kolosov-Muskhelishvili complex potentials with an assumed mapping function of the EP boundary. Two typical approaches have been successfully applied to establish the mapping function. The first was proposed by Galin (1946), which is by constructing a combined biharmonic function across the EP boundary on the condition that the plastic stress state is biharmonic just like the elastic stress field. However, this method does not generally suit. Hence, the second group of methods based on Laurent's decomposition theory was developed to deal with more general cases (Cherepanov, 1963; Detournay, 1986). Mapping functions of the EP boundary in Tresca materials have been well obtained in a closed form, but it has not been achieved for the general case of the Mohr-Coulomb material so far. Detournay (1986) first derived an approximate mapping function in a truncated series form for predicting the developed elastoplastic interface of a cavity either undergoing expansion or in a contracting state. A numerical algorithm is required to determine coefficients of the series by seeking roots of a non-linear system of equations. Subsequently, Detournay and Fairhurst (1987) presented a greatly simplified asymptotic mapping function describing the formed EP boundary around an unloading cavity as in Eq.(7-7). Based on the second assumption previously introduced, the EP boundary is a smooth continuous contour, whose shape is independent of the stress applying on the inner cavity wall. So the form of the conformal mapping function would not change with loading directions of the internal boundary pressure. Therefore, the asymptotic form of mapping function in Eq.(7-7) is followed here in both loading and unloading analyses. The upper signs and lower signs in '$\pm$' and '$\mp$' refer to the loading case and the unloading case respectively.

$$\omega(\zeta) = \alpha\zeta(1 \pm \frac{\beta}{\zeta^2})^{(1\mp\delta)} \tag{7-7}$$

where $\zeta = \xi + i\eta = \rho e^{i\phi}$, which describes the position vectors in the phase plane. $i = \sqrt{-1}$. $\omega(\zeta)$ is a function to conformally map the exterior of the EP boundary in the physical plane onto the exterior region of the unit circle in the phase plane. An oval shaped elastoplastic interface is predicted by this mapping function, and the mapping function for Tresca materials (Galin, 1946) will be recovered when the material friction vanishes. $\alpha = \lambda\chi a$, and $\beta = \tau_\infty / S_p$. In the form of Gaussian hypergeometric function, $\lambda^{1-1/K} = {}_2F_1[(\mp\delta, \mp\delta); 1, \beta^2] = 1 + \delta^2\beta^2 + 0(\beta^4)$, and

$$\chi = \left[\frac{(1+1/K)}{2} \frac{[Y + (K_p - 1)p_{in}]}{[Y - (K_p - 1)P_\infty]} \right]^{K/(K-1)} \tag{7-8}$$

It can be found that the introduced 'scaling' factor χ equals to the ratio (r_{ep}^h / a) of the elastoplastic interface radius to the cavity radius for a cavity expanding (Yu and Houlsby, 1991) or contracting (Yu and Rowe, 1999) under a hydrostatic stress environment (uniform stress with value of P_∞ at infinity). Therefore, the size of EP boundary under a non-uniform stress environment predicted with Eq.(7-7) can be directly related to r_{ep}^h, and lengths of its semi-major axis and semi-minor axis are $[\lambda(1+|\beta|)^{(1\mp\delta)}]r_{ep}^{h}$ and $[\lambda(1-|\beta|)^{(1\mp\delta)}]r_{ep}^{h}$ respectively. Conceptually, the EP boundary is flattened by the non-equal biaxial far-field stresses from a circle shape under corresponding hydrostatic stress conditions, and $[\lambda(1+|\beta|)^{(1\mp\delta)}]$ and $[\lambda(1-|\beta|)^{(1\mp\delta)}]$ are just like two shape factors describing the flat ratio of the non-circular EP boundary, which only depends on the friction angle and far-field stress obliquity (β). In essence, the EP boundary deforms in a self-similar manner within this state. In addition, for frictionless material, the EP boundary becomes an ellipse, and corresponding shape factors are $(1+|\beta|)$ and $(1-|\beta|)$ respectively.

7.3.3 Elastic stress field

Based on the plastic stress components and Kolosov-Muskhelishvili elastic complex potentials, $\Phi(\zeta)$ and $\Psi(\zeta)$ (Muskhelishvili, 1963), continuity conditions of the mean stress and the deviatoric stress along the elastoplastic interface can be expressed as

$$\Phi(\zeta)+\overline{\Phi(\zeta)}=\frac{(\sigma_r^e+\sigma_\theta^e)}{2}=\begin{cases}\dfrac{Y}{K_p-1}-S_p\dfrac{(K_p+1)}{(K_p-1)}\left(\dfrac{r}{\chi a}\right)^{(1/K-1)} & ,\ \text{at } \gamma \quad \text{(a)}\\ P_\infty & ,\ \zeta\to\infty \quad \text{(b)}\end{cases} \tag{7-9}$$

$$\frac{\overline{\omega(\zeta)}}{\omega'(\zeta)}\Phi'(\zeta)+\Psi(\zeta)=\frac{(\sigma_\theta^p-\sigma_r^p+2i\tau_{r\theta}^p)}{2}e^{-2i\theta}=\begin{cases}\pm S_p\left(\dfrac{r}{\chi a}\right)^{(1/K-1)}\dfrac{\overline{\omega(\sigma)}}{\omega(\sigma)} & ,\ \text{at } \gamma \quad \text{(a)}\\ \tau_\infty & ,\ \zeta\to\infty \quad \text{(b)}\end{cases} \tag{7-10}$$

where Γ represents the contour of EP boundary in the physical plane, which corresponds to γ which is the contour of the unit circle centred at the origin of the reference phase plane. $\overline{\omega(\zeta)}$ is the conjugate of $\omega(\zeta)$. σ is the complex variable on the unit circle, and $\bar{\sigma}=1/\sigma$.

The infinity values of these two complex potentials are specified with the far-field stress conditions as

$$\Phi(\infty)=\frac{P_\infty}{2}+O(\zeta^{-2})\quad,\quad\Psi(\infty)=\tau_\infty+O(\zeta^{-2}) \tag{7-11}$$

Based on their behaviours at infinity, we extracted the purely holomorphic parts of $\Phi(\zeta)$, that is $\Phi_0(\zeta)$ ($\Phi_0(\infty)=0$), to analyse the mean stress continuity condition along the EP boundary as

$$\Phi_0(\sigma)+\overline{\Phi_0(\sigma)}=S_p\frac{(K_p+1)}{(K_p-1)}[1-(\frac{r}{\chi a})^{(1/K-1)}] \tag{7-12}$$

where $(\frac{r}{\chi a})^{(1/K-1)}=\left[\frac{\omega(\sigma)\bar{\omega}(\sigma^{-1})}{(\chi a)^2}\right]^{\frac{(1/K-1)}{2}}=\lambda^{(1/K-1)}[(1\pm\beta\sigma^{-2})^{\pm\delta}(1\pm\beta\sigma^{2})^{\pm\delta}]$. Based on the binomial expansion formula, parts of this equation can be expressed as

$$(1\pm\beta\sigma^{-2})^{\pm\delta}=\sum_{k=0}^{\infty}\binom{\pm\delta}{k}(\pm\beta)^k\sigma^{-2k}\quad,\quad(1\pm\beta\sigma^{2})^{\pm\delta}=\sum_{k=0}^{\infty}\binom{\pm\delta}{k}(\pm\beta)^k\sigma^{2k} \tag{7-13}$$

Accordingly, the right part of Eq.(7-12) is easy to be split into two functions which are mutual conjugates and analytic in Ω^+ ($|\zeta|<1$) and Ω^- ($|\zeta|>1$) respectively. The parameter λ is determined by the requirement of its zero-order term to be equal to zero. Eq.(7-12) gives the inner boundary value of $\Phi_0(\zeta)$, hence $\Phi_0(\zeta)$ can be directly obtained with the Cauchy integral method.

$$\Phi_0(\zeta)=-S_p\frac{(K+1)}{(K-1)}\sum_{j=1}^{\infty}\frac{d_{2j}}{\zeta^{2j}} \tag{7-14}$$

where $d_{2j}=\lambda^{(1/K-1)}(\pm\beta)^j\binom{\pm\delta}{j}{}_2F_1[(\mp\delta,\mp\delta+j);j+1,\beta^2]$.

Considering the boundary conditions at infinity, complete expression of the first complex potential is finally reached as

$$\Phi(\zeta)=\frac{P_\infty}{2}+\Phi_0(\zeta) \tag{7-15}$$

The deviatoric stress continuity condition, Eq.(6-12)$_{(a)}$, was not fully satisfied in the deduction of Detournay and Fairhurst (1987) for the unloading analysis. As a result, stress discontinuity was produced along the EP boundary therein. This was attributed to the error that resulted from the approximate nature of the asymptotic mapping function. In fact, as long as the position of EP boundary and stresses along it are known, the elastic stress field becomes a typical boundary value problem. Therefore, stresses across the given EP boundary are necessarily continuous, and the second complex potential, $\Psi(\zeta)$, is directly explored with the Cauchy integral method. Parts of each side in Eq.(6-12)(a) are discussed as

$$\frac{\overline{\omega(\sigma)}}{\omega'(\sigma)}\Phi'(\sigma)=\frac{1}{\sigma}(\frac{\sigma^2\pm\beta}{\sigma^2\mp\beta\mp 2\beta\delta})[\frac{\sigma^2(1\pm\beta\sigma^2)}{\sigma^2\pm\beta}]^{(1\mp\delta)}\Phi'(\sigma)=g_1(\sigma) \tag{7-16}$$

$$(\frac{r}{\chi a})^{(1/K-1)}\frac{\overline{\omega(\sigma)}}{\omega(\sigma)}=(\lambda)^{(1/K-1)}[1+\beta^2\pm\beta\sigma^2\pm\beta\sigma^{-2}]^{\pm\delta}\frac{1}{\sigma^2}[\frac{\sigma^2(1\pm\beta\sigma^2)}{\sigma^2\pm\beta}]^{1\mp\delta}=g_2(\sigma) \tag{7-17}$$

where $g_1(\sigma)$ is holomorphic in the whole Ω^- and equal to zero at infinity since $\Phi'(\infty)=O(\sigma^{-3})$. $g_2(\sigma)$ is holomorphic in the whole Ω^- and of value at infinity as $g_2(\infty)=\pm\beta\lambda^{(1/K-1)}$.

By multiplying $\frac{1}{2\pi i}\frac{d\sigma}{\sigma-\zeta}$ on both sides of Eq. (6-12)(a) and then integrating it along the unit circle in the phase plane from the side of Ω^-, the second complex potential is obtained as

$$\Psi(\zeta)=\pm S_p\left[\hat{r}(\zeta)\right]\frac{1}{\zeta^2}\left[\frac{\zeta^2(1\pm\beta\zeta^2)}{\zeta^2\pm\beta}\right]^{1\mp\delta}-M(\zeta)\Phi'(\zeta)+[1-\lambda^{(1/K-1)}]\tau_\infty \tag{7-18}$$

where $\hat{r}(\zeta)=\lambda^{(1/K-1)}[1+\beta^2\pm\beta\zeta^2\pm\beta\zeta^{-2}]^{\pm\delta}$,

$$M(\zeta)=\frac{1}{\zeta}(\frac{\zeta^2\pm\beta}{\zeta^2\mp\beta\mp 2\beta\delta})[\frac{\zeta^2(1\pm\beta\zeta^2)}{\zeta^2\pm\beta}]^{(1\mp\delta)},\ \Phi'(\zeta)=S_p\frac{(K+1)}{(K-1)}2j\sum_{j=1}^{\infty}\frac{d_{2j}}{\zeta^{2j+1}}.$$

The present derivation of $\Psi(\zeta)$ is more rigorous and straightforward, and its last term vanishes when the frictionless material is considered. In fact, its appearance is due to the small difference of the employed asymptotic mapping function to the exact one. Finally, the elastic stress components are calculable with

$$\sigma_x^e+\sigma_y^e=4\,\mathrm{Re}[\Phi(\zeta)] \tag{7-19}$$

$$\sigma_y^e-\sigma_x^e+2i\tau_{xy}^e=2[\frac{\overline{\omega(\zeta)}}{\omega'(\zeta)}\Phi'(\zeta)+\Psi(\zeta)] \tag{7-20}$$

7.3.4 Permissible range for application

Two fundamental assumptions were adopted in the above derivation, which determined that the solution better serves for the plane under a specified stress state. Firstly, the plastic zone is statically determined, which means that points on the cavity rim are connected with the EP boundary with two families of characteristic lines, and each characteristic line cuts the EP boundary only once (Hill, 1950). Accordingly, limit conditions will be reached when one characteristic line becomes tangent to the elastic-plastic interface as given in Eq.(7-21). The second restriction is to ensure the cavity is completely encompassed by a connected plastic region, and it can be discussed with the Kirsch solution (Detournay, 1986) as in Eq.(7-22).

(1) Static determinacy of plastic zone

$$e^{2i(\lambda-\theta)}=\sigma^2\frac{\omega'(\sigma)}{\overline{\omega'(\sigma)}}\frac{\overline{\omega(\sigma)}}{\omega(\sigma)}=\frac{\sigma^2\mp\beta+2\beta\delta}{\sigma^2\mp\beta+2\beta\delta}=\pm ie^{\pm i\varphi} \tag{7-21}$$

It is shown that the limit condition of this requirement is a relation between the far-field stress obliquity (β) and the friction angle. To meet this requirement at any point of the whole field, this limit condition is only reached at which ($\lambda-\theta$) is extremum (Detournay, 1986). By solving Eq.(7-21) at its extremum, upper limits of $|\beta|$ from this requirement are shown in Fig.7.2. The same results are obtained as those given by Detournay and John (1988) for unloading cases as expected. In contrary to the unloading case, the upper limit decreases with increases of the friction angle in loading analyses. When the friction angle reaches zero, the critical values of $|\beta|$ for loading and unloading cases coincide, which is $\sqrt{2}-1$ (the same value was obtained by Yarushina et al. (2010) with a different method).

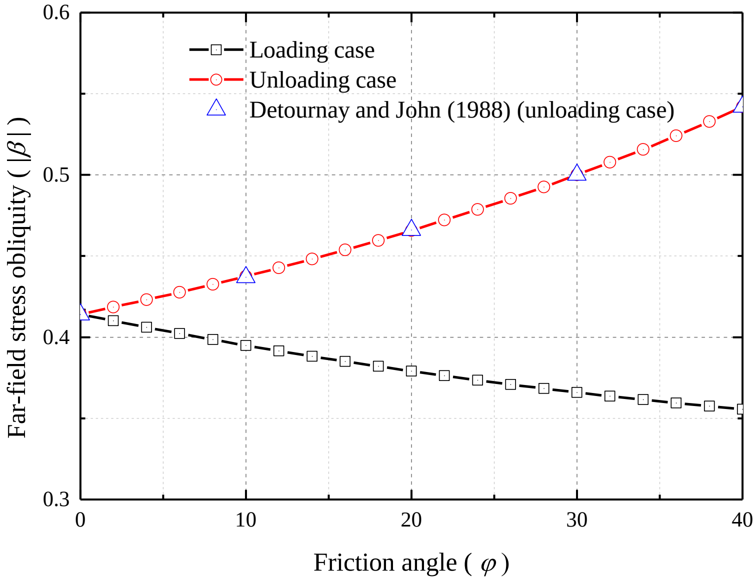

Fig.7.2 Variation of limit far-field stress obliquity with friction angle

（2）Cavity fully enclosed by the plastic zone

$$p_{in}\big|_{\text{loading}} \geq \frac{Y}{K_p+1} - \frac{2K_p}{K_p+1}(P_\infty - 2|\tau_\infty|),\ \ p_{in}\big|_{\text{unloading}} \leq -\frac{Y}{K_p+1} - \frac{2}{K_p+1}(P_\infty + 2|\tau_\infty|) \quad (7\text{-}22)$$

7.4 Results comparison and analysis

Thus far, the static elastic-plastic stress solution for the defined problem has been obtained, and both a loading and an unloading analysis can be analytically achieved. The solution for loading cases is validated by comparing with FEM (finite element method) simulation results and Galin's solution (1946) (as a special case: frictionless material). The solution for unloading conditions is compared with Detournay and Fairhurst's (1987) solution and Yarushina et al.'s solution (2010) (as a special case: frictionless material).

7.4.1 Stress field comparison

(1) Validation of solution for loading cases

The FEM simulation is implemented in Abaqus/Standard 6.12 using a quarter model as shown in Fig.7.3. An 8-node biquadratic plane strain quadrilateral mesh is utilised for meshing. The constitutive model, material properties, and stress conditions are kept the same as those in derivations with the analytical solution. The void ratio is set as 0.4, and other properties are presented in the figures. All results are presented in non-dimensional forms (all stresses are normalised with the cohesion force, and all geometry dimensions are normalised with the initial cavity radius).

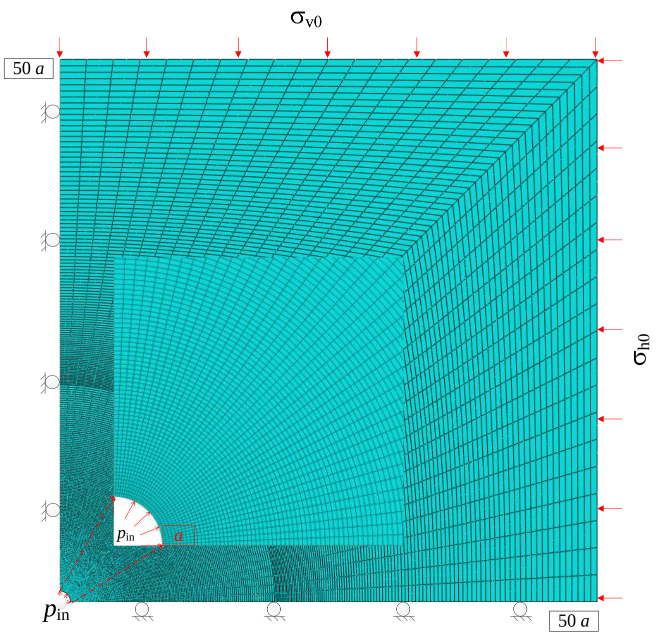

Fig.7.3 FEM model and mesh

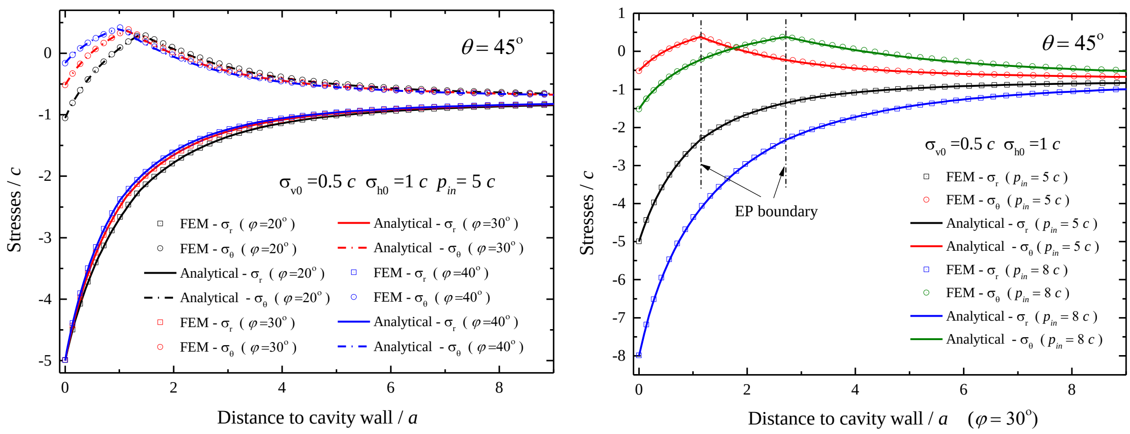

Fig.7.4 Stress distribution with varying friction angle and inner pressure (loading cases)

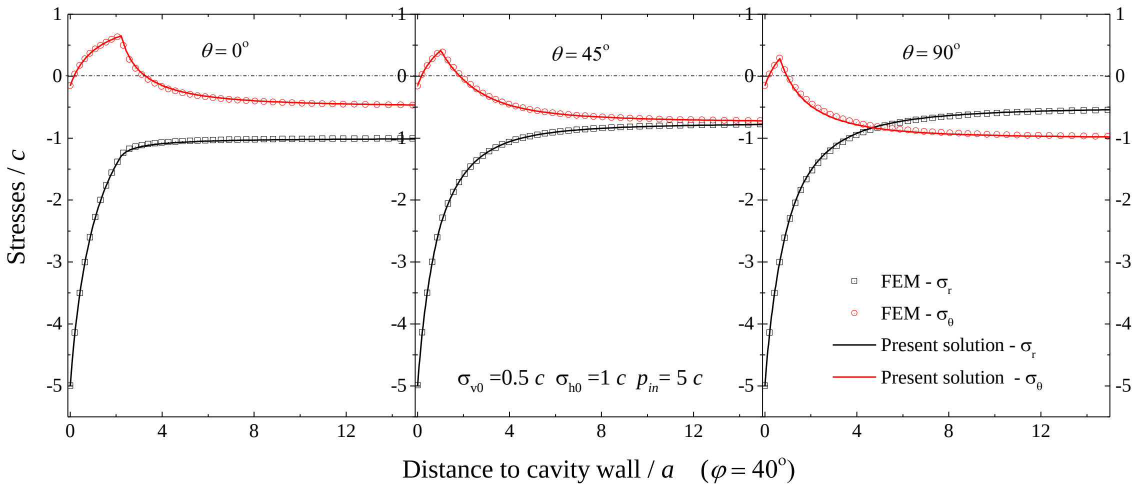

Fig.7.5 Stress distribution along different directions (loading case)

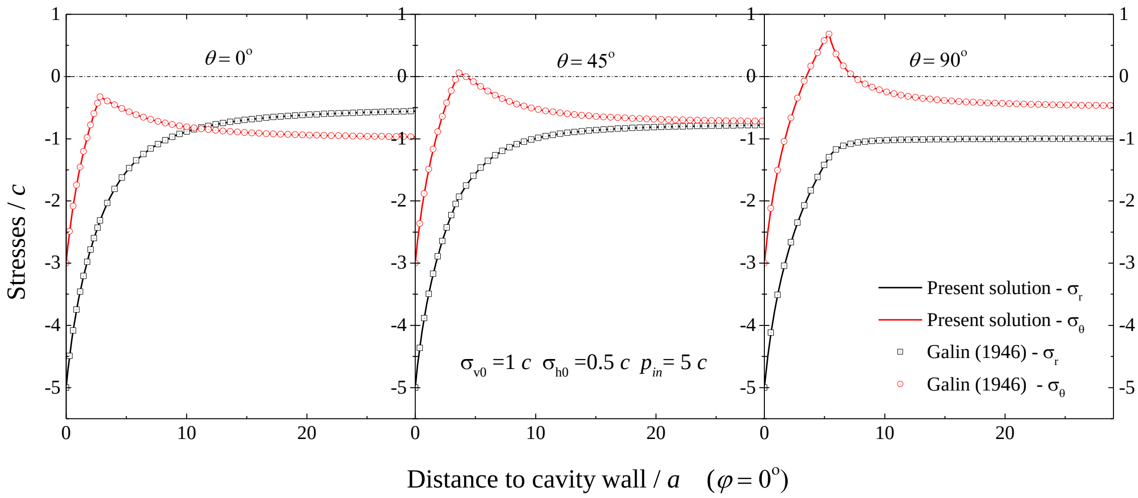

Fig.7.6 Comparison with Galin's solution (1946) (loading case)

Firstly, stresses calculated with the present solution perfectly agree with the numerical simulation results in cases with varying friction angles and stress levels, and the Galin's solution (1946) for frictionless material can also be exactly recovered. It demonstrates that high accuracy with the asymptotic form of mapping function in predicting the formation of EP boundary is achieved. The developed complex potentials also provide an accurate calculation of the stress field around a circular cavity expanding in the Mohr-Coulomb material. In addition, it is shown that, under non-equal biaxial remote-field stresses, not only the extent of the plastic region is angle-dependent, the stress distribution, particularly developments of the tensile stress in the circumferential direction, also varies in directions. This information might be of significance in predicting the failure zone or the most likely potential area of cracks developing around an internally pressurised cavity in engineering practices.

(2) Validation of solution for unloading cases

In Detournay and Fairhurst's (1987) solution, it stated that the elastic stress field and the plastic stress field may be discontinuous along the interface. Therefore, the complex potentials of elasticity were re-derived in this research. Results computed with these two solutions are compared in Fig.7.7. It is shown that they gives almost identical results, and the discontinuous phenomenon of stresses along the elastic-plastic interface is not serious with given stress boundaries and material properties. However, it is noteworthy that the stress discontinuity phenomenon will be amplified if the method of Detournay and Fairhurst is directly applied in a loading analysis. In addition, when the friction angle gets close to zero, the present solution also shows good agreement with results obtained with the unloading-type stress solution given by Yarushina et al. (2010) for Tresca materials. In practice, this solution may provide a quick and effective routine to predict the plastically failed zone around an unloading cavity. For example, the application in predicting the size and shape of failed rock regions around a deep tunnel during excavation within non-uniform in-situ stresses (Detournay and John, 1988).

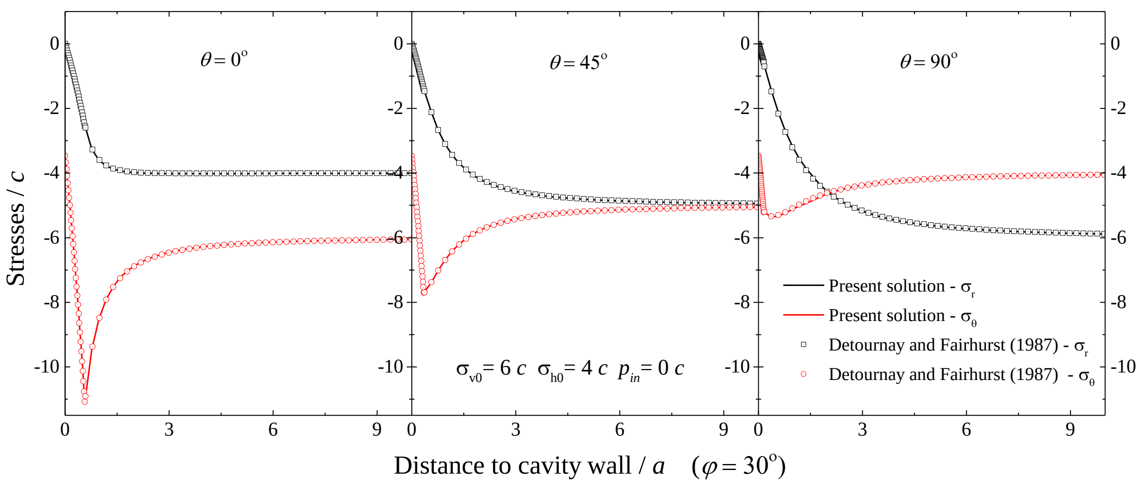

Fig.7.7 Comparison with Detournay and Fairhurst's solution (1987) (unloading case)

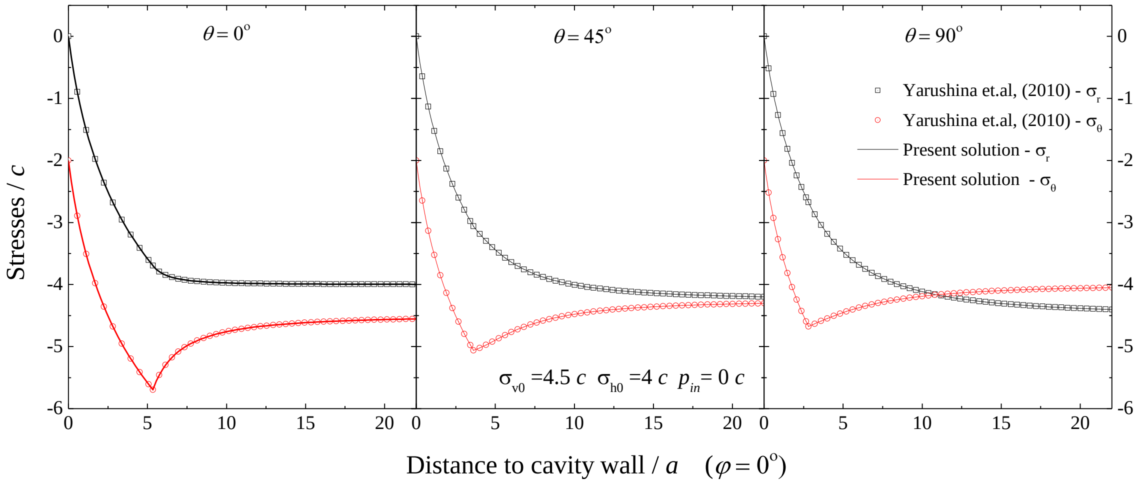

Fig.7.8 Comparison with unloading stress solution for frictionless material

7.4.2 Elastic-plastic interface

Ranges of the plastic deformation with varying friction angles, stress levels and loading types are calculated with Eq.(7-7) as shown in Fig.7.9 and Fig.7.10. The accuracy of this asymptotic mapping function is validated again with the available analytical solutions for frictionless material from Galin (1946) and Yarushina et al. (2010). The developed plastic regions around a cavity under loading and unloading are presented separately. It is corroborated that the axes direction of the EP boundary is determined by the directions of principal stresses at infinity and the loading type. Specifically, under loading conditions, the major axis of the EP boundary coincides with the direction of greatest compression stress at infinity. On the contrary, it lies in the direction of far-field major principal stress for cavity under unloading conditions. In addition, it shows the oval shaped EP boundary shrinks with an increasing friction angle in both loading and unloading conditions. When the friction angle is relatively small (such as 15°), the friction strength has a relatively larger influence on the size of the plastic zone.

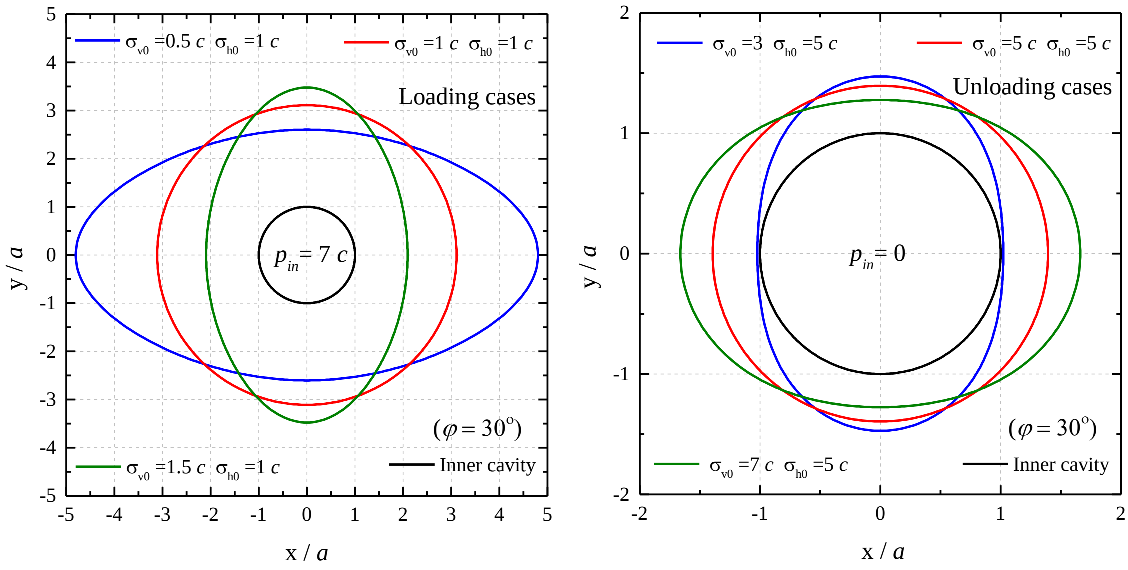

Fig.7.9 Variation of the EP boundary with the stress level

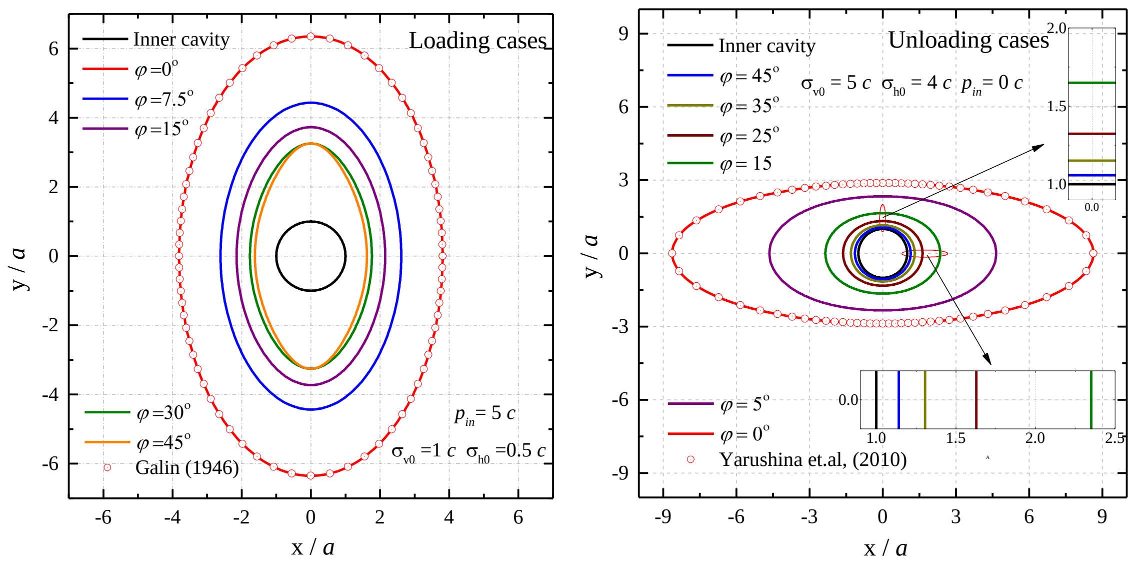

Fig.7.10 EP boundary varying with the friction angle

7.5 Discussion and chapter conclusion

If a kinematic solution of the displacement field is available, the present static solution can be directly applied in a quasi-static analysis which of great interest for engineers in estimating the identification/penetration resistance or ultimate bearing capacity of structures on soil (Yu, 2000). In the present solution, the elastic displacement field is already available with the obtained two elastic complex potentials. However, due to the non-axisymmetric nature of the plastic deformation zone under non-uniform far-field stresses, a two-dimensional deformation analysis in the plastic region is necessarily required, which is not easy to be achieved analytically, if at all possible. Theoretically, the governing equation system of the plastic displacement field is hyperbolic. It is known the method of characteristic is appropriate in solving this type of equations, such as that done by Detournay and Fairhurst (1987) (in the framework of small deformation theory). No rigorous analytical large deformation analysis is available so far, of which the compatibility equation will be more sophisticated. More importantly, the non-axisymmetrical displacement of the inner cavity will lead to the present stress solution no longer rigorously valid in a continuous deformation process. So a rigorous continuous pressure-deformation analysis for general cases under present stress conditions might be not possible in an analytical manner. Alternatively, for the purpose of application, an approximate method may be achievable based on some available findings. In specific, it was found that the obtained EP boundary moves in a self-similar manner in the defined state. Its size was directly related to the radius of EP boundary in the corresponding hydrostatic stress condition, and its shape can be back-calculated with the known shape factors. Detournay and Fairhurst (1987) found the average displacement of the cavity rim could be well predicted by the solution for a cavity deforming in the hydrostatic stress condition. Zhou et al. (2016) also demonstrated that the radial displacement does not significantly vary with the central angle for the cavity within a Tresca material under non-equal biaxial stress at infinity. Accordingly, by assuming the cavity also deforms in a self-similar manner during the continuous expansion or contraction (Zhou et al., 2014b), an approximate quasi-static expansion/contraction analysis may be obtained with the present static stress solution and the average radial displacement calculated with available one-dimensional displacement solutions (e.g. those presented by Yu (2000)). It may have great application potentials, but much attention should be paid to evaluate and quantify its accuracy in future works, especially when a large deformation analysis is considered.

The analytical stress analysis is achieved on the basis of two *a priori* assumptions which make the one-dimensional analysis on the plastic stress field valid and ensure the existence of a continuous EP boundary as a simple contour in advance. Meanwhile, these two assumptions specified a permissible application range of this solution which depends on the far-field stress obliquity (β) and friction angle. This admissible range should be kept in mind in applications with this kind of methods since its accuracy will reduce with the increase of $|\beta|$. The present solution is capable of acquiring the information about developments of the plastic deformation and stress distribution around a circular cavity either under loading or unloading conditions. Detournay and John (1988) presented a good application of the unloading stress solution, which was used to predict the size and shape of the failed rock region caused by the excavation of a deeply buried tunnel. In loading cases, the major axis of EP boundary distributes along the opposite direction even with the same directions of the initial principal stresses. So in analyses (or designs) of deeply buried pressure tunnels or pipes (analogy to an expanding cavity), the present loading-type stress solution can be used to acquire the same type of information.

Chapter 8

Conclusions and suggestions

8.1 Summary and remarks

(1) Size dependency of cone penetration resistance

Cone penetrometers of various sizes have been used in soil explorations for different purposes, and significant size differences of the cone resistance were often reported as reviewed at the beginning of Chapter 2. To account for this size effect, a series of cone penetration tests with 3 different sized penetrometers were performed in the Leighton Buzzard sand of two size fractions with different relative densities as introduced in Chapter 2. Evident size effects in the cone resistance were observed, and they were explained in detail in Chapter 4. It was found:

(a) The interface friction strength may strongly depend on the normalised surface roughness (R_a / d_{50}). For interfaces lying in the intermediate rough zone specified by Fig. 4-8 or Fig. 4-9, the interface friction angle would be very sensitive to the variation of R_a / d_{50}. This may be one main influence of the particle size variation to the cone penetration test.

(b) The mobilised lateral confining pressure in sands depends on the penetrometer size and particle size when their ratio (D / d_{50}) is relatively small (e.g<100).

(c) The relative embedment effect (H / D) has a significant contribution to the size difference of the cone penetration resistance at relatively shallow depths, and the size effect in deep penetrations may be mainly determined by the stress-level and/or strain level dependency of the sand strength.

A size-dependent cavity expansion solution has been developed in Chapter 3 to theoretically quantify the observed size effect in the cone penetration resistance. Based on the classical elastic-perfectly-plastic cavity expansion solution from Yu and Houlsby (1991), a second-order strain gradient was introduced into the Mohr-Coulomb yield criterion for sands to take the size effect into account. A second order governing equation system was established, and complete solutions were numerically calculated with a simple iteration procedure. Different degrees of the size-dependant pressure-expansion response of a cylindrical/spherical cavity can be described by the present solution, and it can fully recover to the conventional solution when a relatively large cavity is concerned or no size-strengthening effect is performing. It assumed that ρ is constant in the present solution. By comparing with some available experimental data of cone penetration tests, it was found this assumption may give satisfactory descriptions of the concerned size effect in miniature cone penetration tests (e.g. $D/d_{50} > 5$). However, for interpretations of tests with more significant size effect (e.g. in some needle penetration tests), improved solutions with non-constant H_g $(=\rho(G/\sigma_{atm}))$ or methods with different inclusions of the strain gradient terms may be required. It was found the introduced empirical coefficient ρ may vary with the sand type, relative density, particle size and the penetrometer size. Overall, the present size-dependent cavity expansion solution can provide a feasible theoretical approach to describe the widely observed size effect in end bearing problems, but more effort is required for a better quantitative analysis. Or the cone penetration tests with different penetrometer sizes may provide a simple experimental way to quantify the non-local property of materials (e.g. H_g).

(2) Size dependency of shaft friction

Apart from the aforementioned size effect in the tip resistance, the size-dependent behaviour may also play a significant role in determining the shaft frictional resistance as observed in present tests and reported by other researchers (discussed in Chapter 4). This scale effect was mainly studied from two aspects, the interface friction strength and the shear-mobilised lateral confining stress, in this research. It was found that the interface friction strength greatly depends on the normalised surface roughness (R_i / d_{50}) especially when it varies in the intermediate roughness zone. An empirical formula in terms of R_i / d_{50} for estimating the critical state interface friction angle of silica sands was fitted based on some existing experimental data, and it was adopted in interpretations of the present penetration tests. Then the commonly used elastic static cavity solution for estimating the mobilised lateral stress was improved with a further consideration of the thickness of the interface shear band (represented by several times of d_{50}). By comparing with experimental results, it was found that better quantitative predictions of the lateral stress mobilised by shafts of relatively small sizes can be made by the present solution than some other commonly used solutions as shown in Section 4.2.2.2.

(3) Two-dimensional elastic analysis of root tip-soil interaction

Based on the complex variable theory, several closed-form elastic solutions for two-dimensional stress and deformation analyses around an elliptical cavity have been presented and validated in Chapter 5. The developed displacement-controlled elastic solutions provide a simple approximate way to quantify the root-soil interaction with a small growth increment in a two-dimensional manner, and they may also be applicable in the study of the burrowing mechanism of earthworm (Ruiz et al., 2016). Both the axial growth and radial thickening of a root tip have been theoretically investigated with these solutions. It showed that the required axial growth pressure decreases with an increasing root diameter, and an evident transverse tensile zone ahead of the root tip will be caused by a purely radial swelling, which provides a direct basis in theory for the inverse-peristalsis root growth model proposed by Abdalla et al. (1969).

(4) Influences of the shear stress in static and quasi-static cavity expansions

A static elastoplastic stress solution for a circular cavity within a plane subjected to non-equal biaxial stresses at infinity and uniform normal and shear stresses at the cavity wall was presented in Chapter 6. The plastic response was modelled by the Tresca yield criterion, and the Hooke’s law was adopted to describe the elastic behaviour. By extending the pioneering work of Parasyuk (1948), an explicit conformal mapping function describing the elastic-plastic boundary was obtained based on Laurent’s decomposition theorem, and explicit Kolosov-Muskhelishvili elastic complex potentials were derived based on the Fourier series method and the Cauchy integral method. Admissible application ranges of this solution were presented in Section 6.5, and influences of the additional shear stress on the whole stress field were discussed in Section 6.6. It was found that the permissible application range varies with the applying direction of the internal shear stress, and the plastic zone enlarges with the increase of the internal shear stress.

Furthermore, based on the derived static stress solution and a large strain deformation analysis, an analytical quasi-static analysis was carried out for a circular cavity continuously expanding in a hydrostatic stress environment. It was found that the shear stress imposes a certain influence on the pressure-expansion behaviour, and a drop around

6% of the limit expansion pressure may be caused when the shear stress holding capacity at the internal interface is fully mobilised in this model. This analytical quasi-static solution may be applicable in analyses of the rotating penetration/indention problems.

(5) Two-dimensional elastoplastic stress analysis around a circular cavity under loading or unloading

Static elastic and plastic stress fields around a circular cavity being subject to non-equal biaxial far-field stresses were investigated in Chapter 7. A combined analytical stress solution for an expanding/contracting cavity in the Mohr-Coulomb material was presented. The elastic-plastic boundary in a given static stress state was described with the asymptotic form mapping function proposed by Detournay and Fairhurst (1987). Accordingly, the statically determined plastic stress field was computed as a one-dimensional problem, and a two-dimensional stress analysis of the elastic stress field was carried out based on the complex variable theory of elasticity. Explicit Kolosov-Muskhelishvili elastic complex potentials were derived for a cavity either under loading or unloading. Calculated results with the present solution in loading cases agreed well with the FEM simulation results. By comparing with Detournay and Fairhurst's (1987) solution for unloading conditions, good agreements were also obtained in spite of the nonsignificant stress discontinuity exists along the elastic-plastic boundary in their solution. In the present elastic-plastic cavity solution, a non-equal initial stress field (e.g. in-situ soil stress) can be taken into account, and it is applicable in estimating the plastic failure zone and stress distribution around a circular cavity (e.g. tunnel, pipeline) either under loading or unloading condition within the given permissible application stress ranges.

8.2 Suggestions for future work

(1) Only three sizes of cone penetrometers (12mm, 6mm, 3mm) and dry sand samples were used in present cone penetration tests. To further study potential influences of the size effect in needle cone penetration tests (applications to estimate the soil resistance of root-tip growth), tests with smaller sized penetrometers (around 1mm) and more types of soils are suggested. In addition, penetration tests with deeper penetration depths or higher stress levels are also suggested to more generally quantify the size effect caused by the local deformation, and advanced visualisation techniques (e.g. X-ray scanning, transparent soil, GeoPIV) are also recommended in future tests.

(2) As previously discussed, the present size-dependent solution probably can be improved by using a non-constant gradient coefficient (H_g) or considering the potential influences of strain gradient terms to other inherent material properties simultaneously. Some attempts have already been made by following these ideas (e.g. those given in my first-year and second-year annual reports to the university, which were not presented in the thesis), but more theoretical and experimental effort is needed to properly describe the strain-gradient dependent behaviour of soils. In addition, the employed numerical method is not always able to high-efficiently solve the developed governing equation system which may have a significant boundary layer response (Holmes, 2012). So more advanced numerical methods to address this problem will be attempted in the future.

(3) To model the root tip-soil interaction in an analytical manner, the present theoretical analyses were based on the plane strain assumption and a linear elastic model. In fact, a three-dimensional analysis with more realistic soil models may give more appropriate descriptions of the real process of root-soil interaction. In addition, the complex and dynamically varying properties of soil in the rhizosphere and material exchanges between the root and the surrounding environment have not been considered in the present physical model. More investigations in these aspects may be beneficial for improving the accuracy in physically modelling the root tip-soil interaction.

Appendix A

Readings of cone penetration tests with the 12mm penetrometer

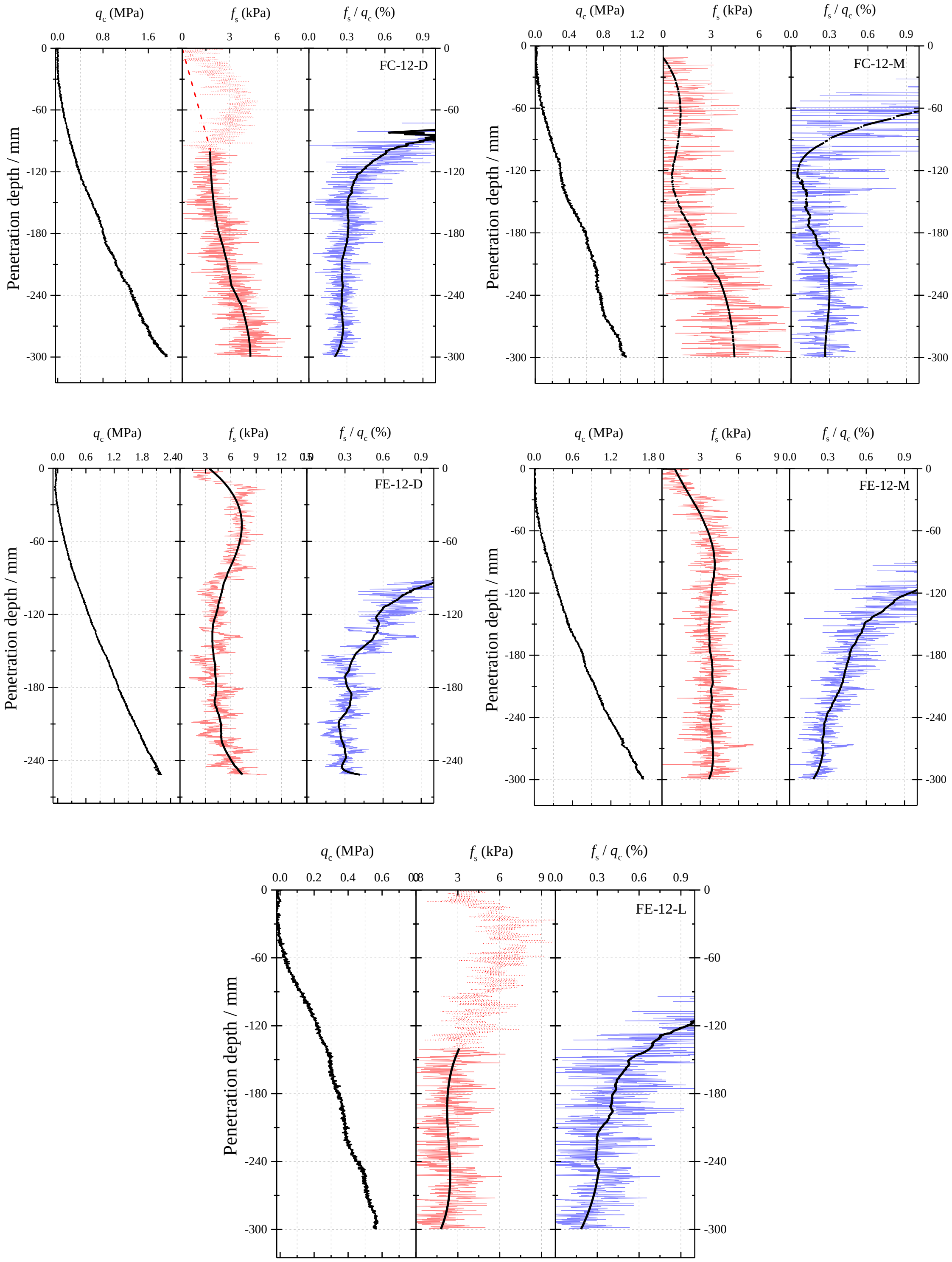

Fig. A- 1 Data with the 12mm sized penetrometer

Appendix B

Elastic solution for hollow cylinder under loading

As depicted in Fig. B- 1, a hollow cylinder with internal and external radius '*a*' and '*b*' respectively is subjecting to uniform pressures both on its internal and external surfaces. To this topic, elastic solutions (e.g. Lame's solution) both for plane strain and plane stress conditions have been well developed, which are available in a lot of treaties (Timoshenko and Goodier, 1951; Ugural and Fenster, 1995; Yu, 2000). With the plane strain assumption, the stress and displacement distribution in the circular ring can be calculated with

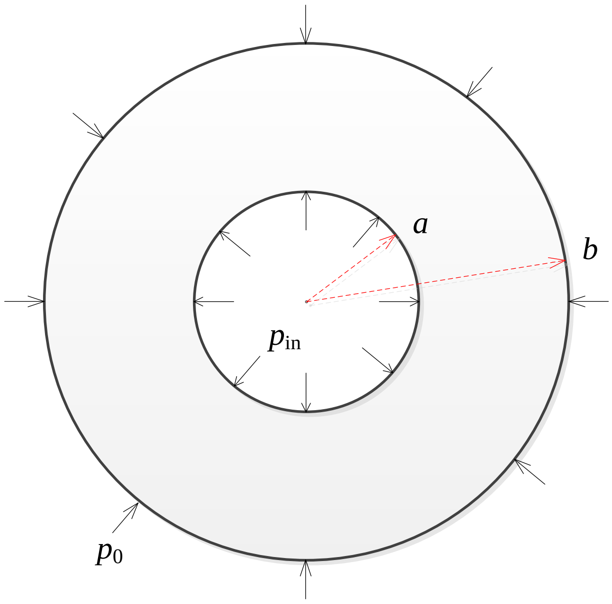

Fig. B- 1 Thick-walled cylinder subjecting to uniform pressures at boundaries

$$\sigma_r = -p_0 + (p - p_0)[\frac{1}{(b/a)^2 - 1} - \frac{1}{(r/a)^2 - (r/b)^2}] \quad \text{(B- 1)}$$

$$\sigma_\theta = -p_0 + (p - p_0)[\frac{1}{(b/a)^2 - 1} + \frac{1}{(r/a)^2 - (r/b)^2}] \quad \text{B- 2)}$$

$$u_e = \frac{r}{2G}\left\langle -p_0(1-2\nu) + (p - p_0)[\frac{(1-2\nu)}{(b/a)^2 - 1} + \frac{1}{(r/a)^2 - (r/b)^2}]\right\rangle \quad \text{(B- 3)}$$

Appendix C

Purely elastic stress solutions (Yu, 2000)

$$\sigma_r = P_\infty(1-\frac{R_0^{\ 2}}{r^2}) - \tau_\infty(1+\frac{3R_0^{\ 4}}{r^4}-\frac{4R_0^{\ 2}}{r^2})\cos 2\theta - p_{in}\frac{R_0^{\ 2}}{r^2} \tag{C- 1}$$

$$\sigma_\theta = P_\infty(1+\frac{R_0^{\ 2}}{r^2}) + \tau_\infty(1+\frac{3R_0^{\ 4}}{r^4})\cos 2\theta + p_{in}\frac{R_0^{\ 2}}{r^2} \tag{C- 2}$$

$$\tau_{r\theta} = \tau_\infty(1-\frac{3R_0^{\ 4}}{r^4}+\frac{2R_0^{\ 2}}{r^2})\sin 2\theta + mk\frac{R_0^{\ 2}}{r^2} \tag{C- 3}$$

Appendix D

Re-derivation of mapping function (referring to Parasyuk (1948))

To transform the exterior of the EP boundary in the physical plane onto the exterior region of the unit circle in the phase plane, a conformal mapping function with the following form is introduced (England, 2003).

$$\omega(\zeta)=\alpha'\zeta+\alpha'_0+\sum_{n=1}^{\infty}\frac{\alpha'_n}{\zeta^n} \quad \text{(D- 1)}$$

Due to symmetric facts of the geometry and stress environment, the mapping function $\omega(\zeta)$ has the following features (Detournay, 1986).

$$\omega(\zeta)=-\omega(-\zeta) \quad , \quad \omega(\zeta)=\overline{\omega(\bar{\zeta})} \quad \text{(D- 2)}$$

As a result, α_0 and coefficients of the even order terms are equal to zero, and remaining coefficients are real numbers. $\omega(\zeta)$ can be rewritten as

$$z=x+iy=\omega(\zeta)=\alpha\zeta+\sum_{j=0}^{\infty}\frac{\alpha_{2j+1}}{\zeta^{2j+1}} \quad \text{(D- 3)}$$

By multiplying both sides of Eq. (6-12)(a) with $\frac{1}{2\pi i}\frac{d\sigma}{\sigma-\zeta}$, a Cauchy integral is established as

$$\frac{1}{2\pi i}\int_{\gamma}\left[\frac{\bar{\omega}(\sigma^{-1})}{\omega(\sigma)}\Phi'(\sigma)+\Psi(\sigma)\right]\frac{d\sigma}{\sigma-\zeta}=\frac{k}{2\pi i}\int_{\gamma}\left\langle\frac{\sqrt{[\omega(\sigma)\overline{\omega(\sigma)}]^2-m^2R_0^{\,4}}+mR_0^{\,2}i}{\omega(\sigma)\overline{\omega(\sigma)}}\right\rangle\frac{\overline{\omega(\sigma)}}{\omega(\sigma)}\frac{d\sigma}{\sigma-\zeta} \quad \text{(D- 4)}$$

The right part of Eq.(D- 4) should be bounded at infinity (Chakrabarty, 2006; Savin, 1970), hence terms of $j\geq 1$ in the mapping function should vanish as shown in Eq.(D-5).

$$\frac{\overline{\omega(\sigma)}}{\omega(\sigma)}=\frac{\bar{\omega}(\sigma^{-1})}{\omega(\sigma)}=\frac{\bar{\alpha}\sigma^{-1}+\bar{\alpha}_1\sigma+\bar{\alpha}_3\sigma^3+\cdots}{\alpha\sigma+\alpha_1\sigma^{-1}+\alpha_3\sigma^{-3}+\cdots}=\frac{\bar{\alpha}_1}{\alpha}+M(\sigma) \quad \text{(D- 5)}$$

where $M(\sigma)$ is analytic on the exterior of contour 'γ', and $M(\infty)=0$. Similarly, we find

$$\frac{\bar{\omega}(\sigma^{-1})}{\omega(\sigma)}\Phi'(\sigma)=N(\sigma) \quad \text{(D- 6)}$$

where $N(\sigma)$ is analytic on the exterior of contour 'γ', and $N(\infty)=0$.

Meanwhile, $\Psi(\sigma)$ is holomorphic in Ω^- (including infinity points). Finally, according to Harnack's theorem (Muskhelishvili, 1963), integrating Eq.(D- 4) along γ from Ω^+ side gives

$$\alpha_1 = \bar{\alpha}_1 = \frac{\tau_\infty}{k}\alpha \tag{D- 7}$$

Therefore, the mapping function is with form as Eq.(6-14).

References

Abdalla, A.M., Hettiaratchi, D.R.P., Reece, A.R., 1969. The mechanics of root growth in granular media. Journal of Agricultural Engineering Research 14, 236-248.

Abouzar, S., Sepideh, D.M., 2015. Development of a miniature cone penetrometer for calibration chamber testing. Geotechnical Testing Journal 38, 878–892.

Aifantis, E.C., 1984. On the mechanics of modulated structures. Springer.

Aifantis, E.C., 1987. The physics of plastic deformation. International Journal of Plasticity 3, 211-247.

Aifantis, E.C., 1996. Higher order gradients and size effects, in: Carpinteri, A. (Ed.), Size-scale effects in the failure mechanisms of materials and structures, E & FN Spon, London, pp. 231-242.

Aifantis, E.C., 1999. Strain gradient interpretation of size effects. International Journal of Fracture 95, 299-314.

Aifantis, E.C., 2003. Update on a class of gradient theories. Mechanics of Materials 35, 259-280.

Al Hattamleh, O., Muhunthan, B., Zbib, H.M., 2004. Gradient plasticity modelling of strain localization in granular materials. International Journal for Numerical and Analytical Methods in Geomechanics 28, 465-481.

Alawneh, A.S., Malkawi, A.I.H., Al-Deeky, H., 1999. Tension tests on smooth and rough model piles in dry sand. Canadian Geotechnical Journal 36, 746-753.

API, 2000. RP2A-WSD: Recommended Practice for Planning, Designing and Constructing Fixed Offshore Platforms—Working Stress Design, 21st ed., Washington, DC.

Arshad, M.I., Tehrani, F.S., Prezzi, M., Salgado, R., 2014. Experimental study of cone penetration in silica sand using digital image correlation. Geotechnique 64, 551-569.

ASAE, 2003. Standards EP542, Procedures for Using and Reporting Data Obtained with the Soil Cone Penetrometer. American Society of Agricultural Engineers, St. Joseph, Mich. USA.

ASAE, 2004. Standard S313. 3, Soil Cone Penetrometer. American Society of Agricultural Engineers, St. Joseph, Mich. USA.

ASTM-D5778-12, 2012. Standard Test Method for Electronic Friction Cone and Piezocone Penetration Testing of Soils. ASTM International, West Conshohocken, PA.

Atroshchenko, E., 2010. Stress Intensity Factors for Elliptical and Semi-Elliptical cracks subjected to an arbitrary mode I loading. Ph.D. thesis thesis. University of Waterloo.

Atwell, B., Newsome, J., 1990. Turgor pressure in mechanically impeded lupin roots. Functional Plant Biology 17, 49-56.

Atwell, B.J., 1990. The effect of soil compaction on wheat during early tillering. New Phytologist 115, 29-35.

Atwell, B.J., 1993. Response of roots to mechanical impedance. Environmental and Experimental Botany 33, 27-40.

Aydan, Ö., Sato, A., Yagi, M., 2014. The inference of geo-mechanical properties of soft rocks and their degradation from needle penetration tests. Rock Mechanics and Rock Engineering 47, 1867-1890.

Balachowski, L., 2006. Scale effect in shaft friction from the direct shear interface tests. Archives of Civil and Mechanical Engineering 6, 13-28.

Balachowski, L., 2007. Size effect in centrifuge cone penetration tests. Archives of Hydro-Engineering and Environmental Mechanics 54, 161-181.

Baldi, G., Bellotti, R., Ghionna, V.N., Jamiolkowski, M., Lo Presti, D.F.C., 1991. Modulus of sands from CPTs and DMTs, 12th International conference on soil mechanics and foundation engineering, Rio de Janeiro, pp. 165-170.

Baligh, M.M., 1976. Cavity expansion in sands with curved envelopes. Journal of the Geotechnical Engineering Division 102, 1131-1146.

Barley, K.P., 1962. The effects of mechanical stress on the growth of roots. Journal of Experimental Botany 13, 95-110.

Barley, K.P., Farrell, D.A., Greacen, E.L., 1965. The influence of soil strength on the penetration of a loam by plant roots. Soil Research 3, 69-79.

Bemben, S.M., Myers, H.J., 1974. The influence of rate of penetration on static cone resistance in Connecticut River Valley varved clay, Proc., European Symp. on Penetration Testing. National Swedish Council for Building Research Stockholm, pp. 33-43.

Bengough, A.G., 2012. Root elongation is restricted by axial but not by radial pressures: so what happens in field soil? Plant and Soil 360, 15-18.

Bengough, A.G., Bransby, M.F., Hans, J., McKenna, S.J., Roberts, T.J., Valentine, T.A., 2006. Root responses to soil physical conditions; growth dynamics from field to cell. Journal of Experimental Botany 57, 437-447.

Bengough, A.G., Campbell, D.J., O'sullivan, M.F., 2000. Penetrometer techniques in relation to soil compaction and root growth, Soil environmental analysis: physical methods, pp. 377-403.

Bengough, A.G., Kirby, J.M., 1999. Tribology of the root cap in maize (Zea mays) and peas (Pisum sativum). New Phytologist 142, 421-425.

Bengough, A.G., Loades, K., McKenzie, B.M., 2016. Root hairs aid soil penetration by anchoring the root surface to pore walls. Journal of Experimental Botany 67, 1071-1078.

Bengough, A.G., McKenzie, B., Hallett, P., Valentine, T., 2011. Root elongation, water stress, and mechanical impedance: a review of limiting stresses and beneficial root tip traits. Journal of Experimental Botany 62, 59-68.

Bengough, A.G., McKenzie, B.M., 1997. Sloughing of root cap cells decreases the frictional resistance to maize (Zea mays L.) root growth. Journal of Experimental Botany 48, 885-893.

Bengough, A.G., Mullins, C.E., 1990. Mechanical impedance to root growth: a review of experimental techniques and root growth responses. Journal of Soil Science 41, 341-358.

Bengough, A.G., Mullins, C.E., 1991. Penetrometer resistance, root penetration resistance and root elongation rate in two sandy loam soils. Plant and Soil 131, 59-66.

Bengough, A.G., Mullins, C.E., Wilson, G., 1997. Estimating soil frictional resistance to metal probes and its relevance to the penetration of soil by roots. European Journal of Soil Science 48, 603-612.

Berezantzev, V., 1961. Load bearing capacity and deformation of piled foundations. Proc. 5th ICSMFE, Paris, 1961 2, 11-12.

Biarez, J., Burel, M., Wack, B., 1961. Contribution to the study of the bearing capacity of foundations, Proceedings of the 5th International Conference on Soil Mechanics and Foundation Engineering, pp. 603-609.

Bigoni, D., Laudiero, F., 1989. The quasi-static finite cavity expansion in a non-standard elasto-plastic medium. International Journal of Mechanical Sciences 31, 825-837.

Bishop, R.F., Hill, R., Mott, N.F., 1945. The theory of indentation and hardness tests. Proceedings of the Physical Society 57, 147–159.

Bizet, F., Bengough, A.G., Hummel, I., Bogeat-Triboulot, M.-B., Dupuy, L.X., 2016. 3D deformation field in growing plant roots reveals both mechanical and biological responses to axial mechanical forces. Journal of Experimental Botany, erw320.

Boeuf-Tremblay, V., Plantureux, S., Guckert, A., 1995. Influence of mechanical impedance on root exudation of maize seedlings at two development stages. Plant and Soil 172, 279-287.

Bolton, M.D., 1986. The strength and dilatancy of sands. Geotechnique 36, 65-78.

Bolton, M.D., 1987. Discussion on the strength and dilatancy of sands. Geotechnique 37, 219-226.

Bolton, M.D., Gui, M.W., 1993. The study of relative density and boundary effects for cone penetration tests in centrifuge. Cambridge University Engineering Department.

Bolton, M.D., Gui, M.W., Garnier, J., Corte, J.F., Bagge, G., Laue, J., Renzi, R., 1999. Centrifuge cone penetration tests in sand. Geotechnique 49, 543-552.

Bolton, M.D., Gui, M.W., Phillips, R., 1993. Review of miniature soil probes for model tests, Proceedings of the 11th Southeast Asian Geotechnical Conference. South East Asian Geotechnical Society, pp. 85-90.

Bolton, M.D., Lau, C.K., 1989. Scale effects in the bearing capacity of granular soils, Proceedings of the 12th International Conference on Soil Mechanics and Foundation Engineering. AA Balkema, pp. 895-898.

Borghi, X., White, D.J., Bolton, M.D., Springman, S., 2001. Empirical pile design based on cone penetrometer data: an explanation for the reduction of unit base resistance between CPTs and piles, Proceeding 5th International Conference on Deep Foundations Practice, Singapore, pp. 125-132.

Boulon, M., Foray, P., 1986. Physical and numerical simulation of lateral shaft friction along offshore piles in sand, Proc., 3rd Int. Conf. on Numerical Methods in Offshore Piling. Institut Francais du Petrol Nantes, France, Nantes, pp. 127-147.

Bouwman, L., Arts, W., 2000. Effects of soil compaction on the relationships between nematodes, grass production and soil physical properties. Applied Soil Ecology 14, 213-222.

Bradford, I.D.R., Durban, D., 1998. Stress and deformation fields around a cylindrical cavity embedded in a pressure-sensitive elastoplastic medium. Journal of Applied Mechanics 65, 374-379.

Bradford, J.M., 1980. The penetration resistance in a soil with well-defined structural units. Soil Science Society of America Journal 44, 601-606.

Brady, B.H., 2004. Rock mechanics: for underground mining. Springer Science & Business Media.

Brown, C., Lahlouh, E., Rotter, J., 2000. Experiments on a square planform steel silo. Chemical Engineering Science 55, 4399-4413.

Bui, M.T., 2009. Influence of some particle characteristics on the small strain response of granular materials. Ph.D. thesis thesis. University of Southampton.

Bustamante, M., Gianeselli, L., 1982. Pile bearing capacity prediction by means of static penetrometer CPT, Proceedings of the 2-nd European Symposium on Penetration Testing, pp. 493-500.

Bykovtsev, G.I., Tsvetkov, Y.D., 1987. The two-dimensional loading problem of an elasto-plastic plane weakened by a hole. Journal of Applied Mathematics and Mechanics 51, 244-250.

Cao, L.F., Teh, C.I., Chang, M.F., 2001. Undrained cavity expansion in modified Cam clay I: Theoretical analysis. Geotechnique 51, 323-334.

Cao, L.F., Teh, C.I., Chang, M.F., 2002. Analysis of undrained cavity expansion in elasto‐plastic soils with non‐linear elasticity. International Journal for Numerical and Analytical Methods in Geomechanics 26, 25-52.

Carminati, A., Moradi, A.B., Vetterlein, D., Vontobel, P., Lehmann, E., Weller, U., Vogel, H.-J., Oswald, S.E., 2010. Dynamics of soil water content in the rhizosphere. Plant and Soil 332, 163-176.

Carminati, A., Vetterlein, D., 2013. Plasticity of rhizosphere hydraulic properties as a key for efficient utilization of scarce resources. Annals of Botany 112, 277-290.

Carminati, A., Zarebanadkouki, M., Kroener, E., Ahmed, M., Holz, M., 2016. Biophysical rhizosphere processes affecting root water uptake. Annals of Botany, mcw113.

Carter, J.P., Booker, J.R., Yeung, S.K., 1986. Cavity expansion in cohesive frictional soils. Geotechnique 36, 349-358.

Cerato, A.B., Lutenegger, A.J., 2007. Scale effects of shallow foundation bearing capacity on granular material. Journal of Geotechnical and Geoenvironmental Engineering 133, 1192-1202.

Chadwick, P., 1959. The quasi-static expansion of a spherical cavity in metals and ideal soils. The Quarterly Journal of Mechanics and Applied Mathematics 12, 52-71.

Chakrabarty, J., 2006. Theory of plasticity (3rd Ed.). Elsevier Butterworth-Heinemann, Oxford, UK.

Chakraborty, T., Salgado, R., 2010. Dilatancy and shear strength of sand at low confining pressures. Journal of geotechnical and geoenvironmental engineering 136, 527-532.

Chattopadhyay, B., Pise, P., 1986. Uplift capacity of piles in sand. Journal of Geotechnical Engineering 112, 888-904.

Chen, S.L., Abousleiman, Y.N., 2012. Exact undrained elasto-plastic solution for cylindrical cavity expansion in modified Cam Clay soil. Geotechnique 62, 447-456.

Cherepanov, G.P., 1963. On a method of solving the elasto-plastic problem. Journal of Applied Mathematics and Mechanics 27, 644-655.

Cho, H.I., Park, H.J., Kim, D.S., Choo, Y.W., 2014. Evaluation of Ko in Centrifuge Model Using Shear Wave Velocity. Geotechnical Testing Journal 37, 20130060.

Chou, P.C., Pagano, N.J., 2013. Elasticity: tensor, dyadic, and engineering approaches. Courier Corporation.

Chow, F.C., 1996. Investigations into the behaviour of displacement piles for offshore foundations. Ph.D. thesis thesis. University of London (Imperial College).

Chung, S.F., Randolph, M.F., Schneider, J.A., 2006. Effect of penetration rate on penetrometer resistance in clay. Journal of Geotechnical and Geoenvironmental Engineering 132, 1188-1196.

Clark, L.J., Barraclough, P.B., 1999. Do dicotyledons generate greater maximum axial root growth pressures than monocotyledons? Journal of Experimental Botany 50, 1263-1266.

Clark, L.J., Bengough, A.G., Whalley, W.R., Dexter, A.R., Barraclough, P.B., 1999. Maximum axial root growth pressure in pea seedlings: effects of measurement techniques and cultivars. Plant and Soil 209, 101-109.

Clark, L.J., Ferraris, S., Price, A.H., Whalley, W.R., 2008a. A gradual rather than abrupt increase in soil strength gives better root penetration of strong layers. Plant and Soil 307, 235-242.

Clark, L.J., Price, A.H., Steele, K.A., Whalley, W.R., 2008b. Evidence from near-isogenic lines that root penetration increases with root diameter and bending stiffness in rice. Functional Plant Biology 35, 1163-1171.

Clark, L.J., Whalley, W.R., Barraclough, P.B., 2003. How do roots penetrate strong soil?, Roots: The Dynamic Interface between Plants and the Earth. Springer, pp. 93-104.

Cockroft, B., Barley, K.P., Greacen, E.L., 1969. The penetration of clays by fine probes and root tips. Soil Research 7, 333-348.

Collin, F., Caillerie, D., Chambon, R., 2009. Analytical solutions for the thick-walled cylinder problem modeled with an isotropic elastic second gradient constitutive equation. International Journal of Solids and Structures 46, 3927-3937.

Collins, I.F., Pender, M.J., Yan, W., 1992. Cavity expansion in sands under drained loading conditions. International Journal for Numerical and Analytical Methods in Geomechanics 16, 3-23.

Collins, I.F., Yu, H.S., 1996. Undrained cavity expansions in critical state soils. International Journal for Numerical and Analytical Methods in Geomechanics 20, 489-516.

Conte, E., Donato, A., Troncone, A., 2013. Progressive failure analysis of shallow foundations on soils with strain-softening behaviour. Computers and Geotechnics 54, 117-124.

Cosgrove, D.J., 1993. Wall extensibility: its nature, measurement and relationship to plant cell growth. New Phytologist 124, 1-23.

Croser, C., Bengough, A.G., Pritchard, J., 2000. The effect of mechanical impedance on root growth in pea (Pisum sativum). II. Cell expansion and wall rheology during recovery. Physiologia Plantarum 109, 150-159.

Crozier, R.J.M., Hunter, S.C., 1970. Similarity solution for the rapid uniform expansion of a cylindrical cavity in a compressible elastic-plastic solid. The Quarterly Journal of Mechanics and Applied Mathematics 23, 349-363.

CUR, 2001. Bearing capacity of steel pipe piles, Report 2001-8 Centre for Civil Engineering Research and Codes, Couda, The Netherlands.

Dave, T.N., Dasaka, S., 2012. Assessment of portable traveling pluviator to prepare reconstituted sand specimens. Geomechanics and Engineering 4, 79-90.

De Beer, E.E., 1948. Donnees concernant la resistance au cisaillement deduites des essais de penetration en profondeur. Geotechnique 1, 22-40.

De Beer, E.E., 1963. The scale effect in the transposition of the results of deep-sounding tests on the ultimate bearing capacity of piles and caisson foundations. Geotechnique 13, 39-75.

De Beer, E.E., 1965. The scale effect on the phenomenon of progressive rupture in cohesionless soils, 6th Soil Mechanics and Foundation Engineering Conference, pp. 13-17.

De Beer, E.E., 1970. Experimental determination of the shape factors and the bearing capacity factors of sand. Geotechnique 20, 387-411.

De Nicola, A., Randolph, M.F., 1993. Tensile and compressive shaft capacity of piles in sand. Journal of Geotechnical Engineering 119, 1952-1973.

De Nicola, A., Randolph, M.F., 1999. Centrifuge modelling of pipe piles in sand under axial loads. Geotechnique 49, 295-318.

De Ruiter, J., 1982. The static cone penetration test. State-of-the-art report, Proc. of the 2nd European Symposium on Penetration Testing, ESOPT-II, Amsterdam, pp. 389-405.

De Ruiter, J., Beringen, F.L., 1979. Pile foundations for large North Sea structures. Marine Georesources & Geotechnology 3, 267-314.

Deeks, A.D., White, D.J., 2006. Centrifuge modelling of jacked piles, Proceedings, International Conference on Physical Modelling in Geotechics, pp. 821-826.

DeJong, J.T., Westgate, Z.J., 2009. Role of initial state, material properties, and confinement condition on local and global soil-structure interface behavior. Journal of Geotechnical and Geoenvironmental Engineering 135, 1646-1660.

Detournay, E., 1986. An approximate statical solution of the elastoplastic interface for the problem of Galin with a cohesive-frictional material. International Journal of Solids and Structures 22, 1435-1454.

Detournay, E., Fairhurst, C., 1987. Two-dimensional elastoplastic analysis of a long, cylindrical cavity under non-hydrostatic loading, International Journal of Rock Mechanics and Mining Sciences & Geomechanics Abstracts. Elsevier, pp. 197-211.

Detournay, E., John, C.M.S., 1988. Design charts for a deep circular tunnel under non-uniform loading. Rock Mechanics and Rock Engineering 21, 119-137.

Dexter, A.R., 1986. Model experiments on the behaviour of roots at the interface between a tilled seed-bed and a compacted sub-soil-III. Entry of pea and wheat roots into cylindrical biopores. Plant and Soil 95, 149-161.

Dexter, A.R., Tanner, D.W., 1973. The force on spheres penetrating soil. Journal of Terramechanics 9, 31-39.

Dietz, M.S., 2000. Developing an holistic understanding of interface friction using sand with direct shear apparatus. Ph.D. thesis thesis. University of Bristol.

Durban, D., Fleck, N.A., 1997. Spherical cavity expansion in a Drucker-Prager solid. Transactions-American Society of Mechanical Engineers Journal of Applied Mechanics 64, 743-750.

Durban, D., Masri, R., 2004. Dynamic spherical cavity expansion in a pressure sensitive elastoplastic medium. International Journal of Solids and Structures 41, 5697-5716.

Durgunoglu, H.T., Mitchell, J.K., 1973. Static penetration resistance of soils, Research report for NASA Headquarters. University of California, Berkeley.

Durgunoglu, H.T., Mitchell, J.K., 1975. Static penetration resistance of soils: I-analysis, In Situ Measurement of Soil Properties. ASCE, pp. 151-171.

Eid, W.K., 1987. Scaling effect in cone penetration testing in sand. Ph.D. thesis thesis. Virginia Polytechnic Institute.

Elkadi, A., Van Mier, J., 2006. Experimental investigation of size effect in concrete fracture under multiaxial compression. International Journal of Fracture 140, 55-71.

Enever, Wubailin, J., 2001. Scale effects in hollow cylinder tests. Frontiers of Rock Mechanics and Sustainable Development in the 21st Century, 209-212.

England, A.H., 2003. Complex variable methods in elasticity. Dover Publications, Inc, Mineola, New York.

Eshel, N.N., Rosenfeld, G., 1970. Effects of strain-gradient on the stress-concentration at a cylindrical hole in a field of uniaxial tension. Journal of Engineering Mathematics 4, 97-111.

Fahey, M., Carter, J.P., 1993. A finite element study of the pressuremeter test in sand using a nonlinear elastic plastic model. Canadian Geotechnical Journal 30, 348-362.

Fahey, M., Lehane, B.M., Stewart, D., 2003. Soil stiffness for shallow foundation design in the Perth CBD. Australian Geomechanics Journal 38, 61-90.

Faure, A.G., 1994. Stress field developed by root growth: theoretical approach. Journal of Agricultural Engineering Research 58, 53-67.

Ferguson, K.A., Ko, H.Y., 1981. Centrifugal model of the cone penetrometer, Cone Penetration Testing and Experience. ASCE, pp. 108-127.

Finnie, I.M.S., Randolph, M.F., 1994. Punch-through and liquefaction induced failure of shallow foundations on calcareous sediments, Proceedings of International Conference on Behaviour of Offshore Structures, Boston, MA, pp. 217-230.

Fioravante, V., 2002. On the shaft friction modelling of non-displacement piles in sand. Soils and Foundations 42, 23-33.

Fioravante, V., Guerra, L., Jamiolkowski, M., 2010a. On the shaft capacity of non-displacement piles in sand from centrifuge tests, 7th International Conference on Physical Modeling in Geotechnics.

Fioravante, V., Guerra, L., Jamiolkowski, M., 2010b. Tensile shaft capacity of bored piles in sand from centrifuge modelling, in: Frost, J.D. (Ed.), Proceedings of Research

Symposium on Characterization and Behavior of Interfaces, 21 September 2008, . IOS Press, Atlanta, Georgia, USA, pp. 131-138.

Fleck, N.A., Muller, G.M., Ashby, M.F., Hutchinson, J.W., 1994. Strain gradient plasticity: theory and experiment. Acta Metallurgica et Materialia 42, 475-487.

Fleming, K., Weltman, A., Randolph, M.F., Elson, K., 2009. Piling engineering (3rd Ed.). Taylor & Francis, London and New York.

Foray, P., 1991. Scale and boundary effects on calibration chamber pile tests, Proceedings of the First International Symposium on Calibration Chamber Testing/ISOCCTl, Potsdam, New York. DTIC Document, pp. 147-160.

Foray, P., Balachowski, L., Rault, G., 1998. Scale effects in shaft friction due to the localization of deformations, Proceedings of the International Conference Centrifuge, pp. 211-216.

Forrestal, M.J., Tzou, D.Y., 1997. A spherical cavity-expansion penetration model for concrete targets. International Journal of Solids and Structures 34, 4127-4146.

Frost, J.D., DeJong, J.T., Recalde, M., 2002. Shear failure behavior of granular–continuum interfaces. Engineering Fracture Mechanics 69, 2029-2048.

Galin, L.A., 1946. Plane elastic-plastic problem: plastic regions around circular holes in plates and beams. Prikladnaia Matematika i Mekhanika 10, 365-386.

Gamelin, T.W., 2001. Complex analysis. Springer, Berlin, Heidelberg, New York.

Gao, X.L., 2002. Analytical solution of a borehole problem using strain gradient plasticity. Journal of Engineering Materials and Technology 124, 365-370.

Gao, X.L., 2003a. Elasto-plastic analysis of an internally pressurized thick-walled cylinder using a strain gradient plasticity theory. International Journal of Solids and Structures 40, 6445-6455.

Gao, X.L., 2003b. Strain gradient plasticity solution for an internally pressurized thick-walled spherical shell of an elastic–plastic material. Mechanics Research Communications 30, 411-420.

Gao, X.L., 2006. An expanding cavity model incorporating strain-hardening and indentation size effects. International Journal of Solids and Structures 43, 6615-6629.

Gao, X.L., Wei, X.X., Wang, Z.K., 1991. A general analytical solution of a strain-hardening elasto-plastic plate containing a circular hole subjected to biaxial loading—with applications in pressure vessels. International Journal of Pressure Vessels and Piping 47, 35-55.

Garnier, J., 2002. Size effects in shear interfaces, in: Springman, S. (Ed.), Proceedings of the Workshop on Constitutive and Centrifuge Modelling: Two Extremes. CRC Press, Monte Verità, Switzerland, pp. 335-345.

Garnier, J., Gaudin, C., Springman, S.M., Culligan, P.J., Goodings, D., Konig, D., Kutter, B., Phillips, R., Randolph, M.F., Thorel, L., 2007. Catalogue of scaling laws and similitude questions in geotechnical centrifuge modelling. International Journal of Physical Modelling in Geotechnics 7, 1-23.

Garnier, J., König, D., 1998. Scale effects in piles and nails loading tests in sand, Proceedings of the International Conference Centrifuge. Tokyo, pp. 205-210.

Gerard, C.J., Mehta, H.C., Hinojosa, E., 1972. Root growth in a clay soil. Soil Science 114, 37-49.

Ghionna, V.N., Jamiolkowski, M., 1991. A critical appraisal of calibration chamber testing of sands, in: Huang, A.-B. (Ed.), Proceedings of the First International Symposium on Calibration Chamber Testing. Elsevier, Potsdam, New York, pp. 13-40.

Gibson, R.E., Anderson, W.F., 1961. In situ measurement of soil properties with the pressuremeter. Civil Engineering and Public Works Review 56, 615-618.

Gooderham, P.T., 1973. Soil physical conditions and plant growth. Ph.D. thesis. University of Reading.

Goss, M.J., 1977. Effects of mechanical impedance on root growth in barley (Hordeum vulgare L.) I. Effects on the elongation and branching of seminal root axes. Journal of Experimental Botany 28, 96-111.

Greacen, E.L., Farrell, D.A., Cockroft, B., 1968. Soil resistance to metal probes and plant roots, Transactions of the 9th Congress of the International Society of Soil Science, pp. 769-779.

Greacen, E.L., Oh, J.S., 1972. Physics of root growth. Nature 235, 24-25.

Gregory, P.J., Nortcliff, S., 2013. Soil conditions and plant growth. John Wiley & Sons.

Griffith, A.A., 1921. The phenomena of rupture and flow in solids. Philosophical transactions of the royal society of london. Series A, containing papers of a mathematical or physical character, 163-198.

Gui, M.W., Bolton, M.D., Garnier, J., Corte, J., Bagge, G., Laue, J., Renzi, R., 1998. Guidelines for cone penetration tests in sand, Proceedings of the International Conference on Centrifuge Modelling (Centrifuge 98), Tokyo, Japan, pp. 23-25.

Haling, R.E., Brown, L.K., Bengough, A.G., Young, I.M., Hallett, P.D., White, P.J., George, T.S., 2013. Root hairs improve root penetration, root–soil contact, and

phosphorus acquisition in soils of different strength. Journal of Experimental Botany 64, 3711-3721.
Hallett, P.D., Bengough, A.G., 2013. Managing the soil physical environment for plants, in: Gregory, P.J., Nortcliff, S. (Eds.), Soil Conditions and Plant Growth, pp. 238-268.
Hamza, M., Anderson, W., 2005. Soil compaction in cropping systems: a review of the nature, causes and possible solutions. Soil and Tillage Research 82, 121-145.
Hansen, J.B., 1970. A revised and extended formula for bearing capacity.
Hardin, B.O., Black, W.L., 1966. Sand stiffness under various triaxial stresses. Journal of Soil Mechanics and Foundations Division 94, 353–369.
Henrici, P., 1993. Applied and computational complex analysis, discrete Fourier analysis, Cauchy integrals, construction of conformal maps, univalent functions. John Wiley & Sons.
Hettiaratchi, D.P.R., Ferguson, C.A., 1973. Stress-deformation behaviour of soil in root growth mechanics. Journal of Agricultural Engineering Research.
Hettiaratchi, D.R.P., Goss, M.J., Harris, J.A., Nye, P.H., Smith, K.A., 1990. Soil Compaction and Plant Root Growth [and Discussion]. Philosophical Transactions of the Royal Society of London. Series B: Biological Sciences 329, 343-355.
Hettler, A., 1982. Approximation formulae for piles under tension, IUTAM Conference on Deformation and Failure of Granular Materials, Delft, pp. 603-608.
Hettler, A., Gudehus, G., 1988. Influence of the foundation width on the bearing capacity factor. Soils and Foundations 28, 81-92.
Hill, R., 1950. The mathematical theory of plasticity. Oxford University Press, London.
Ho, T.Y.K., Jardine, R.J., Anh-Minh, N., 2011. Large-displacement interface shear between steel and granular media. Geotechnique 61, 221.
Holden, J., 1991. History of the first six CRB calibration chambers, Proceedings of the 1st International Symposium on Calibration Chamber Testing, Potsdam, NY Edited by A.-B. Huang, Elsevier, pp. 1-12.
Holden, J.C., 1971. Laboratory research on static cone penetrometers. University of Florida, Gainsville, Department of Civil Engineering, Internal Report, CE-SM-71-1.
Holmes, M.H., 2012. Introduction to perturbation methods. Springer Science & Business Media.
Houlsby, G.T., Hitchman, R., 1988. Calibration chamber tests of a cone penetrometer in sand. Geotechnique 38, 39-44.

Hu, G., 1965. Bearing capacity of foundations with overburden shear. Sols-Soils 13, 11-18.

Huang, A.-B., Hsu, H.-H., 2005. Cone penetration tests under simulated field conditions. Geotechnique 55, 345-354.

Huang, W.C., 1972. Theoretical study of stress concentrations at circular holes and inclusions in strain hardening materials. International Journal of Solids and Structures 8, 149-192.

Hughes, J.M.O., Wroth, C.P., Windle, D., 1977. Pressuremeter tests in sands. Geotechnique 27, 455-477.

Hunter, S.C., Crozier, R.J.M., 1968. Similarity solution for the rapid uniform expansion of a spherical cavity in a compressible elastic-plastic solid. The Quarterly Journal of Mechanics and Applied Mathematics 21, 467-486.

Iijima, M., Griffiths, B., Bengough, A.G., 2000. Sloughing of cap cells and carbon exudation from maize seedling roots in compacted sand. New Phytologist 145, 477-482.

Iijima, M., Higuchi, T., Barlow, P.W., 2004. Contribution of root cap mucilage and presence of an intact root cap in maize (Zea mays) to the reduction of soil mechanical impedance. Annals of Botany 94, 473-477.

Iijima, M., Higuchi, T., Barlow, P.W., Bengough, A.G., 2003. Root cap removal increases root penetration resistance in maize (Zea mays L.). Journal of Experimental Botany 54, 2105-2109.

Inglis, C.E., 1913. Stresses in a plate due to the presence of cracks and sharp corners. Spie Milestone series MS 137, 3-17.

Ivlev, D.D., 1959. On the determination of displacements in the Galin problem. Journal of Applied Mathematics and Mechanics 23, 1414-1416.

Jaeger, R.A., DeJong, J.T., Boulanger, R.W., Low, H.E., Randolph, M.F., 2010. Variable penetration rate CPT in an intermediate soil, Proc., 2nd Int. Symp. on Cone Penetration Testing. Omnipress Madison, WI.

Jamiolkowski, M., Lo Presti, D.C.F., Manassero, M., 2003. Evaluation of relative density and shear strength of sands from CPT and DMT. Soil Behavior and Soft Ground Construction 7, 201-238.

Jardine, R.J., Chow, F., Overy, R., Standing, J., 2005. ICP design methods for driven piles in sands and clays. Thomas Telford London.

Jardine, R.J., Lehane, B.M., Everton, S.J., 1993. Friction coefficients for piles in sands and silts, Offshore Site Investigation and Foundation Behaviour. Springer, pp. 661-677.

Jin, K., Shen, J., Ashton, R.W., Dodd, I.C., Parry, M.A., Whalley, W.R., 2013. How do roots elongate in a structured soil? Journal of Experimental Botany 64, 4761-4777.

Jones, K., Bang, S., Cho, Y., 2007. Pullout capacity of embedded suction anchors in sand. Ocean Engineering 34, 2107-2114.

Katzir, Z., Rubin, M.B., 2011. A simple formula for dynamic spherical cavity expansion in a compressible elastic perfectly plastic material with large deformations. Mathematics and Mechanics of Solids 16, 665-681.

Kerchman, V.I., Erlikhman, F.M., 1988. A variational method of solving an elastic-plastic problem for a body with a circular hole. Journal of Applied Mathematics and Mechanics 52, 105-110.

Kerisel, J., 1964. Deep foundations basic experimental facts, Proceedings of a Conference on Deep Foundations, Mexico City, pp. 5-44.

Kim, J.H., Choo, Y.W., Kim, D.J., Kim, D.S., 2015. Miniature Cone Tip Resistance on Sand in a Centrifuge. Journal of Geotechnical and Geoenvironmental Engineering, 04015090.

Kim, K., Prezzi, M., Salgado, R., Lee, W., 2008. Effect of penetration rate on cone penetration resistance in saturated clayey soils. Journal of Geotechnical and Geoenvironmental Engineering 134, 1142-1153.

Kim, K.K., Prezzi, M., Salgado, R., 2006. Interpretation of cone penetration tests in cohesive soils, Joint Transportation Research Program.

Kimura, T., Kusakabe, O., Saitoh, K., 1985. Geotechnical model tests of bearing capacity problems in a centrifuge. Geotechnique 35, 33-45.

Kingston, E., Clayton, C.R., Priest, J., Best, A.I., 2008. Effect of grain characteristics on the behaviour of disseminated methane hydrate bearing sediments, Proceedings of the 6th International Conference on Gas Hydrates (ICGH 2008), Vancouver, British Columbia, Canada.

Kirby, J.M., Bengough, A.G., 2002. Influence of soil strength on root growth: experiments and analysis using a critical‐state model. European Journal of Soil Science 53, 119-127.

Kishida, H., Uesugi, M., 1987. Tests of the interface between sand and steel in the simple shear apparatus. Geotechnique 37, 45-52.

Klinkvort, R.T., Hededal, O., Springman, S.M., 2013. Scaling issues in centrifuge modelling of monopiles. International Journal of Physical Modelling in Geotechnics 13, 38-49.

Klotz, E.U., 2000. The influence of state on the capacity of driven piles in sands. Ph.D. thesis. City University London.

Klotz, E.U., Coop, M.R., 2001. An investigation of the effect of soil state on the capacity of driven piles in sands. Geotechnique 51, 733-751.

Kolb, E., Hartmann, C., Genet, P., 2012. Radial force development during root growth measured by photoelasticity. Plant and Soil 360, 19-35.

Kolk, H., Baaijens, A., Senders, M., 2005. Design criteria for pipe piles in silica sands, Proc., 1st Int. Symp. on Frontiers in Offshore Geotechnics. Balkema Perth, Australia, pp. 711-716.

Koolen, A., Vaandrager, P., 1984. Relationships between soil mechanical properties. Journal of Agricultural Engineering Research 29, 313-319.

Krabbenhoft, S., Clausen, J., Damkilde, L., 2012. The bearing capacity of circular footings in sand: comparison between model tests and numerical simulations based on a nonlinear Mohr failure envelope. Advances in Civil Engineering 2012, 1-10.

Kraft, L.M., 1990. Computing axial pile capacity in sands for offshore conditions. Marine Geotechnology 9, 61-92.

Kurup, P.U., Tumay, M.T., 1998. Calibration of a miniature cone penetrometer for highway applications. Transportation Research Record: Journal of the Transportation Research Board 1614, 8-14.

Kurup, P.U., Voyiadjis, G.Z., Tumay, M.T., 1994. Calibration chamber studies of piezocone test in cohesive soils. Journal of Geotechnical Engineering 120, 81-107.

Kutter, B.L., Abghari, A., Cheney, J.A., 1988. Strength parameters for bearing capacity of sand. Journal of geotechnical engineering 114, 491-498.

Kuznetsov, V.V., 1972. Stress concentration near an elliptical hole in an elastic-plastic plate. International Applied Mechanics 8, 531-536.

Ladanyi, B., 1972. In-situ determination of undrained stress-strain behavior of sensitive clays with the pressuremeter. Canadian Geotechnical Journal 9, 313-319.

Ladanyi, B., Johnston, G.H., 1974. Behavior of circular footings and plate anchors in permafrost. Canadian Geotechnical Journal 11, 531-553.

Ladjal, S., 2013. Scale effect of cavity expansion in soil with application to plant root growth. P.h.D thesis. University of Natural Resources and Life Sciences, Vienna.

Landl, M., Huber, K., Schnepf, A., Vanderborght, J., Javaux, M., Bengough, A.G., Vereecken, H., 2016. A new model for root growth in soil with macropores. Plant and Soil, 1-18.

Last, N., 1979. Cone penetration tests on samples of dry Hokksund sand in a rigid walled chamber. Norwegian Geotechnical Institute, Internal report, Oslo.

Last, N.C., 1984. Seminar on Cone Penetration Testing in the Laboratory, Department of Civil Engineering, Southampton University.

Law, P.H., 2008. Investigations of mobility and impact behaviour of granular flows. Ph.D. thesis. The Hong Kong University of Science and Technology.

Lawrence, J.D., 1972. A catalog of special plane curves. Dover, Mineola.

Lee, S.W., Bolton, M.D., Mair, R.J., Hagiwara, T., Soga, K., Dasari, G.R., 2001. Centrifuge modelling of injection near tunnel lining. International Journal of Physical Modelling in Geatechnics 1, 9-24.

Lee, S.Y., 1990. Centrifuge modelling of cone penetration testing in cohesionless soils. Ph.D. thesis. University of Cambridge.

Lee, Y.S., Gong, H., 1987. Application of complex variables and pseudo-stress function to power-law materials and stress analysis of single rigid inclusion in power-law materials subjected to simple tension and pure shear. International Journal of Mechanical Sciences 29, 669-694.

Lehane, B.M., Gaudin, C., Schneider, J.A., 2005a. Scale effects on tension capacity for rough piles buried in dense sand. Geotechnique 55, 709-719.

Lehane, B.M., Jardine, R.J., Bond, A.J., Frank, R., 1993. Mechanisms of shaft friction in sand from instrumented pile tests. Journal of Geotechnical Engineering 119, 19-35.

Lehane, B.M., O'loughlin, C., Gaudin, C., Randolph, M.F., 2009. Rate effects on penetrometer resistance in kaolin. Geotechnique 59, 41-52.

Lehane, B.M., Schneider, J.A., Xu, X., 2005b. A review of design methods for offshore driven piles in siliceous sand. UWA Report GEO 5358.

Lehane, B.M., Schneider, J.A., Xu, X., 2005c. The UWA-05 method for prediction of axial capacity of driven piles in sand. Frontiers in Offshore Geotechnics: ISFOG, 683-689.

Lehane, B.M., White, D.J., 2005. Lateral stress changes and shaft friction for model displacement piles in sand. Canadian Geotechnical Journal 42, 1039-1052.

Leitman, M.J., Villaggio, P., 2009. Plastic zone around circular holes. Journal of Engineering Mechanics 135, 1467-1471.

Levadoux, J.-N., Baligh, M.M., 1986. Consolidation after undrained piezocone penetration. I: Prediction. Journal of geotechnical engineering 112, 707-726.

Lima, D.C.d., Tumay, M.T., 1991. Scale effects in cone penetration tests, Geotechnical Engineering Congress—1991. ASCE, pp. 38-51.

Lin, J., Wu, W., 2012. Numerical study of miniature penetrometer in granular material by discrete element method. Philosophical Magazine 92, 3474-3482.

Lings, M.L., Dietz, M.S., 2004. An improved direct shear apparatus for sand. Geotechnique 54, 245-256.

Lings, M.L., Dietz, M.S., 2005. The peak strength of sand-steel interfaces and the role of dilation. Soils and Foundations 45, 1-14.

Lipiec, J., Hatano, R., 2003. Quantification of compaction effects on soil physical properties and crop growth. Geoderma 116, 107-136.

Lipiec, J., Horn, R., Pietrusiewicz, J., Siczek, A., 2012. Effects of soil compaction on root elongation and anatomy of different cereal plant species. Soil and Tillage Research 121, 74-81.

Lipiec, J., Medvedev, V.V., Birkas, M., Dumitru, E., Lyndina, T.E., Rousseva, S., Fulajtar, E., 2003. Effect of soil compaction on root growth and crop yield in Central and Eastern Europe. International Agrophysics, 61-70.

Liu, W.W., 2010. Axisymmetric centrifuge modelling of deep penetration in sand. Ph.D. thesis. University of Nottingham.

Lo Presti, D., 1987. Mechanical behaviour of Ticino sand from resonant column tests. thesis. Ph. D. thesis, Politecnico Di Torino.

Loukidis, D., Salgado, R., 2010. Effect of relative density and stress level on the bearing capacity of footings on sand. Geotechnique 61, 107-119.

Love, A.E.H., 1927. A treatise on the mathematical theory of elasticity (4th Ed.). Cambridge University Press, London.

Lozhkin, V.N., 2001. A Generalization of Galin's Problem in the Theory of Ideal Plasticity. Journal of Mathematical Sciences 103, 363-367.

Lunne, T., Robertson, P.K., Powell, J.J.M., 1997. Cone Penetration Testing in Geotechnical Practice. Blackie Academic & Professional

Lyamin, A.V., Salgado, R., Sloan, S.W., Prezzi, M., 2007. Two-and three-dimensional bearing capacity of footings in sand. Geotechnique 57, 647-662.

Marshall, A.M., 2009. Tunnelling in sand and its effect on pipelines and piles. Ph.D. thesis. University of Cambridge.

Marshall, A.M., 2012. Tunnel-pile interaction analysis using cavity expansion methods. Journal of Geotechnical and Geoenvironmental Engineering 138, 1237-1246.

Martinez, A., Frost, J.D., Hebeler, G.L., 2015. Experimental Study of Shear Zones Formed at Sand/Steel Interfaces in Axial and Torsional Axisymmetric Tests. Geotechnical Testing Journal 38, 409–426.

Masri, R., Durban, D., 2006a. Dynamic cylindrical cavity expansion in an incompressible elastoplastic medium. Acta Mechanica 181, 105-123.

Masri, R., Durban, D., 2006b. Quasi-static cylindrical cavity expansion in an elastoplastic compressible Mises solid. International Journal of Solids and Structures 43, 7518-7533.

Materechera, S.A., Alston, A.M., Kirby, J.M., Dexter, A.R., 1992. Influence of root diameter on the penetration of seminal roots into a compacted subsoil. Plant and Soil 144, 297-303.

Materechera, S.A., Dexter, A.R., Alston, A.M., 1991. Penetration of very strong soils by seedling roots of different plant species. Plant and Soil 135, 31-41.

Maugis, D., 1992. Stresses and displacements around cracks and elliptical cavities: exact solutions. Engineering Fracture Mechanics 43, 217-255.

Mayne, P.W., 2001. Stress-strain-strength-flow parameters from enhanced in-situ tests, Proceedings, International Conference on In Situ Measurement of Soil Properties and Case Histories, Bali,Indonesia, pp. 27-48.

Mayne, P.W., Kulhawy, F.H., 1991. Calibration chamber database and boundary effect correction for CPT data, in: Huang, A.-B. (Ed.), Proceedings of the First International Symposium on Calibration Chamber Testing/ISOCCT1. Elsevier, New York, Potsdam, New York, pp. 257-264.

McDowell, G.R., 2002. On the yielding and plastic compression of sand. Soils and Foundations 42, 139-145.

McGarry, D., 2003. Tillage and Soil Compaction, in: García-Torres, L., Benites, J., Martínez-Vilela, A., Holgado-Cabrera, A. (Eds.), Conservation Agriculture: Environment, Farmers Experiences, Innovations, Socio-economy, Policy. Springer Netherlands, Dordrecht, pp. 307-316.

Mckenzie, B.M., Mullins, C.E., Tisdall, J.M., Bengough, A.G., 2013. Root–soil friction: quantification provides evidence for measurable benefits for manipulation of root‐tip traits. Plant, Cell and Environment 36, 1085-1092.

Menq, F.-Y., Stokoe, K.H., Di Benedetto, H., Doanh, T., Geoffroy, H., Sauzéat, C., 2003. Linear dynamic properties of sandy and gravelly soils from large-scale resonant tests. Di Benedetto et al., editor, Deformation Characteristics of Geomaterials, 63-71.

Mesri, G., Hayat, T., 1993. The coefficient of earth pressure at rest. Canadian Geotechnical Journal 30, 647-666.

Meyerhof, G.G., 1951. The Ultimate Bearing Capacity of Foudations. Geotechnique 2, 301-332.

Meyerhof, G.G., 1961. The ultimate bearing capacity of wedge shaped foundations, Proc. 5th Int. Conf on Soil Mechanics and Foundation Engineering, Paris, pp. 105-109.

Meyerhof, G.G., 1983. Scale effects of ultimate pile capacity. Journal of Geotechnical Engineering 109, 797-806.

Mickovski, S.B., Bransby, M.F., Bengough, A.G., Davies, M.C.R., Hallett, P.D., 2010. Resistance of simple plant root systems to uplift loads. Canadian Geotechnical Journal 47, 78-95.

Mindlin, R.D., 1964. Micro-structure in linear elasticity. Archive for Rational Mechanics and Analysis 16, 51-78.

Mirabet, V., Das, P., Boudaoud, A., Hamant, O., 2011. The role of mechanical forces in plant morphogenesis. Annual Review of Plant Biology 62, 365-385.

Misra, R.K., Dexter, A.R., Alston, A.M., 1986a. Maximum axial and radial growth pressures of plant roots. Plant and Soil 95, 315-326.

Misra, R.K., Dexter, A.R., Alston, A.M., 1986b. Penetration of soil aggregates of finite size. II. Plant roots. Plant and Soil 94, 59-85.

Misra, R.K., Gibbons, A.K., 1996. Growth and morphology of eucalypt seedling-roots, in relation to soil strength arising from compaction. Plant and Soil 182, 1-11.

Mitchell, J.K., Soga, K., 2005. Fundamentals of soil behavior (3rd Ed.). John Wiley & Sons, Inc.

Miura, S., Toki, S., 1982. A sample preparation method and its effect on static and cyclic deformation-strength properties of sand. Soils and Foundations 22, 61-77.

Mo, P.-Q., Marshall, A.M., Yu, H.-S., 2016. Interpretation of Cone Penetration Test Data in Layered Soils Using Cavity Expansion Analysis. Journal of Geotechnical and Geoenvironmental Engineering, 04016084.

Mo, P.Q., 2014. Centrifuge Modelling and Analytical Solutions for the Cone Penetration Test in Layered Soils. Ph.D. thesis. University of Nottingham.

Mo, P.Q., Marshall, A.M., Yu, H.S., 2014. Elastic‐plastic solutions for expanding cavities embedded in two different cohesive‐frictional materials. International Journal for Numerical and Analytical Methods in Geomechanics 38, 961-977.

Mo, P.Q., Yu, H.S., 2016. Undrained cavity expansion analysis with a unified state parameter model for clay and sand. Geotechnique, 1-13.

Monfared, S.D., 2014. Miniature Cone Penetration Test on Loose Sand. Master of Engineering Science thesis. The University of Western Ontario.

Mühlhaus, H.-B., Aifantis, E.C., 1991. A variational principle for gradient plasticity. International Journal of Solids and Structures 28, 845-857.

Muromachi, T., 1974. Experimental study on application of static cone penetrometer to subsurface investigations of weak cohesive soils, Proceedings of the European Symposium on Penetration Testing, ESOPT, Stockholm, pp. 285-293.

Muskhelishvili, N.I., 1963. Some basic problems of the mathematical theory of elasticity (4th Ed.). P. Noordhoff, Groningen, Netherlands.

Nakata, Y., Kato, Y., Hyodo, M., Hyde, A.F.L., Murata, H., 2001. One-dimensional compression behaviour of unuformly granded sand related to single particle crushing strength. Soils and Foundations 41, 39-51.

Nawaz, M.F., Bourrie, G., Trolard, F., 2013. Soil compaction impact and modelling. A review. Agronomy for Sustainable Development 33, 291-309.

Ngan-Tillard, D.J.M., Cheng, X.H., Van Nes, J., Zitha, P.L.J., 2005. Application of x-ray computed tomography to cone penetration tests in sands. Proceedings of the Geo-Frontiers, 24-26.

Ngan-Tillard, D.J.M., Verwaal, W., Mulder, A., Engin, H.K., Ulusay, R., 2011. Application of the needle penetration test to a calcarenite, Maastricht, the Netherlands. Engineering Geology 123, 214-224.

Nguyen, P.T., 1977. Mechanics of soil deformation in relation to root growth. Ph.D. thesis. University of Newcastle upon Tyne.

Ni, Q., Hird, C.C., Guymer, I., 2010. Physical modelling of pile penetration in clay using transparent soil and particle image velocimetry. Geotechnique 60, 121-132.

Ning, J., Ren, H., Guo, T., Li, P., 2013. Dynamic response of alumina ceramics impacted by long tungsten projectile. International Journal of Impact Engineering 62, 60-74.

Nix, W.D., Gao, H., 1998. Indentation size effects in crystalline materials: a law for strain gradient plasticity. Journal of the Mechanics and Physics of Solids 46, 411-425.

Ochensberger, W., Celigoj, C.C., Ulz, M.H., 2013. Amendment to the Galin plane elastoplastic solution. Journal of Engineering Mechanics 139, 1658-1662.

Oda, M., Koishikawa, I., Higuchi, T., 1978. Experimental study of anisotropic shear strength of sand by plane strain test. Soils and Foundations 18, 25-38.

Okamoto, T., Tsurumi, S., Shibasaki, K., Obana, Y., Takaji, H., Oono, Y., Rahman, A., 2008. Genetic dissection of hormonal responses in the roots of Arabidopsis grown under continuous mechanical impedance. Plant Physiology 146, 1651-1662.

Paik, K., Salgado, R., 2003. Estimation of active earth pressure against rigid retaining walls considering arching effects. Geotechnique 53, 643-654.

Paikowsky, S.G., Player, C.M., Connors, P.J., 1995. A dual interface apparatus for testing unrestricted friction of soil along solid surfaces. Geotechnical Testing Journal 18, 168-193.

Palmer, M.C., O'Rourke, T.D., Olson, N.A., Abdoun, T., Ha, D., O'Rourke, M.J., 2009. Tactile pressure sensors for soil-structure interaction assessment. Journal of Geotechnical and Geoenvironmental Engineering 135, 1638-1645.

Paniagua, P., Andò, E., Silva, M., Emdal, A., Nordal, S., Viggiani, G., 2013. Soil deformation around a penetrating cone in silt. Géotechnique Letters 3, 185-191.

Papamichos, E., Van Den Hoek, P., 1995. Size dependency of Castlegate and Berea sandstone hollow-cylinder strength on the basis of bifurcation theory, Proc. 35th US Symp. Rock Mechanics. Balkema Rotterdam, Netherlands, pp. 301-306.

Papanastasiou, P., Durban, D., 1997. Elastoplastic analysis of cylindrical cavity problems in geomaterials. International Journal for Numerical and Analytical Methods in Geomechanics 21, 133-149.

Parasyuk, O.S., 1948. An elastic-plastic problem with a non-biharmonic plastic state. Prikladnaya Matematika i Mekhanika 13, 367-370.

Parkin, A.K., Lunne, T., 1982. Boundary effects in the laboratory calibration of a cone penetrometer for sand, in: Verruijt, A., Beringen, F.L., Leeuw, E.H.D. (Eds.), Proceedings of the 2nd European Symposium on Penetration Testing, ESOPT-II, , Amsterdam. A.A.Balkema Publication, Rotterdam, pp. 761–768.

Perkins, S.W., Madson, C.R., 2000. Bearing capacity of shallow foundations on sand: A relative density approach. Journal of Geotechnical and Geoenvironmental Engineering 126, 521-530.

Phillips, R., Valsangkar, A.J., 1987. An experimental investigation of factors affecting penetration resistance in granular soils in centrifuge modelling. University of Cambridge Department of Engineering, Cambridge University, U.K.

Porcino, D., Fioravante, V., Ghionna, V.N., Pedroni, S., 2003. Interface behavior of sands from constant normal stiffness direct shear tests. Geotechnical Testing Journal 26, 1-13.

Pournaghiazar, M., Russell, A.R., Khalili, N., 2012. Linking cone penetration resistances measured in calibration chambers and the field. Géotechnique Letters 2, 29-35.

Rad, N.S., Tumay, M.T., 1987. Factors affecting sand specimen preparation by raining. Geotechnical Testing Journal 10, 31-37.

Randolph, M.F., 2003. Science and empiricism in pile foundation design. Geotechnique 53, 847-875.

Randolph, M.F., Dolwin, R., Beck, R., 1994. Design of driven piles in sand. Geotechnique 44, 427-448.

Richards, B.G., Greacen, E.L., 1986. Mechanical stresses on an expanding cylindrical root analog in antigranulocytes media. Soil Research 24, 393-404.

Rix, G.J., Mayne, P.W., 1993. G max-qc relationships for clays. Geotechnical Testing Journal 16, 54-60.

Rix, G.J., Stokoe, K.H., 1991. Correlation of initial tangent modulus and cone penetration resistance, International symposium on calibration chamber testing. Elsevier Publishing, New York. DTIC Document, pp. 351-362.

Robertson, P.K., Cabal, K.L., 2015. Guide to cone penetration testing for geotechnical engineering (6th Ed.). Gregg Drilling & Testing, Inc., California.

Rosenberg, Z., Dekel, E., 2008. A numerical study of the cavity expansion process and its application to long-rod penetration mechanics. International Journal of Impact Engineering 35, 147-154.

Roy, M., Tremblay, M., Tavenas, F., Rochelle, P.L., 1982. Development of pore pressures in quasi-static penetration tests in sensitive clay. Canadian Geotechnical Journal 19, 124-138.

Ruiz, S., Straub, I., Schymanski, S.J., Or, D., 2016. Experimental Evaluation of Earthworm and Plant Root Soil Penetration–Cavity Expansion Models Using Cone Penetrometer Analogs. Vadose Zone Journal 15.

Saada, A.S., 1974. Elasticity: theory and applications. Pergamon Press, Inc.

Sadeghi, A., Tonazzini, A., Popova, L., Mazzolai, B., 2013. Robotic mechanism for soil penetration inspired by plant root, Robotics and Automation (ICRA), 2013 IEEE International Conference on. IEEE, pp. 3457-3462.

Sadeghi, A., Tonazzini, A., Popova, L., Mazzolai, B., 2014. A novel growing device inspired by plant root soil penetration behaviors. PloS one 9, e90139.

Sagaseta, C., 1987. Analysis of undraind soil deformation due to ground loss. Geotechnique 37, 301-320.

Salgado, R., Mitchell, J.K., Jamiolkowski, M., 1997. Cavity expansion and penetration resistance in sand. Journal of Geotechnical and Geoenvironmental Engineering 123, 344-354.

Salgado, R., Mitchell, J.K., Jamiolkowski, M., 1998. Calibration chamber size effects on penetration resistance in sand. Journal of Geotechnical and Geoenvironmental Engineering 124, 878-888.

Salgado, R., Prezzi, M., 2007. Computation of cavity expansion pressure and penetration resistance in sands. International Journal of Geomechanics 7, 251-265.

Sanglerat, G., 1972. The penetrometer and soil exploration. Elsevier Publishing Company, Amsterdam.

Satapathy, S., 2001. Dynamic spherical cavity expansion in brittle ceramics. International Journal of Solids and Structures 38, 5833-5845.

Savin, G.N., 1970. Stress distribution around holes. National Aeronautics and Space Administration, Washington, D.C.

Schanz, T., Vermeer, P.A., 1996. Angles of friction and dilatancy of sand. Geotechnique 46, 145-151.

Schmertmann, J.H., 1978. Guidelines for cone penetration test. (Performance and design). U. S. Department of Transportation, Washington, D.C.

Schmidt, S., Gregory, P.J., Grinev, D.V., Bengough, A.G., 2013. Root elongation rate is correlated with the length of the bare root apex of maize and lupin roots despite contrasting responses of root growth to compact and dry soils. Plant and Soil, 1-10.

Schnaid, F., 1990. A study of the cone-pressuremeter test in sand. Ph.D. thesis. University of Oxford.

Schnaid, F., Lehane, B.M., Fahey, M., 2004. In situ test characterization of unusual geomaterials. Geotechnical and Geophysical Site Characterization 1, 49-74.

Schnaid, F., Yu, H.S., 2007. Interpretation of the seismic cone test in granular soils. Geotechnique 57, 265-272.

Schneider, J.A., 2007. Analysis of piezocone data for displacement pile design. Ph.D. thesis. University of Western Australia.

Schneider, J.A., Lehane, B.M., Schnaid, F., 2007a. Velocity effects on piezocone measurements in normally and over consolidated clays. International Journal of Physical Modelling in Geotechnics 7, 23-34.

Schneider, J.A., White, D.J., Lehane, B.M., 2007b. Shaft friction of piles driven in siliceous, calcareous and micaceous sands, Proceedings of the 6th International Offshore Site Investigation and Geotechnics Conference: Confronting New Challenges and Sharing Knowledge. Society of Underwater Technology, London. UK.

Selvadurai, A.P.S., 2000. Partial differential equations in mechanics 2. Springer Science & Business Media.

Shahrour, M.I., 2013. Behaviour of soil-structure interfaces subjected to a large number of cycles. Application to piles. Ph.D. thesis. University of Grenoble.

Sharma, P.K., Ingram, K., Harnpichitvitaya, D., 1995. Subsoil compaction to improve water use efficiency and yields of rainfed lowland rice in coarse-textured soils. Soil and Tillage Research 36, 33-44.

Siddiquee, M.S.A., Tanaka, T., Tatsuoka, F., Tani, K., Morimoto, T., 1999. Numerical Simulation of Bearing Capacity Characteristics of Strip Footing on Sand. Soils and Foundations 39, 93-109.

Silva, M.F., White, D.J., Bolton, M.D., 2006. An analytical study of the effect of penetration rate on piezocone tests in clay. International Journal for Numerical and Analytical Methods in Geomechanics 30, 501-527.

Silvestri, V., Fahmy, Y., 1995. Influence of apex angle on cone penetration factors in clay. ASTM Geotechnical Testing Journal 18, 315-323.

Sinnreich, J., 2011. The scaling effect of bored pile radius on unit shear capacity. International Journal of Geotechnical Engineering 5, 463-467.

Sokolnikoff, I.S., 1956. Mathematical theory of elasticity (2ed Ed.). McGraw-Hill New York.

Stafford, J.V., Tanner, D.W., 1983. Effect of rate on soil shear strength and soil-metal friction II. Soil-metal friction. Soil and Tillage Research 3, 321-330.

Stevenson, A.C., 1945. Complex potentials in two-dimensional elasticity. Proceedings of the Royal Society of London. Series A. Mathematical and Physical Sciences 184, 129-179.

Stolzy, L.H., Barley, K.P., 1968. Mechanical resistance encountered by roots entering compact soils. Soil Science 105, 297-301.

Strack, O.E., 2002. Analytic solutions of elastic tunneling problems. Ph.D. thesis thesis. Delft University of Technology.

Sudduth, K.A., Hummel, J.W., Drummond, S.T., 2004. Comparison of the Veris Profiler 3000 to an ASAE-standard penetrometer. Applied Engineering in Agriculture 20, 535.

Suzuki, Y., 2015. Investigation and interpretation of cone penetration rate effects. Ph.D. thesis. The University of Western Australia.

Suzuki, Y., Lehane, B.M., 2015. Analysis of CPT end resistance at variable penetration rates using the spherical cavity expansion method in normally consolidated soils. Computers and Geotechnics 69, 141-152.

Sweeney, B., 1987. Liquefaction evaluation using a miniature cone penetrometer and a large scale calibration chamber. Ph.D. thesis thesis. Stanford University.

Tan, F.S.C., 1990. Centrifuge and theoretical modelling of conical footings on sand. Ph.D. thesis thesis. Cambridge University.

Tatsuoka, F., Okahara, M., Tanaka, T., Tani, K., Morimoto, T., Siddiquee, M.S.A., 1991. Progressive failure and particle size effect in bearing capacity of a footing on sand, Geotechnical Special Publication, No. 27. ASCE, pp. 788-802.

Taylor, H.M., Gardner, H.R., 1963. Penetration of Cotton Seedlingn Taproots As Influenced By Bulk Density, Moisture Content, and Strength of Soil. Soil Science 96, 153-156.

Tehrani, F.S., Han, F., Salgado, R., Prezzi, M., Tovar, R.D., Castro, A.G., 2016. Effect of surface roughness on the shaft resistance of non-displacement piles embedded in sand. Geotechnique 66, 386-400.

Tejchman, J., Herle, I., 1999. A" Class A" Prediction of the Bearing Capacity of Plane Strain Footings on Sand. Soils and Foundations 39, 47-60.

Terzaghi, K., 1943. Theoretical soil mechanics. John Wiley & Sons, Inc., New York.

Thomas, D., 1965. Static penetration tests in London clay. Geotechnique 15, 174-179.

Timoshenko, S.P., Goodier, J.N., 1951. Theory of elasticity (2nd Edition). McGRAW-HILL.

Timoshenko, S.P., Goodier, J.N., 1970. Theory of elasticity (3rd Ed.). McGraw-Hill, Inc., London.

To, J., Kay, B.D., 2005. Variation in penetrometer resistance with soil properties: the contribution of effective stress and implications for pedotransfer functions. Geoderma 126, 261-276.

Tokar, G., 1990. Generalization of Galin's problem to frictional materials and discontinuous stress fields. International Journal of Solids and Structures 26, 129-147.

Tollner, E., Verma, B., 1987. Lubricated and non-lubricated cone penetrometer performance comparison in six soils. Transactions of the ASAE 30, 1611-1618.

Toolan, F.E., Lings, M.L., Mirza, U.A., 1990. An appraisal of API RP2A recommendations for determining skin friction of piles in sand, Proc. 22nd Offshore Technology Conference, Houston, Tex., pp. 33-42.

Toyosawa, Y., Itoh, K., Kikkawa, N., Yang, J.-J., Liu, F., 2013. Influence of model footing diameter and embedded depth on particle size effect in centrifugal bearing capacity tests. Soils and Foundations 53, 349-356.

Tracy, S.R., Black, C.R., Roberts, J.A., Dodd, I.C., Mooney, S.J., 2015. Using X-ray computed tomography to explore the role of abscisic acid in moderating the impact of soil compaction on root system architecture. Environmental and Experimental Botany 110, 11-18.

Tracy, S.R., Black, C.R., Roberts, J.A., Mooney, S.J., 2011. Soil compaction: a review of past and present techniques for investigating effects on root growth. Journal of the Science of Food and Agriculture 91, 1528-1537.

Tsagrakis, I., Efremidis, G., Aifantis, E.C., 2004. Size effects in thick-walled hollow cylinders: deformation versus flow theory of gradient plasticity. Journal of the Mechanical Behavior of Materials 15, 149-168.

Tsagrakis, I., Efremidis, G., Konstantinidis, A., Aifantis, E.C., 2006. Deformation vs. flow and wavelet-based models of gradient plasticity: Examples of axial symmetry. International Journal of Plasticity 22, 1456-1485.

Tsubakihara, Y., Kishida, H., Nishiyama, T., 1993. Friction between cohesive soils and steel. Soils and Foundations 33.

Tumay, M.T., Kurup, P., Boggess, R., 1998. A continuous intrusion electronic miniature cone penetration test system for site characterization, Proceedings, International Conference on Site Characterization, pp. 1183-1188.

Tumay, M.T., Titi, H.H., Senneset, K., Sandven, R., 2001. Continuous intrusion miniature piezocone penetration test in quick soil deposits, Proceedings of the Fifteenth

International Conference on Soil Mechanics and Geotechnical Engineering, Istanbul, Turkey, 27-31 August 2001. Volumes 1-3. AA Balkema, pp. 523-526.

Turner, J.P., Kulhawy, F.H., 1994. Physical modeling of drilled shaft side resistance in sand. Geotechnical Testing Journal 17, 282-290.

Ubeda-Tomás, S., Beemster, G.T., Bennett, M.J., 2012. Hormonal regulation of root growth: integrating local activities into global behaviour. Trends in Plant Science 17, 326-331.

Ueno, K., Miura, K., Maeda, Y., 1998. Prediction of ultimate bearing capacity of surface footings with regard to size effects. Soils and Foundations 38, 165-178.

Uesugi, M., Kishida, H., 1986a. Frictional resistance at yield between dry sand and mild steel. Soils and Foundations 26, 139-149.

Uesugi, M., Kishida, H., 1986b. Influence factors of friction between steel and dry sands. Soils and Foundations 26, 33-46.

Ugural, A.C., Fenster, S.K., 1995. Advanced strength and applied elasticity (3rd ed.). Prentice-Hall PTR, New Jersey, USA.

Unger, D.J., 2005. Perfectly plastic caustics for the opening mode of fracture. Theoretical and Applied Fracture Mechanics 44, 82-94.

Unger, D.J., 2010. Large plastic deformations accompanying the growth of an elliptical hole in a thin plate. Journal of Elasticity 99, 117-130.

Valentine, T.A., Hallett, P.D., Binnie, K., Young, M.W., Squire, G.R., Hawes, C., Bengough, A.G., 2012. Soil strength and macropore volume limit root elongation rates in many UK agricultural soils. Annals of Botany 110, 259-270.

Vardoulakis, I., Aifantis, E.C., 1989. Gradient dependent dilatancy and its implications in shear banding and liquefaction. Ingenieur-Archiv 59, 197-208.

Vardoulakis, I., Aifantis, E.C., 1991. A gradient flow theory of plasticity for granular materials. Acta Mechanica 87, 197-217.

Verruijt, A., 1997. A complex variable solution for a deforming circular tunnel in an elastic half-plane. International Journal for Numerical and Analytical Methods in Geomechanics 21, 77-89.

Vesic, A., 1977. Design of pile foundations. NCHRP synthesis of highway practice.

Vesic, A.S., 1963. Bearing capacity of deep foundations in sand. Highway Research Record.

Vesic, A.S., 1972. Expansion of cavities in infinite soil mass. Journal of Soil Mechanics and Foundations Division 98, 265-290.

Vesic, A.S., 1973. Analysis of ultimate loads of shallow foundations. Journal of Soil Mechanics and Foundations Division No. 1, 45-73.

Vollsnes, A.V., Futsaether, C.M., Bengough, A.G., 2010. Quantifying rhizosphere particle movement around mutant maize roots using time - lapse imaging and particle image velocimetry. European Journal of Soil Science 61, 926-939.

Voorhees, W., Farrell, D., Larson, W., 1975. Soil strength and aeration effects on root elongation. Soil Science Society of America Journal 39, 948-953.

Vrakas, A., 2016. Relationship between small and large strain solutions for general cavity expansion problems in elasto-plastic soils. Computers and Geotechnics 76, 147-153.

Waldron, L.J., Constantin, G.K., 1970. Soil resistance to a slowly moving penetrometer. Soil Science 109, 221-226.

Warren, T.L., Forrestal, M.J., 1998. Effects of strain hardening and strain-rate sensitivity on the penetration of aluminum targets with spherical-nosed rods. International Journal of Solids and Structures 35, 3737-3753.

Wernick, E., 1978. Skin friction of cylindrical anchors in non-cohesive soils, Symposium on Soil Reinforcing and Stabilising Techniques, Sydney, pp. 201-219.

Whalley, W., Lipiec, J., Stępniewski, W., Tardieu, F., 2000. Control and measurement of the physical environment in root growth experiments, in: Smit, A.L., Bengough, A.G., Engels, C., van Noordwijk, M., Pellerin, S., van de Geijn, S. (Eds.), Root methods: A handbook. Springer-Verlag Berlin Heidelberg, pp. 75-112.

Whalley, W.R., Dexter, A.R., 1993. The maximum axial growth pressure of roots of spring and autumn cultivars of lupin. Plant and Soil 157, 313-318.

Whalley, W.R., Leeds-Harrison, P.B., Clark, L.J., Gowing, D.J.G., 2005. Use of effective stress to predict the penetrometer resistance of unsaturated agricultural soils. Soil and Tillage Research 84, 18-27.

Whalley, W.R., To, J., Kay, B.D., Whitmore, A.P., 2007. Prediction of the penetrometer resistance of soils with models with few parameters. Geoderma 137, 370-377.

Whalley, W.R., Watts, C.W., Gregory, A.S., Mooney, S.J., Clark, L.J., Whitmore, A.P., 2008. The effect of soil strength on the yield of wheat. Plant and Soil 306, 237-247.

White, D.J., Bolton, M.D., 2005. Comparing CPT and pile base resistance in sand. Proceedings of the ICE-Geotechnical Engineering 158, 3-14.

White, D.J., Lehane, B.M., 2004. Friction fatigue on displacement piles in sand. Geotechnique 54, 645-658.

White, D.J., Take, W.A., Bolton, M.D., 2003. Soil deformation measurement using particle image velocimetry (PIV) and photogrammetry. Geotechnique 53, 619-631.

Whiteley, G.M., Dexter, A.R., 1981. The dependence of soil penetrometer pressure on penetrometer size. Journal of Agricultural Engineering Research 26, 467-476.

Whiteley, G.M., Dexter, A.R., 1983. Behaviour of roots in cracks between soil peds. Plant and Soil 74, 153-162.

Whiteley, G.M., Dexter, A.R., 1984. The behaviour of roots encountering cracks in soil-I. Experimental methods and results. Plant and Soil 77, 141-149.

Whiteley, G.M., Hewitt, J.S., Dexter, A.R., 1982. The buckling of plant roots. Physiologia Plantarum 54, 333-342.

Whiteley, G.M., Utomo, W.H., Dexter, A.R., 1981. A comparison of penetrometer pressures and the pressures exerted by roots. Plant and Soil 61, 351-364.

Wichtmann, T., Triantafyllidis, T., 2009. Influence of the grain-size distribution curve of quartz sand on the small strain shear modulus G max. Journal of Geotechnical and Geoenvironmental Engineering 135, 1404-1418.

Wu, H.C., Chang, K.J., 1978. Angled elliptic notch problem in compression and tension. Journal of Applied Mechanics 45, 258-262.

Wu, W., Ladjal, S., 2014. Scale effect of cone penetration in sand, 3rd International Symposium on Cone Penetration Testing,, Las Vegas, Nevada, USA, pp. 459-465.

Yamaguchi, H., Kimura, T., Fujii, N., 1976. On the influence of progressive failure on the bearing capacity of shallow foundations in dense sand. Soils and Foundations 16, 11-22.

Yamamoto, N., Randolph, M.F., Einav, I., 2009. Numerical study of the effect of foundation size for a wide range of sands. Journal of Geotechnical and Geoenvironmental Engineering 135, 37-45.

Yang, W., Hussein, M.F.M., Cox, C., Marshall, A., 2011. Physical and numerical modelling of ground-borne vibration from a surface source, Proceedings of the 8th International Conference on Structural Dynamics, EURODYN 2011, Leuven, Belgium, pp. 748-753.

Yang, Z., Jardine, R.J., Zhu, B., Foray, P., Tsuha, C., 2010. Sand grain crushing and interface shearing during displacement pile installation in sand. Geotechnique 60, 469-482.

Yarushina, V.M., Dabrowski, M., Podladchikov, Y.Y., 2010. An analytical benchmark with combined pressure and shear loading for elastoplastic numerical models. Geochemistry, Geophysics, Geosystems 11.

Yu, H.S., 1990. Cavity expansion theory and its application to the analysis of pressuremeters. thesis. University of Oxford.

Yu, H.S., 2000. Cavity expansion methods in geomechanics. Kluwer Academic Publishers, The Netherlands.

Yu, H.S., 2006. The First James K. Mitchell Lecture In situ soil testing: from mechanics to interpretation. Geomechanics and Geoengineering: An International Journal 1, 165-195.

Yu, H.S., Carter, J.P., 2002. Rigorous similarity solutions for cavity expansion in cohesive-frictional soils. International Journal of Geomechanics 2, 233-258.

Yu, H.S., Houlsby, G.T., 1991. Finite cavity expansion in dilatant soils: loading analysis. Geotechnique 41, 173-183.

Yu, H.S., Houlsby, G.T., 1995. A large strain analytical solution for cavity contraction in dilatant soils. International Journal for Numerical and Analytical Methods in Geomechanics 19, 793-811.

Yu, H.S., Mitchell, J.K., 1998. Analysis of cone resistance: review of methods. Journal of Geotechnical and Geoenvironmental Engineering 124, 140-149.

Yu, H.S., Rowe, R.K., 1999. Plasticity solutions for soil behaviour around contracting cavities and tunnels. International Journal for Numerical and Analytical Methods in Geomechanics 23, 1245-1279.

Zbib, H.M., 1994. Strain gradients and size effects in nonhomogeneous plastic deformation. Scripta Metallurgica et Materialia 30, 1223-1226.

Zbib, H.M., Aifantis, E.C., 1989. A gradient-dependent flow theory of plasticity: application to metal and soil instabilities. Applied Mechanics Reviews 42, S295-S304.

Zervos, A., Papanastasiou, P., Vardoulakis, I., 2008. Shear localisation in thick-walled cylinders under internal pressure based on gradient elastoplasticity. Journal of Theoretical and Applied Mechanics 38, 81-100.

Zhang, Y.D., Buscarnera, G., Einav, I., 2016. Grain size dependence of yielding in granular soils interpreted using fracture mechanics, breakage mechanics and Weibull statistics. Geotechnique 66, 149-160.

Zhao, J., 2011. A unified theory for cavity expansion in cohesive-frictional micromorphic media. International Journal of Solids and Structures 48, 1370-1381.

Zhao, J., Sheng, D., Sloan, S.W., 2007. Cavity expansion of a gradient-dependent solid cylinder. International Journal of Solids and Structures 44, 4342-4368.

Zhao, Y., 2008. In situ soil testing for foundation performance prediction. Ph.D. thesis thesis. University of Cambridge.

Zhou, H., Kong, G., Li, P., Liu, H., 2015. Flat Cavity Expansion: Theoretical Model and Application to the Interpretation of the Flat Dilatometer Test. Journal of Engineering Mechanics 142, 04015058.

Zhou, H., Kong, G., Liu, H., 2016. A semi-analytical solution for cylindrical cavity expansion in elastic–perfectly plastic soil under biaxial in situ stress field. Geotechnique, 1-12.

Zhou, H., Liu, H., Kong, G., 2014a. Influence of shear stress on cylindrical cavity expansion in undrained elastic–perfectly plastic soil. Géotechnique Letters 4, 203-210.

Zhou, H., Liu, H., Kong, G., Huang, X., 2014b. Analytical solution of undrained cylindrical cavity expansion in saturated soil under anisotropic initial stress. Computers and Geotechnics 55, 232-239.

Zhu, F., Clark, J.I., Phillips, R., 2001. Scale effect of strip and circular footings resting on dense sand. Journal of Geotechnical and Geoenvironmental Engineering 127, 613-621.

Zhu, H.T., Zbib, H.M., Aifantis, E.C., 1997. Strain gradients and continuum modeling of size effect in metal matrix composites. Acta Mechanica 121, 165-176.

Zohrabi, M., Fairfield, C.A., Sibbald, A., 1995. Boundary conditions and chamber size effects on CPT, Proc. Int. Symp. on Cone Penetration Testing, CPT'95, Linkoping, Sweden, pp. 363–368.